Thermodynamics, processing, and repellent release characteristics of the polymer/mosquito repellent system poly(lactic acid) (PLA)/ethyl butylacetylaminopropionate (IR3535)

Dissertation

zur Erlangung des Doktorgrades der Ingenieurwissenschaften
(Dr.-Ing.)

der

Naturwissenschaftlichen Fakultät II
Chemie, Physik und Mathematik

der Martin-Luther-Universität
Halle-Wittenberg

vorgelegt von

Frau Fanfan Du

Gutachter
1. Prof. Dr. René Androsch
2. Prof. Dr. Walter W. Focke

Datum der öffentlichen Verteidigung: 17.11.2023

Dedicated to my family!

For all their love and support

ACKNOWLEDGEMENTS

ABSTRACT

Mosquito-borne tropical diseases, such as malaria, are still a worldwide public health issue, causing hundreds of thousands of deaths each year. Compared to indoor mosquito bite protection, including the use of long-life insecticidal bed nets and indoor residual spraying, outdoor vector control is still underdeveloped. Therefore, developing effective outdoor vector control strategies is crucial to reduce the burden of mosquito-borne diseases. The purpose of this thesis was to develop a new wearable mosquito-repellent personal protection device by incorporating the bio-repellent ethyl butylacetylaminopropionate (IR3535) into biodegradable and biocompatible poly(L-lactic acid) (PLLA) for controlled release of repellent and to achieve long-term protection against mosquito bites and the transmission of diseases. In this dissertation, the thermodynamic miscibility, crystallization behaviors, industrial processing and repellent release characteristics of polymer/repellent PLLA/IR3535 system were studied.

Firstly, since gaining information about the thermodynamic miscibility may be complicated due to crystallization of PLLA, a non-crystallizable poly(D,L-lactic acid) (PDLLA) was employed to clarify possible liquid-liquid phase separation. The results reveal that PDLLA and IR3535 are miscible in the entire concentration range, with the glass transition temperature of solutions showing a negative deviation from the linear mixing rule, suggesting rather weak enthalpic interactions of the system components.

Secondly, when using crystallizable PLLA as a system component, demixing/phase separation occurs by cooling PLLA/IR3535 solutions from elevated temperature to low temperature which is based on crystallization-based solid-liquid thermally induced phase separation. The phase separation temperature increases with decreasing the cooling rate and IR3535 concentration. The crystallization rate of PLLA in PLLA/IR3535 solutions with PLLA content from 10 to 50 m% increases with PLLA content at the same crystallization temperature but decreases with crystallization temperature at the same composition. PLLA scaffolds host the mosquito-repellent in the intra- and interspherulitic pores. The pore sizes are tuneable by both the crystallization temperature and the polymer content, with intraspherulitic pore sizes increasing with crystallization temperature and IR3535 content.

Then, PLLA/IR3535 mixtures with polymer-rich composition were prepared by melt extrusion, extrusion-based 3D printing and electrospinning to realize personalized design for industrial application to prevent mosquito bites. Incorporation of the repellent IR3535 into PLLA by electrospinning allows for entrapping larger amounts of IR3535, exceeding 40 m%, compared to melt extrusion and 3D printing that up to 25 m%. IR3535 acts as a plasticizer for PLLA, resulting in a decrease in glass transition temperature as well as in the elastic modulus. Quantification of the release of IR3535 into the environment indicates a low release rate with a time constant of the order of magnitude of 1–2 years of extruded strands with a diameter of about 2 mm, 10 days of 3D-printed strands with a diameter of 300 μm and a few days of fibers with a diameter of 1 μm at body temperature, respectively.

In summary, the formation mechanism and fabrication techniques of polymer scaffolds/parts hosting functional repellent in this work can help to better understand and predict their structure in polymer/repellent or polymer/drug systems, as well as the release characteristics of repellent

/drug. It will also further provide guidance for the optimization of processing conditions of related polymer/solvent systems and pave the way for wider application in biomedical fields like tissue engineering and drug delivery, as well as in agriculture and food packaging.

LIST OF ABBREVIATIONS AND SYMBOLS

Chemicals and acronyms

3D	Three-dimensional
AM	Additive manufacturing
β-CD	Beta-cyclodextrin
BJ	Binder jetting
CAD	Computer-aided design
CAM	Computer-aided manufacturing
CDC	Centers for Disease Control
$CHCl_3$	Chloroform
CO_2	Carbon dioxide
DCM	Dichloromethane
DDR	Draw-down ratio
DDS	Drug delivery system
DDT	Dichlorodiphenyltrichloroethane
DEET	*N,N*-diethyl-3-methylbenzamide
DEPA	*N,N*-diethylphenylacetamide
DMF	*N,N*-dimethylformamide
EOs	Essential oils
EPA	Environmental Protection Agency
EtOH	Ethanol
EVA	Poly(ethylene-*co*-vinyl acetate)
FDM	Fused deposition modeling
HDPE	High density polyethylene
Icaridin	1-(1-Methylpropoxycarbonyl)-2-(2-hydroxyethyl) piperidine
IR3535	Ethyl butylacetylaminopropionate
IRS	Indoor residual spraying
ITNs	Insecticide-treated nets
L-L TIPS	Liquid-liquid thermally induced phase separation
LLDPE	Linear low-density polyethylene
LLINs	Long-lasting insecticidal nets
LP	Liquid paraffin
MJ	Material jetting
NG	Nucleation and growth mechanism
PA 6	Polyamide 6/Nylon 6
PA 66	Polyamide 66/Nylon-6,6
PAM	Pressure-assisted microsyringe
PBAT	Poly(butylene adipate-*co*-terephthalate)
PBS	Poly(butylene succinate)
PCL	Poly(ε-caprolactone)
PDI	Polydispersity index
PDLA	Poly(D-lactic acid)/Poly(D-lactide)
PDLLA	Poly(D,L-lactic acid)/Poly(D,L-lactide)

PE	Polyethylene
PET	Poly(ethylene terephthalate)
PGA	Poly(glycolic acid)
PHA	Poly(hydroxyalkanoate)
PLA	Poly(lactic acid)/Poly(lactide)
PLLA	Poly(L-lactic acid)/Poly(L-lactide)
PMD	*para*-Methane 3,8-diol
PMDA	Pyromellitic dianhydride
PMMA	Poly(methyl methacrylate)
PP	Polypropylene
PVA	Polyvinyl acetate
PVC	Polyvinyl chloride
SC	Stereocomplex
SD	Spinodal decomposition
SL	Sheet lamination
SLA	Stereolithography
SLS	Selective laser sintering
S-L TIPS	Solid-liquid thermally induced phase separation
TE	Tissue engineering
TIPS	Thermally induced phase separation
UCST	Upper critical solution temperature

Variables

d_a	Thickness of amorphous layer
d_c	Thickness of crystal lamellae
E'	Storage modulus of elasticity
E''	Loss modulus of elasticity
G'	Shear modulus of elasticity
LP	Long period
M_n	Number-average molar mass
M_w	Weight-average molar mass
$\tan \delta$	Loss factor
T_b	Boiling point
T_c	Crystallization temperature
T_{cc}	Cold crystallization temperature
T_g	Glass transition temperature
T_m	Melting temperature
T_m^0	Equilibrium melting temperature
X_c	Degree of crystallization
ΔH_c	Enthalpy of crystallization
ΔH_m	Enthalpy of melting
ΔH_m^0	Equilibrium enthalpy of melting
τ	Characteristic release-time of repellent
χ	Flory-Huggins interaction parameter

IV

Methods

AFM	Atomic force microscopy
DMA	Dynamic mechanical analysis
DSC	Differential scanning calorimetry
FSC	Fast scanning chip calorimetry
FT-IR	Fourier-transform infrared spectroscopy
GPC	Gel permeation chromatography
NMR	Nuclear magnetic resonance
POM	Polarized optical microscopy
SAXS	Small-angle X-ray scattering
SEM	Scanning electron microscopy
TGA	Thermogravimetric analysis
TMDSC	Temperature-modulated differential scanning calorimetry
WAXS	Wide-angle X-ray scattering
XRD	X-ray diffraction

TABLE OF CONTENTS

PREAMBLE

Tropical diseases transmitted by mosquitoes, such as malaria, dengue, yellow fever, chikungunya, zika, or lymphatic filariasis, occur worldwide, threatening the health of billions of people and posing hundreds of thousands of deaths each year. Climate change, the impact of environmental change on the habitat of vectors, rapid unplanned urbanization, the globalization of international exchange, trade and travel, more recently, the COVID-19 pandemic are some factors that result in the reemergence and dissemination of these arboviral infectious diseases. Various new technologies, including the use of sterile insect technique and transgenic and Wolbachia-infected mosquitoes, have been developed to break the transmission of pathogens.[1,2] However, they are not ready for large-scale implementation, and there are also some arguments on the release of genetically engineered organisms to the environment. With no cost-effective vaccine or medication available, the use of vector control insecticides/repellents remains the only key strategy to manage epidemics.[1]

The use of long-lasting insecticidal bed nets and indoor residual spraying recommended by the World Health Organization (WHO) has been effective in reducing indoor transmission, however, they do not provide protection when humans are outdoors where people spend more time during the day and early evening. The market has available products containing repellent, such as creams, aerosols, sprays, coils and roll-ons for personal protection against mosquitoes, however, which have a very short protection time and may need to be reapplied frequently. Therefore, it is imperative to develop new strategies and tools to obtain personal protection devices that are not only effective but also have long-term durability. Wearable polymer/mosquito-repellent personal protection devices that prolong the protection time by incorporating repellents into polymers, within the effective repellent concentration range, have attracted increasing attention and research.

In this dissertation, the biodegradable and biocompatible poly(L-lactic acid) (PLLA), as an alternative to petroleum-based polymers, and the bio-repellent ethyl butylacetyl-aminopropionate (IR3535), even used for pregnant women and children, were investigated to obtain wearable mosquito-repellent personal protection devices with a low-release rate of repellent and sufficient efficiency to prevent mosquito bites. The thermodynamic miscibility, crystallization behaviors, industrial processing routes and repellent release characteristics of the polymer/repellent PLLA/IR3535 system were systematically studied. The observed results and corresponding interpretations are presented in this dissertation in form of research publications, which are described briefly below.

At first, the phase behavior of non-crystallizable poly(D,L-lactic acid) (PDLLA) and IR3535 was investigated, as the crystallization of PLLA may obscure the thermally induced phase separation (TIPS) information in the course of formation of PLLA scaffolds hosting repellent IR3535. The miscibility of PDLLA and IR3535 in the entire composition range was analyzed by cloud-point measurements and glass transition temperature by using conventional differential and fast scanning chip calorimetry (DSC and FSC) combined with *in-situ* liquid evaporation for controlled change in system composition (Chapter 4.1).

Then, crystallizable PLLA as a system component was used to form polymer scaffolds accommodating the repellent IR3535 by TIPS. The demixing behavior/phase separation was demonstrated by cloud-point measurements and DSC. The influences of the polymer/repellent ratio and conditions of solution-crystallization, including the cooling rate for non-isothermal crystallization and crystallization temperature for isothermal crystallization, on the final scaffold structures were evaluated (Chapter 4.2).

The interior architecture of fabricated scaffolds/devices is generally determined by the processing technique. Three different industrial technologies, melt extrusion, extrusion-based three-dimensional (3D) printing and electrospinning, were applied for the PLLA/IR3535 system to obtain products in different shapes to prevent mosquito bites. The effects of processing conditions and parameters on the morphology, thermal and mechanical properties, and crystalline structure of the processed parts were investigated (Chapters 4.3, 4.4, 4.5). The repellent-release kinetics was obtained on individual extruded/printed strands and electrospun fibers and depends on the evaporation temperature and the IR3535 content.

Since wearable biopolymer/mosquito-repellent protection devices have meaningful and potential prospects in preventing mosquito bites and as a result reducing the infection numbers of tropical diseases, this dissertation, ranging from the basic research of the PLA/IR3535 system to the industrial processing, like melt-extrusion, electrospinning and advanced 3D-printing techniques, provides important and beneficial guidance for further developments of long-lasting wearable mosquito-repellent personal protection devices. A schematic diagram showing the outline of the dissertation is shown in Figure I:
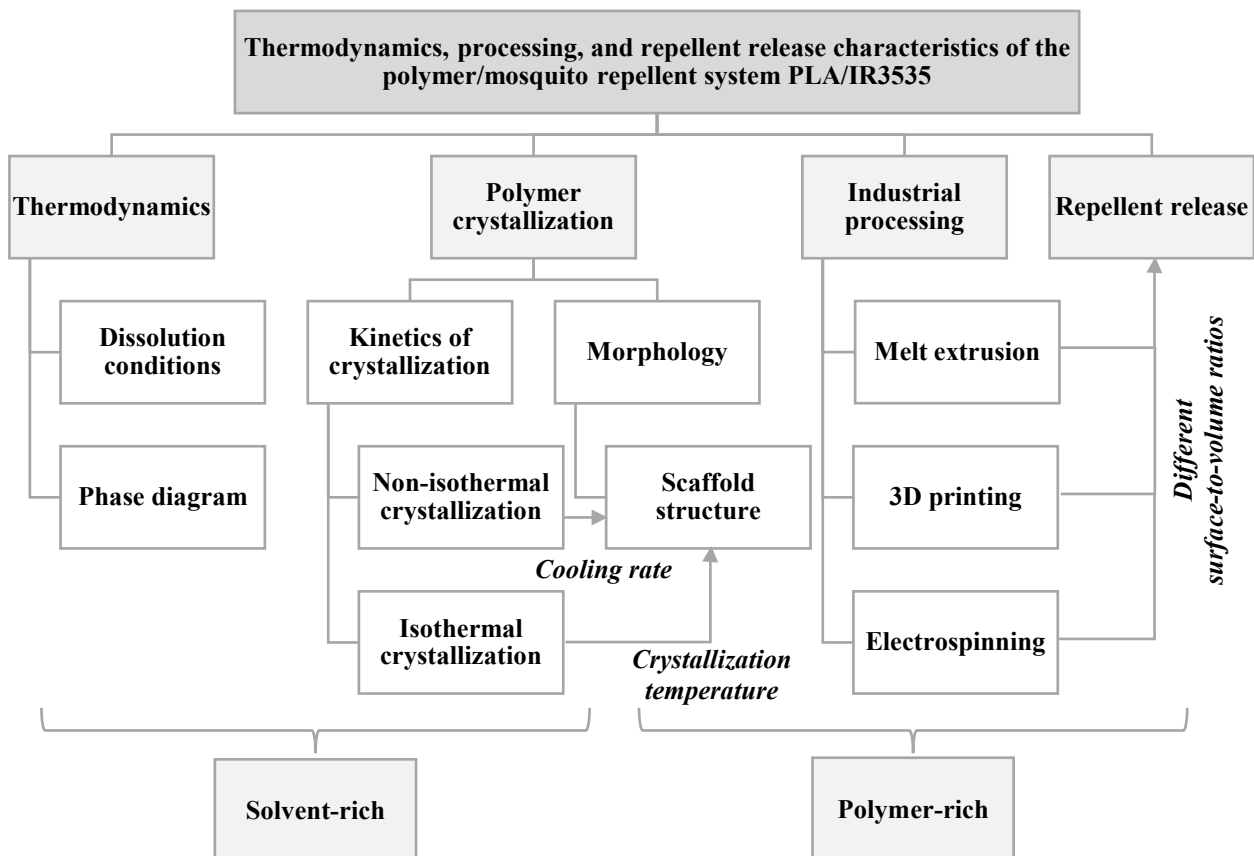
Figure I. Outline of the dissertation.

1. INTRODUCTION

1.1 Background of mosquito-bite protection

1.1.1 Mosquito-borne tropical diseases

Vector-borne diseases, mainly caused by mosquito-transmitted parasites and viruses, account for more than 17 % of all infectious diseases, resulting in more than 700 000 deaths each year.[3] By 2030, about 50 % of the world's population is expected to be at risk of these vector-borne diseases.[3] Vectors are living organisms, including mosquitoes, ticks, fleas, lice, sandflies and other arthropods, capable of transmitting infectious pathogens between humans, or from animals to humans.[4]

Mosquito-borne tropical diseases, such as malaria, lymphatic filariasis, dengue, yellow fever, chikungunya, zika, or Japanese encephalitis, occur at the global scale and involve a wide range of viral and other pathogenic agents, posing hundreds of thousands of deaths annually. Malaria is a leading cause of global morbidity and mortality. According to the latest world malaria report from WHO, approximately 247 million cases of malaria and 619 000 malaria-related deaths occurred worldwide in 2021.[5] This represents about 2 million more cases compared to 245 million in 2020, and 51 000 more deaths compared to the first year of pandemic. During the two peak years of the COVID-19 pandemic (2020–2021), some deaths were related to disruptions in the provision of malaria prevention, diagnosis and treatment. In 2021, 95 % of malaria cases and 96 % of malaria deaths occurred in Africa. Children under 5 years old were the most vulnerable group, accounting for about 80 % of all malaria deaths in the African region.[6] The WHO Western Pacific, Eastern Mediterranean, the Americas and South-East Asia regions also report significant numbers of cases and deaths. In addition, mosquito bites can inflict secondary infection, discomfort, pain, and allergic reactions in susceptible individuals, and systemic reactions like hives and angioedema of the skin. Figure 1 shows the incidence of Malaria in 2020.[7] Most cases occurred in Africa and there is no country in the European region that reported cases of malaria.
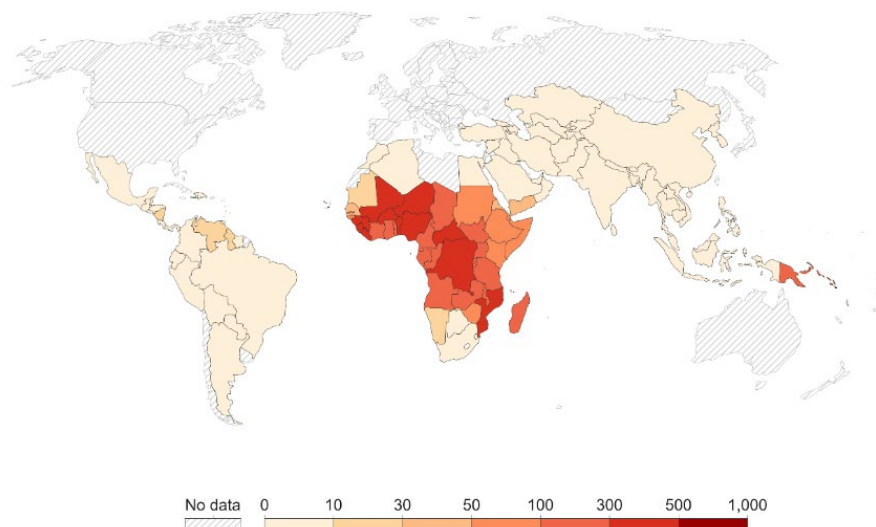
Figure 1. Incidence of malaria worldwide in 2020. Incidence is the number of new cases of malaria in a year per 1000 population at risk. Image is obtained from World Health Organization (via World Bank).[7]

Mosquito-borne diseases are spread to individuals through the bite of an infected mosquito.[8] When one person gets bitten by a mosquito carrying the parasite of diseases, the parasite enters his bloodstream and is then carried to the organs, like liver, where it multiplies. If a mosquito bites one person with malaria, it will get infected and then transmit the parasite to the next person when it bites, continuing the cycle of transmission.[9] There are more than 3500 species of mosquitoes in the world, and they are very adaptable and widely distributed, from tropical to temperate regions, and even in the Arctic.[10] Nevertheless, not all species of mosquito bite and transmit diseases. There are probably fewer than 10 species of mosquitoes that specifically bite people, but it is these 10 species that transmit most human diseases.[11] Mosquitoes are divided into males and females. Generally, male mosquitoes feed on nectar and do not suck blood, while the female mosquitoes need to suck blood because they need a lot of protein when laying eggs. However, there is no protein in nectar, only the protein in the blood of humans and animals can meet their needs. Typically, there are three categories of mosquitoes that transmit diseases. The first kind is the *Anopheles* mosquito that transmits malaria, which is the most serious and deadly disease in tropical regions. The second kind is the *Culex* mosquito, our common house mosquito, which transmit the West Nile fever and Japanese encephalitis virus. The third kind is the *Aedes* mosquito, known as the flower mosquito, which transmits diseases such as dengue fever, yellow fever, and zika. Moreover, not all mosquitoes transmit diseases under the same environmental conditions: some species feed at night while others feed during the day. Table 1 shows some important mosquito species and the diseases they transmit and the corresponding pathogen types.

Table 1. Mosquito species and the diseases they transmit and the corresponding pathogen types.[4,12,13]

Mosquito species	Caused Diseases	Type of pathogen
Anopheles	Malaria	Parasite
	Lymphatic filariasis	Parasite
Culex	Japanese encephalitis	Virus
	Lymphatic filariasis	Parasite
	West Nile fever	Virus
Aedes	Chikungunya	Virus
	Dengue fever	Virus
	Lymphatic filariasis	Parasite
	Rift Valley fever	Virus
	Yellow fever	Virus
	Zika	Virus

1.1.2 Protection methods

In response to this issue, one of the top threats to global health, a two-pronged approach is commonly used to control mosquito-borne diseases in impoverished tropical and sub-tropical countries. The first is parasite control by means of diagnosing/detecting disease parasites and treating infected people, as well as intermittent preventive treatments for pregnant women, and the second is vector control. For parasite control, the current frontline drugs for the treatment

of malaria are Artemisinin-based drugs or their combination with other drugs, however, the parasites have been developing increasing resistance to these drugs.[5] Over the past half-century, every generation of antimalaria drugs initially created great hope but quickly failed, which has been observed repeatedly. At present, there is no obvious new drug/candidate identified for large-scale production to replace the Artemisinin-based treatment drugs, which means this pipeline of malaria control methods is being compromised and will be sub-optimal. In terms of vector control, there is a wide range of strategies, which are mainly classified into chemical and non-chemical methods. The chemical methods include the use of insecticide-treated materials as long-lasting insecticidal nets (LLINs) and Indoor Residual Spray (IRS), while non-chemical methods involve the use of biological and genetic innovations. LLINs and IRS are highly effective in preventing malaria transmission and are recommended for use in areas with moderate to high malaria transmission. Biological methods include the utilization of natural predators, such as fish or insects, to control mosquito larvae, while genetic innovations involve the use of gene-editing tools to insert a new gene or induce alteration or silencing a particular gene or release mass-reared sterile males in a particular region to suppress an insect population.[1] The potential limitation of biological control methods is that they may be less effective in areas with high levels of environmental degradation or pollution, which can reduce the effectiveness of natural predators and other biological control agents. Additionally, introducing non-native species as biological control agents or the use of genetically modified mosquitoes can sometimes have unintended consequences, such as the disruption of local ecosystems or potential impacts on biodiversity. The ongoing efforts on developing vaccines for mosquito-transmitted diseases are put for several years, however, an effective vaccine is still challenging due to the complex nature of the pathogens and the way they interact with the human immune system.[5] Besides, ensuring widespread distribution and uptake of vaccines in the communities most affected by these diseases can be difficult, and requires collaboration between governments, healthcare providers, and local communities.[5]

Long-lasting insecticidal nets (LLINs)

The use of insecticide-treated nets (ITNs), particularly LLINs, has been a key factor in the global decline of mosquito-borne diseases since 2000. An ITN, usually a bed net, is designed to physically obstruct mosquitoes, while also being treated with safe, residual insecticide for killing and repelling mosquitoes that carry infectious parasites, thus reducing the risk of mosquito-borne diseases.[14] LLINs are low-cost and easy-to-implement methods for malaria prevention. Sleeping under an LLIN is regarded as one of the most effective strategies to prevent malaria, as it creates a dual defense by forming both physical and chemical barriers against mosquitoes. When mosquitoes try to bite someone sleeping under an LLIN, they are not only blocked by the netting but also killed/repelled by the insecticide coating on this netting,[15] as shown in Figure 2a. However, LLINs have limitations, such as requiring regular washing to maintain their insecticidal properties and providing protection only during sleeping hours. In addition, there are concerns about the emergence of vector resistance to insecticides, particularly pyrethroids, in some countries in Africa. Despite these limitations, LLINs remain a valuable tool in malaria control and have contributed significantly to the reduction of malaria burden worldwide.

Indoor residual spraying (IRS)

Many malaria vectors are regarded as "endophilic", to put it another way, the mosquito vectors rest inside houses after feeding on a blood meal. These mosquitoes are particularly vulnerable to IRS control,[16] which involves spraying insecticides on the interior walls and ceilings of houses to kill resting mosquitoes, as presented in Figure 2b. IRS is not a method that directly prevents people from being bitten by mosquitoes, instead, it commonly kills mosquitoes if they settle on the sprayed surface and come into contact with the insecticide. Indoor residual insecticide spraying with dichloro-diphenyl-trichloroethane (DDT) is the most used chemical method in the fight against mosquitoes, but DDT cannot last long and is regarded as an organic pollutant, which can persist in the environment for many years and has been linked to health issues such as low sperm counts, testicular anomalies, premature delivery of fetuses, and small for gestational age fetuses.[17] Furthermore, mosquitoes are developing resistance to DDT, making it less effective as a control measure.
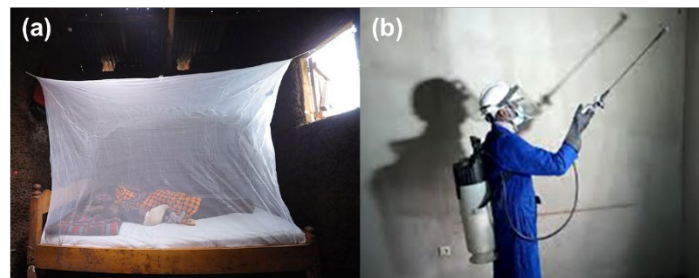
Figure 2. LLIN (a) and IRS (b) protection. Images are obtained from Ref. [18] and Ref. [19].

Outdoor protection

Compared to indoor vector control against mosquito bites, including LLINs and IRS, outdoor vector control is still underdeveloped.[20] Results show there is a much higher occurrence of mosquito-human biting activities outdoors compared to indoors, as well as during the early parts of the night, implying a higher potential for outdoor malaria transmission.[21] It was found that the biting behavior of mosquitoes conducted outdoors is related to the height above ground, but not the specific body part. The bite distribution of human beings is shown in Figure 3. Mosquitoes prefer to bite the human body area below knee whatever standing or seating, while biting all body areas except the head when laying down.[20]

Some outdoor vector interventions include environmental management, mosquito traps and personal protective measures. Environmental management includes removal of mosquito breeding sites by eliminating standing water in and around households and communities. Mosquito traps are devices that attract and capture mosquitoes by carbon dioxide, light, heat, or chemical attractants. Personal protective measures include the use of repellents, mosquito nets/tents and protective clothing. Since antiquity, people have known how to use repellents. Burning plant parts to create smoke or hanging plants indoors or sprinkling leaves on the floor, or applying herbs or essential oils extracted from plants on the body are common and indigenous techniques.[22] Historically, the use of repellents to protect individuals from mosquito bites has been recognized as a part of a larger integrated vector-borne disease control strategy. There are a variety of mosquito repellents available on the market, both natural and synthetic,
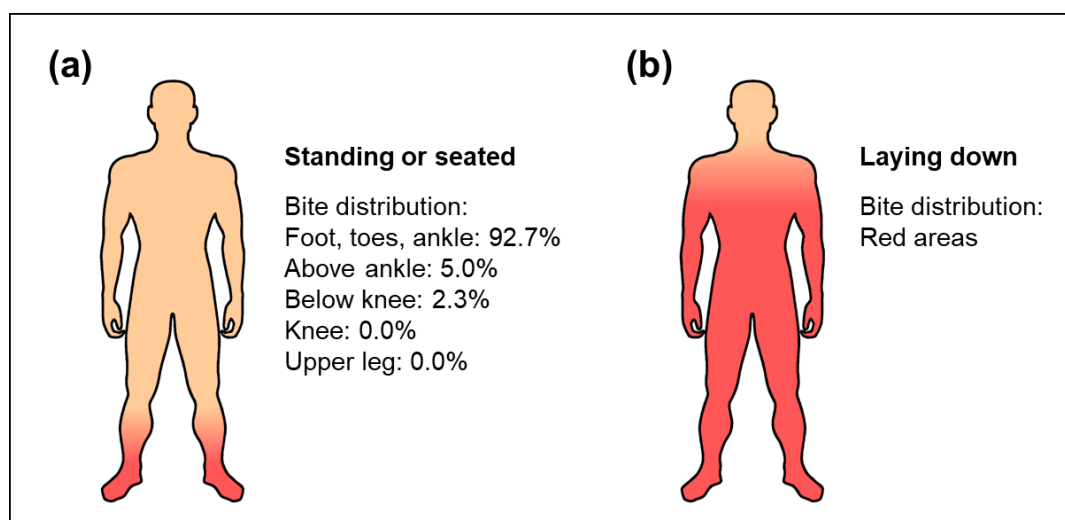
Figure 3. Red areas represent the preferred areas of mosquito biting on the human body, at standing or seated humans (a) and at people lying flat on the ground (b). Images were adapted according to Ref. [20] with permission from Springer.

in the form of sprays, aerosols, candles, coils, sticks and other topical applications including creams and lotions for personal protection to repel mosquitoes.[23]

1.1.3 Mosquito repellents

The word ''repellent'' originated from Latin verb ''*repellere*'', which means ''*to drive back*'' or ''*to refuse*''.[24] Therefore, repellents are chemically volatile substances that cause the insects to move in the opposite direction of the stimulus.[25] The action mechanism of repellents, whether natural or synthetic, is related to forming a vapor barrier around the skin with an unpleasant odor to the insect, which deflects its path preventing contact with the host.[24,26] Repellents reduce the risk of landing and biting by hematophagous insects, like mosquitoes, which can lead to the spread of numerous infectious diseases and allergic reactions.

Natural repellents

Currently, the use of natural repellents extracted from plants in a sustainable manner has attracted interest worldwide since they are considered safer, environmentally friendly, biodegradable, cheaper and more easily accessible. Several types of plant compounds have been found to exhibit some repellent activity, including nitrogenous compounds (mainly alkaloids), phenols, terpenes, quinones, nitriles, furans, and lactones.[27,28] Natural repellents are typically essential oils (EOs), including citronella oil, lemon eucalyptus oil, lavender, cinnamon oil, thyme oil, Greek catmint oil, soybean oil, tea tree oil, Geraniol, etc.[26,28,29] Citronella oil, first registered as a repellent by the United States Environmental Protection Agency (US EPA), is the most common natural EO against mosquitoes. Limonene is a natural chemical, with a lemon-like flavor and smell/odor, used in many food products, soaps and perfumes. Limonene is also a registered active ingredient used as insecticide, insect repellent, and dog and cat repellent.[30] *para*-Methane 3,8-diol (PMD), discovered in the 1960s during mass screenings of plants used in Chinese traditional medicine, is a potent natural repellent extracted from the leaves of lemon eucalyptus trees.[31,32] PMD, also known as Quwenling, has a lower vapor pressure than volatile monoterpenes found in most plant oils, conferring a longer protection.[33] It is noted that a main component of lemon eucalyptus oil is citronellal, with a content of 85 %,

which is one of the most effective botanical repellents, however, it is highly volatile, resulting in a short protection time.[28] Eucalyptol, also known as 1,8-cineole, is a natural compound found in many plants, including eucalyptus, tea tree, and lavender.[28] 1,8-cineole has been found to have some insecticidal and repellent activity against mosquitoes and other pests. However, its effectiveness as a repellent may vary depending on the species of mosquito and the applied concentration of the compound.[34–36]

Although natural repellents have high consumer acceptance and are effective when freshly applied, most essential oils evaporate quickly and thus provide a short protection time. In addition, the low boiling point of natural repellents limits their incorporation into most polymers because large amounts of repellent are lost during processing.

Synthetic repellents

Synthetic repellents are manufactured by the chemical industry on a large scale.[26] The main synthetic repellents such as *N,N*-diethyl-3-methylbenzamide (DEET), ethyl butylacetyl-aminopropionate (IR3535), 1-(1-Methylpropoxycarbonyl)-2-(2-hydroxyethyl) piperidine (Icaridin/Picaridin), *N,N*-diethylphenylacetamide (DEPA) and Permethrin (synthetic pyrethroid) are shown in Table 2. The abbreviations of repellent names in the above parentheses are either trade names or general acronyms. In the following chapters, mostly abbreviations are used.

DEET is the most effective/strongest repellent, being the gold-standard of repellents,[37] developed by the U.S. Army in 1946 for protection military personnel in insect-infested areas and registered and used by the general public in 1957 against various types of hematophagous arthropods.[38] Although it is the most toxic of repellents available, however, it is still one of the most used and reference compounds for repellent efficacy studies. The mechanism of action of DEET is interfering with receptors in insect antennae that detect the primary attractants emitted by humans and other animals.[39]

IR3535, with a chemical structure similar to that of the natural substance β-alanine —a β amino acid, being a component of pantothenic acid (Vitamin B5)— developed by Merck in the mid-1970s and registered (licensed for sale) as an active ingredient until 1999.[40,41] IR3535 is reported as a promising bio-repellent[42,43] since it shows less adverse side effects on human beings and the environment. Based on information from the Centers for Disease Control (CDC) and EPA, IR3535 is considered safe for the use of pregnant women and children.[44–46] It causes less irritation to mucous membranes and possesses lower oral and dermal toxicity than DEET. Moreover, no toxicity has been reported so far. Thus, it could be an attractive alternative to DEET in disease-inflicted endemic regions, although it requires frequent reapplication every 6–8 h.[24]

Icaridin, also called picaridin, KBR 3023 and Bayrepel[TM], is a synthetic repellent developed by Bayer in the 1980s based on molecular modeling.[41] It was made to resemble the natural compound piperine, which is found in the plants that can produce black pepper.[47] Icaridin is considered to have low toxicity and less dermatologic and olfactory irritation. Additionally, it does not damage plastics and synthetics. The effectiveness of picaridin is on par with DEET, nevertheless, reapplication is required every 4–6 h.[48]

Permethrin is an odorless, biodegradable synthetic pyrethroid insecticide that is chemically similar to the natural insecticide pyrethrin, which is derived from the extract of chrysanthemum flower.[49] In 1979, it was registered as both a repellent and an insecticide. It is the most common insecticide used on fabrics, like clothing, bed nets, etc., and acts via insect's nervous system by blocking the movement of sodium ions into the nerve cells, leading to muscle spasms, paralysis and deaths.[24,49,50] Permethrin requires direct contact with arthropods, making this compound poorly suited for skin application. Impregnating permethrin individually, either by spraying or dipping, into the clothing is considered an affordable and cost-effective technique, but it provides less consistent protection and is not as long-lasting as pre-treated clothing, which allows permethrin to be impregnated into the fabric during the manufacturing process.[51] While individually treated clothing may require reapplication of permethrin after several washes, typically five washes recommended,[52] pre-treated clothing may retain its effectiveness for several washes or even up to several months.[51] However, pre-treated clothing is generally more expensive than individually treated. In addition, permethrin may have harmful effects on the environment if not used properly, for example, it can harm aquatic organisms such fish, and other beneficial insects like bees and butterflies, which are important for pollination and maintaining the balance of ecosystems.[49,53,54]

DEPA, a compound developed around the same time as DEET, arose as an alternative repellent to DEET in response to the unavailability of a key chemical component, 3-methylbenzoic acid, for the manufacture of DEET in India.[55] It has been found to have similar levels of repellency to DEET. DEPA does not exhibit cytotoxicity or mutagenicity, making it suitable for direct application to the skin. However, it has moderate oral toxicity and low to moderate dermal toxicity which limits its use.

Table 2 summarizes safety information of synthetic repellents and their general information.

Criteria for selection of repellents

There are several principles that need to be considered when choosing an insect repellent, including (a) Efficiency; repellents should be efficient and have a long protection time, being over 8 hours to avoid successive reapplication.[26] (b) Toxicity and acceptance; repellents should not be toxic to human beings nor have an unpleasant odor or have an irritating effect on the skin, clothes, etc. Compared to synthetic repellents, natural repellents are preferred.[56] (c) Costs; repellents should be cost-effective for economic viability making the final product affordable for people from poor regions, where mosquito-borne diseases are most prevalent. (d) Stability; thermal stability is required to withstand high polymer processing temperatures. The repellent should be chemically stable, such as stable towards moisture from sweating and sunshine.[57] (e) Volatility; volatility is generally related to vapor pressure and diffusivity in the air. An effective repellent should be the least volatile and then forms a gas barrier to offer long-lasting protection in the effective range. (f) Phase behavior; at room temperature solid repellents are preferred to liquid repellents since solid repellents are easier to formulate into long-life controlled-release polymer systems than liquid repellents. Regarding liquid repellents, they are more likely dissolve and swell the polymer, which influences the dimension stability as the repellents migrate from polymer bulk to the surface and then evaporate/release over time causing shrinkage of products.[26,56,57]

Table 2. Safety information of synthetic repellents and their general information.

Repellent	Safety information[58]						Physical properties		Ref.
	Oral	Inhalation	Dermal	Eye Irritation	Skin Irritation	Others[26]	T_g (°C)	T_b (°C)	
DEET [a]	Low	Very low	Low	Low	Very low	Repellent with the strongest effect, standard reference, skin permeability, attacks plastic materials, not recommended for children and pregnant women, efficient against mosquitoes and ticks.	-75	284.2	[59,60]
IR3535 [b]	Very low	Very low	Very low	Moderate	Very low	Low toxicity, very few adverse effects, active against flies and mosquitoes.	-88	Slightly below 300 °C; about 110 °C at 0.02 kPa	[45,61]
Icaridin [c]	Low	Very low	Low	Low	Very low	Low toxicity, not eyes or skin irritating, effective against mosquitoes, flies and ticks.	No freezing, melting, crystallization or glass transition was observed at 20–170 °C	296	[62]

10

Table 2 (*continued*)

Repellent	Safety information[58]						Physical properties		Ref.
	Oral	Inhalation	Dermal	Eye Irritation	Skin Irritation	Others[26]	T_g (°C)	T_b (°C)	
Permethrin [d]	Low	No data	Low	Low	Very low	Highly toxic to environment, few adverse effects for humans, active against flies and mosquitoes.	Melting point: 33–35 °C	305	[63]
DEPA [e]	Moderate	Low	Low to moderate	No data	Low	Low toxicity, very few adverse effects, multi-insect repellent, active against flies and mosquitoes.	No data	288–291	[64, 65]

Molecular formula of repellents:

a   b   c   d   e

11
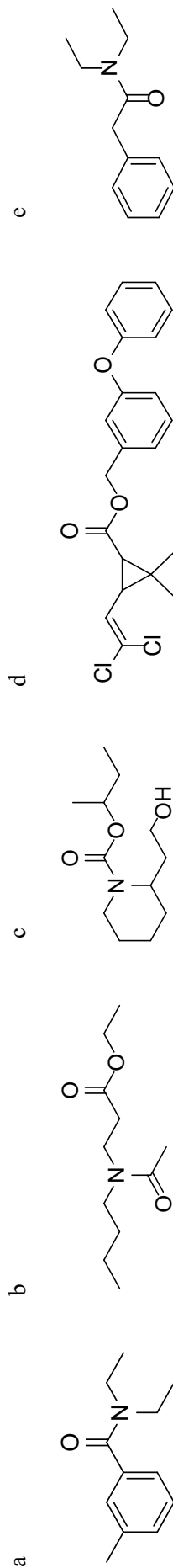
1.2 Repellent-release devices based on polymer scaffolds

1.2.1 Repellent release devices

As discussed above, the majority of natural or synthetic repellents exist in the form of classical formulations. These classical formulations include creams, roll-ons, aerosols, sprays, candles, coils, sticks, protective clothing and insecticide-treated clothing/bed nets/tents for personal protection against mosquitoes, however, they have limited effectiveness and durability. Electric motivated mosquito liquids or mats attached to a vaporizer are a popular method, however, the usage of vaporizer is restricted to the places with convenient electricity supply. Typically, repellents evaporate according to a zero-order rate law that the evaporation rate depends on temperature and vapor pressure.[66] Thus, the key to developing a long-lasting repellent is slowing down the evaporation rate. However, a minimum repellent evaporation rate is required to maintain effective. Taking DEET as an example, the minimum evaporation rate to repellent mosquitoes is 2.6 $\mu g/(cm^2 \cdot h)$ studied by Reifenrath and Robinson.[67] The encapsulation and release of the repellents from several polymer carriers/reservoirs as new formulations has emerged as an alternative approach for the development of invention of repellent release devices in outdoor environment for long protection. As for the carriers/reservoirs of repellents, they can include nanoemulsions/microemulsions (core composed of liquid lipid material wrapped by a surfactant monolayer), solid lipid nanoparticles (core composed of solid lipid material and wrapped by a surfactant monolayer), polymer micelles (micelles formed by amphiphilic block copolymers that self-assemble in water to form a core-shell structure; the hydrophobic blocks of the copolymer aggregate to form the inner core, while the hydrophilic blocks form a shell around the core, stabilizing the micelle in water), cyclodextrins (inclusion complexes), liposomes (aqueous core enclosed by a phospholipid bilayer), micro/nanofibers and microporous polymer,[26,28,68] as shown in Figure 4.

Microemulsions are thermodynamically stable dispersions of two immiscible liquids (usually oil and water) stabilized by a surfactant and/or a co-surfactant. Microemulsions have lower production costs due to little and no organic solvents being needed and are easy to prepare, however, high surfactant levels are required.[68] Compared to microemulsions, nanoemulsions require less surfactant and have good long-term kinetic stability due to the small droplet size, which makes them less prone to flocculation, coalescence or creaming. However, nanoemulsions can still be thermodynamically unstable and may break down over time due to Ostwald ripening or coalescence. As for solid lipid nanoparticles, they are biocompatible and safe (irritation of components decreases), as well as improve the solubility and bioavailability of poorly soluble drugs. There are some drawbacks of solid lipid nanoparticles, such as poor encapsulation efficiency due to crystallization, and physical instability during high-temperature storage, which could lead to drug leakage or degradation.[28] With regard to the polymer micelles, the unique core-shell structure allows for the encapsulation of high hydrophobic drugs in the core, while the hydrophilic shell provides stability and biocompatibility. However, polymeric micelles also have some limitations like the potential for drug leakage or premature release during storage, as well as challenges in controlling the size and the tendency to aggregate.[68] Cyclodextrins with a hydrophobic cavity inside the ring increase the solubility of lipophilic molecules and mask odor, but high concentrations may cause skin irritation. Polymeric micro- and nanoparticles offer control over molecular weight and lower material costs, but there is a

possibility of particle agglomeration. Liposomes can encapsulate both hydrophilic and hydrophobic drugs within their aqueous core and lipid bilayer, respectively. This makes liposomes suitable for delivering a wide range of drugs with different physicochemical properties. Liposomes also can protect the encapsulated drug from degradation and improve its pharmacokinetics by prolonging its circulation time. However, potential instability and aggregation, as well as variability in size and surface charge should be considered.[68] Micro/nanofibers are manufactured by electrospinning which is a simple and low-cost process. Micro/nanofibers have a high encapsulation efficiency due to their high surface-to-volume ratio and can be designed to release drugs in a controlled manner, improving the efficacy of the drugs. But it is difficult to manufacture nanofibers with a diameter less than 10 nm by electrospinning. Microporous polymer structures/polymer scaffolds, with high porosity and large surface area, have indeed gained the most attention and interest in the fields of drug release systems, tissue engineering, energy storage, micro-/ultra-filtration, gas separation, or catalysis.[69] The so-called microporous polymeric scaffolds used for drug delivery are often designed as temporary structures with the desired geometry and physical, chemical, and mechanical properties.[70] The design of a scaffold includes the selection of its constitutive material, its architecture and often the surface and/or bulk treatments to achieve the desired drug release profile.[71–73] Scaffold materials employed for drug release must meet certain physical and biological criteria, such as having an interconnected network of pores that can trap insoluble or only partially soluble active liquid, thereby controlling the release of active at sustained and effective levels over an extended period of time.[70]
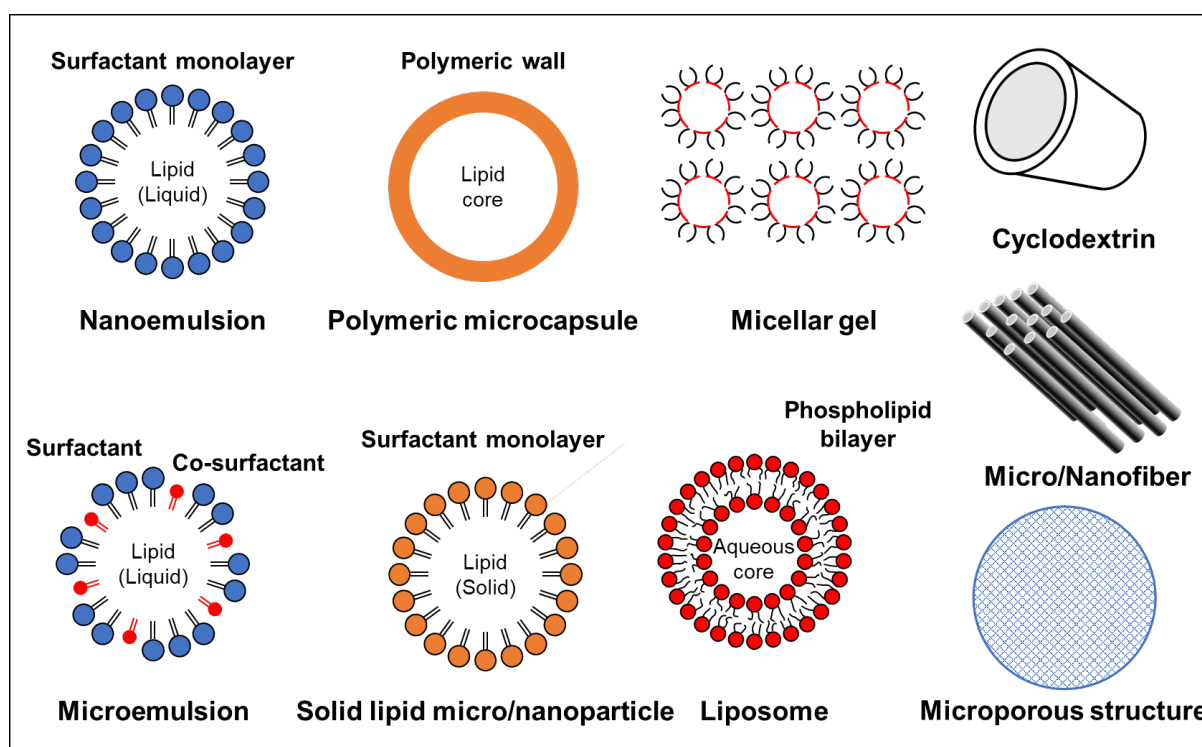
Figure 4. Different controlled-repellent-release systems.[26,28,68]

A controlled release system is designed to release an active or drug to the target at a controlled rate and maintain a consistent concentration of the active or drug within the system over a specified or extended period of time. There are some key advantages of the controlled release system include (a) prolonged activity by providing a sustained low amount of the active or drug

at an effective level to perform its function over a long period; (b) environmental pollution reduction by reducing/minimizing the undesirable side effects of drug or other compound losses like repellents or insecticides by evaporation and degradation or masking of any odor because toxic material becomes chemically non-toxic when combined with polymers; (c) cost reduction by reducing the cost and time of repeated or over-applications of drugs.[68,74] When selecting a controlled release system, it is important to consider a range of factors, including the nature of the polymer, stability of the combination during processing, the desired release rate, the shape and size of the final product, the duration of protection time, and cost and ease of formulation and application. By taking these factors into account, it becomes possible to select the most appropriate controlled release system for a specific application and to achieve the desired therapeutic or protective effect with minimal adverse effects.

In order to predict the effectiveness of repellents entrapped into the polymer matrix, it is important to understand the external factors, including evaporation, temperature and abrasion. Evaporation is a major factor that affects the loss of repellents, and it is closely related to the vapor pressure of the active ingredient.[75,76] Repellents with lower boiling points have higher vapor pressures and can repel mosquitoes over a longer distance, but they also evaporate more quickly, reducing their duration of effectiveness. In contrast, repellents with higher boiling points have lower vapor pressures and are less effective over long distances, but they can still create a barrier that prevents mosquitoes from landing and biting the skin. These repellents may also have a longer duration of effectiveness due to the slower evaporation rate. If the boiling point is too high, then it would be ineffective in repelling mosquitoes. Temperature is a further important factor that affects the effectiveness of repellents. Higher temperatures can increase the evaporation rate of the active ingredient, reducing the duration of effectiveness, and *vice versa*.[75] Abrasion can happen due to the friction with clothing or other objects, as well as some physical activities, such as sweating or swimming, which makes repellent lost. Other factors like wind velocity, humidity, and so on also influence the protection time.[75–77]

Wearable repellent-release devices based on microporous polymer scaffolds exhibit excellent performance, therefore the used polymer materials, preparation mechanism and manufacture techniques and parameters of microporous polymer scaffolds hosting drugs are discussed as follows.

1.2.2 Polymers

Polymers are divided into petroleum-based polymers and bio-based polymers according to the source of raw materials. Petroleum-based polymers rely on conventional feedstocks like oil, coal, or gas, while bio-based polymers are derived from renewable resources like biomass and are therefore sustainable. Figure 5 shows different types of biopolymers and fossil-based polymers and whether they are biodegradable or not.[78] It is important to note that not all bio-based polymers are biodegradable, and *vice versa*. Polymers listed in the first quadrant like poly(lactic acid) (PLA), poly(hydroxyalkanoates) (PHA), poly(butylene succinate) (PBS), cellulose or starch blends are derived from bio-based polymers and are also biodegradable. Then in the second quadrant, there are bio-derived polymers that are not biodegradable. For example, bio-polyethylene (bio-PE), produced using ethylene derived from bioethanol, is bio-based but non-biodegradable. These polymers which originate from bio-sources though are

non-biodegradable but provide significant carbon reduction at the beginning of life. This is because plants utilize atmospheric carbon dioxide (CO_2) during their growth. The conventional polymers displayed in the third quadrant, like PE, polypropene (PP), poly(ethylene terephthalate) (PET), poly(methyl methacrylate) (PMMA), polyvinyl chloride (PVC), etc., are fossil-based and non-biodegradable. In addition, there are some polymers that are fossil-based but biodegradable shown in the fourth quadrant, such as poly(butylene adipate-*co*-terephthalate) (PBAT) and poly(caprolactone) (PCL).[79–82]
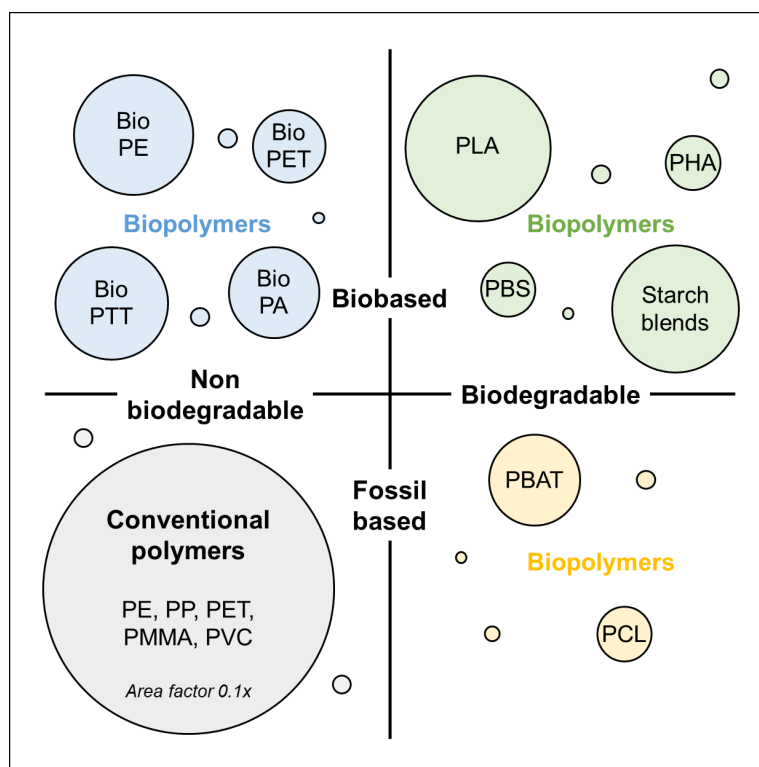
Figure 5. Types of biopolymers *vs* fossil-based polymers with regards to biodegradability, and corresponding examples. The area of the circle represents the proportion of the indicated polymer in the global production capacities of biopolymers in 2022.[78]

Polymers can be modified through various methods to improve their properties or create new properties.[83,84] Modification methods can be divided into chemical, physical and biological modifications.[84] Chemical modification involves changing the chemical structure of the polymer through chemical reactions, such as cross-linking, copolymerization, functionalization and hydrolysis.[83] Physical modification refers to changing the physical properties of the polymer without changing its chemical structure, like polymer blending, plasticization, surface modification and mechanical deformation.[83] While biological modification involves using enzymes or microorganisms to modify the polymer, such as biodegradation and biofunctionalization. Here, plasticization is discussed. A plasticizer is a substance incorporated into a material to increase its flexibility, ductility, durability and processability.[85] Adding a plasticizer to one polymer results in a decrease in the glass transition temperature. The mechanical properties of the polymer could be improved by adding the plasticizers, including reducing Young's modulus and tensile strength and increasing elongation and crack resistance.[86] Nevertheless, concerns have been raised that some plasticizers can leach out of the polymers and migrate into the surrounding environments over time,[86–88] which not only changes

the mechanical properties making the samples more rigid but also may cause side effects if the plasticizers have potential risks to human health and the environment, such as phthalates.[88]

Plasticizers are classified into external plasticizers including primary plasticizers (typically low molar mass compounds added in high concentrations) and secondary plasticizers (higher molar mass compounds added in smaller concentrations), and internal plasticizers (which are incorporated into the polymer chain during synthesis or polymerization).[86–89] The mechanism of action of plasticizers has generally evolved three major theories: lubricity theory, gel theory and free volume theory, as shown in Figure 6. According to the lubricity theory, plasticizer molecules act as lubricants, weakening polymer-polymer interactions known as van der Waals by shielding the molecules, thereby increasing the flexibility and softness of the material (see Figure 6a).[87–89] The gel theory assumes that a plasticized polymer forms a weak 3D network with plasticizers. The plasticizers are bonded to polymer chains to reduce the attachment points/sites of polymer to polymer (see Figure 6b).[87–89] Regarding the free volume theory, adding the plasticizers into the polymer can increase the free volume, the internal space available within a polymer, making the polymer soft and rubbery. The free volume comes from motion of chain ends, motion of side chains and motion of the main chain (see Figure 6c).[87–89]
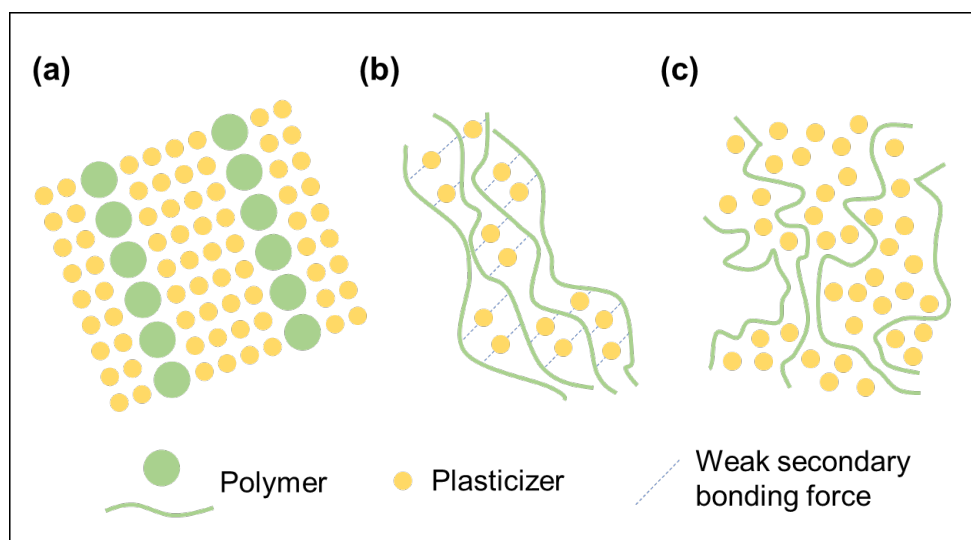
Figure 6. Theories of plasticization: lubricity theory (a), gel theory (b), free volume theory (c).

Poly(lactic acid)

PLA, an aliphatic polyester belonging to the family of α-hydroxy acid-derived polymers, has been highly regarded as one of the promising biodegradable, biocompatible, bioresorbable, and compostable polymers[90] used for packaging, agriculture, automotive, electronics and biomedical fields.[91]

Lactic acid, as the monomer of PLA, exists two enantiomers: L-lactic acid and D-lactic acid. The relative contents of the optically active monomers can be adjusted to confer targeted utility in the final polymers.[92] When optically pure monomers are utilized in the polymerization process, stereoregular polymers known as poly(L-lactic acid) (PLLA) or poly(D-lactic acid) (PDLA) are produced, which exhibit a semicrystalline structure. In contrast, the polymerization of racemic lactide/lactic acid or mesolactide leads to the formation of poly(D,L-lactic acid)

(PDLLA), which is an amorphous polymer attributable to the random distribution of L- and D-lactic acid units in the polymer chains. The degradation rate of PDLLA is higher than that of semicrystalline PLLA or PDLA with higher strength and modulus of elasticity. Generally, there are four methods employed for the synthesis of PLA, including direct polycondensation, azeotropic condensation polymerization, solid state polymerization, ring-opening polymerization,[90,93] as shown in Figure 7. Regarding direct polycondensation, at first, the prepolymer with a low molecular weight between 2 kDa to 10 kDa is produced and then the polymer with a high molecular weight over 100 kDa by using a chain coupling agent. The second method is azeotropic condensation polymerization. The PLA with high molecular weight can be obtained by continuously dehydrating the system. Another synthesis route is the obtainment of the intermediate oligomer with molecular weight between 1 kDa to 5 kDa first by oligomerization of lactic acid. Then PLA with high molecular weight is gained by solid state polymerization of the intermediate oligomer or ring-opening polymerization of lactide produced by depolymerization of the intermediate oligomer or dimerization of lactic acid.
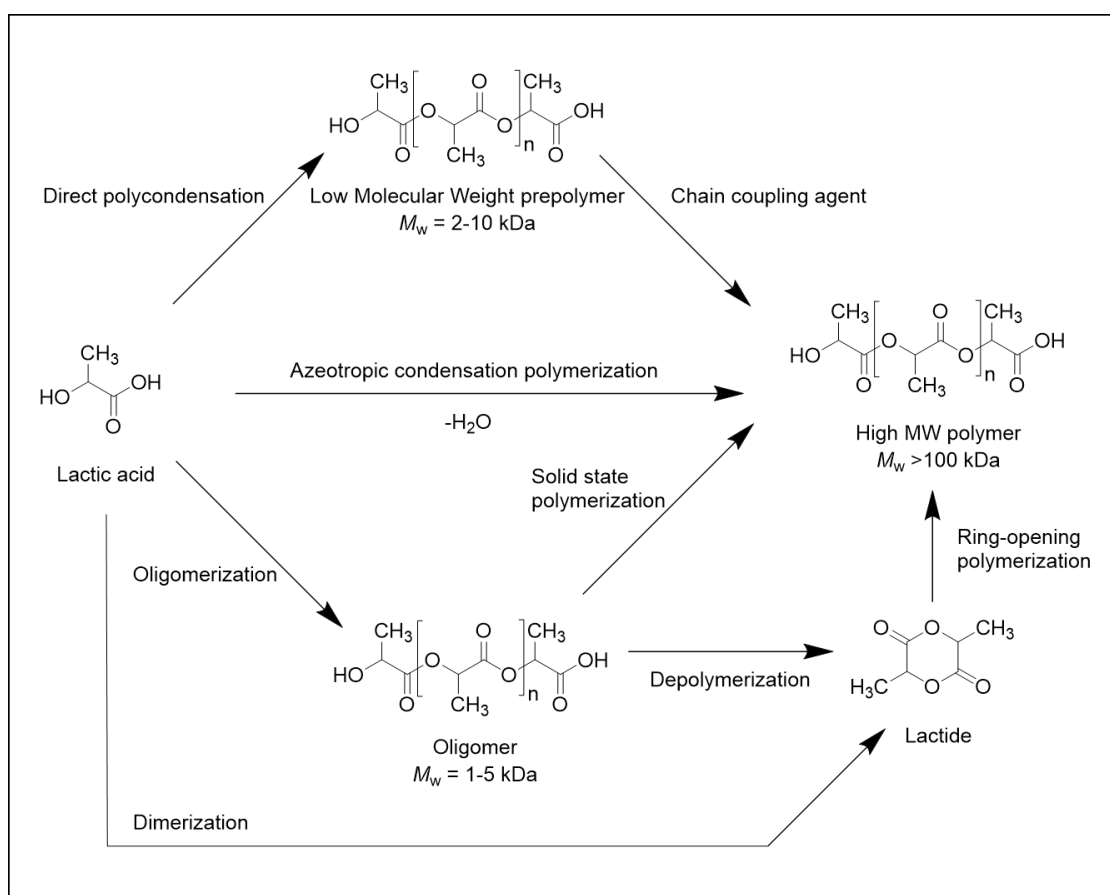
Figure 7. Chemical synthesis of PLA,[90,92,93] including direct polycondensation, azeotropic condensation polymerization, solid state polymerization, ring-opening polymerization.

PLLA is an emblematical polymorphic polymer, capable of crystallizing into various modifications (α, α', α'', β, γ, ϵ, mesophase forms) depending on the crystallization/processing conditions.[94,95] The two most common modifications of PLLA are the α and α' forms, which are dependent on crystallization temperature. The thermally stable α form is generally developed during crystallization at high crystallization temperature ($T_c > 120$ °C), while the metastable α' form is produced at low crystallization temperature ($T_c < 100$ °C) in the cold and

melt crystallizations.[96,97] A mixture of α and α' crystals is formed in the crystallization temperature range of 100 to 120 °C. Within this crystallization temperature range, PLLA exhibits a bimodal temperature-dependent crystallization kinetics, deviating from the typical bell-shaped curve. The curves of the spherulite growth rate of PLLA as a function of the crystallization temperature also presented double peaks, with a maximum growth rate observed at about 110 °C. The β-form is produced by stretching the α-form at very high drawing ratio and high temperature.[98–100] The γ-form is formed through epitaxial crystallization.[101] Table 3 shows the unit cell structure, chain conformation, and formation condition for the various polymorphs of PLLA.

1.2.3 Mechanism/Principle – Thermally-induced phase separation (TIPS)

The majority of microporous polymer structures/scaffolds capable of producing properly controlled release of repellent are obtained based on the TIPS of polymer solutions.[71,102] TIPS is normally used because of its ease of control and a low tendency towards generation defects.

In 1981, Castro[103] first applied TIPS for the formation of a microporous structure in polyolefins. In contrast to other phase separation processes induced by diffusion, the change of solvent, pressure or composition, TIPS is driven by temperature change. Briefly, TIPS of a polymer/solvent system includes the following steps: (a) A homogeneous solution is formed at an elevated temperature by mixing of a polymer and a high-boiling-point and low-molecular-weight liquid referred to as the diluent.[104] (b) The solution is cast into the desired shape and then quenched or cooled at a controlled rate to induce phase separation and solidification of the polymer. (c) The diluent entrapped into the polymer matrix is typically removed by solvent extraction or sublimation to produce a microporous structure. Following these steps, microporous polymer structures can be formed via liquid-liquid thermally induced phase separation (L-L TIPS) or via solid-liquid thermally induced phase separation (S-L TIPS) with subsequent solidification of the polymer.[105,106] TIPS depends on the system thermodynamics and the sequence of phase separation events under certain cooling conditions. It is noted that TIPS can also be observed in polymer/polymer blends.[107–111] In the following, polymer scaffolds obtained from polymer solutions by TIPS are discussed.

L-L TIPS

The miscibility in binary polymer-solvent systems at a fixed temperature T and pressure P, can be expressed in terms of Gibbs free energy of mixing (ΔG_{mix}) and its second derivatives with respect to the polymer volume fraction, ϕ_p, as follows:[112]

$$\Delta G_{mix} < 0 \tag{1}$$

$$(\partial^2 \Delta G_{mix}/\partial \phi_p{}^2)_{T,P} > 0 \tag{2}$$

If one of the two criteria is not met, two phases coexist in equilibrium.

Phase separation through L-L TIPS can occur during the cooling process when a polymer is dissolved in a poor solvent or there is a very weak affinity between the polymer and solvent. L-L TIPS is a reversible thermodynamically driven process in which a solution de-mixes into two

Table 3. Unit cell structure, chain conformation, and formation condition for the various polymorphs of PLLA.[94,95]

Form	Crystal system	Lattice parameters (nm)	Chain conformation	Formation condition	Ref.
α	Orthorhombic or pseudo-orthorhombic	$a = 1.034$–1.078; $b = 0.597$–0.645; $c = 2.780$–2.888	10_3 helix or distorted 10_3 helix	Cold or melt crystallization at $T_c \geq 120$ °C, solution crystallization	[98,113,114]
α′ (Newly termed "δ")	Orthorhombic	$a = 1.080$; $b = 0.620$; $c = 2.880$	10_3 helix	Cold or melt crystallization at $T_c \leq 100$ °C	[115]
α″	-	-	-	Under high-pressure CO_2 and low temperature	[116]
β	Orthorhombic	$a = 1.031$–1.041; $b = 1.770$–1.821; $c = 0.880$–0.900	3_1 helix	Solution spinning, stretching, shearing, solid-state extrusion, terminal modification	[98,100]
γ	Trigonal	$a = b = 1.052$; $c = 0.880$; $\alpha = \beta = 90$, $\gamma = 120°$	3_1 helix		[99]
γ	Orthorhombic	$a = 0.995$; $b = 0.625$; $c = 0.880$	3_1 helix	Epitaxial crystallization	[101]
ε	Orthorhombic	$a = 1.539$–1.616; $b = 1.215$–1.261; $c = 2.857$–2.900	10_7 helix	Solution crystallization	[117,118]
Mesophase	-	-	-	Under low-pressure CO_2 and very low temperature, plasticizer, strain-induced crystallization	[119–122]

- represents the data haven't yet obtained.

distinct liquid phases with different polymer concentrations. Different phases can form by varying the solution composition, temperature, and pressure.[123,124]

The Flory-Huggins theory is an essential theory that simply describes the thermodynamics of polymer solutions. The Flory-Huggins equation for the polymer-solvent system is shown in equation (3).[112]

$$\frac{\Delta G_{mix}}{RT} = \frac{\phi_p}{x_p}\ln\phi_p + \frac{\phi_d}{x_d}\ln\phi_d + \chi\phi_d\phi_p \tag{3}$$

Where ΔG_{mix} is the Gibbs free energy of mixing per lattice site, R is the gas constant and T is the absolute temperature, ϕ_p and ϕ_d are the volume fraction of polymer and solvent, x_p and x_d are the number of lattice sites being occupied respectively by the a polymer molecule and a solvent molecule, and χ is the Flory-Huggins polymer-solvent interaction parameter.[112]

The first two terms on the right side of the Flory-Huggins equation are always negative, signifying the combinatorial entropy contribution, while the third term, which represents the enthalpic contribution, can be either positive or negative, depending on the sign of χ. The polymer-solvent system with weak interactions exhibits a large and positive χ value, leading to a positive ΔG_{mix} and thus thermodynamically favorable liquid-liquid phase separation. By contrast, when the strength of interactions between polymer and solvent is high, that is, χ is small, the occurrence of liquid-liquid phase separation is more difficult, that is, lower temperatures are needed to achieve upper critical solution temperature (UCST), or higher temperatures are needed to reach lower critical solution temperature (LCST). In this situation, the homogenous one-phase region in the phase diagram expands, and therefore the binodal curve, the boundary of liquid-liquid phase separation, shifts to lower temperatures for UCST or higher temperatures for LCST.[125]

The binodal curve distinguishes the homogeneous one-phase liquid region from the heterogeneous two-phase liquid-liquid region, while the spinodal curve divides the two-phase region into unstable and metastable regions, as shown in Figure 8. Two liquid phases are separated through a nucleation and growth mechanism (NG) in the metastable regions and spontaneously through spinodal decomposition (SD) mechanism because there is no activation barrier against phase separation in the unstable region. If the starting point of the system lies at point X in Figure 8, cooling of the system results in the separation of a single-phase mixture solution into two liquid phases at a point R_x on the binodal, and formation of an emulsion of a polymer-lean phase (L_x) in the polymer-rich phase. The morphology of an emulsion generally depends on the polymer content in the initial mixture, ϕ_x, and polymer content at UCST, ϕ_{UCST}. The polymer-rich phase is dispersed in the polymer-lean phase at $\phi_x < \phi_{UCST}$, and the resulting morphology after removing the solvent is composed of solid polymer beads or a powder-like structure; at $\phi_x \approx \phi_{UCST}$ an interpenetrating phase/co-continuous phase is formed; and droplets of the polymer-lean phase are dispersed in the polymer-rich phase at $\phi_x > \phi_{UCST,}$ and a foam with a closed-pore structure is formed after removing the solvent.[102,126] It is noted L-L TIPS through a pure SD mechanism can only be achieved in a solution with the concentration at the critical point. In all other scenarios, the metastable area must be passed first. The transition between NG and SD mechanisms should be regarded as a gradual change and not a sudden change. High cooling rates can be used to prevent phase separation in the metastable area.[127]
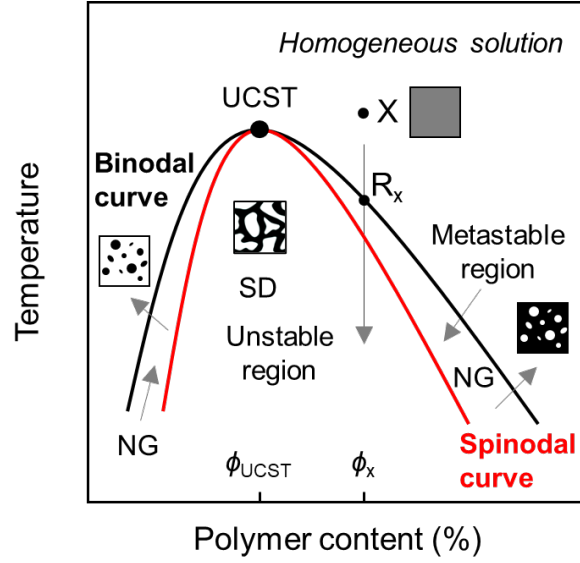
Figure 8. Schematic phase diagrams of L-L TIPS of polymer/thermodynamically poor solvent system adapted from Refs. [105,106,126].

S-L TIPS

For binary polymer-solvent systems involving a polymeric component which is able to crystallize, the polymer melting point can be related to the mixture composition[112] as shown in the equation (4) below.

$$\frac{1}{T_m} = \frac{R}{\Delta H_u} \frac{V_u}{V_d} \left(\phi_d - \chi \phi_d^2 \right) + \frac{1}{T_m^0} \tag{4}$$

Where T_m and T_m^0 are the equilibrium melting temperatures of the crystalline polymer in solution and the pure polymer, respectively; V_d is the molar volume of the solvent, V_u is the molar volume of the repeat unit, ΔH_u is the heat of fusion per repeat unit, ϕ_d is the volume fraction of the solvent, and χ is the Flory-Huggins interaction parameter.

Then T_m can be obtained by solving equation (4), see below.

$$T_m = \frac{1}{\frac{R}{\Delta H_u V_d}(\phi_d - \chi \phi_d^2) + \frac{1}{T_m^0}} \tag{5}$$

Figure 9 shows T_m as a function of polymer content, illustrating the S-L TIPS occurs by cooling a crystallizable polymer/good solvent mixture.[106,126] A solution (point Y) with an interaction parameter $\chi = 0$ demixes into two phases during cooling at a point L_y on the linear crystallization curve. One phase is composed of polymer crystals ($\phi_p = 1$), and the other phase is an amorphous solution with the polymer content ϕ_y. Further cooling the system, the polymer concentration in the solution decreases along the crystallization line, as indicated by the arrow. The crystallization temperature varies/shifts according to χ, that is, the interaction between polymer and solvent. For $\chi < 0$, the relationship shows a concave curvature regarding the horizontal composition axis; for $\chi > 0$, a convex curvature is observed;[106] as shown also by the arrow. During cooling the system, the two phases separated through an NG mechanism. The two-phase dispersion of polymer crystals in its solution in the solvent is formed. The mass fraction of polymer crystals increases with the initial polymer content in the mixture. With

regard to a large positive χ, the plot tends to be stable at low polymer concentrations. In this case, liquid-liquid phase separation followed by solid-liquid phase separation (via solidification of the polymer) is usually observed.[106,125,127]

The phase separation mechanism is an important tool that can be used to guide the processing of various materials. By understanding the specific mechanisms that govern phase separation, materials with specific properties, morphologies and microstructures can be fabricated using different processing techniques.
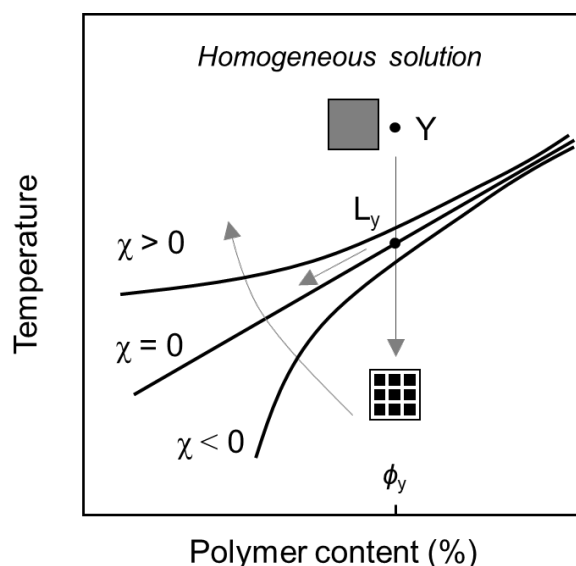

Figure 9. Schematic phase diagrams of S-L TIPS of polymer/thermodynamically good solvent system adapted from Refs. [105, 106, 126].

1.2.4 Scaffold fabrication techniques

With the intention of developing a new cost-effective repellent formulation with improved effectiveness and safety, it is necessary to investigate the manufacturing techniques, conditions and parameters that can have an impact on efficacy and safety. Microporous polymeric scaffolds are typically produced by techniques such as solvent casting, melt molding, electrospinning and 3D printing.[72] The selection of a fabrication technique depends on the nature of the polymer and solvent, as well as the desired final characteristics and applications.

Solvent casting

Solvent casting is one of the simplest techniques to obtain thin film-based scaffolds through removing the solvent from a polymer solution cast in a mold. The process involves dissolving the polymer in a solvent, transferring the solution into a suitable mold, and holding it at a fixed temperature until the solvent completely evaporated.[72] The high porosity of porous scaffolds obtained by solvent casting techniques is limited. In order to improve the porosity, this technique can be modified by adding salt particles, known as salt leaching. The salt particles are distributed throughout the scaffold after solvent evaporation, and then can be removed by the addition of water that solubilizes the particles.[72] However, the pores are mainly distributed on the surface of the scaffolds, causing by the limited permeation of water through the inner parts. In addition, freeze-drying technique can produce solid porous 3D scaffolds. The solvent is frozen and sublimed at a temperature below the glass transition temperature of this solvent.[128]

Melt molding

Melt molding is an easy method to adjust polymer scaffold structures without using chemical solvents, that is, residual toxic solvents in the matrix are not an issue. Thermoplastic polymers are commonly used for melt molding because they can be easily heated and cooled into different solid shapes. The polymers are heated above the glass transition temperature (of amorphous polymers) or melting point (of crystalline polymers) to form a liquid and then cool it and solidify in a mold. The advantage of this technique is that the shape of materials can be controlled by mold with a flexible geometry, allowing processing of multicomponent systems. However, high processing temperatures are required, and low levels of porosity, inadequate pore interconnectivity, closed cellular structures, or dense surface skin layers are produced.[129,130] Melt molding techniques include melt extrusion, compression molding, injection molding.[131] Melt extrusion can be used to fabricate strands, films, etc., with a fixed cross-sectional profile defined by a die. The schematic diagram of melt-extrusion process with a twin-screw extruder, as well as the geometry of screw are presented in Figure 10. As for compression molding, the low flow stress is used in the process compared to melt extrusion and injection molding. Compression molding yields products with high density and little material shrinkage or swelling after demolding, leading to enhanced robustness. Injection molding is suitable to manufacture products with tight dimensional tolerances, imparting products with high porosity and interconnectivity.
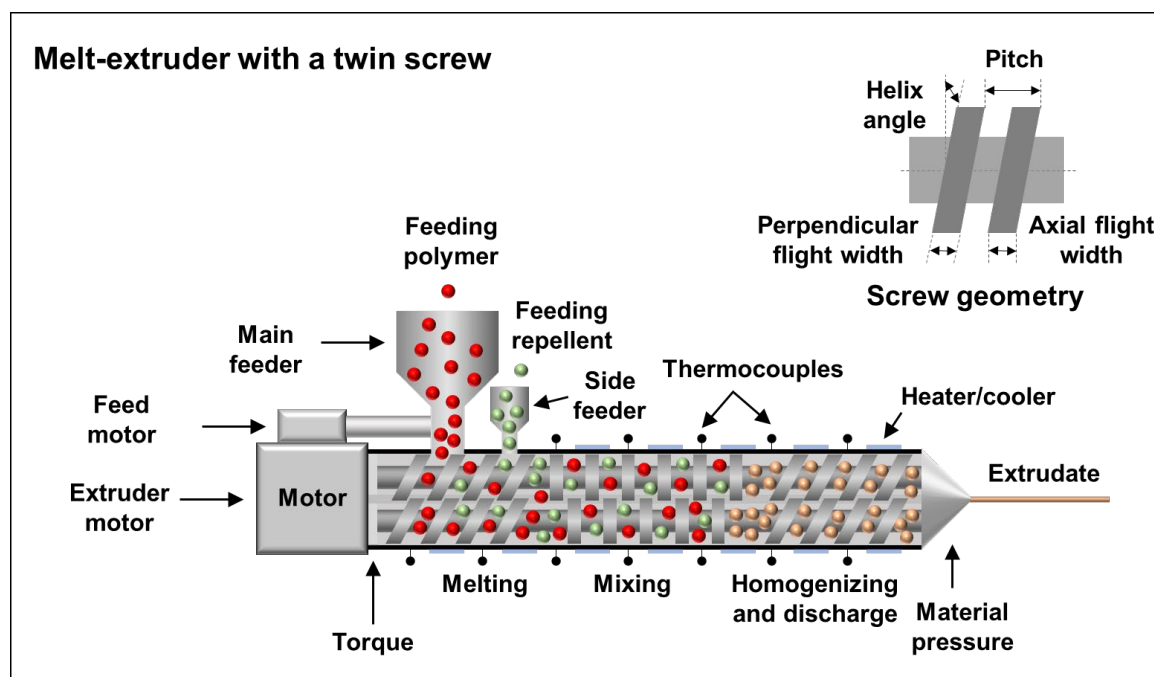
Figure 10. A schematic diagram of the melt-extrusion process with a twin-screw extruder and extruder screw geometry. This schematic diagram was created, inspired by the Ref. [132, 133].

Electrospinning

Electrospinning is a versatile technique, employed not only in university laboratories but also increasingly being applied in industry, that can fabricate continuous fibers with diameters ranging from a few micrometers down to a few nanometers.[134] The concept of electrospinning can be traced back to an earlier study conducted by William Gilbert in 1600, when he observed that a water droplet close to an electrically charged amber formed a cone shape, that later

became known as the Taylor cone,[135] and small droplets were ejected from the tip of the cone. Electrospinning was explored for producing nanofibers until the 1990s.[136] Since then, the electrospinning technique has been further developed. By applying high voltage to a polymer solution/polymer melt, liquid jets are formed by overcoming the surface tension of the pendant drop, which can be deposited on a collector as solid fibers generating a nonwoven mat with a high specific surface-to-volume ratio, thus the electrospun fibers can be also used in biomedical, filtration systems, chemical/optical sensor, energy storage and catalysis.[137,138] The technique can be separated in two categories. They are referred to as solution electrospinning and melt electrospinning,[139] as shown in Figure 11. Solution electrospinning uses a solvent to dissolve the polymer, while melt electrospinning employs a heating system at the instrumental apparatus to provide a polymer in a liquid state in the absence of a solvent. The solution electrospinning process is related to solvent evaporation and mass transfer, thereby producing ultrafine fibers, whereas the melt electrospinning process is carried out through heat transfer and quenching of the melted jet. The solvent-free and mass transfer-free melt electrospinning allows direct deposition of fibers on the collector/substrate, resulting in the generation of micrometer-scale fibers that are wider than those produced by solution electrospinning (typically nanofibers). This method offers advantages such as the absence of toxic solvents and high throughput for large-scale fabrication. However, it presents certain limitations like a large diameter of the electrospun fibers, as well as a high processing temperature mentioned above.
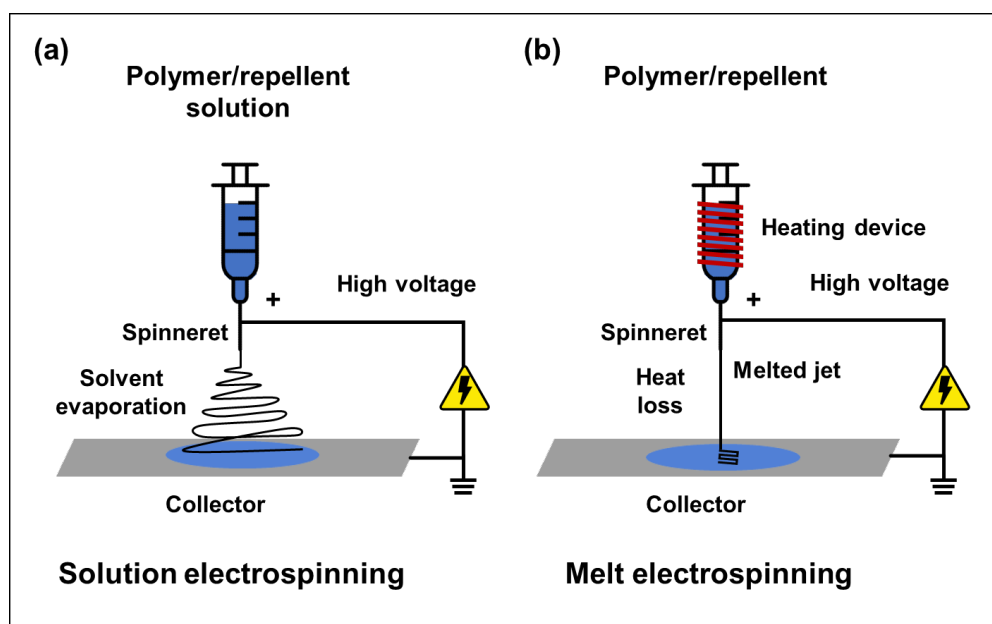
Figure 11. Schematic diagrams of solution electrospinning (a) and melt electrospinning (b). A high voltage is applied to produce a charged jet that can be kept in a continuous form to produce fibers. For solution electrospinning, the ejected jet initially travels in a straight line in the near-field zone and undergoes stretching and thinning upon whipping motions in the far-field zone. In terms of melt electrospinning, a heating device is attached to maintain a molten jet. Typically, the jet travels in a straight line and generates micrometer-scale fibers.[72, 140–142]

For solution electrospinning, the morphology, fiber diameter and structure of the electrospun nanostructures can be tailored according to parameters, including solution, processing and ambient parameters, for a specific application. The effect of selected parameters on the morphology of electrospun polymer nanofibers is shown in the Table 4. In electrospinning, the

Table 4. Parameters effecting the morphology of electrospun polymer nanofibers produced by solution electrospinning.[143]

Parameters		Effect on fiber morphology
Solution parameters	Molar mass of polymer ↑	Formation of droplets and beads ↓
		Formation of irregular shape with larger pores ↓
	Polymer concentration/viscosity ↑	Formation of beads ↓
		In the optimal range, fiber diameter ↑
	Solution conductivity ↑	Uniform bead-free fibers ↓
		Fibers with broad diameter distribution
	Solvent volatility ↑	Pores formed on the fiber surface (microtexture)
Processing parameters	Voltage ↑	First fiber diameter ↑ then ↓, after that with bead formation
	Distance between tip and collector ↑	Fiber diameter ↓
		In too short or too far distance, beads can form
		For uniform fibers formation, minimum distance is required
	Feed rate/flow rate ↑	Fiber diameter ↑
		At very high feed rate, bead formation happens
Ambient parameters	Temperature ↑	Fiber diameter ↓ and viscosity ↓
	Humidity ↑	Circular pores generated on the fibers
	Air velocity ↑	Fiber diameter ↑

↑ represents the increase of the corresponding parameters; ↓ represents the decrease the corresponding parameters.

obtained structures can range from droplet, elongated droplet, stretched droplet to uniform fibers.

Here melt spinning has to be mentioned. Melt spinning and melt electrospinning are two related but different processes used to manufacture fibers from molten polymer. For melt spinning, the processing line consists of two stages, melting extrusion and drawing.[144] The melting extrusion line includes an extruder, metering pump and spin pack with spinneret and filter media, as shown in Figure 12. The molten material is extruded through a spinneret with a certain number of holes to form continuous filaments that are then cooled usually by air. The cooling process and drawing ratio are key factors to control the crystallinity and mechanical properties of fibers. If a second stage of hot drawing is performed, then the fibers are further stretched and the polymer chains are more oriented, thereby enhancing the degree of crystallinity and the mechanical properties of the fibers.[142] This process typically produces conventional fibers with diameters ranging from a few microns to several millimeters, while melt electrospinning produces ultrafine fibers with diameters varying from a few hundred nanometers to a few microns.
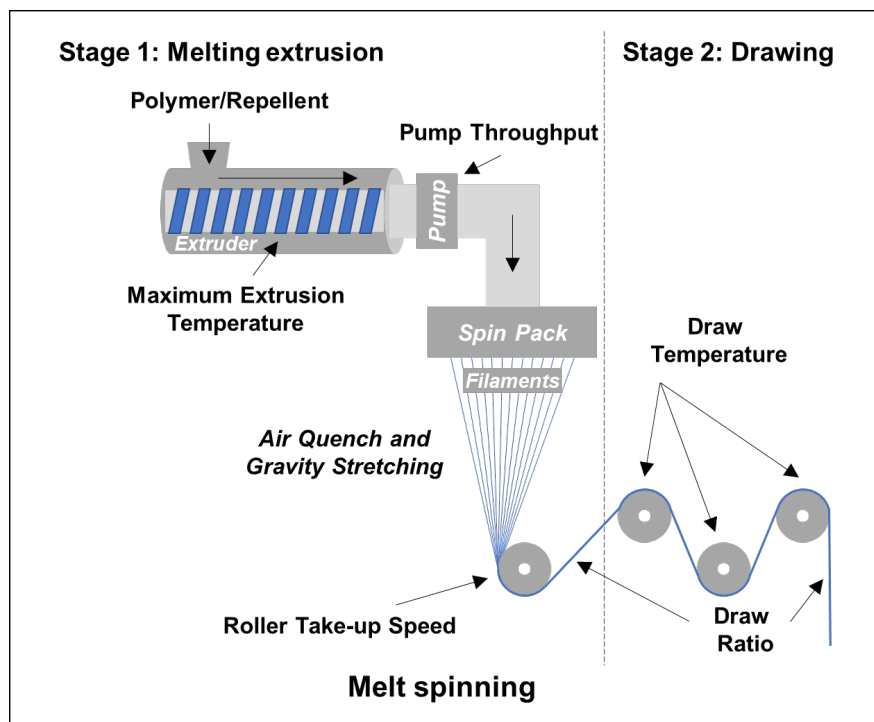
Figure 12. Schematic diagram of melt spinning,[144] including a melt-extrusion stage that relates to melting the polymer and/or other compounds, extruding them through a spinneret, solidifying by rapid cooling, and a drawing stage that involves drawing/stretching the resulting filaments to orient the polymer chains along the fiber axis to improve the mechanical properties. The fiber diameters span from a few micrometers to several millimeters.

3D printing

3D printing, an additive manufacturing (AM) technique, is used to fabricate 3D objects from digital models by deposing layer-by-layer of printed materials. The computer-aided design/manufacturing (CAD/CAM) software enables the design of different geometries and multilayers, multi-compartments, among others. In the recent decade, 3D printing started to grow strongly in the pharmaceutical field, such as drug delivery and personalized medicine, as they can tailor dosage forms according to the needs of each individual.[145,146] The 3D printing technique created the opportunity for the development of tailored single and multi-drug products.[145,147] Manufacturing complex, customized and personalized products in a low-cost manufacturing process is required for optimal health recovery.

The 3D printers used in the pharmaceutical field include extrusion-based fused deposition modeling (FDM) and pressure-assisted microsyringe (PAM); powder-based selective laser sintering (SLS) and binder jetting (BJ); liquid-based stereolithography (SLA) and material jetting (MJ); sheet lamination (SL).[145,146,148,149] The most common AM technique is FDM because of process simplicity and associated low cost.[148] In general, there are five main parameters that affect FDM, which are structure parameters including infill percentage, infill pattern, raster angle and layer thickness, and thermal processing parameters.[145,150] Infill percentage/density is the "fullness" of the inside of a printed product ranging from 0 % to 100 %, with 0 % making a part hollow and 100 % completely solid. Infill percentage impacts the weight of a printed part, print time, material consumption, buoyancy, and strength, although in combination with other factors like material and layer height.[151] Infill pattern is the structure

and shape of the inside of a printed product, varying from simple lines to more complex geometries. Different infill patterns possessing different perimeters and volumes show different drug release profiles, thus allowing for different pharmaceutical applications. Raster angle is the angle between the deposition path of filament and the outer contour in the printing process, which influences dimensional accuracy, surface roughness and mechanical properties of printed parts.[152] Typical 3D printers use Cartesian coordinates, named after mathematician René Descartes, to determine the position of the nozzle, including the planar *x* and *y* axes and vertical *z* axis. Layer thickness/height is one of the important factors for FDM, which is essentially the vertical resolution of the *z*-axis, affecting the printing time and dimensional accuracy. In general, a part with a larger layer thickness requires less printing time but sacrifices the dimensional accuracy/smoothness, and *vice versa*.[153] Hence, trade-off of the advantages in FDM technique is necessary.[145] For each individual application, there is an optimal balance of process parameters. In terms of thermal processing parameters, nozzle and printing platform temperature are mainly considered. Nozzle temperature, above the melting temperature of polymer, enables a higher fluidity and a better adhesion between the deposited layers. It is noted that the nozzle temperature should be below the decomposition temperature of the used materials. The printing platform temperature is set slightly over the glass transition temperature of the polymer filaments to enhance the adherence and connection between the previously printed and the new layers.[145] Figure 13 shows a schematic diagram of FDM printing. The advantages of FDM include low cost, scalability and suitability for a wide range of thermoplastics. However, voids are formed during processing which not only influence the porosity but also reduce the mechanical strength of the part. The microstructure of each layer is different because of layer-by-layer printing method, introducing the anisotropic nature of components. The printed part may deviate from the expected solid design, such as the warping effect reducing the overall height of printed parts. In addition, postprocessing is needed if the surface of the parts is not smooth.[154] 3D printing can not only be used to obtain the internal microporous structures, based on TIPS, of polymer strands, but it can also be used to obtain macroscopic scaffold structures with compartments through CAD design.
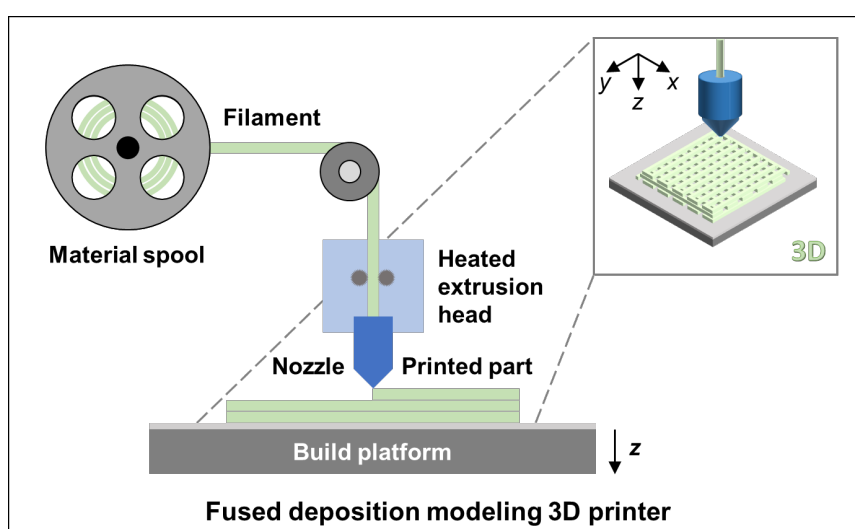

Figure 13. Schematic diagram of FDM printing, which is adapted from Ref. [155]. The thermoplastic material is melted and extruded through a small nozzle, and then deposited on a build platform layer by layer along a path according to the CAD/CAM files uploaded to the 3D printer, and finally, a 3D object is created.

1.3 State of the art of repellent release devices based on polymer scaffolds

1.3.1 Petroleum-based polymer/repellent release devices

The approach of forming a solid polymeric matrix/scaffold hosting a mosquito repellent as a functional liquid was introduced as an example of the petroleum-based polymer/repellent system —linear low-density polyethylene (LLDPE)/citronellal— by Akhtar and Focke.[104] The binary mixtures of LLDPE and citronellal show UCST phase behavior. Microporous co-continuous polymer/repellent morphologies were obtained by rapid cooling the LLDPE/citronellal solutions with a mass ratio of 40:60 from 150 °C to different sub-ambient temperatures. This enables the trapping of repellents into the microporous polymer matrix by TIPS for controlled release of the drug and potential development of long-lasting insect repellent bracelets and anklets.

Mapossa et al.[124] attempted to develop the incorporation of DEET or icaridin, both being well-established mosquito repellents, into poly(ethylene-*co*-vinyl acetate) (EVA) or LLDPE, by twin-screw extrusion compounding to increase the duration of repellence activity. A co-continuous phase structure was obtained by rapid quenching the homogeneous polymer/repellent melts into ice-water, inducing a spinodal phase separation of the components and formation of a microporous scaffold, as shown in Figure 14. It is worth noting that the strands, with an outer skin layer, containing up to 30 m% of either DEET or icaridin are sufficient to protect against mosquitoes for up to 12 weeks when ageing at 50 °C. Here, low loading of the organoclay Dellite 43B, organo-modified with dimethyl benzyl hydrogenated tallow ammonium, was introduced to assist the compounding into the polymer. In addition, if the organoclay is properly exfoliated and dispersed in the polymer matrix, then the release rate of mosquito repellents from the microporous strands can also be reduced.[156,157]
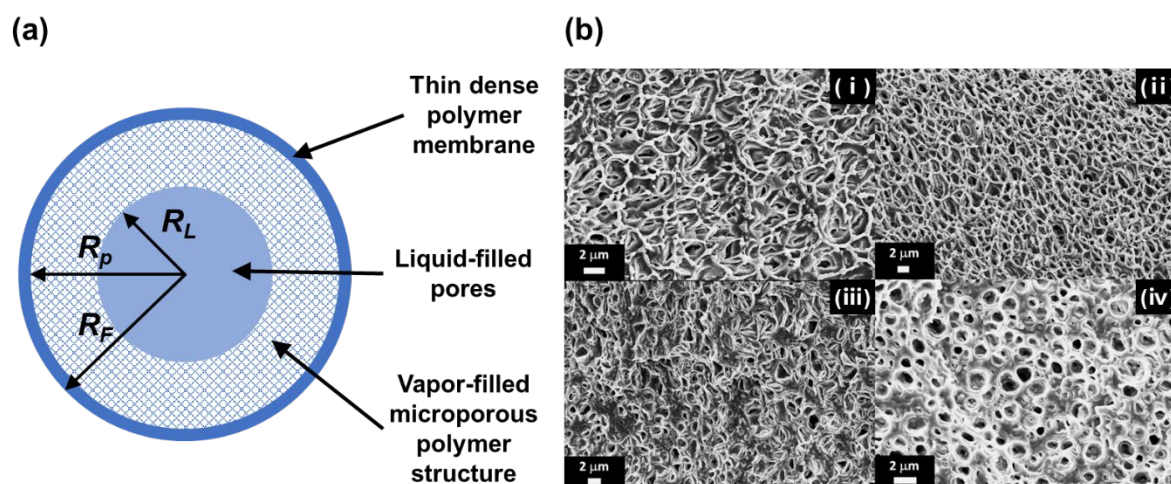
Figure 14. Model of the microporous strand showing the liquid core location, the vapor-filled microporous region and the outer skin layer that functions like a membrane that limits the rate at which the repellent is released (a) and scanning electron microscopy (SEM) micrographs of microporous structure for extruded LLDPE strands (b) including 20 m% DEET (i), 30 m% DEET (ii), 20 m% icaridin (iii) and 30 m% icaridin (iv). All strands contained 5 m% Dellite 43B clay. The figure is adapted from Ref. [124].

Similarly, bicomponent core-sheath fibers were prepared, based on a polymer containing a volatile repellent as a concentrate in the core and a less permeable polymer as the sheath, using high-density polyethylene (HDPE) as a sheath and DEET in EVA as a concentrate in the core by melt spinning.[123] The bicomponent core-sheath fibers were knitted into fabrics containing 17 m% DEET, like socks, which displayed for up to 33 weeks, that is, up to 8 months of repellency in the foot-in-cage repellence test. In addition, a nanofiller, either pyrogenic silica or an organoclay, was also introduced to the polymer/repellent systems EVA/DEET and EVA/icaridin by twin-screw extrusion compounding to slow down the release rate of repellent and to achieve long-term repellence efficacy.[158] All extruded strands, with up to 30 m% DEET or icaridin, showed a relatively smooth outer surface that acted as a diffusion barrier, but the inner morphology varied from dense to highly porous. The release rate of repellent from swellable EVA matrix was higher with DEET than with icaridin, with nanosilica than with clay, with higher repellent loadings than with lower loadings, and for thinner strands in comparison to thicker strands. The possible mechanism of repellent release was discussed by using semi-empirical models, clarifying that the repellents were released from the swellable EVA matrix strands.

In addition, repellent nanofibers composed of repellent and polyamide, an extremely versatile and indispensable class of polymer material, were successfully developed by electrospinning,[159–161] such as encapsulation/incorporation of picaridin and DEET into polyamide-6,6 (PA 66), respectively and permethrin into polyamide-6 (PA 6) to get monofilament or coaxial fibers. For the PA 66/DEET system, the fibers containing up to 29 m% DEET were obtained and the active lifetime for a lightweight fabric is estimated to be over 200 h.[161] In comparison, repellent can still be detected at 100 °C after 300 min for picaridin-loaded fibers containing up to 50 m% of picaridin, with a half-life of approximately 130 h when the temperature was extrapolated to 20 °C.[160]

1.3.2 Bio-based polymer/repellent release devices

From the standpoint of long-term environmental sustainability, the use of biopolymers is the preferred alternative to traditional petroleum-based polymers; moreover, biopolymers are expected to degrade in a reasonable time at the end of their life cycle, avoiding adverse effects on the environment. Therefore, biocompatible and biodegradable polymers are used as reservoirs/carriers for the desired active and simultaneously release the active in a control way to prevent the mosquito bites.

As mentioned before, PLA is an environment-friendly aliphatic polyester produced from short-term renewable resources, such as potato, corn, and sugarcane, and is used in the fields of packaging, agriculture, automotive, electronics, and as biomedical material because of its food safety compliance, biodegradability, as well as biocompatibility.[90,91,162,163] In recent years, PLA is regarded as an excellent candidate for preparation of porous foams,[164] membranes and scaffolds. PLLA/DEET scaffolds were reported successfully by Sungkapreecha et al.[59,165] PLLA and DEET form microporous scaffolds by S-L TIPS, as shown in Figure 15 and proved in Figure 16a. The scaffold with an entrapped DEET-rich solution was adjusted by the crystallization conditions and the solvent concentration.[165] As the crystallization of polymer can potentially obscure the information of the liquid-liquid phase separation in the polymer/
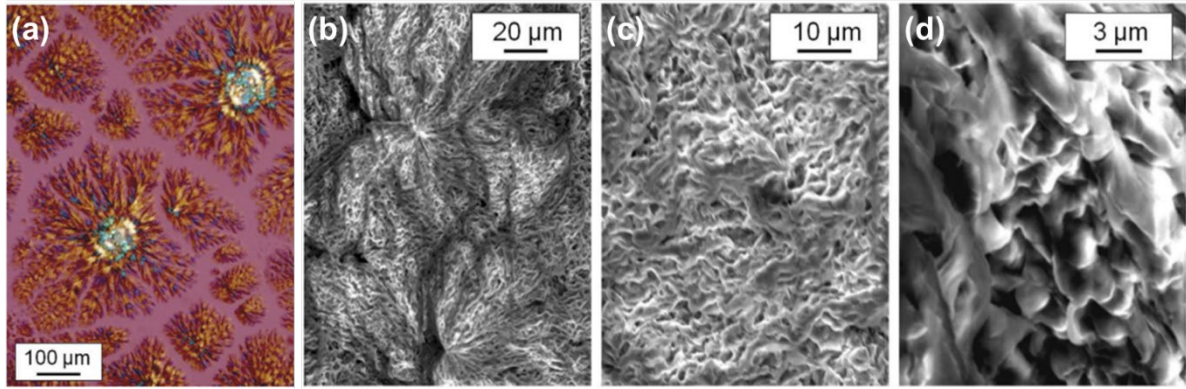
Figure 15. Polarized optical microscopy (POM) image of a slowly cooled sample of the PLLA/DEET system containing 10 % PLLA from 150 °C to room temperature (a) and ESEM images of the corresponding sample after removal of the liquid phase by vacuum-drying at 50 °C, taken at different magnifications with scale bars indicating 20 μm (b), 10 μm (c) and 3 μm (d), respectively. The figure is adapted from Ref. [59].

-/solvent system during cooling, a non-crystallizable PDLLA was employed to clarify the phase separation mechanism. The results reveal that PDLLA/DEET solutions undergo L-L TIPS when the temperature is slightly below ambient temperature and exhibit UCST behavior[59] with the critical temperature and critical concentration controlled by the polymer molar mass,[166] as depicted in Figure 16b. The effect of D-units in PLA chains, that is, stereo-regularity of PLA, on the L-L demixing of solutions on cooling was analyzed.[167] Regardless of the D-unit content, L-L demixing of solutions is suppressed by vitrification of the systems on fast cooling; in addition, S-L TIPS of solution of DEET and PLLA containing 4 % D-unit observed at around 55 °C on slow cooling is not preceded by L-L demixing.[167]
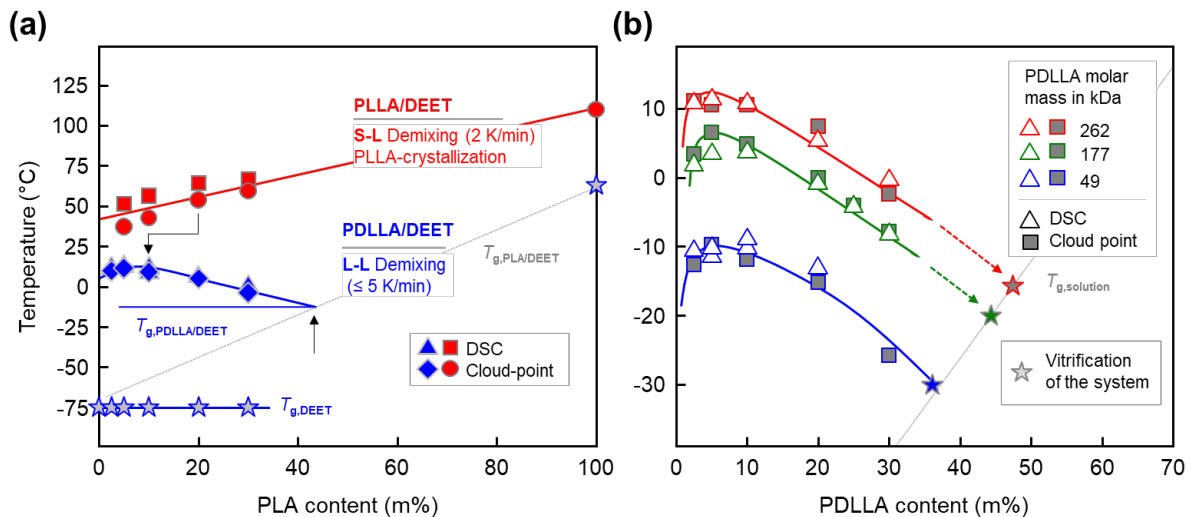
Figure 16. Phase-transition temperatures as a function of the concentration of non-crystallizable PDLLA (blue) with a mass-average molar mass (M_w) of 262 kDa and polydispersity index (PDI) of 1.6 and crystallizable PLLA (red) with M_w of 117 kDa and PDI of 1.8 (a), and PDLLA with M_w of 49, 177, and 262 kDa, respectively, marked by the blue, green, and red symbols/lines in binary mixtures with DEET (b). The figure is adapted from Ref. [59] and Ref. [166].

PLLA/DEET mixtures with up to 4.5 m% of DEET were also prepared by melt extrusion. The addition of DEET as a plasticizer decreased the glass transition temperature of PLLA. The presence of DEET also influences the crystallization kinetics of PLLA, delaying the nucleation but causing higher crystal growth rates.[168]

Bonadies et al.[169] incorporated more than 50 m% of DEET into PLLA fibers with defect-free and uniform morphology and a diameter of around 1 μm by solvent electrospinning, as shown in Figure 17. Thermal and structural characterizations indicated that DEET assisted crystallization of PLLA into α crystal form during electrospinning and the resulting nonwoven mat was non-oriented. Evaporation/release of DEET was delayed in the electrospun fibers, which may allow controlled release of the insect repellent.
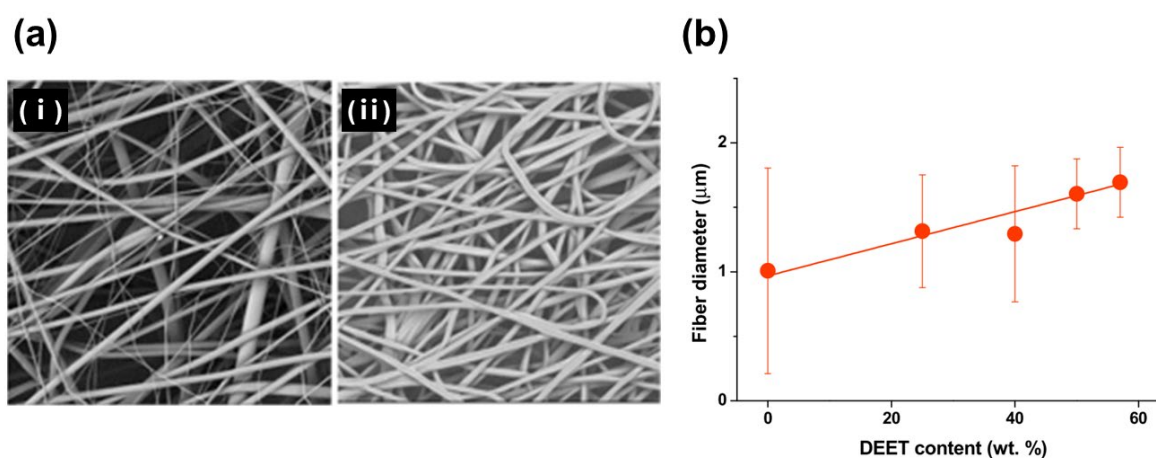

Figure 17. SEM micrographs of PLLA/DEET fibers, containing 0 m% (a, i) and 44 m% (a, ii) DEET, prepared from PLLA/DEET/CHCl₃ solutions and diameter of PLLA/DEET fibers as a function of DEET content (average and standard deviation estimated by analysis of more than 100 fibers) (b). The figure is adapted from Ref. [169].

Ferreira et al.[170] attempted to obtain monofilaments of non-crystallizable PDLLA, with 11.3 % D-unit, and DEET by melt spinning. It is possible to produce PDLLA monofilaments containing up to 20 m% DEET, however, the DEET content greatly limited the attainable take-up speed or draw-down ratio and mechanical integrity, as shown in Figure 18. 20 m% DEET content in PDLLA/DEET monofilament enables the formation of α-crystals by stress-induced crystallization during the melt spinning, by contrast, PDLLA monofilaments without DEET and with 10 m% DEET were amorphous under the same conditions. In order to enhance the mechanical integrity and simultaneously serving as a tailorable release barrier to the DEET, a crystallized PLLA as sheath was introduced for a bicomponent sheath-core structure with amorphous PDLLA/DEET as the core by melt spinning.[171] However, only the thermal behavior of bicomponent PLLA-PDLLA/DEET (sheath-core) monofilaments was studied. The presence of DEET increased the mobility of the PLA chains, resulting in a lowered T_g, and favored the formation of the α'-crystal structure.
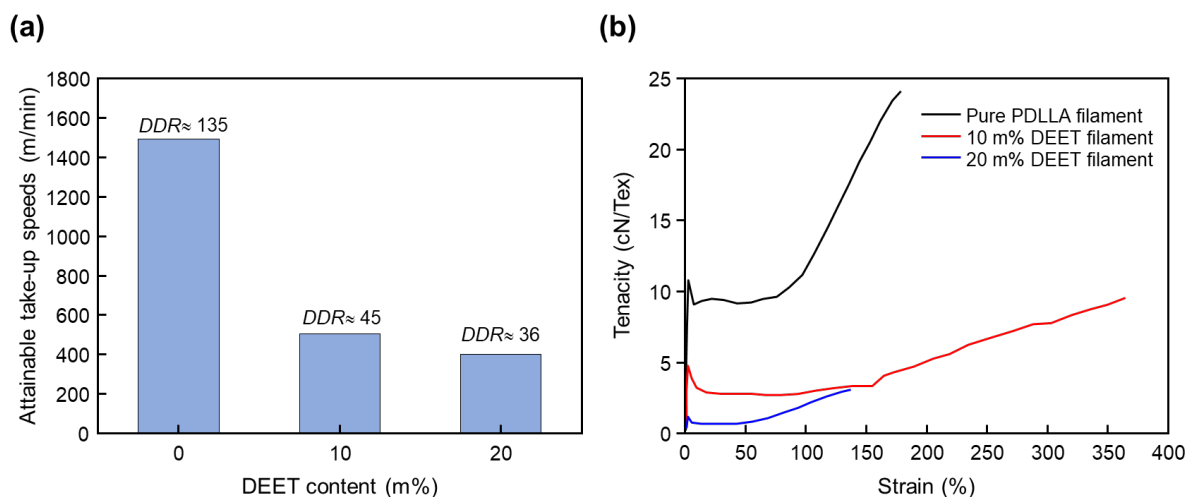
(a)

(b)

Figure 18. Attainable take-up speeds and the approximated associated draw-down ratio (DDR) for melt-spun PDLLA monofilaments with varying DEET content (a) and tenacity of PDLLA/DEET monofilaments as a function of strain (b). The figure is adapted from Ref. [171].

PLLA strands, with M_n of 44 kDa and PDI of 2.95 and 2.3 % of D-unit content, containing DEET and IR3535 were prepared by twin screw extrusion by Mapossa et al.[172] Thermal and rheological studies showed that both DEET and IR3535 have a plasticizing effect on for PLLA. The release rates of repellent measured at 50 °C showed initial fast release behavior and then slowed down to a near constant rate at longer times, indicating non-Fickian Type II transport controlling the release process.

PBS, a bio-sourced and biodegradable polymer, with a much higher crystallization rate and faster degradation rate than PLLA was used as carrier for development of repellent-release devices and environment-friendly disposal after usage. The incorporation of DEET into PBS, including DEET-rich and polymer-rich composition, respectively, was studied by Yener et al.[173,174] Regarding DEET-rich solutions with up to 30 m% PBS, PBS-scaffolds hosting DEET were obtained by S-L TIPS/crystallization-controlled TIPS during cooling the PBS/DEET homogeneous solutions formed at elevated temperature. The morphology of scaffolds depends on the cooling condition and polymer content.[173] As for polymer-rich mixtures with up to 40 m% of DEET, PBS/DEET strands were prepared by twin-screw extrusion. The quantification of release of DEET at temperatures between 60 and 100 °C by thermogravimetric analysis (TGA) suggested a slow-release rate at 25 °C, with a corresponding time constant of around 1.5 years, albeit the repellent efficiency is unknown.[174]

Recently, cellulose diacetate, a biodegradable polymer made by treating natural cellulose with acetic acid, combined with organoclay as controlled release nanocomposite device for natural plant-based insect repellents, such as citronellol, terpineol and methyl salicylate, were developed by extrusion-compounding.[175] The addition of the organoclay significantly modified the internal morphology of the strands due to clay dispersion and intercalation, and significantly accelerated the release rates when ageing the extruded strands at 40 °C.

In addition, water-soluble beta-cyclodextrin (βCD)-based polymer, obtained using pyromellitic dianhydride (PMDA) as a linking molecule, was used to produce fibers by solution electrospinning and then DEET was loaded in the electrospun fibers with an average fiber

diameter of 2.8 ± 0.8 µm. DEET loading was performed using diethyl ether as solvent and the loading capacity was evaluated as 130 mg/g. The release of DEET from the polymer matrix was assessed by TGA and lasted for over 2 weeks at room temperature.[176]

A summary of polymer/repellent release devices fabricated by different techniques is shown in Table 5.

Table 5. A summary of polymer/repellent release devices fabricated by different techniques.

System	TIPS	Extrusion	Electro-spinning	Melt-spinning	3D-printing	Ref.
Petroleum-based P/R						
LLDPE/Citronellal	√					[104]
HDPE/(EVA/DEET)				√		[123]
LLDPE (or EVA)/DEET (or Icaridin)		√				[124]
EVA/DEET (Icaridin)		√				[158]
PET (PVA)/B. amyloliquefaciens spores		√	√			[13]
PA6/Permethrin			√			[159]
PA66/Picaridin			√			[160]
PA66/DEET			√			[161]
Bio-based P/R						
PDLLA/DEET	√			√		[59,166,170]
PLLA/DEET	√	√	√			[59,165,168,169,172]
PBS/DEET	√	√				[173,174]
PDLLA/IR3535	√					[61]
PLLA/IR3535	√	√	√		√	[172,177,178]
PLLA/Permethrin			√			[179]
PLA/Nepeta essential oil			√			[180]
Cellulose diacetate-organoclay/Citronellol (or Terpineol/Methyl salicylate)		√				[175]
PMDA-βCD/DEET			√			[176]

P represents polymer; R represents repellent.

2. PROBLEM STATEMENT

Mosquitoes are the main vector to transmit harmful tropical diseases, like malaria, dengue fever, and zika, etc. In the absence of effective vaccines and with biology control not ready for large-scale implementation, and there are some debates regarding the release of genetically engineered organisms to the environment, the control of these diseases mainly relies on parasite control by detection and treatment of infected people, as well as vector control. Vector control is currently the main method advocated by WHO, including the use of long-life insecticidal bed nets and indoor residual spray, both of which are indoor mosquito bite protection, relying on the mosquitoes coming indoors to get into contact with the insecticide. However, outdoor vector control measures are insufficiently developed. Therefore, developing outdoor protection measures are urgent since people stay outside for long periods during the day and early night. On the market available products have problems related to the short time of protection, that is, they lack long-term protection/lifetimes due to the high volatility of repellents and require frequent reapplication to maintain effectiveness as mosquito populations have developed the resistance to repellent/insecticide. This promoted the exploration and development of new tools and strategies for wearable products/devices with longer-lasting mosquito repellency.

Previous studies have demonstrated and highlighted the usage of polymer scaffolds as reservoirs/carriers for repellents can prevent contact of mosquitoes with the human skin, thereby playing a significant role in diminishing disease transmission. Incorporation of insect repellent into polymers is an effective strategy to increase the duration of repellence activity and avoid the frequent application of repellents, as well as reduce skin absorption of repellent. From the perspective of long-term environmental friendliness and sustainability, the usage of biopolymers is the preferred substitute for petroleum-based polymers. At the end of the lifecycle of biopolymers, they are expected to degrade within a reasonable time to avoid adverse environmental impacts. Mosquito repellents act by forming a vapor barrier to prevent contact with the insect with the human skin and should show a slow, constant evaporation rate, which means a minimum vapor pressure is needed to remain effective over a long period of time. Among them, DEET and icaridin are most incorporated into polymers to form different structures to tailor their release rates. However, some side effects on pregnant women and children who are most vulnerable to mosquito-borne diseases are reported. Therefore, an effective, safe and environmentally friendly repellent needs to be selected. The thermodynamics and crystallization kinetics of the new system, which are vital information and guidance for preparation for microporous structure and subsequent repellent release, are currently unknown. It is necessary to investigate the manufacturing techniques, conditions and parameters that can affect the size and shape, structures, thermal and mechanical properties and repellent release profiles of the final product, thus influencing the efficacy and safety of the final application.

3. RESEARCH SUBJECTS

To overcome the limitations of outdoor vector control, as well as detrimental side-effects of repellents, a new development of a biopolymer/mosquito-repellent system, here PLA/IR3535, with intended long-lasting repellency and process-depending scaffold structures, is investigated.

For selection of a polymer, PLA is an excellent candidate for preparation of scaffolds, porous membranes, and foams in recent years. PLA is a biopolymer and found in many applications because of its biodegradability, food safety compliance, and biocompatibility. As for the repellent, IR3535 is structurally similar to the natural substance β-alanine which is a component of pantothenic acid (vitamin B_5), which has less side effects on the environment and human beings and is also used for pregnant women and children. Compared to DEET, IR3535 is proved to be a potential repellent to realize long lasting repellency protection due to its high boiling point and low vapor pressure. In addition, the incorporation of IR3535 into PLA is hardly mentioned in the literature.

The aims of this thesis are to

(1) determine the optimum PLA dissolution conditions and identify the phase separation mechanism.

(2) evaluate the scaffold formation from solutions composed of crystallizable PLLA and the repellent IR3535. Controlled drug delivery, that is, controlled rate of repellent release, is reached by crystallization-controlled formation of a PLLA scaffold with porous structures, which depends on the PLLA/repellent ratio, the molecular architecture of the polymer, and the conditions of solution-crystallization. All these parameters are thoroughly investigated regarding their effect on the final scaffold structure forming by TIPS on cooling PLLA/IR3535 solutions, ultimately allowing tailoring the drug release rate. The quantitative relations between the conditions of solution-crystallization of PLLA and the structure of the PLLA scaffold are established.

(3) explore and develop new fabrication techniques to obtain repellent-loaded polymer devices with different surface-to-volume ratios and geometries. The effects of processing conditions and parameters on the morphology, thermal and mechanical properties and crystalline structure of the processed parts are investigated.

(4) estimate the release of IR3535 from parts processed by different processing techniques and conditions and extrapolate the evaporation rate to the application temperature.

The corresponding strategies are following:

(1) In order to clarify the phase mechanism, in which possible L-L TIPS may mask the S-L TIPS, non-crystallizable PDLLA is used first. From a macroscopic point of view, the dissolution conditions are confirmed by cloud point measurements; from a thermodynamic point of view, the solubility of PDLLA/IR3535 is verified by glass transition behavior measured by combining DSC and FSC.

(2) Crystallizable PLLA scaffolds hosting the repellent IR3535 are fabricated by TIPS. Different PLLA/IR3535 ratios and conditions of solution-crystallization of PLLA, including non-isothermal crystallization with different cooling rates and isothermal crystallization by varying the isothermal temperature, are respectively studied to form different morphologies of PLLA scaffolds. A relationship between scaffolds and formation conditions is then developed.

(3) New fabrication techniques, like melt extrusion, FDM-based 3D-printing and electrospinning, are trialed for polymer-rich PLLA/IR3535 mixtures. The repellent content and thermal stability of obtained products are characterized by TGA, nuclear magnetic resonance (NMR) and Fourier-transform infrared (FTIR) spectroscopy; the structure of obtained products are evaluated by calorimetry (DSC), microscopy (POM, SEM, atomic force microscopy (AFM)) and X-ray scattering (wide-angle X-ray scattering (WAXS) and small-angle X-ray scattering (SAXS)); the mechanical properties of obtained products were studied by tensile test and dynamic mechanical analysis (DMA).

(4) The repellent release kinetics is investigated by TGA at different temperatures. The temperature dependence of characteristic release times (τ) is determined by fitting the experimental mass loss curves with a single-exponential decay function and then the τ is extrapolated to body/room temperature.

(5) Deriving conclusions about the formation mechanism and fabrication techniques of polymer scaffolds accommodating functional repellent to help better understand and predict the structure of polymer scaffolds in polymer/repellent systems or polymer/drug systems and the release characteristics of repellent, respectively. In addition, the experimental tools and specially designed methods used in this work can be available for similar analysis of polymer/solvent systems.

4. RESULTS AND DISCUSSION

The results and discussion part in this cumulative dissertation are presented as a series of research publications, introduced based on graphical abstracts.

4.1 Full-composition-range glass transition behavior of the polymer/solvent system poly(lactic acid)/ethyl butylacetylaminopropionate (PLA/IR3535®)

Fanfan Du[1], Christoph Schick[2,3], and René Androsch[1,*]

[1] Interdisciplinary Center for Transfer-oriented Research in Natural Sciences, Martin Luther University Halle-Wittenberg, 06099 Halle/Saale, Germany

[2] University of Rostock, Institute of Physics and Competence Center CALOR, Albert-Einstein-Str. 23–24, 18059 Rostock, Germany

[3] Butlerov Institute of Chemistry, Kazan Federal University, 18 Kremlyovskaya Street, Kazan 420008, Russia

Graphical abstract:
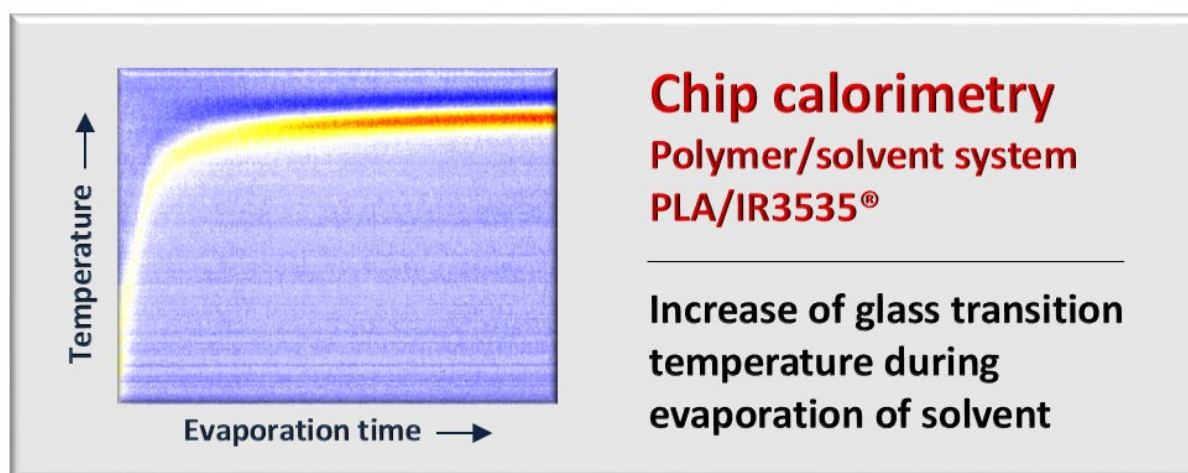
Highlights:

❖ The system poly (lactic acid)/ethyl butylacetylaminopropionate (PLA/IR3535®) is considered as a drug-delivery system.
❖ PLA and IR3535® are fully miscible.
❖ The glass transition temperature of polymer-rich solutions follows the Gordon-Taylor equation.
❖ Chain connectivity causes two glass transitions at intermediate polymer concentrations.
❖ Fast scanning calorimetry permits glass transition analysis during successive solvent evaporation.
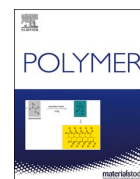
Full-composition-range glass transition behavior of the polymer/solvent system poly (lactic acid) / ethyl butylacetylaminopropionate (PLA/IR3535®)

Fanfan Du [a], Christoph Schick [b,c], René Androsch [a,*]

[a] *Interdisciplinary Center for Transfer-oriented Research in Natural Sciences, Martin Luther University Halle-Wittenberg, 06099 Halle/Saale, Germany*
[b] *University of Rostock, Institute of Physics and Competence Center CALOR, Albert-Einstein-Str. 23–24, 18059 Rostock, Germany*
[c] *Butlerov Institute of Chemistry, Kazan Federal University, 18 Kremlyovskaya Street, Kazan, 420008, Russia*

A B S T R A C T

The polymer/solvent system poly (lactic acid)/ethyl butylacetylaminopropionate (PLA/IR3535®) is considered as a drug-delivery system, in which a polymer hosts a liquid with a functionality as insect repellent. Such devices require solubility of the components at high temperature and observation of crystallization-induced solid-liquid phase separation on cooling. Precise knowledge of the thermodynamic solubility of the components is then difficult to obtain due to possible superposition of liquid-liquid phase separation with polymer crystallization. Therefore, in the present study the miscibility of the polymer/solvent system PLA/IR3535® was explored by employing non-crystallizable PLA, by analysis of the glass transition behavior in the full composition range. The data revealed that the two components are miscible regardless the system composition, with the glass transition temperature of solutions showing a negative deviation from the linear mixing rule, suggesting rather weak enthalpic interactions of the system components. The study included application of conventional and fast scanning chip calorimetry, which allowed for controlled and stepwise evaporation of solvent by repeated exposing the system to elevated temperature and evaluation of the glass transition temperature during in-between cooling and reheating. This novel approach permits an efficient analysis of the glass transition temperature as function of the system composition in a single experiment in a wide range of solvent concentrations.

1. Introduction

Poly (lactic acid) (PLA) is a linear polyester produced from short-term renewable resources and exhibits a balanced thermo-mechanical property profile allowing for its use as both commodity and engineering thermoplastics with applications in the fields of packaging, agriculture, automotive, or electronics [1–4]. Furthermore, PLA is compostable/biodegradable and biocompatible, promoting its use, among others, as biomedical material [4–6]. All properties depend on the presence of crystals, controlled, in case of PLA, by the molecular architecture, that is, the presence of D- and L-isomers in the macromolecular chain [7,8]. Macromolecules containing only D- or L-isomers, that is, PDLA and PLLA homopolymers, respectively, crystallize well from point-of-view of the maximum achievable crystal fraction, while in random PDLLA copolymers containing both units, crystallizability reduces. Typically, PLLA containing more than about 10% co-units,

randomly placed along the chain, are amorphous or exhibit negligible crystallinity [9–11]. Nowadays, a large variety of PLA grades of different crystallizability is available fitting all needs, for example regarding biodegradability/bioresorbability or the thermo-mechanical behavior.

Special fields of application of PLA arise from the preparation of scaffolds, porous membranes, or foams, e.g., in tissue engineering [12–17]. Such structures typically form via thermally induced phase separation (TIPS), employing organic solvents for obtaining a solution at elevated temperature. The solution then demixes on cooling via crystallization-induced solid-liquid (S-L) or liquid-liquid (L-L) phase separation [18–21]. The approach of forming a polymeric solid scaffold hosting a liquid with a functionality as a mosquito repellent when slowly evaporating was introduced on example of the polymer/repellent system polyethylene/citronellal [22]. A recent study proved that PLA is a further promising environment-friendly candidate as polymeric carrier for such repellents [23]. More specific, PLA forms at elevated

---

temperature a solution with *N,N*-diethyl-3-methylbenzamide (DEET), being the gold standard of mosquito repellents [24]. Systems containing crystallizable PLLA show S-L TIPS on cooling, with the PLLA crystals forming a scaffold with a morphology and superstructure tunable by the crystallization conditions and the solvent concentration [25]. Even electrospinning for preparation of PLLA fiber mats containing up to 50 m % (m% = mass %) DEET is possible [26]. While scaffold formation, for anticipated use of PLA as drug/repellent-delivery carrier, typically occurs in solvent-rich compositions, further research proved possible use of DEET as a functional plasticizer for PLA, efficiently decreasing the glass transition temperature T_g in PLA-rich mixtures [27]. As such, the polymer/solvent system PLLA/DEET offers multiple opportunities for specific material developments.

For evaluation of the thermodynamic miscibility of solvent-rich PLA/ DEET mixtures, non-crystallizable PDLLA was employed to avoid that L-L TIPS is masked by crystallization. An upper critical solution temperature (UCST) was identified, with the critical temperature and polymer concentration being slightly below ambient temperature and around 10 m%, slightly depending on the polymer molar mass, respectively [28, 29].

DEET belongs to the most efficient mosquito repellents, and exposure of human beings to DEET seems not to impose a potential risk to the general population [30]. Furthermore, though there exist reports of detection and accumulation of DEET in the environment, mainly surface water and soil, concentrations are distinctly lower than needed causing detrimental effects to environmental species [30–32]. Despite the excellent performance of DEET, there is a growing interest of the human society for using natural alternatives instead synthetically produced DEET. Besides plant-based natural repellents like oil of citronella or lemon eucalyptus [33], also bio-inspired insect repellent ethyl butylacetylaminopropionate (IR3535®) is discussed in the literature as alternative for the synthetic counterparts [34,35]. The development of IR3535® by Merck is based on mimicking the naturally occurring amino acid β-alanine, with slight modifications regarding end-groups in order to decrease toxicity and increase efficacy [34].

Despite an unequivocal opinion about considering IR3535® as a bio-repellent is not achieved [36], we attempt exploring its potential for developing a further PLA-based drug-delivery system. In the first step, being subject of the present study, we explore the general solubility of PLA with IR3535®, being a stringent demand for applying the technique of S-L TIPS for obtaining a solid polymer/liquid repellent system. In order to gain insight about the thermodynamic miscibility of the PLA/IR3535® system, cloud-point/turbidity measurements were performed for solvent-rich mixtures up to 50 m% polymer, while for all compositions the glass transition behavior was analyzed. Evaluation of the glass transition temperature of two-component systems consisting of a polymer and a solvent provides information of both the homogeneity/heterogeneity of mixtures but also the thermodynamic miscibility and the strength of enthalpic and entropic interactions in case the system is homogenous [37–41].

2. Experimental

2.1. Materials

We used a non-crystallizable PDLLA random copolymer R207S from Evonik, containing ᴅ- and ʟ-isomers. The intrinsic viscosity of the polymer is between 1.3 and 1.7 dL/g (measured at 25 °C in 0.1% CHCl₃-solution) [42], and the mass-average molar mass and polydispersity are 262 kg/mol and 1.6, respectively [28]. The glass transition temperature of the particular PDLLA grade is around 60 °C. IR3535® was obtained

from Carbolution Chemicals GmbH (Germany). It is a clear liquid with a boiling temperature of 141 °C [43], and a glass transition temperature of close to -90 °C.

PDLLA flakes and IR3535® were placed inside 3.5 mL-glass-vials, which were closed with a lid. Dissolution was performed at 60 °C using a Thermo Scientific Reacti-Therm block heater/stirrer within few minutes, with the polymer content being between 5 and 50 m%.

2.2. Instrumentation

The turbidity of the mixtures of PDLLA and IR3535® was analyzed by visual inspection of the appearance of the samples in the glass vials in the temperature range from about -65 °C and +90 °C. For sub-ambient-temperatures, a dry ice/ethanol mixture was used as coolant while samples were heated using a hotplate. For demonstration of cloudiness, selected dissolution experiments were performed involving PDLLA with a mass-average molar mass of 177 kDa (grade R205S from Evonik) [28] and DEET, obtained from Sigma Aldrich (Germany) [44], as solvent.

For analysis of the glass transition behavior, we employed conventional differential scanning calorimetry (DSC) and fast scanning chip calorimetry (FSC), using DSC 820 and DSC 1 heat-flux calorimeters, and a Flash DSC 1 power-compensation chip calorimeter, respectively, provided by Mettler-Toledo (Greifensee, Switzerland). The DSC 820 was operated in conjunction with a liquid nitrogen accessory while the DSC 1 and Flash DSC 1 were connected with a Huber TC100 intracooler (Offenburg, Germany). The sample environment in all devices was purged with nitrogen at flow rates recommended by the instrument supplier. Both, the DSC 820 and DSC 1 were initially calibrated by the manufacturer, with its validity regularly (weekly) checked by analysis of the temperature and enthalpy of melting of Indium standard. In case of the Flash DSC 1, the used UFS 1 sensors are delivered in a pre-calibrated state [45], with a further correction performed by the user after a conditioning of the sensor, in order to accommodate the specific temperature of the cold-junctions of the thermocouples used for obtaining the temperature signal [46].

In case of DSC measurements, samples were placed in 40 μL aluminum pans and covered with a lid, unless controlled evaporation of solvent was desired. Glass transition temperatures were obtained on heating the samples at a rate of 20 K/min, considering that linear cooling to temperatures of -95 °C (DSC 1) or -120 °C (DSC 820) is restricted to values well below 10 K/min; in case of the DSC 1, we used cooling rates of 10 and 2 K/min in the temperature ranges from -20 to -50 °C and -50 to -90 °C, respectively, and in case of the DSC 820, cooling was performed at a rate of 2 K/min. For samples with a PDLLA content of 50 m%, or less, glass transition temperatures were measured on individual samples. For observation of heat capacities, a DSC raw data were subject to baseline-subtraction and correction using sapphire as standard.

For the composition-range between 50 and 100 m% polymer, a new analysis technique was introduced. It included the preparation of a sample containing 50 m% polymer and controlled evaporation of solvent and analysis of glass transition temperatures by DSC and FSC. Partial evaporation of solvent occurred by exposing the sample to elevated temperature for a predefined time, followed by cooling and reheating for analysis of the mass loss via measurement of the sample-heat capacity and of the glass transition temperature, with the procedure repeated until the solvent was completely evaporated. In case of using the DSC 1, the instrumental setup was unchanged compared to the T_g-analysis of individual samples, except that the aluminum pan was kept uncovered. In addition, the sample mass, and with that the loss of solvent in each cycle of the experiments was monitored by weighting

using a balance. Though analysis of the kinetics of solvent evaporation was out of the scope of the present work, temperature-modulated DSC (TMDSC) was applied for quasi-isothermal measurement of the reduction of the reversing heat capacity due to the mass loss during evaporation. TMDSC involved a saw-tooth temperature-time profile, with a programmed amplitude and period of modulation of 1 K and 240 s, respectively, and calculation of the reversing heat capacity based on evaluation of the amplitudes of the first harmonics of the Fourier transforms of the modulated heat-flow rate and sample temperature, as described in the literature [47–49].

The main advantage/difference of employing an FSC instead of DSC is the distinct reduction of the measurement time due to the much higher scanning rates. Otherwise, there is no qualitative difference regarding the applied thermal profiles. The FSC sensor-support temperature was set to -90 °C and the sample environment was purged with nitrogen gas using a flow rate of 40 mL/min. Solvent evaporation and repeated vitrification/devitrification of the sample imposed significant stress to the chip membrane, as was recognized by strong baseline curvature. For this reason, the sample was not loaded directly onto the chip membrane, instead on a small piece of gold leaf with a thickness of 100 nm [50], placed in the center of the sensor on a thin silicone-oil film, effectively allowing for shrinkage and expansion of the samples without straining the membrane [50]. Note that the addenda heat capacity of the gold leaf is negligible, thus not requiring additional symmetry corrections. Care was taken for placing the gold leaf and sample into the center of the heatable area of the sensor, assuring absence of larger lateral temperature gradients [51]. Further details about the experimental setup and temperature-time profiles are given below. The FSC cycle-experiment has been performed and analyzed twice, employing different operators and sensors.

3. Results and discussion

3.1. Miscibility of mixtures of PDLLA and IR3535® by turbidity inspection

Fig. 1 shows photographs of mixtures of PDLLA (262 kDa) and IR3535® containing 10, 20, 30, and 50 m% PDLLA (from left to right), taken at temperatures between -62 °C and +90 °C (from bottom to top). All samples reveal a clear appearance and suggest that the two components form homogeneous solutions within the analyzed range of temperatures and concentrations. Note that preparation of mixtures

containing more than 50 m% polymer was not attempted due to the high viscosity of the solvent/polymer compound, even at elevated temperature, hindering efficient mixing by magnetic stirrers. The temperature-range covered in the experiment of Fig. 1 is based on the use of a dry/ethanol mixture at the low-temperature side, and on the maximum temperature being used in DSC/FSC experiments involving controlled evaporation of solvent.

In order to demonstrate the different optical appearance of heterogeneous mixtures, Fig. 2 compares with the left and right collection of photographs the systems PDLLA/IR3535® and PDLLA/DEET, respectively. In contrast to the experiment presented with Fig. 1, in which PDLLA with a mass-average molar mass of 262 kDa was used, Fig. 2 shows images of samples containing PDLLA with a mass-average molar mass of 177 kDa. In case of the system PDLLA/IR3535®, within the analyzed concentration range of 10–50 m% polymer and temperature range from -62 °C to room temperature (RT), the mixtures are clear and confirm formation of homogeneous solutions. A similar situation is detected for PDLLA/DEET mixtures at RT, however, for samples of the PDLLA/DEET system containing 10, 20, and 30 m% polymer, L-L demixing occurs on cooling as indicated by distinct turbidity. Earlier research provided detailed information about the UCST phase behavior of the system PDLLA/DEET, including the polymer molar-mass dependence [28,29]. With respect to the present study, the images of Fig. 2 suggest, within the analyzed temperature and concentration ranges, a qualitatively different subambient-temperature miscibility of PDLLA when using IR3535® or DEET as solvent. At room temperature, and higher temperatures, both dissolve PDLLA while only in case of DEET occurs demixing on lowering the temperature. Worthwhile noting that besides PDLLA with molar masses of 262 kDa (Fig. 1), and 177 kDa (Fig. 2), similar observations were detected on using PDLLA with a molar mass of 49 kDa (not shown), however, with cooling experiments performed down to -20 °C only in the latter case.

3.2. Glass transition temperature of the system PDLLA/IR3535® at concentrations up to 50 m% PDLLA

Fig. 3 shows DSC heating curves in specific-heat-capacity units, obtained on heating neat PDLLA (black), neat IR3535® (orange), and PDLLA/IR3535® solutions containing between 5 and 50 m% polymer, as indicated in the legend. Analysis of PDLLA reveals a glass transition temperature $T_{g, PDLLA}$ of around 55 °C which is expected based on data available in the literature [52–54]. For neat IR3535®, the data of Fig. 3
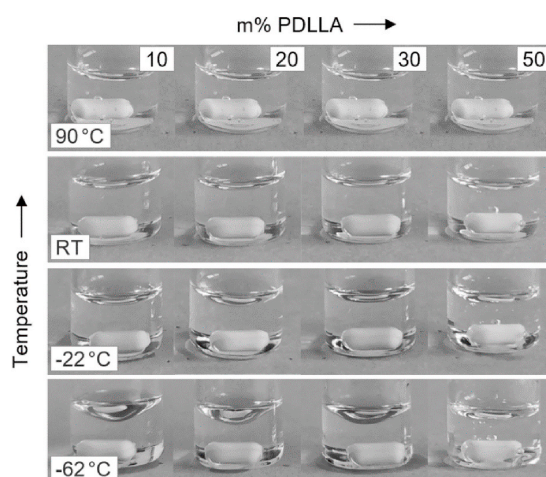

Fig. 1. Optical appearance of mixtures of PDLLA (262 kDa) and IR3535® containing 10, 20, 30, and 50 m% PDLLA (from left to right), at temperatures between -62 and + 90 °C (from bottom to top).
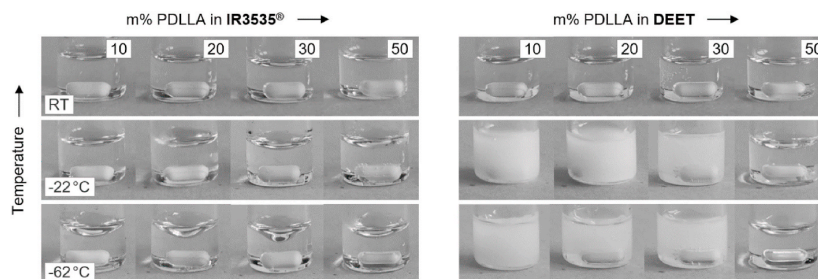
Fig. 2. Optical appearance of mixtures of PDLLA (177 kDa) and IR3535® (left) or DEET (right). The polymer content is 10, 20, 30, and 50 m% PDLLA (from left to right). Images were taken at temperatures between -62 °C and room temperature (RT) (from bottom to top).

suggest a value $T_{g, IR3535}$ close to -90 °C, with further data in scientific reports, for comparison, not available. Addition of low amount of up to 10 m% PDLLA into IR3535® has negligible effect on the glass transition temperature, however, if the polymer content in PDLLA/IR3535® solutions exceeds 10 m% then both a shift to higher temperature and significant broadening of the glass-transition-temperature range is detected. The latter phenomenon is indicated in Fig. 3 with the gray lines labeled 'approximate begin/end of glass transition'. As such, for the solution containing 50 m% PDLLA (upper curve, brown), the glass transition begins on heating at about -80 °C and stretches to about -40 °C. The two vertical arrows emphasize furthermore the observation of different slopes of the curve within the glass transition-temperature range, being interpreted as occurrence of two different glass transitions. This result is not necessarily pointing to a macroscopic phase separation but different local neighborhood of solvent and polymer molecules in the solutions. In fact, distinct broadening of glass transitions and even detection of two discrete transition temperatures at intermediate polymer concentration is reported for several polymer-solvent systems including polystyrene-tricresyl phosphate [55], polystyrene-dialkyl phthalate [56], polymethylmethacrylate-ionic liquid [57], or poly (α-methyl styrene) with its hexamer [58]. The experimental observations are often discussed in terms of the Lodge-McLeish model which was introduced to explain self-concentration effects on the glass transition behavior in miscible polymer blends [59–61]. In short, the low-temperature transition is caused by small solvent molecules and not largely affected by the presence of few macromolecules. The high-temperature part of the glass transition, in contrast, is attributed to polymer relaxation at the scale of the Kuhn length caused by so-called chain connectivity affecting the local environment of a repeat unit [56].

3.3. Glass transition temperature of the system PDLLA/IR3535® by DSC evaporation experiments

Fig. 4 shows with the left graph the temperature-time profile of a typical DSC cycle experiment for establishing a correlation between the composition of polymer-rich PDLLA/IR3535® solutions and the glass transition temperature. As sample with an initial polymer concentration of 50 m% and an initial mass of 7–8 mg is heated in an open pan from -90 °C, being the low temperature-limit of the used device, to the evaporation temperature of 125 °C and isothermally annealed for about 60 min. During annealing, the sample is subject to temperature-modulation, allowing calculation of the absolute reversing heat capacity being proportional to the sample mass, thus allowing following solvent evaporation. Afterwards, the sample is cooled at 10 K/min to -50 °C, with the selection of the cooling rate and target temperature based on the goal to warrant a linear change of temperature as a function of time during cooling, permitting analysis of the glass transition temperature. After heating to 25 °C, the sample mass is checked using a balance, providing ultimate information about the evaporation process. Then the sample is re-inserted into the DSC, in order to continue the non-complete evaporation process. For the chosen evaporation parameters of 125 °C and about 60 min, a total of 11 cycles was needed to complete the evaporation process, that is, to achieve constant sample mass and glass transition temperature in two subsequent cycles of the experiment.

The right graph of Fig. 4 shows typical DSC heating (lower part, red) and cooling curves (upper part, blue) obtained on a sample exposed to the temperature-time profile of the cycle experiment shown in the left part of Fig. 4. The various curves are staggered according to the cycle number for improved visibility of the change of the glass transition temperature. It is obvious that for a given composition of the solution,
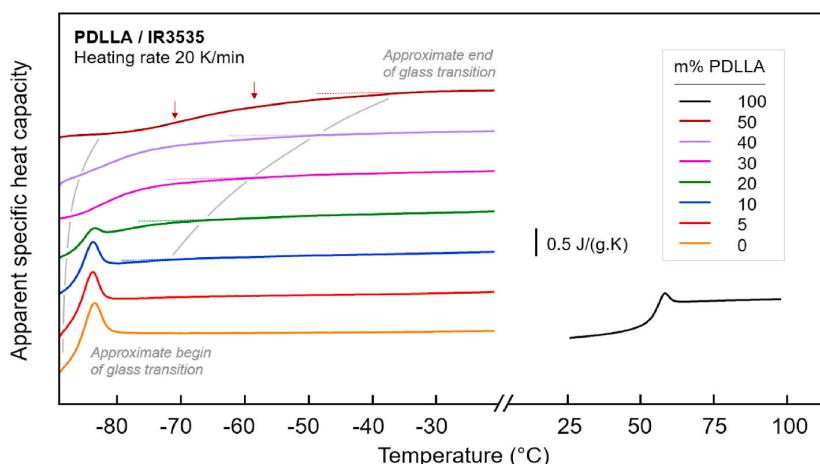
Fig. 3. DSC heating curves in specific-heat-capacity units, obtained on heating neat PDLLA (black), neat IR3535® (orange), and PDLLA/IR3535® solutions containing between 5 and 50 m% polymer, as indicated in the legend. Data are obtained using the Mettler-Toledo DSC 1. The two arrows at the top curve serves as a guide to the eye only, emphasizing the approximate midpoints of curve sections of different slope. (For interpretation of the references to color in this figure legend, the reader is referred to the Web version of this article.)

Fig. 4. Temperature-time profile of a typical DSC cycle experiment for controlled and stepwise evaporation of solvent and analysis of glass transition temperatures (left). DSC heating and cooling curves for evaluation of glass transition temperatures (right), corresponding to the red- and blue-colored 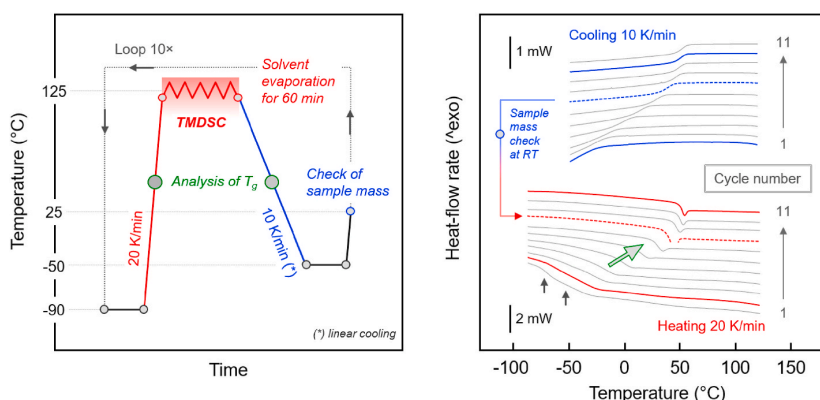segments in the left plot, respectively. The sets of heating and cooling curves represent data obtained in the various cycles of the experiment, with the curves staggered for optimum visibility of the glass transition temperature. (For interpretation of the references to color in this figure legend, the reader is referred to the Web version of this article.)

the glass transition temperature can be evaluated during cooling and during heating, as indicated with the dashed curves. After a specific evaporation step, T_g is obtained on cooling (blue dashed curve), and then the sample is analyzed regarding its composition by weighting. With the heating segment to the next evaporation step, T_g of the particular sample-composition is measured again (red dashed curve). The bottom curve in the lower set of scans represents the heating scan of the initial sample containing 50 m% of polymer. As shown in Fig. 3 (upper curve, brown), a rather broad glass transition is detected, apparently composed of two separate events as indicated with the two vertical arrows. With increasing cycle number, that is, with progress of evaporation and polymer-enrichment of the solution, the glass transition narrows and shifts to higher temperature towards $T_{g,\,PDLLA}$ slightly above 50 °C (see green arrow). With decreasing solvent concentration, the glass transition gets increasingly superimposed with a small enthalpy-recovery peak due to aging of the polymer-rich glass; for neat PLA, dedicated glass-relaxation studies are available in literature [62–67], however, these are out of interest in the present work. The cooling curves in the upper part of the graph reveal similar information about the change of the glass transition temperature with ongoing evaporation of solvent, though for the first three cycles, represented by the bottom three curves of the data set, a reliable determination of T_g is impossible due to the low-temperature limit of the scan of -50 °C.

Fig. 5 shows with the left graph the progress of evaporation of IR3535® during repeated annealing of the system at 125 °C, as detected by weighting the sample after each evaporation step (blue squares) and by monitoring the absolute heat capacity (red data). Both data sets are

consistent and reveal that after exposing the initial solution containing 50 m% polymer for about 600 min to 125 °C all solvent is lost. Though such measurement provides an idea about the evaporation kinetics, we are aware that the evaporation rate strongly depends on the specific experimental setup [68,69], like initial sample mass, sample surface-to-volume ratio, or furnace purging-conditions, requiring further quantification dedicated experiments, being out of the scope here. Interpretation of the evolution of the sample mass is straightforward. The initial mass was close to the 8 mg, and after complete evaporation of solvent, the sample mass dropped down to close-to 4 mg, as expected. Quantitative analysis of the reversing heat capacity in terms of the mass loss is not as straightforward as the direct analysis of the sample mass. The heat capacity of phase-separated two-component systems depends on the concentration of the components and their individual heat capacities according to a linear mixing rule [70]. In case of solutions, additional minor excess heat capacity is expected [71–73]. While for PLA the heat capacity is known [74], for IR3535® data are not available. Preliminary estimation of the heat capacity of IR3535® at 125 °C revealed a value slightly higher than for PLA, however, due to experimental uncertainties, a quantitative discussion of the obtained reversing heat capacities is not recommended. With the assumption that excess heat capacities due to thermodynamic interaction of the two components are negligible, such quantification would provide the opportunity of direct access of the sample mass. However, as the composition/mass of the solutions is determined directly, without any uncertainty beyond weighting errors, in-depth discussion of the heat capacity is not needed at present.
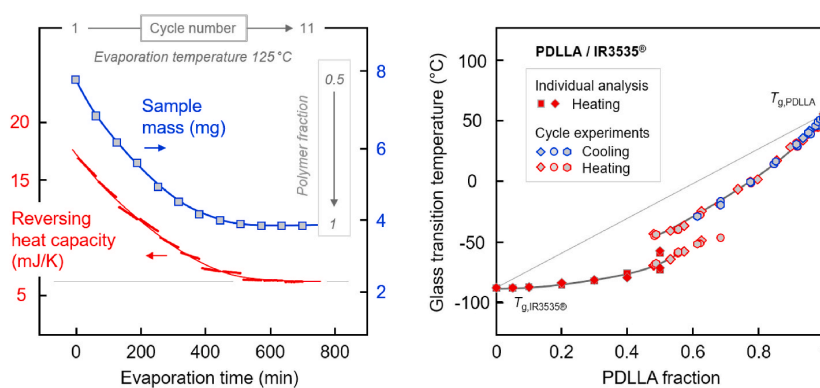

Fig. 5. Sample mass (blue) and reversing heat capacity (red) of a PDLLA/IR3535® solution initially containing 50 m% polymer as function of the cumulative time of evaporation within the DSC cycle experiment of Fig. 4 (left). Glass transition temperature of neat PDLLA, neat IR3535®, and PDLLA/ IR3535® solutions as a function of the PDLLA fraction (right). Data of solvent-rich compositions up to 50 m % PDLLA were obtained on individual samples of different polymer content (red filled squares) (see also Fig. 3) by using both DSC 1 and DSC 820, while data of polymer-rich compositions were gained by DSC-cycle-evaporation experiments (gray filled symbols) (see also Fig. 4), using the DSC 1. Red and blue coloring of symbols indicates that data were obtained during heating and cooling, respectively. The gray line represents a linear mixing rule. (For interpretation of the references to color in this figure legend, the reader is referred to the Web version of this article.)

The right graph of Fig. 5 shows glass transition temperatures of neat PDLLA, neat IR3535®, and PDLLA/IR3535® solutions as a function of the PDLLA fraction. Data of solvent-rich compositions up to 50 m% PDLLA were obtained on individual samples of different polymer content (red filled squares), according to Fig. 3. Data of polymer-rich compositions were gained by DSC-cycle-evaporation experiments according to Fig. 4 (gray filled symbols). Red and blue coloring of symbols indicates that data were obtained during heating and cooling, respectively. There has been performed a total of three cycle experiments, represented by different symbols, in order to assure reproducibility.

The experimentally observed glass transition temperatures of PDLLA/IR3535® solutions, throughout the entire composition range, show a negative deviation from the linear mixing rule (see gray line), pointing to specific enthalpic interactions between the two components. Moreover, the data reveal that for solvent-rich solutions up to about 40 m% polymer the glass transition temperature of the neat solvent seems nearly preserved, that is, the relaxation behavior of the system is primarily governed by the maintained mobility of the small solvent molecules. At polymer concentrations of about 40–70%, an extreme broadening of the glass-transition-temperature range is detected, spanning up to 40 K, and even suggesting occurrence of discrete transition temperatures with a low-temperature solvent-controlled and high-temperature polymer-controlled glass transition temperature. For polymer-rich compositions, the glass-transition-temperature range narrows again, with the glass transition temperature linked to that of the polymer. There is a striking qualitative similarity of the concentration-dependence of the glass transition temperature with data available in the literature (see Fig. 5 in [56]), obtained on the system polystyrene/dialkyl phthalate). For solvent- and polymer-rich compositions up to 30–40 m% of the second component rather narrow and single glass transition events are detected while at intermediate concentrations of solvent and polymer locally different compositions due to the covalent bonding of structural motifs in case of macromolecules, often termed chain connectivity, are probed by broadened glass transitions.

3.4. Glass transition temperature of the system PDLLA/IR3535® by FSC evaporation experiments

Recently, the mass-loss rate of a specific ionic liquid was measured using FSC, by exposing the sample for defined times to elevated temperature, and following the mass loss via the decrease of the absolute heat capacity assessed on cooling and re-heating the system [75]. A similar approach of employing FSC as controlled evaporation device for gaining information about sublimation vapor pressures and enthalpies was applied for thermally unstable substances of low volatility [76–78].

However, as far as we are aware, application of FSC for controlling the composition of polymer/solvent mixtures and simultaneous analysis of the glass transition behavior is not reported yet and is therefore described here for the first time. A further motivation for using FSC as an addendum technique to classical DSC is the tremendous decrease of the experiment time, as heating and cooling scans are performed at much higher rate and as solvent evaporation proceeds much faster due to the smaller sample size and the larger surface to volume ratio.

Fig. 6 shows in the left part the FSC temperature-time profile for analysis of the glass transition temperature of PDLLA/IR3535® solutions as a function of the concentration of the solvent. The initial solution containing 50 m% polymer is heated at a rate of 100 K/s to 90 °C and then annealed for a period of 1 s. The annealing step is followed by cooling the solution to -80 °C using the same rate of 100 K/s. The cycle of heating, isothermal annealing, and cooling is repeated 300×. Each repetition leads to evaporation of solvent, with the connected mass loss quantified by analysis of the absolute heat capacity of the sample. Note that we are aware that the temperature-time profile can further be tailored towards a precise evaluation of the evaporation rate, e.g., by assuring strict isothermal evaporation conditions when heating and cooling at higher rate of temperature-change. In the present work, rather low heating and cooling rates were employed in order to minimize thermal lags [79], being advantageous for estimation of glass transition temperatures.

The right graph of Fig. 6 shows as an example a set of 301 FSC cooling scans (top set of curves) and heating scans (bottom set of curves) in units of absolute heat capacities C_p, being proportional to the sample mass m. Red and blue colored curves denote the first and the last scan of the cycle-experiment, respectively. At the begin of the experiment, the solution contains 50 m% solvent and exhibits a rather broad glass transition centered at around -45 °C (see red vertical arrow). With increasing cycle number, solvent evaporates, causing a lowering of C_p due to the mass loss and a significant shift of the glass transition temperature to a higher value (see gray/black arrow). At the end of the experiment, after 300 cycles, the sample does not contain solvent anymore, and the glass transition temperature increased to about 55 °C, as expected for pure PDLLA (see blue vertical arrow). In the final cooling and heating scans the measured heat capacity C_p at 80 °C is about 0.185 µJ/K following the procedure described in [81]. With the knowledge of the specific heat capacity c_p of PLA at identical temperature [= 2.04 µJ/(µg K)] [74], the final sample mass m is estimated to about 91 ng [≈ 0.185 µJ/K/2.04 µJ/(µg K) = C_p/c_p]. Below, further information about the change of the experimental heat capacity with increasing cycle number is provided, as used for estimation of the composition of the sample.
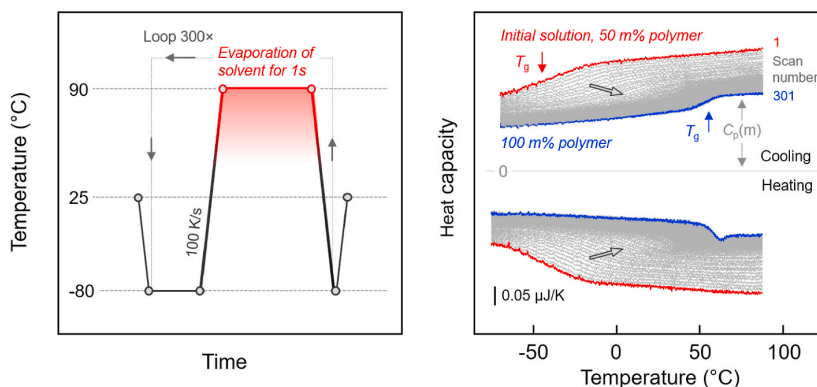
Fig. 6. FSC temperature-time profile for combined evaporation of solvent and analysis of glass transition temperatures of the PDLLA/IR3535® polymer/solvent system (left). Sets of 301 FSC cooling scans (upper part) and heating scans (lower part) (right). Red and blue colored curves represent the first and final cycle of the loop, respectively. (For interpretation of the references to color in this figure legend, the reader is referred to the Web version of this article.)

Automated analysis of the glass transition temperature from 301 cooling and heating scans involved in a first step smoothing of the FSC curves, to reduce the noise, followed by calculation of the first derivative of the heat capacity as a function of temperature. As such, the inflection point in the heat-capacity step during the glass transition in the FSC curves turns into a maximum. Fig. 7 shows with the left and right plots such first-derivative FSC curves, however, plotted vertically for easy recognition of the dependence of T_g on the cycle number. The ordinate of the curves (out of plane) is color-coded such that low and high values appear blue and yellow/red, respectively. This way, the change of T_g due to evaporation of the solvent from initially close-to -50 °C, when 50 m% solvent is evident in the sample, to about 55 °C, after complete evaporation, is advantageously presented. Note that we are aware that automated data evaluation of a set of 300 curves using a first-derivative approach instead of the more precise determination of the fictive temperature lacks high precision in the determination of T_g in heating experiments when there is observed a relaxation-caused overshoot. However, for the scope of present work, this imprecision we consider justified, in particular as the error becomes only evident in the final stage of the evaporation experiment (see also the enthalpy-recovery peaks in the heating curves in the right plot of Fig. 6).

Presentation of the glass transition temperature as a function of the cycle number, as in Fig. 7, does not provide the desired concentration-dependence needed to derive conclusions about component interactions. Therefore, with the left graph in Fig. 8 successive evaporation of solvent in each cycle of the experiment is estimated by plotting the absolute heat capacity measured at -70 °C (blue curve) and at 80 °C (red curve), that is, at temperatures lower and higher than the glass transition temperature, respectively, as a function of the cycle number. Note that these curves represent data obtained from cooling and heating scans, as suggested in [80]. With the squares and circles is emphasized the heat-capacity level of samples containing 50 and 0 m% solvent, respectively. At the chosen evaporation conditions (annealing at 90 °C for 1 s, and passing the temperature-range below 90 °C at a rate of temperature-change of 100 K/s), solvent evaporates fast within the first about 50 cycles of the experiment and then evaporation proceeds a much lower rate. Again, interpretation of the solvent evaporation kinetics is out of the scope of the present work. This notwithstanding, not shown preliminary experiments involving lower annealing temperatures of 85 and 80 °C confirm the expectation of lower evaporation rate with decreasing temperature [81] and, indeed, suggest the possibility of obtaining information about the temperature-dependence of

evaporation of liquids from polymeric host structures.

Data shown in the left plot of Fig. 8 provide information about the system composition, that is, about the polymer fraction in each cycle of the experiment, assuming negligible excess heat capacity. With these data, it is possible to present the glass transition temperature as a function of polymer content, as shown with the right graph in Fig. 8. The color-mapped first-derivative-FSC heating curves of the right plot of Fig. 7 were normalized regarding the maximum first-derivative value in each scan, and are then shown as a function of the polymer content instead the cycle number. As evaporation is non-linear versus time/cycle number, scans are not equidistant along the polymer-content axis, which, however, does not affect recognizing the general trend of the dependence of the glass transition temperature on the composition of the solutions, including the width of the transition (red color). The glass-transition-temperature plot additionally contains data of solvent-rich solutions collected using DSC (square symbols) (see also Fig. 5, right graph). Referring to Fig. 5, in which DSC glass transition temperatures were shown as a function of the sample composition, the data of Fig. 8 provide information that FSC can be a valuable and effective tool to characterize the glass-transition behavior of solutions. DSC and FSC experiments yield similar results, with the experiment-time, however, drastically reduced in case of using FSC.

3.5. Discussion of the concentration-dependence of the glass transition behavior of the system PDLLA/IR3535®

The glass transition temperatures of the pure components IR3535® and PDLLA are around -88 °C and 55 °C, respectively. The gray lines in Figs. 5 and 8 represent linear mixing behavior, that is, concentration-weighted additivity of the glass transition temperatures of the pure components. The experimentally observed data, both DSC and FSC, disprove such additivity rather suggest a strong negative deviation, related to the mixing thermodynamics/strength of interaction between the system components. Quantification of such interaction in both miscible polymer blends [82,83] and polymer/small-molecule (solvents, drugs, plasticizers) systems [84–89] often is attempted by fitting the concentration-dependence of the glass transition temperature employing equations proposed by Couchman and Karasz [90,91] (Eq. (1)), Fox [92] (Eq. (2)), or Gordon and Taylor [93] (Eq. (3)). All these equations predict a negative deviation from a linear mixing rule of the glass transition temperatures of the neat components and a monotonic concentration dependence, holding for the experimental observations in the
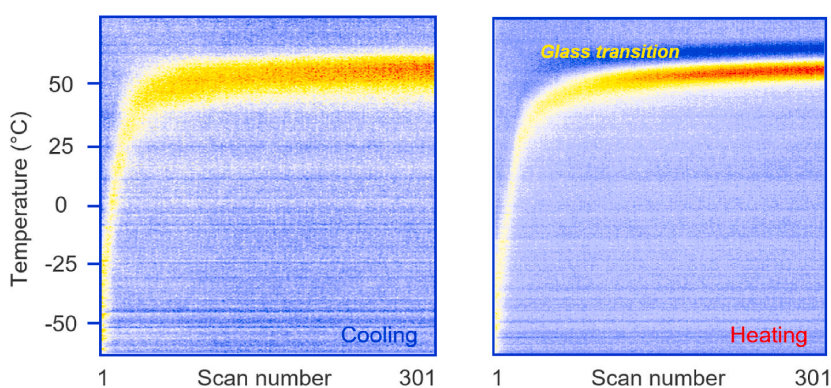
Fig. 7. Color-mapped set of the first derivative of FSC cooling (left) and heating scans (right), recorded in sequence according to the temperature-time profile shown in Fig. 6. Note that the first-derivative curves obtained from the FSC scans are plotted vertically vs temperature, emphasizing the increase of the glass transition temperature with increasing cycle number/ evaporation of solvent. Blue and red colors indicate low and high values of the first derivative in the color map. (For interpretation of the references to color in this figure legend, the reader is referred to the Web version of this article.)

Fig. 8. Absolute heat capacity at 80 °C (red curve) and -70 °C (blue curve) as a function of the cycle number (left). Glass transition temperature of the polymer/ solvent system PDLLA/IR3535® as a function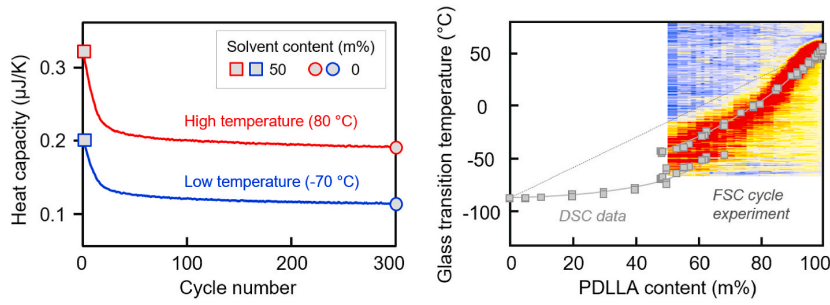 of the polymer content, obtained from normalized FSC first-derivate heating curves. Square symbols represent data collected by DSC (right). (For interpretation of the references to color in this figure legend, the reader is referred to the Web version of this article.)

Table 1
List of material parameters used for calculation of solution glass transition temperatures according to Eq. (1)–(3).

Parameter	Unit	Value	Comment/Source
$T_{g,IR3535}$	K	185	by experiment
$\Delta c_{p,IR3535}$ (@T_g)	J/(g K)	0.64	by experiment
ρ_{IR3535} (@T_g) [a]	g/cm³	~1.00	ρ_0 (T_0 = 293 K) = 0.987 g/cm³ [43]
$T_{g,PDLLA}$	K	328	by experiment
$\Delta c_{p,PDLLA}$ (@T_g)	J/(g K)	0.60	by experiment
ρ_{PLA} (@T_g)	g/cm³	1.24	[95]

[a] ρ (T) = ρ_0 (T_0)/(1 + β × (T - T_0)).

present study for both polymer- and solvent-rich compositions:

$$\ln T_g = \frac{w_1 \ln T_{g,1} + w_2 \mathbf{K} \ln T_{g,2}}{w_1 + \mathbf{K} w_2}; \quad \mathbf{K} = \frac{\Delta c_{p,2}}{\Delta c_{p,1}} \quad (1)$$

$$\frac{1}{T_g} = \frac{w_1}{T_{g,1}} + \frac{w_2}{T_{g,2}} \quad (2)$$

$$T_g = \frac{w_1 T_{g,1} + \mathbf{k} w_2 T_{g,2}}{w_1 + \mathbf{k} w_2}; \quad \mathbf{k} = \frac{\rho_1 \Delta\beta_2}{\rho_2 \Delta\beta_1} \approx \frac{\rho_1 \, T_{g,1}}{\rho_2 \, T_{g,2}} \quad (3)$$

In Eqs. (1)–(3), $T_{g,1}$ and $T_{g,2}$ are the glass transition temperatures of solvent and polymer, respectively, with their corresponding weight

fractions w_1 and w_2. Δc_p and ρ represent the change of the specific heat capacity and the density of the respective component at the glass transition temperature, and $\Delta\beta$ is the change of the thermal expansivity at T_g. Worth noting that the k-parameter in Eq. (3) considers the temperature-dependence of the volume fractions and different thermal expansivities of the components. Typically, the ratio is simplified by the using Simha-Boyer rule [94] ($\Delta\beta \times T_g$ = constant). Table 1 provides a list of parameters used for calculation of the composition-dependence of the glass transition temperature of the solutions, including additional information about the source. Note that the density of IR3535® at its glass transition temperature is not available in the literature, which therefore was calculated using a room-temperature-reference value (ρ_0) [43] and an estimate of the coefficient of the volume thermal expansion β of 10^{-4} 1/K. For PDLLA, the temperature-dependence of the specific volume is reported in the literature [95].

Fig. 9 shows experimentally obtained glass transition temperatures of the system PDLLA/IR3535® as a function of the composition (symbols) (see also Figs. 5 and 8) and predictions based on Eq. (1)–(3) (blue and red lines). While the Fox and Couchman equations underestimate the observed negative deviation of experimental data from linearity, the Gordon-Taylor equation provides a rather excellent prediction since perfectly agreeing with the experimental data, at least for polymer-rich compositions ($w_2 > 0.5$). The Gordon-Taylor-equations assumes ideal volume mixing, and absence of specific enthalpic interactions of the system components [96,97], leading to the preliminary conclusion that in case of the system PDLLA/IR3535® such interactions are absent or
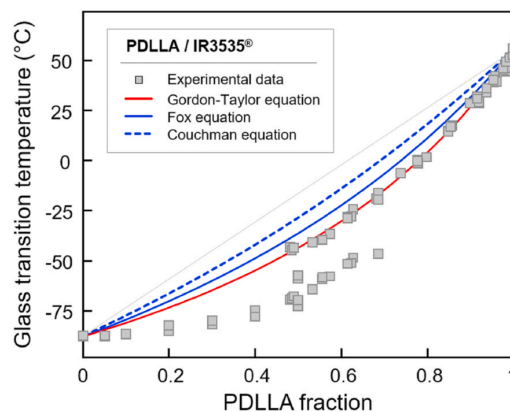

Fig. 9. Glass transition temperature of the system PDLLA/IR3535® as a function of the composition. Experimental data are represented by symbols while predictions based on Eq. (1)–(3) are shown with the blue and red lines, as indicated in the legend. (For interpretation of the references to color in this figure legend, the reader is referred to the Web version of this article.)

very weak. In fact, liquid-liquid demixing is not observed in the entire temperature-range analyzed, suggesting thermodynamic miscibility for all concentrations between the glass transition temperature and temperatures well-above 100 °C. As such it is impossible to assess calorimetrically (even if typically very small) enthalpies of mixing/demixing, or confirm their absence, and judging whether the system forms ideal or regular solutions. For this reason, and since the IR3535®-data of Table 1 require further establishment and verification by independent studies, we prefer to not provide a final and quantitative opinion about the free enthalpy of mixing of the system beyond being negative. For solvent-rich compositions, the ideal-solution Gordon-Taylor prediction fails which may indicate presence of stronger enthalpic effects than in case of polymer-rich compositions.

4. Conclusions

The polymer/solvent system PLLA/IR3535® exhibits promising applications as a drug delivery devise [98,99]. In such a device, the liquid mosquito repellent IR3535® would slowly evaporate from a partially crystallized PLLA scaffold formed during cooling solutions via thermally induced phase separation, providing protection of human beings for mosquito bites and transmission of diseases. While for the PLLA/DEET counterpart studies of the phase behavior are available, little is known about the system PLLA/IR3535®. Therefore, the present work is a first attempt to shed light on the miscibility of the system components.

Since information about the thermodynamic miscibility may be masked by crystallization of PLLA, a non-crystallizable PDLLA grade was employed. Cloud-point measurements and calorimetric analyses showed that PDLLA and IR3535® are miscible in the entire concentration range as solutions remained clear within the investigated temperature range from subambient temperature up to 125 °C. Detailed analyses of the glass transition behavior revealed a negative deviation of the glass transition temperature of solutions from a linear mixing rule, fitting the Gordon-Taylor equation for polymer-rich composition with the assumption of volume additivity and absence of or only weak specific enthalpic interactions between the system components. At around equal concentration of polymer and solvent, the glass transition strongly broadens and even two separate glass transition events are detected related to self-concentration effects and chain connectivity affecting the local environment of the polymer repeat unit. For solvent-rich compositions, the ideal-solution Gordon-Taylor prediction is not valid, possibly indicating presence of stronger enthalpic interaction of the system components than in case of polymer-rich compositions.

As a qualitatively new approach of analyzing the composition-dependence of glass transition temperatures of polymer solutions, the study included application of conventional and fast scanning chip calorimetry for controlled and stepwise evaporation of solvent by repeated exposure the system to elevated temperature and evaluation of the glass transition temperature during in-between cooling and reheating. This strategy avoids labor-intensive and time-consuming preparation of individual polymer-rich solutions for subsequent analysis, if possible at all.

Declaration of competing interest

The authors declare that they have no known competing financial interests or personal relationships that could have appeared to influence the work reported in this paper.

Acknowledgments

References

[1] R. Auras, L.T. Lim, S.E.M. Selke, H. Tsuji, Poly(lactic Acid): Synthesis, Structures, Properties, Processing, and Applications, Wiley, Hoboken, 2010.

[2] C. Zhang, Biodegradable polyesters: synthesis, properties, applications, in: S. Fakirov (Ed.), Biodegradable polyesters, Wiley-VCH, Weinheim, 2015.

[3] M.L. Di Lorenzo, R. Androsch, Synthesis, structure and properties of poly(lactic acid), Adv. Polym. Sci. 279 (2018). Springer International Publishing.

[4] M.L. Di Lorenzo, R. Androsch, Industrial applications of poly(lactic acid), Adv. Polym. Sci. 282 (2018). Springer International Publishing.

[5] A.J. Lasprilla, G.A. Martinez, B.H. Lunelli, A.L. Jardini, R. Maciel Filho, Poly-lactic acid synthesis for application in biomedical devices—a review, Biotechnol. Adv. 30 (2012) 321–328.

[6] M.S. Singhvi, S.S. Zinjarde, D.V. Gokhale, Polylactic acid: synthesis and biomedical applications, J. Appl. Microbiol. 127 (2019) 1612–1626.

[7] D.A. Garlotta, Literature review of poly(lactic acid), J. Polym. Environ. 9 (2001) 63–84.

[8] S. Farah, D.G. Anderson, R. Langer, Physical and mechanical properties of PLA, and their functions in widespread applications—a comprehensive review, Adv. Drug Deliv. Rev. 107 (2016) 367–392.

[9] J.J. Kolstad, Crystallization kinetics of poly (L-lactide-co-meso-lactide), J. Appl. Polym. Sci. 62 (1996) 1079–1091.

[10] S. Saeidlou, M.A. Huneault, H. Li, C.B. Park, Poly(lactic acid) crystallization, Prog. Polym. Sci. 37 (2012) 1657–1677.

[11] R. Androsch, C. Schick, M.L. Di Lorenzo, Kinetics of nucleation and growth of crystals of poly(ʟ-lactic acid), Adv. Polym. Sci. 279 (2018) 235–272.

[12] Y.S. Nam, T.G. Park, Porous biodegradable polymeric scaffolds prepared by thermally induced phase separation, J. Biomed. Mater. Res. 47 (1999) 8–17.

[13] F.J. Hua, G.E. Kim, J.D. Lee, Y.K. Son, D.S. Lee, Macroporous poly(ʟ-lactide) scaffold 1. Preparation of a macroporous scaffold by liquid–liquid phase separation of a PLLA–dioxane–water system, J. Biomed. Mater. Res. 63 (2002) 161–167.

[14] F. Yang, R. Murugan, S. Ramakrishna, X. Wang, Y.-X. Ma, S. Wang, Fabrication of nano-structured porous PLLA scaffold intended for nerve tissue engineering, Biomaterials 25 (2004) 1891–1900.

[15] M.S. Mohammadi, M.N. Bureau, S.N. Nazhat, Polylactic acid (PLA) biomedical foams for tissue engineering, in: Biomedical Foams for Tissue Engineering Applications, Woodhead Publishing, 2014, pp. 313–334.

[16] Ch Schugens, V. Maquet, C. Grandfils, R. Jerome, Ph Teyssie, Biodegradable and macroporous polylactide implants for cell transplantation: 1. Preparation of macroporous polylactide supports by solid-liquid phase separation, Polymer 37 (1996) 1027–1038.

[17] Ö.C. Önder, E. Yilgör, I. Yilgör, Fabrication of rigid poly(lactic acid) foams via thermally induced phase separation, Polymer 107 (2016) 240–248.

[18] D.R. Lloyd, K.E. Kinzer, H.S. Tseng, Microporous membrane formation via thermally induced phase separation. I. Solid-liquid phase separation, J. Membr. Sci. 52 (1990) 239–261.

[19] D.R. Lloyd, S.S. Kim, K.E. Kinzer, Microporous membrane formation via thermally induced phase separation. II. Liquid-liquid phase separation, J. Membr. Sci. 64 (1990) 1–11.

[20] T. Ishigami, Y. Nii, Y. Ohmukai, S. Rajabzadeh, H. Matsuyama, Solidification behavior of polymer solution during membrane preparation by thermally induced phase separation, Membranes 4 (2014) 113–122.

[21] P. van de Witte, P.J. Dijkstra, J.W.A. van den Berg, J. Feijen, Phase separation processes in polymer solutions in relation to membrane formation, J. Membr. Sci. 117 (1996) 1–31.

[22] M.U. Akhtar, W.W. Focke, Trapping citronellal in a microporous polyethylene matrix, Thermochim. Acta 613 (2015) 61–65.

[23] C. Sungkapreecha, N. Iqbal, A.M. Gohn, W.W. Focke, R. Androsch, Phase behavior of the polymer/drug system PLA/DEET, Polymer 126 (2017) 116–125.

[24] J.R. Roberts, J.R. Reigart, Does anything beat DEET? Pediatr. Ann. (33) (2004) 444–453.

[25] C. Sungkapreecha, N. Iqbal, W.W. Focke, R. Androsch, Crystallization of poly(ʟ-lactic acid) in solution with the mosquito-repellent N,N-diethyl-3-methylbenzamide, Polym. Cryst. 2 (2019) e10029.

[26] I. Bonadies, A. Longo, R. Androsch, D. Jehnichen, M. Göbel, M.L. Di Lorenzo, Biodegradable electrospun PLLA fibers containing the mosquito-repellent DEET, Eur. Polym. J. 113 (2019) 377–384.

[27] M.L. Di Lorenzo, A. Longo, N,N-Diethyl-3-methylbenzamide (DEET): a mosquito repellent as functional plasticizer for poly (ʟ-lactic acid), Thermochim. Acta 677 (2019) 180–185.

[28] C. Sungkapreecha, M.J. Beily, J. Kressler, W.W. Focke, R. Androsch, Phase behavior of the polymer/drug system PLA/DEET: effect of PLA molar mass on subambient liquid-liquid phase separation, Thermochim. Acta 660 (2018) 77–81.

[29] C. Sungkapreecha, W.W. Focke, R. Androsch, Competition between liquid-liquid de-mixing, crystallization, and glass transition in solutions of PLA of different stereochemistry and DEET, Chin. J. Polym. Sci. 38 (2020) 174–178.

[30] S.D. Costanzo, A.J. Watkinson, E.J. Murby, D.W. Kolpin, M.W. Sandstrom, Is there a risk associated with the insect repellent DEET (N, N-diethyl-m-toluamide) commonly found in aquatic environments? Sci. Total Environ. 384 (2007) 214–220.

[31] J.A. Weeks, P.D. Guiney, A.I. Nikiforov, Assessment of the environmental fate and ecotoxicity of N, N-diethyl-m-toluamide (DEET), Integrated Environ. Assess. Manag. 8 (1) (2012) 120–134.

[32] D. Aronson, J. Weeks, B. Meylan, P.D. Guiney, P.H. Howard, Environmental release, environmental concentrations, and ecological risk of N,N-diethyl-m-toluamide (DEET), Integrated Environ. Assess. Manag. 8 (1) (2012) 135–166.

[33] T.M. Katz, J.H. Miller, A.A. Hebert, Insect repellents: historical perspectives and new developments, J. Am. Acad. Dermatol. 58 (2008) 865–871.

[34] H.F. Khater, A.M. Selim, G.A. Abouelella, N.A. Abouelella, K. Murugan, N.P. Vaz, M. Govindarajan, Commercial mosquito repellents and their safety concerns, in: Malaria, IntechOpen, 2019.

[35] Z. Iyigundogdu, S. Kalayci, A.B. Asutay, F. Sahin, Determination of antimicrobial and antiviral properties of IR3535, Mol. Biol. Rep. 46 (2) (2019) 1819–1824.

[36] C. Grison, D. Carrasco, F. Pelissier, A. Moderc, Reflexion on bio-sourced mosquito repellents: nature, activity, and preparation, Frontiers in Ecology and Evolution 8 (8) (2020).

[37] P.R. Couchman, F.E. Karasz, A classical thermodynamic discussion of the effect of composition on glass-transition temperatures, Macromolecules 11 (1978) 117–119.

[38] P.R. Couchman, Compositional variation of glass-transition temperatures. 2. Application of the thermodynamic theory to compatible polymer blends, Macromolecules 11 (1978) 1156–1161.

[39] X. Lu, R.A. Weiss, Relationship between the glass transition temperature and the interaction parameter of miscible binary polymer blends, Macromolecules 25 (1992) 3242–3246.

[40] M. Song, D.J. Hourston, H.M. Pollock, A. Hammiche, Modulated differential scanning calorimetry: 14. Effect of molecular interactions on glass transition behaviour and increment of heat capacity in miscible polymer blends, Polymer 40 (1999) 4763–4767.

[41] R. Nair, N. Nyamweya, S. Gönen, L.J. Martínez-Miranda, S.W. Hoag, Influence of various drugs on the glass transition temperature of poly (vinylpyrrolidone): a thermodynamic and spectroscopic investigation, Int. J. Pharmaceutics 225 (2001) 83–96.

[42] Evonik, R207S Product information. https://healthcare.evonik.com/product/health-care/en/products/biomaterials/resomer/pages/medical-devices.aspx. (Accessed 13 February 2020).

[43] Ethyl Carbolution, Butylacetylaminopropionate Product information. https://www.carbolution.de/product_info.php?products_id=3221. (Accessed 13 February 2020).

[44] Sigma Aldrich, N,N-Diethyl-3-methylbenzamide Product information. www.sigmaaldrich.com/catalog/product/aldrich/d100951?lang=de&region=DE. (Accessed 11 June 2020).

[45] E. Iervolino, A.W. Van Herwaarden, F.G. Van Herwaarden, E. Van De Kerkhof, P.P. W. Van Grinsven, A.C.H.I. Leenaers, V.B.F. Mathot, P.M. Sarro, Temperature calibration and electrical characterization of the differential scanning calorimeter chip UFS1 for the Mettler-Toledo Flash DSC 1, Thermochim. Acta 522 (2011) 53–59.

[46] J.E.K. Schawe, S. Pogatscher, in: Fast scanning calorimetry, C. Schick, V. Mathot (Eds.), Material Characterization by Fast Scanning Calorimetry: Practice and Applications, Springer, 2016.

[47] R. Androsch, B. Wunderlich, Temperature-modulated DSC using hisgher harmonics of the Fourier transform, Thermochim. Acta 333 (1999) 27–32.

[48] R. Androsch, I. Moon, S. Kreitmeier, B. Wunderlich, Determination of heat capacity with a sawtooth-type, power-compensated temperature-modulated DSC, Thermochim. Acta 357 (2000) 267–278.

[49] R. Androsch, Heat capacity measurements using temperature-modulated heat flux DSC with close control of the heater temperature, J. Therm. Anal. Calorim. 61 (2000) 75–89.

[50] A. Wurm, A. Herrmann, M. Cornelius, E. Zhuravlev, D. Pospiech, R. Nicula, C. Schick, Temperature dependency of nucleation efficiency of carbon nanotubes in PET and PBT, Macromol. Mater. Eng. 300 (2015) 637–649.

[51] K. Jariyavidyanont, A. Abdelaziz, R. Androsch, C. Schick, Experimental analysis of lateral thermal inhomogeneity of a specific chip-calorimeter sensor, Thermochim. Acta 674 (2019) 95–99.

[52] K. Liao, D. Quan, Z. Lu, Effects of physical aging on glass transition behavior of poly(dl-lactide), Eur. Polym. J. 38 (2002) 157–162.

[53] A. Pinheiro, J.F. Mano, Study of the glass transition on viscous-forming and powder materials using dynamic mechanical analysis, Polym. Test. 28 (2009) 89–95.

[54] M.O. Omelczuk, J.W. McGinity, The influence of polymer glass transition temperature and molecular weight on drug release from tablets containing poly (DL-lactic acid), Pharm. Res. (N. Y.) 9 (1992) 26–32.

[55] D.J. Plazek, E. Riande, H. Markovitz, N. Raghupathi, Concentration dependence of the viscoelastic properties of polystyrene-tricresyl phosphate solutions, J. Polym. Sci., Polym. Phys. Ed. 17 (1979) 2189–2213.

[56] D.A. Savin, A.M. Larson, T.P. Lodge, Effect of composition on the width of the calorimetric glass transition in polymer–solvent and solvent–solvent mixtures, J. Polym. Sci., Polym. Phys. Ed. 42 (2004) 1155–1163.

[57] M.M. Mok, X. Liu, Z. Bai, Y. Lei, T.P. Lodge, Effect of concentration on the glass transition and viscoelastic properties of poly (methyl methacrylate)/ionic liquid solutions, Macromolecules 44 (2011) 1016–1025.

[58] W. Zheng, S.L. Simon, The glass transition in athermal poly(α-methyl styrene)/oligomer blends, J. Polym. Sci., Polym. Phys. Ed. 46 (2008) 418–430.

[59] T.P. Lodge, T.C. McLeish, Self-concentrations and effective glass transition temperatures in polymer blends, Macromolecules 33 (2000) 5278–5284.

[60] T.P. Lodge, E.R. Wood, J.C. Haley, Two calorimetric glass transitions do not necessarily indicate immiscibility: the case of PEO/PMMA, J. Polym. Sci., Polym. Phys. Ed. 44 (2006) 756–763.

[61] Y. He, T.R. Lutz, M.D. Ediger, Segmental and terminal dynamics in miscible polymer mixtures: tests of the Lodge–McLeish model, J. Chem. Phys. 119 (2003) 9956–9965.

[62] P. Pan, B. Zhu, Y. Inoue, Enthalpy relaxation and embrittlement of poly (L-lactide) during physical aging, Macromolecules 40 (2007) 9664–9671.

[63] X. Monnier, A. Saiter, E. Dargent, Physical aging in PLA through standard DSC and fast scanning calorimetry investigations, Thermochim. Acta 648 (2017) 13–22.

[64] H.N. Iqbal, C. Sungkapreecha, R. Androsch, Enthalpy relaxation of the glass of poly (L-lactic acid) of different d-isomer content and its effect on mechanical properties, Polym. Bull. 74 (2017) 2565–2573.

[65] R. Androsch, M.L. Di Lorenzo, C. Schick, Effect of molar mass on enthalpy relaxation and crystal nucleation of poly (L-lactic acid), Eur. Polym. J. 96 (2017) 361–369.

[66] R. Androsch, E. Zhuravlev, J.W. Schmelzer, C. Schick, Relaxation and crystal nucleation in polymer glasses, Eur. Polym. J. 102 (2018) 195–208.

[67] X. Monnier, N. Delpouve, A. Saiter-Fourcin, Distinct dynamics of structural relaxation in the amorphous phase of poly (L-lactic acid) revealed by quiescent crystallization, Soft Matter 16 (2020) 3224–3233.

[68] N. Pieterse, W.W. Focke, Diffusion-controlled evaporation through a stagnant gas: estimating low vapour pressures from thermogravimetric data, Thermochim. Acta 406 (2003) 191–198.

[69] W.W. Focke, A revised equation for estimating the vapour pressure of low-volatility substances from isothermal TG data, J. Therm. Anal. Calorim. 74 (2003) 97–107.

[70] D. Günther, F. Steimle, Mixing rules for the specific heat capacities of several HFC-mixtures, Int. J. Refrigeration 20 (1997) 235–243.

[71] R.S. Barnum, S.H. Goh, J.W. Barlow, D.R. Paul, Excess heat capacities for two miscible polymer blend systems, J. Polym. Sci., Polym. Lett. 23 (1985) 395–401.

[72] A. Benisek, E. Dachs, On the nature of the excess heat capacity of mixing, Phys. Chem. Miner. 38 (2011) 185–191.

[73] B.E. Eichinger, Heat capacity of dilute polymer solutions, J. Chem. Phys. 53 (1970) 561–566.

[74] M. Pyda, R.C. Bopp, B. Wunderlich, Heat capacity of poly (lactic acid), J. Chem. Thermodyn. 36 (2004) 731–742.

[75] M. Ahrenberg, M. Brinckmann, J.W.P. Schmelzer, M. Beck, C. Schmidt, O. Keßler, U. Kragl, S.P. Verevkin, C. Schick, Determination of volatility of ionic liquids at the nanoscale by means of ultra-fast scanning calorimetry, Phys. Chem. Chem. Phys. 16 (2014) 2971–2980.

[76] A. Abdelaziz, D.H. Zaitsau, A.V. Buzyurov, S.P. Verevkin, C. Schick, Sublimation thermodynamics of nucleobases derived from fast scanning calorimetry, Phys. Chem. Chem. Phys. 22 (2020) 838–853.

[77] A. Abdelaziz, D.H. Zaitsau, A. Buzyurov, A.A. Minakov, S.P. Verevkin, Schick C. Fast scanning calorimetry: sublimation thermodynamics of low volatile and thermally unstable compounds, Thermochim. Acta 676 (2019) 249–262.

[78] R.N. Nagrimanov, A.A. Samatov, T.M. Nasyrova, A.V. Buzyurov, T. A. Mukhametzyanov, C. Schick, B.N. Solomonov, S.P. Verevkin, Long-chain linear alcohols: reconciliation of phase transition enthalpies, J. Chem. Thermodyn. 146 (2020) 106103.

[79] S. Van Herwaarden, E. Iervolino, F. Van Herwaarden, T. Wijffels, A. Leenaers, V. Mathot, Design, performance and analysis of thermal lag of the UFS1 twin-calorimeter chip for fast scanning calorimetry using the Mettler-Toledo Flash DSC 1, Thermochim. Acta 522 (2011) 46–52.

[80] A. Abdelaziz, D.H. Zaitsau, T.A. Mukhametzyanov, B.N. Solomonov, P. Cebe, S. P. Verevkin, C. Schick, Melting temperature and heat of fusion of cytosine revealed from fast scanning calorimetry, Thermochim. Acta 657 (2017) 47–55.

[81] J. Paasivirta, S. Sinkkonen, P. Mikkelson, T. Rantio, F. Wania, Estimation of vapor pressures, solubilities and Henry's law constants of selected persistent organic pollutants as functions of temperature, Chemosphere 39 (1999) 811–832.

[82] M. Aubin, R.E. Prud'Homme, Analysis of the glass transition temperature of miscible polymer blends, Macromolecules 21 (1988) 2945–2949.

[83] X. Lu, R.A. Weiss, Relationship between the glass transition temperature and the interaction parameter of miscible binary polymer blends, Macromolecules 25 (1992) 3242–3246.

[84] E.A. Dimarzio, J.H. Gibbs, Molecular interpretation of glass temperature depression by plasticizers, J. Polym. Sci., Part A: General Papers 1 (1963) 1417–1428.

[85] T.S. Chow, Molecular interpretation of the glass transition temperature of polymer-diluent systems, Macromolecules 13 (1980) 362–364.

[86] M. Song, D.J. Hourston, H.M. Pollock, A. Hammiche, Modulated differential scanning calorimetry: 14. Effect of molecular interactions on glass transition behaviour and increment of heat capacity in miscible polymer blends, Polymer 40 (1999) 4763–4767.

[87] L.J. Garfield, S.E. Petrie, Viscosity and glass-transition behavior of polymer—diluent systems[1], J. Phys. Chem. 68 (1964) 1750–1754.

[88] F. Qian, J. Huang, M.A. Hussain, Drug–polymer solubility and miscibility: stability consideration and practical challenges in amorphous solid dispersion development, J. Pharmacol. Sci. 99 (2010) 2941–2947.

[89] R. Nair, N. Nyamweya, S. Gönen, MartíS, S.W. Hoag, Influence of various drugs on the glass transition temperature of poly (vinylpyrrolidone): a thermodynamic and spectroscopic investigation, Int. J. Pharm. 225 (2001) 83–96.

[90] P.R. Couchman, F.E. Karasz, A classical thermodynamic discussion of the effect of composition on glass-transition temperatures, Macromolecules 11 (1978) 117–119.

[91] P.R. Couchman, Compositional variation of glass-transition temperatures. 2. Application of the thermodynamic theory to compatible polymer blends, Macromolecules 11 (1978) 1156–1161.

[92] T.G. Fox, Influence of diluent and of copolymer composition on the glass temperature of a polymer system, Bull. Am. Phys. Soc. 1 (1956) 123.

[93] M. Gordon, J. Taylor, Ideal copolymers and the second-order transitions of synthetic rubbers. I. Non-crystalline copolymers, J. Appl. Chem. 2 (1952) 493–500.

[94] R. Simha, R.F. Boyer, On a general relation involving the glass temperature and coefficients of expansion of polymers, J. Chem. Phys. 37 (1962) 1003–1007.

10

49

[95] Y. Sato, K. Inohara, S. Takishima, H. Masuoka, M. Imaizumi, H. Yamamoto, M. Takasugi, Pressure-volume-temperature behavior of polylactide, poly (butylene succinate), and poly (butylene succinate-co-adipate), Polym. Eng. Sci. 40 (2000) 2602–2609.

[96] H.A. Schneider, The Gordon-Taylor equation Additivity and interaction in compatible polymer blends, Makromol. Chem.: Macromol. Chem. Phys. 189 (1988) 1941–1955.

[97] H.A. Schneider, Glass transition behaviour of compatible polymer blends, Polymer 30 (1989) 771–779.

[98] T. Nogueira Barradas, J. Perdiz Senna, E. Ricci Junior, C. Regina Elias Mansur, Polymer-based drug delivery systems applied to insects repellents devices: a review, Curr. Drug Deliv. 13 (2016) 221–235.

[99] A.B. Mapossa, A. Sitoe, W.W. Focke, H. Izadi, E.L. du Toit, R. Androsch, C. Sungkapreecha, E.M. van der Merwe, Mosquito repellent thermal stability, permeability and air volatility, Pest Manag. Sci. 76 (2020) 1112–1120.

50

4.2 Crystallization-induced polymer scaffold formation in the polymer/drug delivery system poly(L-lactic acid)/ethyl butylacetylaminopropionate (PLLA/IR3535)

*Fanfan Du[†], Hande Ece Yener[†], Georg Hillrichs[‡], Regine Boldt[§], and René Androsch[†,*]*

[†] Interdisciplinary Center for Transfer-oriented Research in Natural Sciences (IWE TFN), Martin Luther University Halle-Wittenberg, D-06099 Halle/Saale, Germany

[‡] Department of Engineering and Natural Sciences, University of Applied Sciences Merseburg, D-06217 Merseburg, Germany

[§] Leibniz-Institut für Polymerforschung e. V. Dresden (IPF), Hohe Strasse 6, D-01069 Dresden, Germany

Graphical abstract:
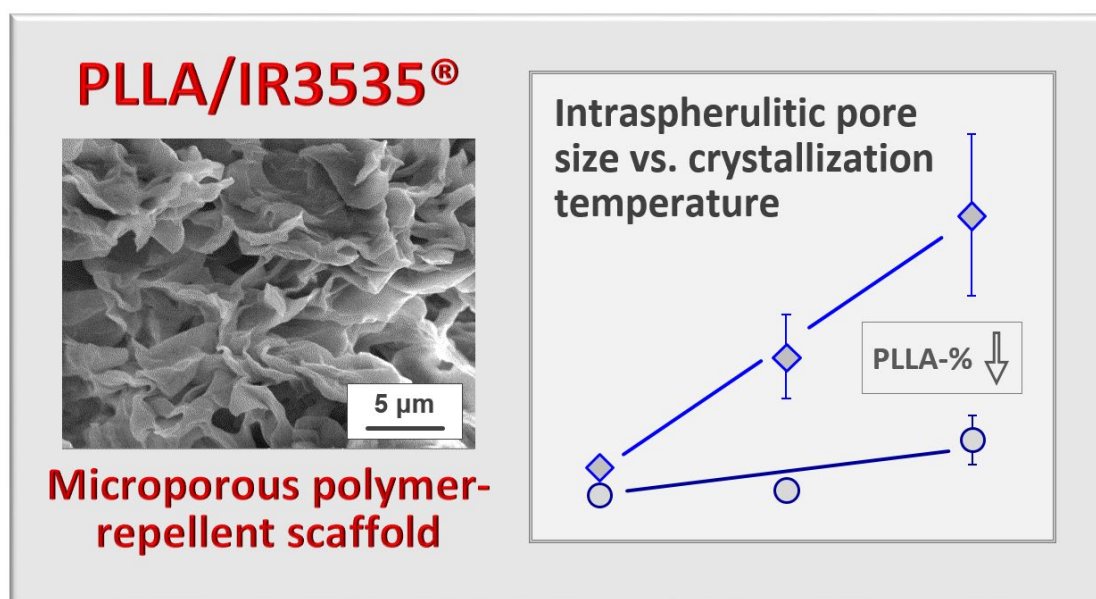
Highlights:

❖ IR3535 was used as a human- and environmentally friendly active mosquito-repellent serving as a solvent to form functional PLLA scaffolds by crystallization-based S-L TIPS.

❖ Compared to the melt-crystallization of neat PLLA, crystallization of PLLA in the presence of IR3535 is faster.

❖ Microporous scaffolds with different fine structures are obtained by regulating the polymer concentration and the crystallization temperature.

❖ IR3535 is hosted in intra- and interspherulitic pores of PLLA, where the intraspherulitic pore size of PLLA increases with crystallization temperature and IR3535 content.

Crystallization-Induced Polymer Scaffold Formation in the Polymer/Drug Delivery System Poly(L-lactic acid)/Ethyl Butylacetylaminopropionate (PLLA/IR3535)

Fanfan Du, Hande Ece Yener, Georg Hillrichs, Regine Boldt, and René Androsch*

ACCESS | Metrics & More   Article Recommendations

ABSTRACT: Polymer/mosquito-repellent scaffolds exhibit increasing importance in long-lasting human skin protection to be used as wearable devices and allowing for controlled release of repellents. In this study, ethyl butylacetylaminopropionate (IR3535) was used as a human and environmental friendly active mosquito-repellent serving as a solvent to form functional poly(L-lactic acid) (PLLA) scaffolds by crystallization-based solid−liquid thermally induced phase separation. Crystallization of PLLA in the presence of IR3535 is faster than melt-crystallization of neat PLLA, and in the investigated concentration range from 5 to 50 mass % PLLA, its maximum crystallization rate increases with the PLLA content, by both, increases of the maximum crystal growth rate and of the nuclei density. By adjusting the polymer concentration and the crystallization temperature, microporous scaffolds of different fine structures are obtained, hosting the mosquito-repellent in intra- and interspherulitic pores for its intended later evaporation.
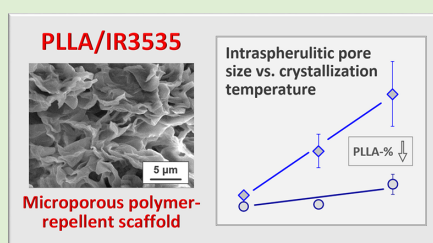
INTRODUCTION

Mosquito-borne tropical infectious diseases, such as malaria, dengue fever, yellow fever, Zika, or lymphatic filariasis, occur at the global scale and involve a wide range of viral and other pathogenic agents, causing hundreds of thousands of deaths each year.[1−3] While effective routes for indoor vector control and personal protection of human beings in endangered areas are available, including, e.g., the use of long-lasting insecticide-treated bed nets or indoor residual spraying,[4−6] outdoor-vector control and protection still are underdeveloped.[7−9] The risk for mosquito bites and possible transmission of parasites/pathogens may be reduced by the use of wearable mosquito-repellent devices, able to generate a protective vapor barrier.[10−12] In addition to alternatives like repellent textiles or systems based on electrospun fibers,[13−17] development of long-lasting polymer-scaffold-based repellent delivery devices seems promising.

As a versatile preparation technique, polymer scaffolds may form on cooling a polymer solution from elevated temperature by thermally induced phase separation (TIPS). TIPS includes liquid−liquid (L−L) and crystallization-induced solid−liquid (S−L) phase separation, with different phase-separation mechanisms.[18−20] L−L phase separation occurs on cooling the solution to a temperature below its thermodynamic stability limit, yielding two liquid phases of different compositions, which, however, on further cooling may turn solid by vitrification or crystallization. S−L phase separation, in contrast, occurs by crystallization of one of the components;

often, though not throughout, it is suggested that crystallization is preceded/assisted by or occurs in conjunction with spinodal L−L phase separation.[21−26]

Several studies available in the literature showed that formation of porous polymer scaffolds holding mosquito repellents, indeed, is an auspicious concept to be applied for outdoor protection against malaria vectors. First attempts to develop such polymer/repellent systems included the extrusion of strands of poly (ethylene-*co*-vinyl acetate) (EVA) or linear low-density polyethylene (LLDPE) with up to 30 mass % *N,N*-diethyl-3-methylbenzamide (DEET) or Icaridin, both being well-established mosquito repellents,[27−29] into ice−water, inducing a spinodal phase separation of the components and formation of a microporous scaffold.[30] It is worth noting that such a concentration of the repellent is sufficient to protect against mosquitos for several weeks. In further work, 40/60 mass % solutions of LLDPE and the natural repellent citronellal, respectively, were rapidly cooled from 150 °C to different subambient temperatures, similarly yielding co-continuous polymer/repellent morphologies.[31]

With the motivation of replacing traditional, petroleum-based polymers by environmental friendly biobased and biodegradable, thus rather easy disposable polymers, our recent work focused on the use of poly(L-lactic acid) (PLLA) and poly (butylene succinate) (PBS),[32−34] as carriers for repellents. For both polymers, TIPS has been proven as a successful route to form scaffolds for many applications, in particular in the biomedical sector.[35−40] For both, PLLA and PBS, basic information about the phase behavior with DEET in the case of solvent-rich compositions were collected, confirming the formation of solutions at elevated temperature as a precondition for S−L TIPS. During cooling to ambient temperature, crystallization of the polymer occurs, with the liquid repellent-rich phase then accommodated in intercrystalline, micrometer-sized pores.[41−45]

DEET is considered the gold-standard of mosquito repellents.[46−48] Nonetheless, there are alternatives with specific advantages and disadvantages available. Though slightly less efficient than DEET against *Anopheles*,[28,49,50] ethyl butylacetylaminopropionate (IR3535) with a chemical structure similar to that of the natural substance β-alanine —a β amino acid, being a component of pantothenic acid (vitamin B_5)—is reported promising since it shows less detrimental side effects on human beings and the environment, as it even may be applied for pregnant women and children.[27] With the additional advantage of biodegradability, IR3535 raised increased interest for its use as a mosquito-repellent. For these reasons, that is, the absence of harmful effects on human beings and on the environment, with the present work, an initial evaluation of the potential of using PLLA and IR3535 for the development of a fully biodegradable polymer-scaffold-based repellent delivery tool is anticipated.

The thermodynamic miscibility of PLLA and IR3535, that is, the ability to form solutions at elevated temperatures has been confirmed in preliminary tests, and in-depth analysis of the phase behavior of noncrystallizable poly (D/L-lactic acid) (PDLLA) and IR3535 revealed the absence of L−L demixing in the entire temperature range from 160 °C to the composition-dependent glass-transition temperature T_g of the mixtures.[51] Note that the employment of noncrystallizable PDLLA is advantageous for evaluation of the thermodynamic miscibility of system components, as in this case, any L−L demixing is not masked by crystallization/S−L demixing. Qualitatively advancing earlier studies about PLLA scaffold formation from solutions with DEET, in this work, the option to tailor the pore size in scaffolds, is the main research target.

■ EXPERIMENTAL SECTION

Materials and Preparation. An extrusion-grade crystallizable PLLA homopolymer was provided from Sulzer Chemtech Ltd. (Winterthur, Switzerland), containing less than 0.3% D-isomers, determined by chiral gas chromatography.[52] The mass-average molar mass and polydispersity were 117 kDa and 1.8, respectively.[53] IR3535 with a purity of 98% was obtained from Carbolution Chemicals GmbH (St. Ingbert, Germany) and used as received without further purification. It is a clear liquid at room temperature, with a glass-transition temperature of close to −90 °C.[54] The estimated metastable boiling point at atmospheric pressure is slightly below 300 °C and about 110 °C at 0.02 kPa, and the vapor pressure is reported to be around 0.15 Pa at 20 °C.[55,56]

For easy dissolution of the polymer in the solvent, PLLA pellets were sliced using an SLEE microtome (Mainz, Germany) to obtain thin sections with a thickness of 100 μm, and then placed together with IR3535 inside 3.5 mL glass vials, which were closed with a lid.

Dissolution was performed at 160 °C or higher temperatures up to 165 °C, depending on the composition, in a silicone oil bath. The polymer concentration in the solutions was 5, 10, 20, 30, 40, and 50 mass % (in the following abbreviated m%); complete dissolution of the polymer was generally achieved after few minutes.

Instrumentation. *Cloud-Point Measurements.* The demixing behavior of the solutions was observed visually by cloud-point measurements, that is, by analysis of the temperature at which the optical appearance of the solutions turns from clear to turbid during cooling, with the turbidity caused by the scattering of light at phase boundaries. A Leica digital microscope system DMS300 (Wetzlar, Germany) was used to monitor the turbidity of the solutions in the closed 3.5 mL vials as a function of temperature during cooling from 160 °C to room temperature in the silicone oil bath. All measurements were repeated at least two times to ensure reproducibility.

Differential Scanning Calorimetry (DSC). DSC was employed to obtain temperatures and enthalpies of crystallization/S−L TIPS of PLLA/IR3535 solutions at higher cooling rates compared to cloud-point measurements, as well as to analyze the isothermal crystallization kinetics of the solutions. Measurements were performed using a calibrated heat-flux DSC 1 from Mettler-Toledo (Greifensee, Switzerland) equipped with an FRS5 sensor. The device was connected to a Huber TC100 intracooler (Offenburg, Germany) to allow cooling at rates up to 30 K/min. The furnace was purged with nitrogen gas at a flow rate of 60 mL/min.

Two routes of sample preparation/measurements were performed to assure high reliability of data. In a first approach, the solutions with an initial temperature of 160 °C were inserted into pans preheated to 80 °C and then immediately heated in the DSC to 160 °C to avoid formation of crystals before recording the first cooling experiment; solutions containing 5 m% of PLLA were inserted into aluminum pans conditioned at 50 °C before their heating to 140 °C, with the lower insert temperature justified by the lower crystallization temperature. After equilibrating the solutions at 160 °C for 2 min (140 °C for 3 min), cooling scans were recorded. The disadvantage of this preparation technique is the impossibility of sealing/covering the pan with a lid, which then may allow easy evaporation of the solvent during measurement. Furthermore, this technique only allows weighing the sample after the measurement, not permitting possible evaporation of the solvent by comparing the masses before and after the experiment. For these reasons, also conventional preparation was applied, that is, loading the sample into a pan, weighing, covering with a lid, and inserting the sample at 25 °C into the DSC. The sample mass, in this case, was between 6 and 10 mg. Though both preparation routes provided qualitatively similar trends regarding the effect of the solvent on PLLA crystallization, data shown below refer to the conventional preparation technique, as it was possible to assure negligible evaporation of the solvent. The estimated evaporation caused total percentage mass loss is in all cases well below 5 m% after using a single sample for obtaining a set of cooling curves in nonisothermal crystallization experiments (see Figure 2).

A DSC 7 from PerkinElmer (Waltham, MA), operated in conjunction with a liquid-nitrogen accessory was used for cooling at rates higher than 20 K/min. The instrument was calibrated using mercury and indium and the furnace was purged with nitrogen gas at a flow rate of 20 mL/min. Solutions were transferred to 40 μL aluminum pans, which were then closed with a lid. The sample mass was between 3 and 16 mg. Regarding the analysis of neat PLLA, sections with a thickness of 100 μm, cut from a pellet, were placed into a 40 μL aluminum pan and covered with a lid. The sample was heated to 200 °C and kept at this temperature for 3 min before cooling at a predefined rate to 25 °C. A single sample was used for all cooling experiments, with the absence of degradation checked by repeating the first cooling scan.

Also, in case of isothermal crystallization experiments, the above-described two different preparation routes were applied, yielding similar results, however, with the obtained mass loss even lower than 2 m% when using the conventional preparation method. After equilibrating the solutions at 160 °C for 1 min, the samples were

cooled at a rate of 50 K/min to the various crystallization temperatures. A single sample was used for obtaining a set of isothermal crystallization experiments, with the above-reported mass loss measured at the end of the total measurement cycle.

Polarized-Light Optical Microscopy (POM). POM was used to follow crystallization-induced S−L phase separation in PLLA/IR3535 solutions during cooling and observation of crystal-nuclei densities and spherulite growth rates at different isothermal crystallization conditions. A Leica DMRX microscope (Wetzlar, Germany) was operated in transmission mode, with samples located between crossed polarizers. For the temperature treatments, a THMS600 LINKAM hot stage (Waterfield Tadworth, Surrey, U.K.) equipped with a liquid-nitrogen accessory was used. The samples were placed between circular glass coverslips with a diameter of 15 mm, heated to 160 °C (165 °C in case of solutions containing 50 m% PLLA), and kept at this temperature for 1 min before cooling at rates between 2 and 100 K/min in nonisothermal crystallization experiments, or at rates up to 150 K/min to predefined temperatures for isothermal crystallization experiments, with the cooling rate depending on the crystallization temperature. Images were taken with a Motic 2300 CCD camera. For isothermal crystallization experiments, the time-evolution of the number of nuclei and spherulite diameters were analyzed manually.

X-ray Diffraction (XRD). XRD was used for analysis of the structure of PLLA crystals formed during isothermal crystallization at room temperature and at 75 °C. The crystallized samples were placed on a glass slide and heated in a vacuum oven to 50 °C for subsequent isothermal annealing for at least 3 days, allowing evaporation of the liquid IR3535-rich phase. The dried samples were then put inside glass capillaries (Markröhrchen) with a diameter of 1.0 mm for XRD analysis using a Bruker D8 Advance diffractometer (Billerica, MA), using Cu Kα radiation (wavelength λ = 0.154018 nm). The intensity of scattered X-rays was recorded using a two-dimensional 2048 × 2048 pixel Bruker Vantec 500 detector, with the intensity of the 2D-pattern azimuthally integrated for the sake of statistics and subsequent evaluation of the crystal polymorph.

Scanning Electron Microscopy (SEM). SEM was employed for visualization of the microporous structure of PLLA formed by crystallization-controlled TIPS of PLLA/IR3535 solutions. A sufficient amount of solution was taken by a spatula from the vial and poured into a metal cavity with a dimension of $10 \times 5 \times 0.8$ mm³, preconditioned at different temperatures between 25 and 75 °C, to obtain film-like samples with a thickness of 0.8 mm and scaffolds of different morphologies. After isothermal crystallization, the samples were placed into an oven for 7 days at a temperature of 60 °C to evaporate the liquid IR3535-rich phase before evaluation of the remaining scaffold by a Tescan Vega 3 SBU SEM (Dortmund, Germany). The instrument was operated in the high vacuum mode. A tungsten cathode filament was used as an electron gun, and an acceleration voltage of 10 kV was applied. For generation of images, secondary electrons were detected. The sample surfaces were gold-coated before measurements.

■ RESULTS AND INITIAL DISCUSSION

Cloud-Point Measurements. The demixing behavior/ phase separation in the polymer/solvent system PLLA/IR3535 was observed visually by cloud-point measurements during cooling. Figure 1 presents photographs of samples of the PLLA/IR3535 system containing 5, 10, 20, and 30 m% PLLA (from left to right), taken at different temperature between 90 °C (top row) and 40 °C (bottom row) during cooling of the initially homogeneous solutions from 160 °C to ambient temperature. The cooling rate was lower than 2 K/min at temperatures below 100 °C. All samples of different PLLA concentrations between 5 and 30 m% were clear at 90 °C. In the course of cooling the solutions to 40 °C, the initially transparent solutions turned turbid (see bottom row images), suggesting that phase separation occurred. The first visual observation of cloudiness in PLLA/IR3535 solutions contain-
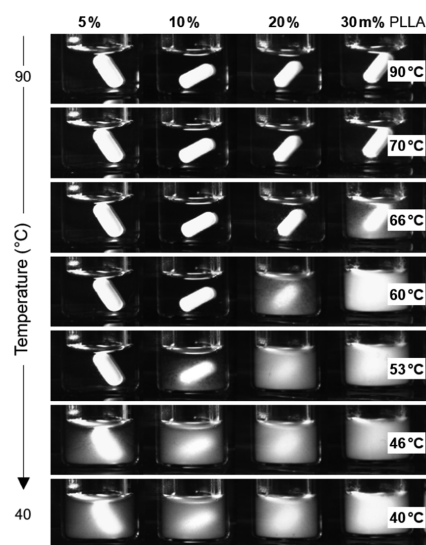

Figure 1. Phase separation of PLLA/IR3535 solutions of different PLLA contents of 5, 10, 20, and 30 m% PLLA (from left to right) during cooling from 90 °C (top row) to 40 °C (bottom row), as obtained by analysis of cloud points.

ing 5, 10, 20, and 30 m% PLLA is detected at temperatures of around 53, 60, 70, and 72 °C, respectively, that is, with increasing concentration of PLLA in the range from 5 to 30 m %, the phase-separation temperature increases.

In general, solutions may demix on cooling via a crystallization-induced S−L- or L−L-phase-separation mechanism. Previous work indicated that noncrystallizable PDLLA and IR3535 are miscible regardless of the system composition, even at subambient temperature. Solvent-rich samples up to 50 m% PDLLA remained clear at the lowest cloud-point-analysis temperature of −62 °C and specifically designed calorimeter experiments revealed a single, though, in some cases, very broad glass transition at temperatures lower than predicted by a linear mixing rule.[51] With the assumption that the mixing behavior is not dependent on the stereoisomerism, that is, on the presence of D-isomer co-units in the chains, the observed cloudiness in the experiment of Figure 1 is attributed to PLLA-crystallization but not L−L-phase separation.

Nonisothermal Crystallization. To confirm the phase-separation mechanism of the PLLA/IR3535 system and quantify its kinetics, DSC was used, enabling higher cooling rates, more precise temperature control, and the possibility of estimation of enthalpies of crystallization compared to visual inspection. Figure 2 shows rate-normalized DSC cooling scans of a specific PLLA/IR3535 solution with 20 m% polymer, recorded at different rates between 2 and 30 K/min (bottom set of curves) and of PLLA and PLLA/IR3535 solutions with different PLLA contents, recorded at 5 K/min (top set of curves). Regarding the effect of the cooling rate on crystallization, a systematic shift of the crystallization peak temperature to lower temperatures and increasing width of the crystallization peak with the cooling rate is detected (see gray arrow), caused by the kinetics of the crystallization process. For the same reason, the peak area decreases with increasing cooling rate, indicating the lower degree of crystallinity.
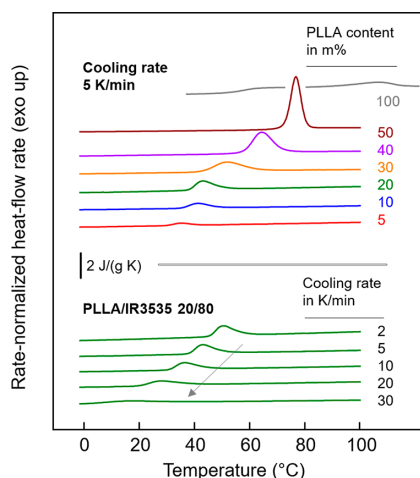
Figure 2. Rate- and mass-normalized DSC cooling scans of PLLA/IR3535 solutions with 20 m% polymer, recorded at different rates between 2 and 30 K/min (bottom set of curves), and of PLLA and PLLA/IR3535 solutions with different PLLA contents, recorded at 5 K/min (top set of curves).

Figure 3. PLLA content normalized enthalpy of crystallization of PLLA/IR3535 solutions as a function of the cooling rate, with the lines drawn to guide the eye. The inset shows the enthalpy of crystallization as a function of the PLLA-content in the solution, obtained after their cooling at a rate of 30 K/min. Data points associated to cooling experiments performed at rates higher than 20 K/min were collected using the PerkinElmer DSC 7, otherwise data were collected employing the Mettler-Toledo DSC 1.

Pure PLLA begins to crystallize on cooling at a rate of 5 K/min at 117 °C, stretching to about 80 °C (see the gray curve in the top right part of Figure 2). On further cooling, a distinct downward step of the DSC signal at about 60 °C due to the glass transition is observed. Crystallization in the presence of IR3535 is connected with a systematic decrease in the crystallization temperature with increasing solvent concentration, which is assumed to be caused by the equilibrium melting point depression according to Flory,[57] as well as slower kinetics of crystal nucleation, caused by the dilution of the polymer.[58−60]

Quantitative data about the fraction of PLLA crystals forming during cooling of PLLA/IR3535 solutions are provided in Figure 3, showing PLLA content normalized enthalpies of crystallization as a function of the cooling rate. The enthalpy of crystallization of pure PLLA (gray squares), after cooling at a rate of 2 K/min is about 32 J/g. This value corresponds to a crystal fraction of, roughly, 34 or 22%, when assuming a bulk enthalpy of crystallization of 93 J/g,[61] or the more recently suggested value of 143 J/g,[62] respectively. Increasing the cooling rate leads to a decrease in the crystallinity and crystallization is fully suppressed on cooling faster than about 20 K/min, being in accord with the literature.[63−65]

The critical cooling rate to suppress crystallization of PLLA in the presence of IR3535, in the investigated range of PLLA concentrations from 5 to 50 m%, increases, such that even on cooling at a rate of 50 K/min, crystallization occurs. The crystallinity obtained after cooling at a specific rate scales with the PLLA content, which is illustrated with the inset in the top right part of Figure 3, showing the enthalpy of crystallization during cooling samples at 30 K/min in the crystallization-relevant temperature range. It is obvious that the data need to pass a maximum; however, whether it is located at 40−50 m% PLLA or at an even higher PLLA concentration is unknown. Note that preparation of samples containing more than 50 m% PLLA was not possible using the above-described dissolution route and that further information may be gained by analysis of
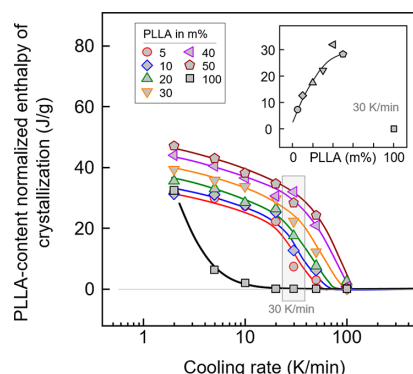
samples prepared by melt-mixing, which is in progress. Summarizing the experiments discussed in Figures 2 and 3, the presence of IR3535 leads to a decrease in the crystallization temperature of PLLA but simultaneously enhances non-isothermal crystallization from the point-of-view of the achievable maximum crystallinity during cooling at a specific rate.

Figure 4 shows optical micrographs of samples of the PLLA/IR3535 system containing between 20 and 50 m% PLLA (from right to left column), cooled from 160 °C (165 °C in case of the sample containing 50 m% PLLA) to ambient temperature at rates of 2, 5, 10, 30, and 50 K/min (from top to bottom). All images show spherulitic crystallization of PLLA with the spherulites, presumably, being composed of solid PLLA crystals separated by amorphous PLLA or a PLLA-rich PLLA/IR3535 solution. In many cases, depending on both the cooling rate and the PLLA concentration, spherulites are isolated and not space-filling. In detail, in terms of the effect of the cooling rate on crystallization, the number of nuclei/spherulites increases when increasing the cooling rate, which may be explained such that the supercooling of the solutions increases with the cooling rate, with the well-known effect on the nucleation kinetics.[65] With regard to the effect of the polymer concentration, most obvious is the finding that a space-filled spherulitic structure often cannot be obtained, even on slow cooling, if the PLLA content is too low. In these cases, the noncrystallized, liquid PLLA/IR3535 phase is located inside and outside the spherulites, likely, with a concentration gradient due to PLLA depletion of the solution during the ongoing crystallization process. Such depletion of the solution on PLLA during crystallization is most obvious for samples containing 20 m% PLLA, or less, when slowly cooled. In this case, spherulitic crystal growth turns to dendritic crystal growth. This notwithstanding, at certain cooling conditions and composition of the solution, intermeshing or even space-filling of spherulites is obtained, eventually leading to a gel-like rather than liquid-like behavior.

The shown images in Figure 4 represent only a selection of samples, as more experiments have been performed, e.g., with a
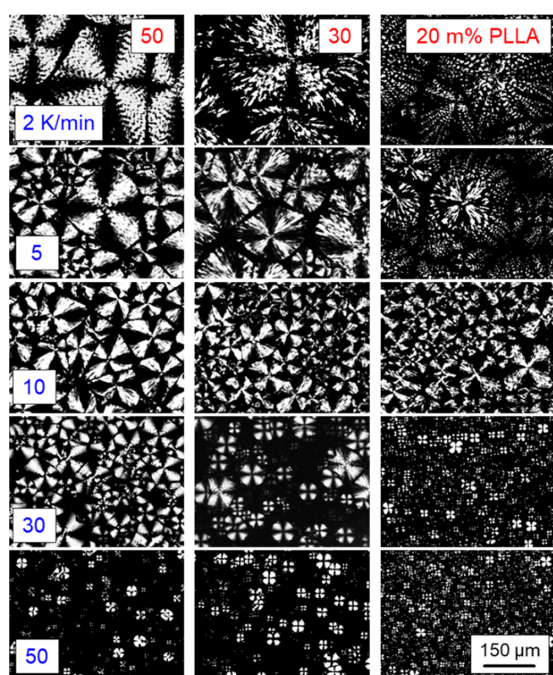
Figure 4. POM micrographs of samples of the polymer/solvent system PLLA/IR3535, obtained after cooling at rates between 2 and 50 K/min (from top to bottom). The different columns represent images obtained on samples with different compositions, containing between 20 (right) and 50 m% PLLA (left).

Figure 5. Peak time of crystallization of neat PLLA and PLLA in solution with IR3535 as a function of the crystallization temperature.

cooling rate of 100 K/min or using samples with a lower PLLA content. Furthermore, it is important to note that in some cases, there is an apparent mismatch observed between enthalpy of crystallization data obtained on cooling (see Figure 3) and the corresponding POM micrographs. For example, images obtained after cooling at 100 K/min showed few isolated spherulites, while the DSC suggested the absence of crystallization. The discrepancy is caused by a slightly different temperature profile in the calorimeter- and hotstage-microscopy experiments. In nonisothermal DSC crystallization experiments, samples were cooled to subambient temperatures, and in the case of hot-stage microscopy, cooling stopped after reaching 25 °C. Afterward, the solutions were allowed to (isothermally) crystallize until completion.

A further comment concerns L−L demixing preceding crystallization-induced S−L demixing. The earlier performed study of the mixing behavior of noncrystallizable PDLLA and IR3535 revealed complete miscibility of the system components in the entire temperature range from abovementioned ambient temperature to the composition-dependent glass transition temperature.[51] With the assumption that in the case of PLA the miscibility is not affected by the stereo-isomerism, for the system PLLA/IR3535, the absence of L−L demixing in the temperature range of crystallization is also assumed.

Isothermal Crystallization. The kinetics of crystallization of neat PLLA from the melt and from solutions with IR3535 is provided in Figure 5, showing DSC crystallization peak times as a function of the crystallization temperature. Note that the peak time of isothermal crystallization is the time of the
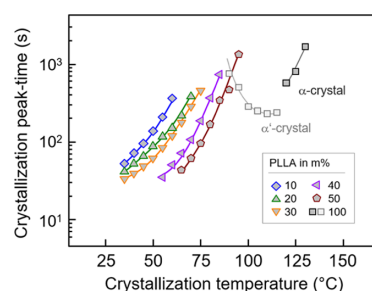
maximum rate of crystal formation, that is, the time of the maximum heat-flow rate in the DSC experiment; it is often close to the crystallization half-time, however, much more reliable to determine. Crystallization of neat PLLA (gray/black squares) at temperatures above and below about 110 °C leads to the formation of α- and α'-crystals, respectively, leading to a discontinuity in the temperature distribution of the total crystallization rate.[66−69] The maximum crystallization rate/ minimum peak time of neat PLLA is detected at around 110 °C; however, in the case of solution crystallization, both the temperature of the minimum peak time as well as the minimum peak time shift to lower values (see colored symbols and lines), though it was not possible to quantify the latter due to instrumental limitations. In other words, the performed measurements do not provide information at which PLLA concentration between 10 and 50 m% crystallization is fastest. However, the data in Figure 5 unambiguously reveal that the maximum crystallization rate of PLLA in the presence of a solvent is about one order of magnitude higher and that the crystallization temperature range shifts to lower temperature compared to neat PLLA.

To obtain information about the crystal polymorph developing during solution crystallization, selected samples containing 30 and 40 m% PLLA, isothermally crystallized at 75 and 25 °C, were analyzed by XRD, with the data shown in Figure 6. Prior measurement, the samples were vacuum-dried at 50 °C for more than 3 days to evaporate the solvent. All samples show two very strong diffraction peaks at scattering angles 2θ of 16.7° and 19.1° and further strong peaks at 14.8° and 22.4°, originating from the (110)/(200), (203), (010), and (015)/(211) lattice planes of the orthorhombic unit cell of
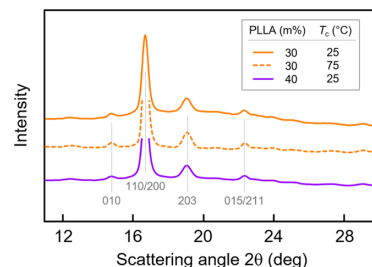

Figure 6. XRD patterns of selected samples of the system PLLA/ IR3535, after isothermal crystallization at 25 and 75 °C, followed by vacuum-drying at 50 °C. Note that curves were scaled individually. Color-coding of curves is based on data shown in Figures 2, 3, and 5.

56

the α-crystal phase. Further, rather weak peaks (not indexed in Figure 6) are detected at 2θ = 12.5, 20.8, 23.0, 24.1, and 25.1°, associated with the (004/103), (204), (115), (016), and (206) planes, respectively.[62,69] As such, similar to the case of the polymer/repellent system PLLA/DEET,[41] solution crystallization yields α- and not α'-crystals, regardless of the low crystallization temperature.

Figure 7 shows POM images of samples of the polymer/solvent system PLLA/IR3535 with different PLLA contents
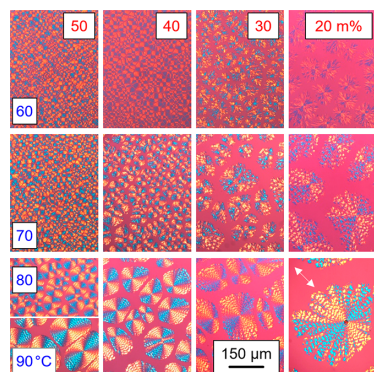

Figure 7. POM micrographs of samples of the polymer/solvent system PLLA/IR3535, containing between 20 and 50 m% PLLA (from right to left). The different rows represent images obtained after isothermal crystallization at 60, 70, and 80 °C (from top to bottom); for the sample containing 50 m% PLLA, an additional image is shown after crystallization at 90 °C. Orange/blue sectoring of spherulites was obtained by inserting a λ-retardation plate, oriented at an angle of 45° with respect to the polarizers, as indicated with the white arrow in the bottom right image.

between 20 and 50 m% (from the right to left column), gained after isothermal crystallization at different temperatures between 60 and 80 °C (from top to bottom row). For the sample containing 50 m% PLLA, an additional image is shown, after crystallization at 90 °C. Note that the shown images only represent a selection. Colored images are obtained by inserting a γ-retardation plate at an angle of 45° with respect to the orientation of the polarizers, revealing with the blue/orange sectoring negative birefringence and alignment of lamellae with their long dimension parallel to the spherulite radius.[70–72] Also, banding is observed due to the rotation of lamellae in their growth direction, in particular, upon crystallization at low supercooling. The band spacing decreases on lowering the crystallization temperature, which is in agreement with earlier studies on the spherulite morphology of PLLA after melt-crystallization;[72,73] however, a further analysis is beyond the scope of this study.

The micrographs show the final morphology after completion of the crystallization process and reveal that the nuclei density increases with decreasing crystallization temperature/increasing supercooling for a given composition, as well as with increasing the polymer concentration for a given crystallization condition. Quantitative information about the temperature dependencies of the areal nucleation density and the nucleation rate are provided in the lower and upper parts of Figure 8, respectively.

The crystal growth kinetics was assessed by evaluating the spherulite size as a function of the time of crystallization.
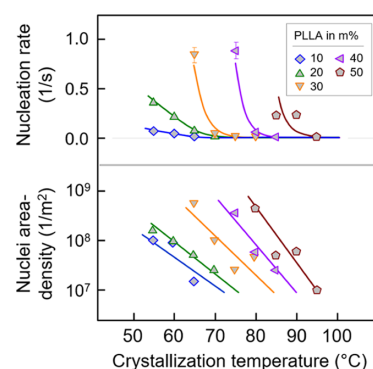

Figure 8. PLLA area-normalized nuclei density (bottom) and the nucleation rate of samples of the system PLLA/IR3535 as a function of the crystallization temperature. Color-coding of data is based on data shown in Figures 2, 3, 5, and 6.

Considering that the polymer content in the solution is continuously decreasing with ongoing crystallization, as shown in Figure 9, the initial spherulite growth rate acquired in the
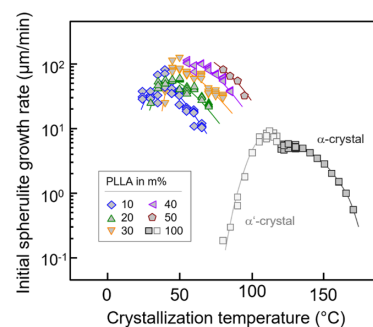

Figure 9. Initial spherulite growth rate of neat PLLA (gray/black squares) and of PLLA crystallizing from solution with IR3535 as a function of the crystallization temperature. Data of neat PLLA were adapted from,[53] Copyright 2016, with permission from Elsevier. Color-coding of data is consistent with data shown in Figures 2, 3, 5, 6, and 8.

beginning of the crystallization process is plotted as a function of crystallization temperature. The gray/black squares show data available in the literature, obtained on the same material[53,68] and reveal the typical polymorphism-controlled bimodal growth-rate distribution for the neat PLLA homopolymer. As indicated, the two maxima are caused by preferred growth of α-crystals at high temperature and α'-crystals at low temperature.[53,68,74] The initial maximum spherulite growth rate of PLLA crystallized from solvent-rich solutions is about one order of magnitude higher compared to neat PLLA as concluded from the corresponding, colored data sets in Figure 9. Obviously, the maximum crystal growth rate decreases with decreasing polymer content within the investigated concentration range, which is attributed to the longer diffusion pathways of polymer molecules when their content decreases. This result is in accord with the observed decreasing slope of the crystallization time dependence of the diameter of a growing spherulite in a solution of a given initial concentration (not shown), often termed depletion.[75,76] In addition to the

observation of an increased maximum crystal growth rate of PLLA when crystallizing from a solution, a shift in the crystallization temperature range is again detected toward lower values when increasing the solvent concentration (also see Figure 5). Furthermore, there is no indication of a change of the crystal polymorph, as two growth-rate maxima as in the case of the neat polymer are not seen. We assume that only α-crystals develop, supported by the XRD data presented in Figure 6.

Microporous Scaffold Structure. Main purpose of the present study is the evaluation of the possibility to generate a microporous PLLA structure as reservoir for the mosquito repellent IR3535, based on PLLA-crystallization-induced S−L TIPS on cooling solutions. Crystallization of PLLA from solvent-rich solutions has been quantified above from the points-of-view of kinetics and crystallinity, as well as regarding the semicrystalline morphology as assessable by POM. Finally, SEM was employed to confirm the formation of intra- and interspherulitic pores, which host either the pure liquid repellent or a repellent-rich solution. After preparation of solutions at elevated temperature (see also Figure 1), followed by crystallization as described below, the liquid solvent-rich phase was removed by evaporation in a vacuum oven, operated at 60 °C. It is worth noting that the evaporation temperature of 60 °C is expected to not affect the semicrystalline morphology at the micrometer-length scale as would be the case in global melting. Even though crystals formed at low temperature exhibit low thermodynamic stability, their reorganization on heating via melting and melt-recrystallization occurs only at a local nanometer-length scale, retaining the overall morphology.[77−79]

Figure 10 shows selected images of the structure of samples which initially contained 10 m% PLLA, subjected to
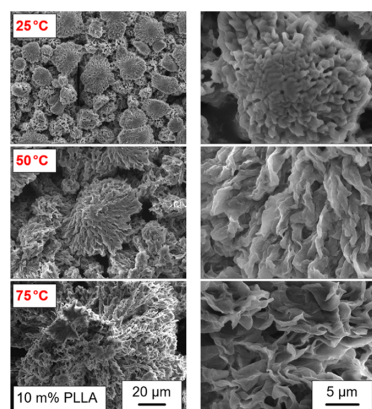

Figure 10. SEM micrographs obtained on samples of the polymer/solvent system PLLA/IR3535, initially containing 10 m% PLLA, crystallized at 25, 50, and 75 °C (from top to bottom), taken at different magnifications.

crystallization-controlled TIPS at temperatures of 25, 50, and 75 °C (from top to bottom), at two different magnifications. In general agreement with the POM micrographs of Figures 4 and 7, the SEM images of Figure 10 confirm the increasing number of spherulitically grown entities with decreasing crystallization temperature. However, in advance to the POM images, the SEM micrographs reveal furthermore the existence of both

inter- and intraspherulitic pores, with the latter, in particular, visible with the higher-resolution images in the right column.

For discussing the effect of the sample composition in addition to the effect of the crystallization temperature (Figure 10), Figure 11 shows images obtained on samples crystallized
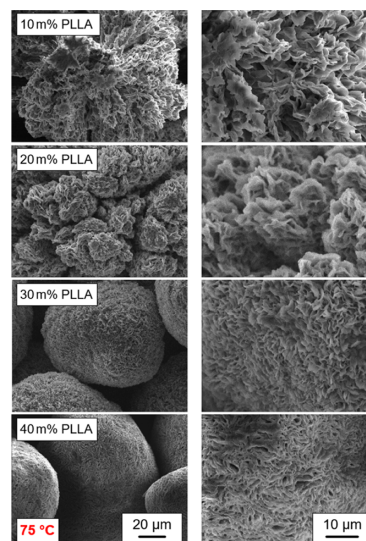

Figure 11. SEM micrographs obtained on samples of the polymer/solvent system PLLA/IR3535, initially containing between 10 and 40 m% PLLA (from top to bottom), crystallized at 75 °C, taken at different magnifications.

at an identical temperature of 75 °C, initially containing between 10 and 40 m% PLLA (from top to bottom), collected at different magnifications. The twofold distribution of cavities, inter- and intraspherulitic, is visible for all compositions; however, the images reveal that with increasing PLLA content, the intraspherulitic pore size seems to decrease, apparently repelling the solvent into interspherulitic regions to a larger degree than in the case of low-polymer-content compositions. On inspecting a larger set of SEM images, it appears that, in particular, the intraspherulitic pore size can be regulated by both the polymer concentration and the crystallization temperature. To prove/disprove this assumption, the intra-spherulitic pore size was quantitatively evaluated by manual selection and analysis of the size of 10−50 pores, considering their anisometry by measuring dimensions in two directions.

Figure 12 shows the evaluated intraspherulitic pore size of PLLA as a function of the crystallization temperature, with the different colors/symbols indicating samples of different compositions. The data confirm the visual impression from Figures 10 and 11 that with increasing crystallization temperature, the intraspherulitic pore size increases. Moreover, the data reveal that the pore size increases with decreasing polymer content, which is in particular obvious in samples crystallized at high temperature. It is worth noting that the observed trends only hold for the surface regions of the spherulites as during growth their fine structure may change from a dense and regular crystal arrangement toward a branched and dendritic morphology. Such dendritic growth has been seen, e.g., in Figure 7 (top right image). Note that scaffold-formation experiments were not performed at even
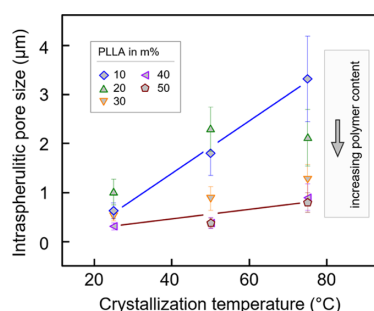
Figure 12. Intraspherulitic pore size as a function of the temperature of crystallization of PLLA in solutions with different contents of IR3535.

higher temperatures than 75 °C due to the rather long crystallization time and low nucleation rate (see also Figures 5, 8, and 9), as well as increasing amount of the repellent located in interspherulitic regions.

CONCLUSIONS

PLLA can be used as a polymer carrier for the mosquito-repellent IR3535. PLLA dissolves in IR3535 at elevated temperatures, and on cooling, PLLA-crystallization-related solid−liquid thermally induced phase separation occurs. Crystallization of PLLA proceeds via nucleation and spherulitic growth, with the liquid repellent located in intra- and interspherulitic regions, which are tunable by both the crystallization temperature and the polymer content in the solutions. Though not explicitly studied, tailoring the microporous structure is assumed possible also by variation of the cooling rate, as this parameter controls the crystallization temperature. The effects of the cooling rate and crystallization temperature on structure formation have been evaluated in detail, providing the necessary knowledge to tailor the bimodal distribution of the repellent inside and outside the spherulites. As such, the performed study provides a sound basis for further research activities in the field of development of mosquito-repellent personal protection devices using a biodegradable polymer as a carrier for environmental friendly after-use disposal and a biodegradable repellent, with less detrimental side effects on human beings and the environment than synthetically produced alternatives.

AUTHOR INFORMATION

Corresponding Author

  René Androsch − *Interdisciplinary Center for Transfer-oriented Research in Natural Sciences (IWE TFN), Martin Luther University Halle-Wittenberg, D-06099 Halle/Saale, Germany;* orcid.org/0000-0002-7924-0159; Email: rene.androsch@iw.uni-halle.de

Authors

  Fanfan Du − *Interdisciplinary Center for Transfer-oriented Research in Natural Sciences (IWE TFN), Martin Luther University Halle-Wittenberg, D-06099 Halle/Saale, Germany*

  Hande Ece Yener − *Interdisciplinary Center for Transfer-oriented Research in Natural Sciences (IWE TFN), Martin Luther University Halle-Wittenberg, D-06099 Halle/Saale, Germany*

  Georg Hillrichs − *Department of Engineering and Natural Sciences, University of Applied Sciences Merseburg, D-06217 Merseburg, Germany*

  Regine Boldt − *Leibniz-Institut für Polymerforschung e. V. Dresden (IPF), D-01069 Dresden, Germany*

Complete contact information is available at:
https://pubs.acs.org/10.1021/acs.biomac.1c00760

Notes
The authors declare no competing financial interest.

REFERENCES

(1) World Health Organization. (2020). World malaria report 2020: 20 years of global progress and challenges. World Health Organization . https://apps.who.int/iris/handle/10665/337660. License: CC BY-NC-SA 3.0 IGO (assessed 15/05/2021).

(2) https://www.who.int/news-room/fact-sheets/detail/dengue-and-severe-dengue (assessed 15/05/2021).

(3) https://www.who.int/news-room/fact-sheets/detail/lymphatic-filariasis (assessed 15/05/2021).

(4) Kleinschmidt, I.; Schwabe, C.; Shiva, M.; Segura, J. L.; Sima, V.; Mabunda, S. J. A.; Coleman, M. Combining indoor residual spraying and insecticide-treated net interventions. *Am. J. Trop. Med. Hyg.* **2009**, *81*, 519−524.

(5) Hamel, M. J.; Otieno, P.; Bayoh, N.; Kariuki, S.; Were, V.; Marwanga, D.; Laserson, K. F.; Williamson, J.; Slutsker, L.; Gimnig, J. The combination of indoor residual spraying and insecticide-treated nets provides added protection against malaria compared with insecticide-treated nets alone. *Am. J. Trop. Med. Hyg.* **2011**, *85*, 1080−1086.

(6) Pluess, B.; Tanser, F. C.; Lengeler, C.; Sharp, B. L. Indoor residual spraying for preventing malaria. *Cochrane Database Syst. Rev.* **2010**, No. CD006657.

(7) Killeen, G. F.; Moore, S. J. Target product profiles for protecting against outdoor malaria transmission. *Malar. J.* **2012**, *11*, No. 17.

(8) Braack, L.; Hunt, R.; Koekemoer, L. L.; Gericke, A.; Munhenga, G.; Haddow, A. D.; Becker, P.; Okia, M.; Kimera, I.; Coetzee, M. Biting behaviour of African malaria vectors: 1. where do the main vector species bite on the human body? *Parasites vectors* **2015**, *8*, No. 76.

(9) Bradley, J.; Matias, A.; Schwabe, C.; Vargas, D.; Monti, F.; Nseng, G.; Kleinschmidt, I. Increased risks of malaria due to limited residual life of insecticide and outdoor biting versus protection by combined use of nets and indoor residual spraying on Bioko Island, Equatorial Guinea. *Malar. J.* **2012**, *11*, No. 242.

(10) Nogueira Barradas, T.; Perdiz Senna, J.; Ricci Junior, E.; Regina Elias Mansur, C. Polymer-based drug delivery systems applied to insects repellents devices: a review. *Curr. Drug Delivery* **2016**, *13*, 221−235.

(11) Mapossa, A. B.; Focke, W. W.; Tewo, R. K.; Androsch, R.; Kruger, T. Mosquito-repellent controlled-release formulations for fighting infectious diseases. *Malar. J.* **2021**, *20*, No. 165.

(12) Revay, E. E.; Junnila, A.; Xue, R. D.; Kline, D. L.; Bernier, U. R.; Kravchenko, V. D.; Qualls, W. A.; Ghattas, N.; Müller, G. C.

Evaluation of commercial products for personal protection against mosquitoes. *Acta Trop.* **2013**, *125*, 226−230.

(13) Ryan, J. J.; Casalini, R.; Orlicki, J. A.; Lundin, J. G. Controlled release of the insect repellent picaridin from electrospun nylon-6, 6 nanofibers. *Polym. Adv. Technol.* **2020**, *31*, 3039−3047.

(14) Cecone, C.; Caldera, F.; Trotta, F.; Bracco, P.; Zanetti, M. Controlled release of DEET loaded on fibrous mats from electrospun PMDA/cyclodextrin polymer. *Molecules* **2018**, *23*, No. 1694.

(15) Bonadies, I.; Longo, A.; Androsch, R.; Jehnichen, D.; Göbel, M.; Di Lorenzo, M. L. Biodegradable electrospun PLLA fibers containing the mosquito-repellent DEET. *Eur. Polym. J.* **2019**, *113*, 377−384.

(16) Han, M. A.; Kim, C. M.; Yun, N. R.; Kim, D. M.; Park, S. M.; Kim, H.; Shin, H. H. The Effect of Long-lasting Permethrin Impregnated Socks on Tick Bite in Korea. *J. Korean Med. Sci.* **2021**, *36*, No. e49.

(17) Ferreira, I.; Brünig, H.; Focke, W.; Boldt, R.; Androsch, R.; Leuteritz, A. Melt-spun poly (D, L-lactic acid) monofilaments containing N, N-diethyl-3-methylbenzamide as mosquito repellent. *Materials* **2021**, *14*, No. 638.

(18) Kim, S. S.; Lloyd, D. R. Thermodynamics of polymer/diluent systems for thermally induced phase separation: 1. Determination of equation of state parameters. *Polymer* **1992**, *33*, 1026−1035.

(19) Kim, S. S.; Lloyd, D. R. Thermodynamics of polymer/diluent systems for thermally induced phase separation: 2. Solid-liquid phase separation systems. *Polymer* **1992**, *33*, 1036−1046.

(20) Kim, S. S.; Lloyd, D. R. Thermodynamics of polymer/diluent systems for thermally induced phase separation: 3. Liquid-liquid phase separation systems. *Polymer* **1992**, *33*, 1047−1057.

(21) Mitra, M. K.; Muthukumar, M. Theory of spinodal decomposition assisted crystallization in binary mixtures. *J. Chem. Phys.* **2010**, *132*, No. 184908.

(22) Zhang, X.; Wang, Z.; Muthukumar, M.; Han, C. C. Fluctuation-assisted crystallization: In a simultaneous phase separation and crystallization polyolefin blend system. *Macromol. Rapid Commun.* **2005**, *26*, 1285−1288.

(23) Hu, W.; Frenkel, D.; Mathot, V. B. F. Lattice-model study of the thermodynamic interplay of polymer crystallization and liquid−liquid demixing. *J. Chem. Phys.* **2003**, *118*, 10343−10348.

(24) Hu, W.; Mathot, V. B. F. Liquid−liquid demixing in a binary polymer blend driven solely by the component-selective crystallizability. *J. Chem. Phys.* **2003**, *119*, 10953−10957.

(25) Zhang, X.; Wang, Z.; Dong, X.; Wang, D.; Han, C. C. Interplay between two phase transitions: Crystallization and liquid-liquid phase separation in a polyolefin blend. *J. Chem. Phys.* **2006**, *125*, No. 024907.

(26) Paul, D. R.; Barlow, J. W. Crystallization from Miscible Polymer Blends. In *Polymer Alloys II. Polymer Science and Technology*, Klempner, D.; Frisch, K. C., Eds.; Springer: Boston, MA,1980; Vol. 11.

(27) Tavares, M.; da Silva, M. R. M.; de Siqueira, L. B. D. O.; Rodrigues, R. A. S.; Bodjolle-d'Almeida, L.; Dos Santos, E. P.; Ricci-Júnior, E. Trends in insect repellent formulations: A review. *Int. J. Pharm.* **2018**, *539*, 190−209.

(28) Lupi, E.; Hatz, C.; Schlagenhauf, P. The efficacy of repellents against Aedes, Anopheles, Culex and Ixodes spp.−A literature review. *Travel Med. Infect. Dis.* **2013**, *11*, 374−411.

(29) Feuser, Z. P.; Colonetti, T.; Grande, A. J.; Uggioni, M. L. R.; Roever, L.; da Rosa, M. I. Efficacy of the DEET, IR3535, and picaridin topical use against Aedes Aegypti: Systematic review. *Infect. Dis. Clin. Pract.* **2020**, *28*, 327−341.

(30) Mapossa, A. B.; Sibanda, M. M.; Sitoe, A.; Focke, W. W.; Braack, L.; Ndonyane, C.; Mouatcho, J.; Smart, J.; Muaimbo, H.; Androsch, R.; Loots, M. T. Microporous polyolefin strands as controlled-release devices for mosquito repellents. *Chem. Eng. J.* **2019**, *360*, 435−444.

(31) Akhtar, M. U.; Focke, W. W. Trapping citronellal in a microporous polyethylene matrix. *Thermochim. Acta* **2015**, *613*, 61−65.

(32) Synthesis, Structure and Properties of Poly(Lactic Acid). In *Advanced Polymer Science*, Di Lorenzo, M. L.; Androsch, R., Eds.; Springer: Cham, 2018; Vol. 279.

(33) Xu, J.; Guo, B. H. Poly (butylene succinate) and its copolymers: Research, development and industrialization. *Biotechnol. J.* **2010**, *5*, 1149−1163.

(34) Xu, J.; Guo, B. H. Microbial Succinic Acid, Its Polymer Poly (Butylene Succinate), and Applications. *Plastics from Bacteria*; Springer: Berlin, Heidelberg, 2010; pp 347−388.

(35) Yang, F.; Murugan, R.; Ramakrishna, S.; Wang, X.; Ma, Y.-X.; Wang, S. Fabrication of nano-structured porous PLLA scaffold intended for nerve tissue engineering. *Biomaterials* **2004**, *25*, 1891−1900.

(36) Mohammadi, M. S.; Bureau, M. N.; Nazhat, S. N. Polylactic Acid (PLA) Biomedical Foams for Tissue Engineering. In *Biomedical Foams for Tissue Engineering Applications*; Woodhead Publishing, 2014; pp 313−334.

(37) Schugen, C.; Maquet, V.; Grandfils, C.; Jerome, R.; Teyssie, P. Biodegradable and macroporous polylactide implants for cell transplantation: 1. Preparation of macroporous polylactide supports by solid-liquid phase separation. *Polymer* **1996**, *37*, 1027−1038.

(38) Önder, Ö. C.; Yilgör, E.; Yilgör, I. Fabrication of rigid poly (lactic acid) foams via thermally induced phase separation. *Polymer* **2016**, *107*, 240−248.

(39) Lo, H.; Ponticiello, M. S.; Leong, K. W. Fabrication of controlled release biodegradable foams by phase separation. *Tissue Eng.* **1995**, *1*, 15−28.

(40) Tanaka, T.; Takahashi, M.; Kawaguchi, S.; Hashimoto, T.; Saitoh, H.; Kouya, T.; Taniguchi, M.; Lloyd, D. R. Formation of microporous membranes of poly (1, 4-butylene succinate) via nonsolvent and thermally induced phase separation. *Desalination Water Treat.* **2010**, *17*, 176−182.

(41) Sungkapreecha, C.; Iqbal, N.; Gohn, A. M.; Focke, W. W.; Androsch, R. Phase behavior of the polymer/drug system PLA/DEET. *Polymer* **2017**, *126*, 116−125.

(42) Sungkapreecha, C.; Iqbal, N.; Focke, W. W.; Androsch, R. Crystallization of poly (L-lactic acid) in solution with the mosquito-repellent N, N-diethyl-3-methylbenzamide. *Polym. Cryst.* **2019**, *2*, No. e10029.

(43) Sungkapreecha, C.; Beily, M. J.; Kressler, J.; Focke, W. W.; Androsch, R. Phase behavior of the polymer/drug system PLA/DEET: Effect of PLA molar mass on subambient liquid-liquid phase separation. *Thermochim. Acta* **2018**, *660*, 77−81.

(44) Sungkapreecha, C.; Focke, W. W.; Androsch, R. Competition between liquid-liquid de-mixing, crystallization, and glass transition in solutions of PLA of different stereochemistry and DEET. *Chin. J. Polym. Sci.* **2020**, *38*, 174−178.

(45) Yener, H. E.; Hillrichs, G.; Androsch, R. Phase behavior of solvent-rich compositions of the polymer/drug system poly (butylene succinate) and N,N-diethyl-3-methylbenzamide (DEET). *Colloid Polym. Sci.* **2021**, *299*, 873−881.

(46) Roberts, J. R.; Reigart, J. R. Does anything beat DEET? *Pediatr. Ann.* **2004**, *33*, 444−453.

(47) Fradin, M. S.; Day, J. F. Comparative efficacy of insect repellents against mosquito bites. *N. Engl. J. Med.* **2002**, *347*, 13−18.

(48) Fradin, M. S. Mosquitoes and mosquito repellents: a clinician's guide. *Ann. Intern. Med.* **1998**, *128*, 931−940.

(49) Thavara, U.; Tawatsin, A.; Chompoosri, J.; Suwonkerd, W.; Chansang, U. R.; Asavadachanukorn, P. Laboratory and field evaluations of the insect repellent 3535 (ethyl butylacetylaminopropionate) and deet against mosquito vectors in Thailand. *J. Am. Mosq. Control Assoc.* **2001**, *17*, 190−195.

(50) Cilek, J. E.; Petersen, J. L.; Hallmon, C. F. Comparative efficacy of IR3535 and DEET as repellents against adult Aedes aegypti and Culex quinquefasciatus. *J. Am. Mosq. Control Assoc.* **2004**, *20*, 299−304.

(51) Du, F.; Schick, C.; Androsch, R. Full-composition-range glass transition behavior of the polymer/solvent system poly (lactic acid)/

ethyl butylacetylaminopropionate (PLA/IR3535). *Polymer* **2020**, *209*, No. 123058.

(52) Product information, Sulzer Chemtec Ltd. , https://www.sulzer.com//media/files/products/polymer_production_technology/brochures/fact_sheet_polylactides.ashx?la=en (assessed 06/04/2021).

(53) Androsch, R.; Di Lorenzo, M. L.; Schick, C. Crystal nucleation in random L/D-lactide copolymers. *Eur. Polym. J.* **2016**, *75*, 474−485.

(54) Carbolution Chemicals GmbH, Ethyl butylacetylaminopropionate Product information: https://www.carbolution.de/product_info.php?products_id=3221 (assessed 06/04/2021).

(55) https://archive.epa.gov (assessed 11/07/2021); Butylacetylaminopropionate, E. WHO Specifications and Evaluations for public health pesticides.

(56) Mapossa, A. B.; Sitoe, A.; Focke, W. W.; Izadi, H.; du Toit, E. L.; Androsch, R.; Sungkapreecha, C.; van der Merwe, E. M. Mosquito repellent thermal stability, permeability and air volatility. *Pest Manage. Sci.* **2020**, *76*, 1112−1120.

(57) Flory, P. J. Thermodynamics of crystallization in high polymers. IV. A theory of crystalline states and fusion in polymers, copolymers, and their mixtures with diluents. *J. Chem. Phys.* **1949**, *17*, 223−240.

(58) Lauritzen, J. I., Jr.; Hoffman, J. D. Theory of formation of polymer crystals with folded chains in dilute solution. *J. Res. Natl. Bur. Stand. A Phys. Chem.* **1960**, *64A*, No. 73.

(59) Martuscelli, E. Influence of composition, crystallization conditions and melt phase structure on solid morphology, kinetics of crystallization and thermal behavior of binary polymer/polymer blends. *Polym. Eng. Sci.* **1984**, *24*, 563−586.

(60) Sanchez, I. C.; Eby, R. K. Thermodynamics and crystallization of random copolymers. *Macromolecules* **1975**, *8*, 638−641.

(61) Fischer, E. W.; Sterzel, H.; Wegner, G. Investigation of the structure of solution grown crystals of lactide copolymers by means of chemical reactions. *Kolloid Z. Z. Polym.* **1973**, *251*, 980−990.

(62) Righetti, M. C.; Gazzano, M.; Di Lorenzo, M. L.; Androsch, R. Enthalpy of melting of α'- and α-crystals of poly (L-lactic acid). *Eur. Polym. J.* **2015**, *70*, 215−220.

(63) Androsch, R.; Iqbal, H. N.; Schick, C. Non-isothermal crystal nucleation of poly (L-lactic acid). *Polymer* **2015**, *81*, 151−158.

(64) Sarasua, J.-R.; Prud'homme, R. E.; Wisniewski, M.; Le Borgne, A.; Spassky, N. Crystallization and melting behavior of polylactides. *Macromolecules* **1998**, *31*, 3895−3905.

(65) Sánchez, M. S.; Mathot, V. B. F.; Vanden Poel, G.; Ribelles, J. L. G. Effect of cooling rate on the nucleation kinetics of poly (L-lactic acid) and its influence on morphology. *Macromolecules* **2007**, *40*, 7989−7997.

(66) Zhang, J.; Duan, Y.; Sato, H.; Tsuji, H.; Noda, I.; Yan, S.; Ozaki, Y. Crystal modifications and thermal behavior of poly (L-lactic acid) revealed by infrared spectroscopy. *Macromolecules* **2005**, *38*, 8012−8021.

(67) Yasuniwa, M.; Tsubakihara, S.; Iura, K.; Ono, Y.; Dan, Y.; Takahashi, K. Crystallization behavior of poly (L-lactic acid). *Polymer* **2006**, *47*, 7554−7563.

(68) Androsch, R.; Schick, C.; Di Lorenzo, M. L. Kinetics of nucleation and growth of crystals of poly (L-lactic acid). *Adv. Polym. Sci.* **2017**, *279*, 235−272.

(69) Pan, P.; Inoue, Y. Polymorphism and isomorphism in biodegradable polyesters. *Prog. Polym. Sci.* **2009**, *34*, 605−640.

(70) Kalb, B.; Pennings, A. J. General crystallization behaviour of poly (L-lactic acid). *Polymer* **1980**, *21*, 607−612.

(71) Di Lorenzo, M. L.; Rubino, P.; Immirzi, B.; Luijkx, R.; Hélou, M.; Androsch, R. Influence of chain structure on crystal polymorphism of poly (lactic acid). Part 2. Effect of molecular mass on the crystal growth rate and semicrystalline morphology. *Colloid Polym. Sci.* **2015**, *293*, 2459−2467.

(72) Lotz, B. Crystal Polymorphism and Morphology of Polylactides. In *Advanced Polmer Science*, Di Lorenzo, M. L.; Androsch, R., Eds.; 2017; Vol. *279*, pp 273−302.

(73) Xu, J.; Guo, B. H.; Zhou, J. J.; Li, L.; Wu, J.; Kowalczuk, M. Observation of banded spherulites in pure poly (L-lactide) and its

miscible blends with amorphous polymers. *Polymer* **2005**, *46*, 9176−9185.

(74) Di Lorenzo, M. L. The crystallization and melting processes of poly (L-lactic acid). *Macromol. Symp.* **2006**, *234*, 176−183.

(75) Cao, Q.; Qiao, X.; Wang, H.; Liu, J. Structures and growth mechanisms of poly-(3-hydroxybutyrate) (PHB) crystallized from solution and thin melt film. *Sci. China, Ser. B: Chem.* **2008**, *51*, 853−858.

(76) De Gennes, P. G. Polymer solutions near an interface. Adsorption and depletion layers. *Macromolecules* **1981**, *14*, 1637−1644.

(77) Androsch, R. In situ atomic force microscopy of the mesomorphic-monoclinic phase transition in isotactic polypropylene. *Macromolecules* **2008**, *41*, 533−535.

(78) Androsch, R.; Zhuravlev, E.; Schick, C. Solid-state reorganization, melting and melt-recrystallization of conformationally disordered crystals (α'-phase) of poly (L-lactic acid). *Polymer* **2014**, *55*, 4932−4941.

(79) Androsch, R.; Zhang, R.; Schick, C. Melt-recrystallization of poly (L-lactic acid) initially containing α'-crystals. *Polymer* **2019**, *176*, 227−235.

4.3 Structure, properties, and release kinetics of the polymer/insect repellent system poly(L-lactic acid)/ethyl butylacetylaminopropionate (PLLA/IR3535)

Fanfan Du[1],*, Rafael Erdmann[2], Albrecht Petzold[3], Andre Wutzler[4], Andreas Leuteritz[5], Michael Nase[2], and René Androsch[1],*

[1] Interdisciplinary Center for Transfer-oriented Research in Natural Sciences (IWE TFN), Martin Luther University Halle-Wittenberg, D-06099 Halle/Saale, Germany

[2] Institute for Biopolymers and Sustainability (ibp), University of Applied Sciences Hof, D-95028 Hof/Saale, Germany

[3] Institute of Physics, Martin Luther University Halle-Wittenberg, D-06099 Halle/Saale, Germany

[4] Polymer Service GmbH Merseburg (PSM), Merseburg, D-06217, Germany

[5] Leibniz-Institut für Polymerforschung Dresden e. V., Hohe Str. 6, D-01069 Dresden, Germany

Graphical abstract:
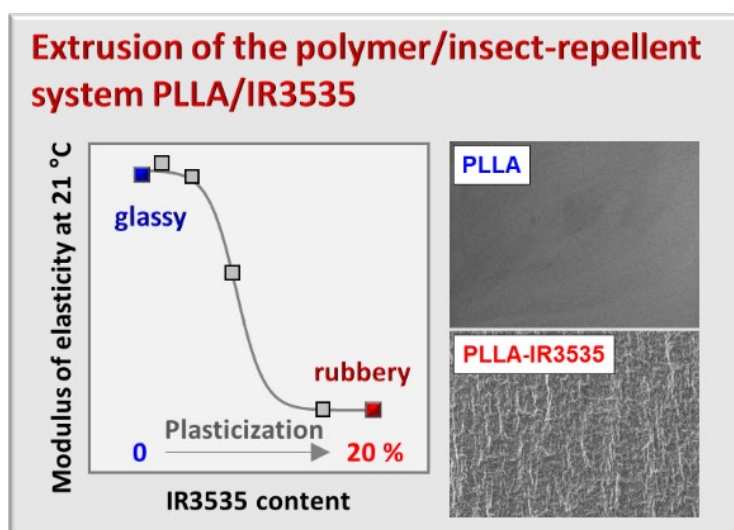
Highlights:

❖ PLLA/IR3535 mixtures with up to 23 m% IR3535 were prepared via melt extrusion.
❖ IR3535 acts as a plasticizer of PLLA.
❖ Addition of IR3535 resulted in a significant decrease in the glass transition temperature of PLLA, as well as in the elastic modulus.
❖ Quantification of the release of IR3535 into the environment by TGA analysis suggests an extremely low release rate extrapolated to body temperature.

pharmaceutics

Article

Structure, Properties, and Release Kinetics of the Polymer/Insect Repellent System Poly (L-Lactic Acid)/Ethyl Butylacetylaminopropionate (PLLA/IR3535)

Fanfan Du [1,*], Rafael Erdmann [2], Albrecht Petzold [3], Andre Wutzler [4], Andreas Leuteritz [5], Michael Nase [2] and René Androsch [1,*]

1   Interdisciplinary Center for Transfer-Oriented Research in Natural Sciences (IWE TFN),
    Martin Luther University Halle-Wittenberg, D-06099 Halle (Saale), Germany
2   Institute for Biopolymers and Sustainability (ibp), University of Applied Sciences Hof,
   D-95028 Hof (Saale), Germany
3   Institute of Physics, Martin Luther University Halle-Wittenberg, D-06099 Halle (Saale), Germany
4   Polymer Service GmbH Merseburg (PSM), D-06217 Merseburg, Germany
5   Leibniz-Institut für Polymerforschung Dresden e. V., Hohe Str. 6, D-01069 Dresden, Germany
*   Correspondence: fanfan.du@iw.uni-halle.de (F.D.); rene.androsch@iw.uni-halle.de (R.A.)

Abstract: The insect repellent ethyl butylacetylaminopropionate (IR3535) was used as a functional additive for poly (L-lactic acid) (PLLA) to modify its structure and mechanical properties and achieve insect repellency. PLLA/IR3535 mixtures at various compositions were prepared via melt extrusion. In the analyzed composition range of 0 to 23 m% IR3535, PLLA and IR3535 were miscible at the length scale represented by the glass transition temperature. Addition of IR3535 resulted in a significant decrease in the glass transition temperature of PLLA, as well as in the elastic modulus, indicating its efficiency as a plasticizer. All mixtures were amorphous after extrusion, though PLLA/IR3535 extrudates with an IR3535 content between 18 and 23 m% crystallized during long-term storage at ambient temperature, due to their low glass transition temperature. Quantification of the release of IR3535 into the environment by thermogravimetric analysis at different temperatures between 50 and 100 °C allowed the estimation of the evaporation rate at lower temperatures, suggesting an extremely low release rate with a time constant of the order of magnitude of 1–2 years at body temperature.

Keywords: poly (L-lactic acid); ethyl butylacetylaminopropionate (IR3535); plasticization; mechanical properties; repellent release

check for **updates**

1. Introduction

The advances in the development of polymer materials over the last century have yielded many biomedical applications [1,2], among others, serving as platforms for advanced medical devices/drug delivery systems, allowing the controlled release of active compounds [3,4]. From a long-term environmental sustainability perspective, the use of biopolymers is the preferred alternative to petroleum-based materials [5,6]; moreover, biopolymers are expected to degrade in a reasonable time at the end of their lifecycle, avoiding adverse effects on the environment [7,8]. Poly (L-lactic acid) (PLLA)—an aliphatic thermoplastic polyester—is such a biopolymer, being widely used in different industrial fields, such as food packaging, agriculture, automotive, electronics, and biomedicine, including tissue engineering and drug delivery applications, because of its biodegradability and biocompatibility [9–12]. Despite these merits, PLLA has a few weaknesses, including brittleness and low crystallization rate, which limit its wider industrial application [10–13]. One of the most effective ways to increase the toughness, ductility, and processability of PLLA is by modifying the polymer with plasticizers [14,15]. Plasticizers require good miscibility with the polymer, low volatility, and adequate stability [16]. An efficient plasticizer

is expected to reduce the glass transition temperature (T_g) of the amorphous domains, such that at the temperature of application the polymer is in a rubbery state. Several substances have been studied as PLLA plasticizers, including glycerol [17], poly (ethylene glycol) [18], poly (propylene glycol) [19], acetyl triethyl citrate [20], glycerol monostearate [21], oligo (lactic acid) [22], β-cyclodextrin/D-Limonene [23], and *N*,*N*-diethyl-3-methylbenzamide (DEET) [24], with small molecules being more efficient than oligo- or polymers regarding the lowering of T_g of the host polymer. However, they may be unstable at the temperature used for melt processing, have a stronger tendency for phase separation from the host polymer, and tend to migrate toward surfaces during storage, thus leading to undesired changes in properties [25].

DEET, mentioned above, is an insect repellent [26,27], thus offering additional functionality beyond the basic plasticizing effect. The polymer/repellent system PLLA/DEET has been investigated in detail from the point of view of general phase behavior [28–31] as well as the generation of semi-finished or final products [24,32,33]. These investigations confirmed both a plasticizing effect of DEET on PLLA and, simultaneously, the possible use of PLLA as an insect repellent carrier. In the present work, we extend the initial work of modifying PLLA with insect repellents by employing ethyl butylacetylaminopropionate (IR3535) instead of DEET. Compared to the gold standard repellent DEET [26,27], IR3535 has fewer side effects on the environment and human beings, allowing possible use by pregnant women and children [34–36] to prevent mosquito-borne tropical diseases, such as malaria, which causes hundreds of thousands of deaths each year [37,38].

Recent studies have proven that PLLA can be used as a carrier/drug delivery reservoir for the repellent IR3535 [39–41]. Early investigations focused on the evaluation of the repellent/solvent-rich part of the PLLA/IR3535 system for the preparation of scaffolds for the controlled release of IR3535 into the environment [40]. IR3535 and PLLA form solutions at elevated temperature, and the solutions demix upon cooling via polymer crystallization caused by solid–liquid (S–L) thermally induced phase separation (TIPS) [42,43], leading to the formation of solid PLLA scaffolds. These scaffolds are tunable regarding pore size through both the crystallization temperature and the polymer content. Microporous scaffolds with different fine structures were obtained, which carried the mosquito repellent in intra- and interspherulitic pores. The intraspherulitic pore size of PLLA increased with crystallization temperature and decreased with the polymer content [40]. In the case of employing amorphous poly (D/L-lactic acid) (PDLLA), an in-depth analysis of the glass transition temperature by using fast scanning chip calorimetry combined with in situ evaporation of the liquid for controlled change in the system composition revealed that PDLLA and IR3535 are thermodynamically miscible over the entire composition range [39]. Crystallization of PLLA in the presence of IR3535 is faster than melt crystallization of neat PLLA, with the maximum crystallization rate increasing with the PLLA content over the investigated range of 5 to 50 mass % (m%) PLLA [40].

Important from the point of view of obtaining end user products, PLLA parts, such as finger rings accommodating up to 25 m% liquid mosquito repellent IR3535, were successfully fabricated by 3D printing, suggesting novel materials/processing routes to obtain PLLA-based controlled repellent release devices [44]. Furthermore, melt extrusion of PLLA/IR3535 strands as an efficient processing route for obtaining semi-finished products has been investigated, focusing on thermal, rheological, and release properties of the samples containing up to 25 m% IR3535 [41]. In the present work, we attempted to expand the initial melt extrusion study, so as to include—additional to the evaluation of the plasticizing effect of IR3535 and the release characteristics—the analysis of the long-term crystallization behavior and its effect on the mechanical performance.

2. Materials and Methods

2.1. Materials and Preparation

PLLA with less than 1% D-isomers, named L-175, was provided by Total-Corbion (Amsterdam, The Netherlands). The melt flow index of the material is reported as 8 g/10 min

(210 °C/2.16 kg) [45]. IR3535, with a purity of 98%, was purchased from Carbolution Chemicals GmbH (St. Ingbert, Germany) [46] and used as received without further purification. It is a clear liquid at room temperature, with a glass transition temperature of close to −90 °C [39]. The estimated boiling points at atmospheric pressure and at 0.02 kPa are slightly below 300 °C and about 110 °C, respectively, and the vapor pressure is reported as being around 0.15 Pa at 20 °C [35,36].

PLLA was dried in a dry-air dryer at 60 °C for 4 h prior to processing. Strands of PLLA and IR3535 mixtures, as well as of neat PLLA, were prepared using a modular co-rotating and intermeshing twin screw extruder LTE20-44/00 (Labtech Engineering Co. Ltd., Samutprakarn, Thailand) with a screw diameter of 20 mm and an L/D ratio of 44. A special screw design with a low number of shear and kneading elements was used for processing. The throughput of the PLLA was variable, depending on the required repellent concentration in the compound (see Table 1). The dry PLLA was fed via the main hopper, and the screw speed for the preparation of the compounds was set at 250 1/min. The temperature profile of the extruder was set from the feeding zone (zone 1) to the die (zone 11) as follows: 185, 185, 185, 185, 185, 190, 190, 200, 200, 210, and 210 °C. The liquid repellent was added via a volumetric pump, preeflow® eco-PEN600 (ViscoTEC Pumpen-u. Dosiertechnik GmbH, Töging am Inn, Germany), at the feeding zone. The melt was extruded through a dual-strand die with a diameter of 3 mm, before being cooled in a water bath at room temperature and subsequently pelletized. It is noted that thermal degradation of IR3535 under the extrusion conditions is excluded, based on dedicated IR3535 stability experiments described elsewhere [35].

Table 1. Sample composition and extrusion parameters.

PLLA/IR3535 Ratio (m%)	Screw Speed (1/min)	Main Feeder (1/min)	Engine Load (%)	Die Pressure (bar)	Melt Temperature (°C)				
					Die	Zone 2	Zone 4	Zone 6	Zone 8
100/0	250	17.0	61	10	190	186	187	191	199
98/2	250	35.8	88	21	189	186	184	191	199
95/5	250	20.8	58	12	190	184	187	190	199
90/10	250	9.8	38	5	186	182	185	189	198
80/20	250	13.1	36	5	188	182	184	187	197
70/30 [1]	250	7.6	10	1	187	182	184	187	197

[1] The surface of the sample was wet when storing at room temperature.

2.2. Instrumentation

Thermogravimetric analysis (TGA): The content of the repellent and degradation behavior of PLLA in mixtures after extrusion, as well as the repellent release kinetics were investigated by a TGA 2 LF/1100/694 (Mettler Toledo, Greifensee, Switzerland). For non-isothermal repellent evaporation experiments, sample pieces with a mass of 7.0 ± 0.3 mg were prepared by cutting sections across the whole strand, that is, perpendicular to the extrusion direction, placing them into alumina crucibles, which were then heated from 30 to 600 °C at 5 K/min, using nitrogen as the purge gas, followed by heating from 600 to 900 °C at 30 K/min in an oxygen atmosphere. The gas flow rate, in both cases, was 50 mL/min. Measured data were automatically subtracted by a blank curve using the instrument software. For isothermal repellent release experiments, samples with a mass of 3.0 ± 0.2 mg were heated to predefined temperatures between 50 and 100 °C at a rate of 20 K/min in a nitrogen atmosphere, and then held at these temperatures for 24 h, to allow evaporation of the liquid repellent. Measured data were automatically compensated for buoyancy, using the instrument software.

Polarized light optical microscopy (POM): The structures of the PLLA/IR3535 mixtures after melt extrusion and after additional annealing at 60 °C for 3–4 weeks were observed using POM. Samples were cut into thin slices with a thickness of 20–30 μm using a CUT-5062 rotary microtome (Slee, Mainz, Germany). Then, thin sections were embedded in immersion oil between two cover glasses with a diameter of 15 mm and observed

with a DMRX optical microscope (Leica, Wetzlar, Germany) in transmission mode using crossed polarizers. The images were captured with a Motic 2300 CCD camera attached to the microscope.

Scanning electron microscopy (SEM): A Vega 3 SBU SEM (Tescan, Dortmund, Germany) was employed for visualization of the structure of the PLLA/IR3535 mixtures after melt extrusion. Non-pelletized strands with a length of about 10 cm were placed in liquid nitrogen, kept there for 15 min, and subsequently cryo-fractured using a plier. The sample cross-sections were gold coated before measurements. The instrument was operated in the high vacuum mode, a tungsten cathode filament was used as an electron gun, and an acceleration voltage of 10 kV was applied.

Differential scanning calorimetry (DSC): DSC was employed to analyze the thermal behavior of PLLA/IR3535 mixtures after melt extrusion. Measurements were performed using a calibrated heat flux DSC 1 (Mettler-Toledo, Greifensee, Switzerland) equipped with an FRS5 sensor. The device was connected to a TC100 intracooler (Huber, Offenburg, Germany), to allow cooling at rates up to 30 K/min. The furnace was purged with nitrogen gas at a flow rate of 60 mL/min. Samples with a mass between 8 and 12 mg were placed into 40 μL aluminum pans with a pin and covered with a lid. Further information regarding thermal profiles is provided below.

Dynamic mechanical analysis (DMA): DMA was performed using an Anton Paar MCR 501 instrument equipped with a CDT600 oven and SRF5 clamps. For non-isothermal tests, rectangular bars with a dimension of $80 \times 10 \times 4$ mm^3 were tested at a frequency of 1 Hz in shear mode, using a 2 K/min temperature ramp from -40 to 140 °C. For measurements of the elastic modulus of extrudates at room temperature, the tensile mode was applied. The rectangular bars for DMA measurements were obtained from the extrudates after reprocessing by injection molding using an IM 12 micro-injector (Xplore, Sittard, The Netherlands) in combination with a MC 15 twin-screw micro-compounder (Xplore, Sittard, The Netherlands). The reprocessing melt temperature and number of revolutions of the screw were between 180 and 210 °C and 50 rpm, respectively. The mold/cavity temperature was room temperature. To assure that reprocessing did not cause evaporation of the repellent, its content was redetermined by TGA using the same test method as described above.

Tensile testing: Uniaxial tensile stress–strain tests according to the standard DIN EN ISO 527-2 [47] were performed on a Zwick/Roell Z020 instrument (ZwickRoell GmbH & Co. KG, Ulm, Germany) at 25 °C at a strain rate of 5 mm/min. The humidity during testing was 45.9%. Dumbbell-shaped specimens with a length of 40 mm, width of 5.0 mm, and thickness of 2 mm were used, and were obtained by reprocessing via injection molding, as described above. In this case, the repellent content in the mixtures after reprocessing was redetermined by TGA.

Fourier transform infrared (FTIR) spectroscopy: FTIR spectra were recorded on a Nicolet iN50 spectrometer/microscope (Thermo Scientific, Waltham, MA, USA) in reflection mode. Background-corrected spectra were measured at a resolution of 2 cm^{-1} in the wavenumber range of 4000 to 600 cm^{-1}, averaging 64 scans. Thin sections of extrudates, cut perpendicular to the extrusion direction, with a thickness of 15 μm, were used for measurements, and the frame size of the microscope window was 300×300 μm^2.

Small-angle and wide-angle X-ray scattering (SAXS and WAXS): X-ray scattering experiments were performed using a Retro-F laboratory setup (SAXSLAB, Massachusetts, USA), equipped with a microfocus X-ray source (AXO Dresden GmbH, Dresden, Germany) and ASTIX multilayer X-ray optics (AXO Dresden GmbH, Dresden, Germany) as the monochromator for CuKα radiation (λ = 0.154 nm), to obtain information about the presence of PLLA crystals and their polymorphic structure, formed after extrusion/additional annealing at 60 °C. The instrument was operated in transmission mode, and, as a sample holder, aluminum discs with a central hole of 2 mm in diameter were used. Measurements were recorded in vacuum using a PILATUS3 R 300 K detector (Dectris Ltd., Baden-Daettwil, Switzerland). The sample-to-detector distance was calibrated using silver behenate, and

measurement times of 300 and 900 s were used for WAXS and SAXS analyses, respectively. The thickness of the cross-section of the extrudates used for the X-ray analyses was about 2 mm, and the beam diameter was 0.25 mm.

3. Results and Discussion

3.1. Repellent Content of Extrudates

The content of IR3535 in the various PLLA/IR3535 mixtures after melt extrusion was evaluated using TGA at a heating rate of 5 K/min and employing samples with an initial mass of around 7 mg. Note that the temperature of mass losses in TGA depends on the heating rate as well as the sample mass [41,44,48,49], with the rather low selected values minimizing thermal lag and increasing the resolution. The left and right plot of Figure 1 show the original TGA curves, percentage mass as a function of temperature, and their first derivative, respectively.
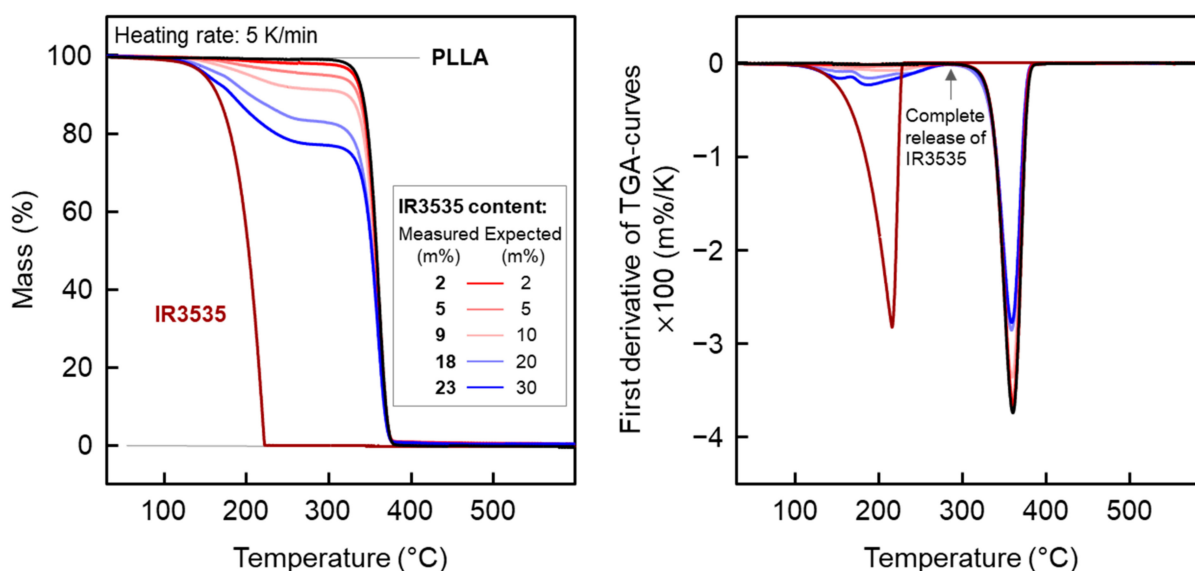

Figure 1. TGA heating curves normalized by the initial mass (**left**) and first derivative of the TGA curves (**right**) of IR3535 and PLLA/IR3535 extrudates, upon heating at 5 K/min in a nitrogen atmosphere. The legend in the left plot provides the measured (**left column**) and expected (**right column**) mass percentage of IR3535 in the extrudates, as derived from the plateau value after evaporation of IR3535. Measurements were performed after storing the strands at room temperature for about 32 weeks after extrusion.

The first low-temperature mass loss event in all samples containing the repellent is due to the evaporation of the repellent IR3535. In the case of neat IR3535 (brown curve), mass loss starts at around 100 °C at the selected conditions, and evaporation is completed at around 230 °C. In PLLA/IR3535 mixtures, the mass loss due to evaporation of IR3535 is slightly delayed/shifted to higher temperature, due to entrapment of the repellent in the polymer matrix, affecting the vapor pressure and diffusion pathways [50–52]. This notwithstanding, when evaporation of IR3535 is completed, for all PLLA/IR3535 mixtures, a nearly constant mass plateau at around 300 °C is observed, allowing an estimation of the actual IR3535 content (see also the vertical arrow in the right plot of Figure 1, confirming zero slope of the TGA curves at around 300 °C). The table in the legend compares the expected IR3535 content, as anticipated with the amount of IR3535 added in the extrusion process (see Table 1), and the content of IR3535 measured by TGA. Considering minor errors in the determination of the effective IR3535 content in the mixtures due to the interplay of the kinetics of evaporation and the heating rate, the observed data suggest that the target

and actual IR3535 concentrations in the extruded strands are very similar, except in the case of the sample with the highest amount on IR3535 (dark blue curve). It is assumed that the observed difference between 30 m% (target) and 23 m% (measured) is caused by minor evaporation of IR3535 during extrusion. In all other cases, obviously, distinct evaporation of the liquid repellent during melt mixing at the chosen extrusion parameters was absent. Further close inspection of the TGA curves reveals a two- or even threefold IR3535 evaporation event in the mixtures with PLLA, which is more easy to recognize in the derivative curves. This does not affect the determination of the actual IR3535 content.

The mass loss event at higher temperature in PLLA/IR3535 mixtures, at around 360 °C, being the minimum in the derivative curve, is caused by decomposition of PLLA, as concluded from the analysis of neat PLLA (black curve) and comparison with literature data [53,54]. The PLLA mass loss in all PLLA/IR3535 mixtures started at the same temperature, being independent of the composition, and suggests that the presence of the liquid repellent has a non-measurable effect on the thermal degradation kinetics of PLLA.

3.2. Morphology and Fracture Behavior of Extrudates

The morphology of neat PLLA and PLLA/IR3535 mixtures after melt extrusion was observed using POM and SEM. The left two images of Figure 2 are POM micrographs of PLLA/IR3535 extrudates containing 0 and 23 m% IR3535, with the images obtained from thin sections taken perpendicular to the extrusion direction of the strands with a diameter of about 2 mm. The micrographs are featureless and indicate the absence of polymer/liquid phase separation at the μm length scale. Though POM alone cannot prove/disprove the presence of crystals [55,56], at least the absence of spherulites, being a typical feature of PLLA melt crystallization at rather low and intermediate supercooling of the melt [57,58], is obvious.
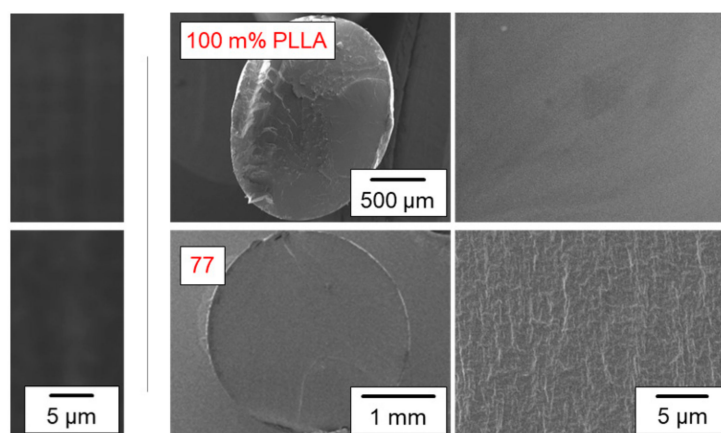

Figure 2. Morphology of extruded strands of neat PLLA (**top** images) and of a PLLA/IR3535 mixture containing 23 m% IR3535 (**bottom**), as observed by POM (**left**) and SEM (**right**), respectively, at different magnifications. The POM images were obtained from the central part of thin sections taken perpendicular to the extrusion direction of the strands with a diameter of about 2 mm, and the SEM images were obtained from cross-sections of cryo-fractured strands coated by gold, providing an overview and details of the structure. The PLLA/IR3535 extrudates for POM and SEM measurements were stored at room temperature for 3 weeks and 7–8 weeks, respectively.

The four images to the right in Figure 2 are SEM micrographs of cross-sectional surfaces of cryo-fractured extruded strands of neat PLLA (top) and of a PLLA/IR3535 mixture containing 23 m% IR3535 (bottom). The two left and right images provide an overview of the cross-section and of details of the structure at higher magnification, respectively. Obviously, the obtained surface of neat PLLA is rather smooth and flat, indicating brittle fracture, while the surface of the PLLA/IR3535 mixture containing 23 m% IR3535 seems

structured, revealing reduced brittleness compared to unmodified PLLA. In addition, a skin–core morphology, which could develop during solidification of the strands in the presence of a temperature gradient when extruding into a water bath [59], as occasionally observed and possibly affecting the repellent release rate, is absent [60–62]. Additionally, in the case of the SEM images, polymer/liquid phase separation and polymer crystallization are not detected. It is worth noting that all samples listed in Table 1 were analyzed by POM and SEM, yielding qualitatively similar results. Summarizing these experiments, (i) macroscopic—at the μm length scale—polymer/repellent phase separation is absent, (ii) spherulitic superstructures related to polymer crystallization are not observed, and (iii) the presence of repellent reduces the tendency for brittle fracture behavior.

3.3. DSC Analysis of Extrudates

The left plot of Figure 3 presents DSC curves of neat PLLA and PLLA/IR3535 extrudates of different composition recorded at a heating rate of 20 K/min. The DSC curve obtained from neat PLLA displays, from low to high temperature, the glass transition at around 60 °C [63], overlapped by an enthalpy recovery peak due to physical aging below T_g [64–66], a cold crystallization peak at about 125 °C, and a melting peak at about 178 °C. Melt crystallization at 125 °C is typically connected with the formation of orthorhombic α-crystals [67–70], which then melt close to 180 °C, as expected for a PLLA grade with only a minor amount of D-isomers in the chain [71,72]. The total enthalpy change observed during heating, which equals the difference between the enthalpy of melting and the enthalpy of cold crystallization, is proportional to the crystal fraction in the sample at the beginning of the heating process in the DSC experiment, and is about zero; that is, the sample is fully amorphous after extrusion into the cold water bath. This observation fits the expectation derived from earlier analyses of the cooling rate dependence of PLLA crystallization [73–75].
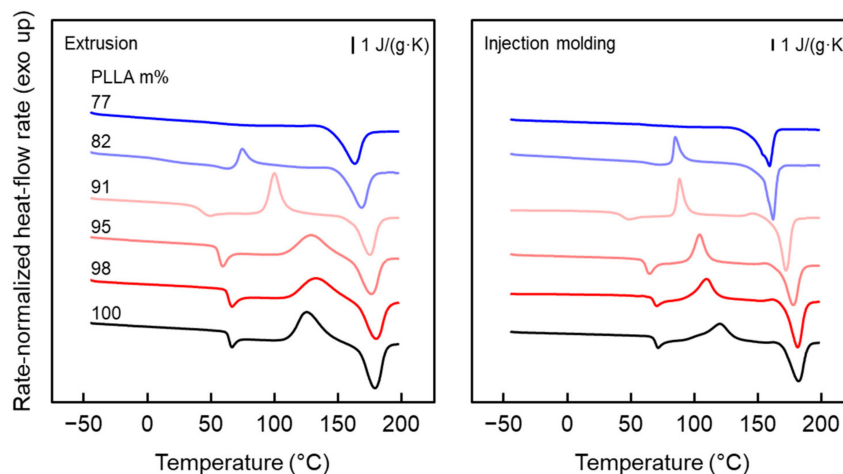

Figure 3. DSC curves: Rate-normalized heat flow rate as a function of temperature for extrudates of neat PLLA and PLLA/IR3535 mixtures (**left**) and injection-molded bars reprocessed from extrudates (**right**) heating at a rate of 20 K/min. Before measurement, samples were stored for 24 days (**left**) and around 4 months (**right**) at room temperature. Note, red and blue color tones are used to indicate glass transition temperatures above and below room temperature, respectively.

The addition of IR3535 results in a gradual decrease in T_g, which reaches 15.0 °C in the mixture containing 18 m% IR3535, indicating that IR3535 acts as a plasticizer for PLLA. In the case of the extrudate with 23 m% IR3535, the glass transition is not detectable, which may be related to the presence of crystals, reducing the heat capacity step at T_g (see top curve of the left plot of Figure 3). Note, red and blue color tones of DSC curves are used to indicate glass transition temperatures above and below room temperature,

respectively; such color coding is applied whenever possible. In addition, the temperatures of cold crystallization and melting systematically decrease with increasing amounts of IR3535 in the mixtures, though the effect is low if the IR3535 content is less than 5 m%. The lowered PLLA crystallization and melting temperatures in the mixtures is probably caused by the equilibrium melting point depression, according to Flory [76–79], and the lowered glass transition temperature, shifting the temperature range of possible crystallization to lower values [80,81]. More important, from the point of view of obtaining information about the initial structure of the extrudates, is the observation that the area of the cold crystallization peak decreases with increasing IR3535 content in the mixtures, while the area of the melting peak remains unchanged. In other words, crystallization of PLLA at the given extrusion and 24-day room temperature storage conditions is enhanced in the presence of IR3535, presumably due to the lowered T_g, widening the temperature range of possible crystallization and increasing the mobility of molecular segments. In the case of the sample that contains 23 m% IR3535, cold crystallization is completely absent, indicating that a high degree of crystallinity was already achieved before the DSC analysis. The right plot of Figure 3 shows similar results for injection-molded bars reprocessed from extrudates stored for around 4 months at room temperature, which were used for mechanical tests.

Quantitative data regarding the glass transition temperature and the PLLA-content-normalized enthalpy change during heating (enthalpy of melting + enthalpy of cold crystallization) are shown in the left and right plots of Figure 4, respectively, as a function of the PLLA content. The different colors/symbols represent data obtained from samples analyzed after storing/annealing at ambient temperature for about 1 month (black/gray squares) (see also the DSC scans of Figure 3), for 6 months (red/gray circles), and for 1 year (blue/gray triangles). In addition, green/gray downward triangles are data obtained from additionally reprocessed/injection-molded samples of neat PLLA and PLLA/IR3535 mixtures stored for 4 months at ambient temperature, which were used for tensile/DMA testing.
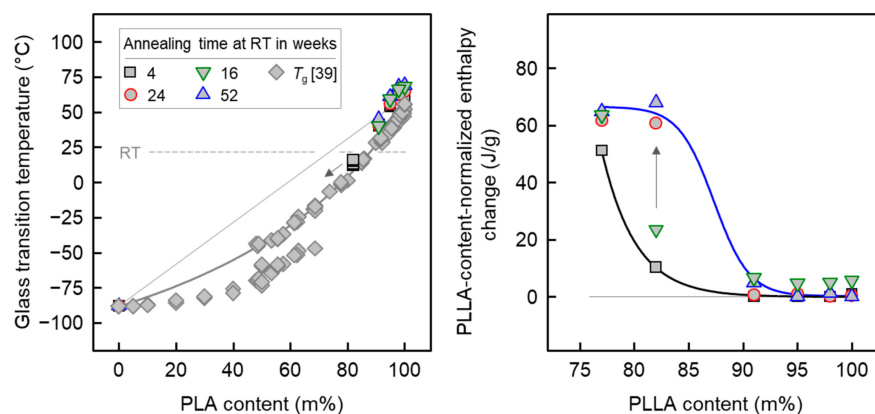

Figure 4. Glass transition temperature (**left**) and change in the enthalpy, normalized to the polymer content, during heating (**right**) of PLLA/IR3535 extrudates as a function of the polymer concentration, as derived from DSC data, exemplarily shown with Figure 3. The different colors/symbols represent data obtained from samples after storing at room temperature for different time, as indicated in the legend. For comparison, the left plot contains additional T_g-data obtained from a system composed of non-crystallizable poly (lactic acid) (PLA) and IR3535, including a fit using the Gordon-Taylor equation, adapted from Polymer, 209, Fanfan Du, Christoph Schick, René Androsch, Full-composition-range glass transition behavior of the polymer/solvent system poly (lactic acid)/ethyl butylacetylaminopropionate (PLA/IR3535®), 123058, Copyright (2020), with permission from Elsevier [39]. Green/gray downward triangles are data obtained from reprocessed (by injection molding) and subsequently for 4 months stored samples of neat PLLA and PLLA/IR3535 mixtures, later on used for tensile/DMA testing.

Regarding glass transition (left plot of Figure 4), it is observed that presence of IR3535 in mixtures with PLLA leads to a decrease in T_g, pointing to miscibility at the length scale that is examined with the glass transition, that is, several nanometers [82,83]. Important in the context of later discussion of the crystallization behavior is the observation that the T_g of mixtures containing more than about 15–20 m% IR3535 is below room temperature (21 °C), which is indicated with the horizontal dashed gray line. For a more complete picture of the miscibility of PLLA and IR3535, the left plot of Figure 4 also contains data observed in earlier work (see diamond symbols), collected over the entire concentration range using a special experimental approach of successive evaporation of repellent and repeated T_g analysis, and additional T_g analyses of solvent-rich compositions, including neat IR3535 [39]. Though a different poly (lactic acid) (PLA) grade was used in that study—containing 50% D-isomers—the miscibility, obviously, is similar to the case of the highly stereoregular PLLA used here. Inspection of data for samples stored for different time periods before the DSC analyses reveals a negligible effect if the concentration of IR3535 is equal or lower than 9 m%. However, for the sample containing 18 m% IR3535, the glass transition became undetectable by DSC after long-term annealing at room temperature, which is likely caused by slow crystallization of PLLA. Since IR3535 cannot be included in the PLLA crystal phase, the amorphous phase probably enriches IR3535, shifting T_g further down to lower temperature (see arrow).

For samples containing less than 9 m% IR3535, the crystallinity is zero, and does not depend on the annealing time at room temperature. In contrast, for samples containing 9 m% IR3535, or more, a distinct effect of the storing time is seen, such that the crystallinity increases with time (right plot of Figure 4, see black arrow). Furthermore, the data allow to conclude that crystallization proceeds faster if the repellent content is higher. While the crystallinity-increase within 1 year of storing the extrudate at ambient temperature is marginal for the sample containing 9 m% IR3535, in the case of the sample containing 23 m% repellent, the maximum possible crystallinity, as indicated with the plateau, is already achieved after short-term annealing for about 1 month. With the knowledge of the bulk enthalpy of melting of PLLA α-crystals [84], and its temperature dependence [85], of close to 100 J/g for crystals melting slightly below 180 °C (see Figure 3), a PLLA crystallinity of almost 70% can be achieved.

3.4. Thermal Stability of Extrudates

The thermal stability of IR3535 after extrusion was confirmed by FTIR measurements, as presented with the left plot in Figure 5. For neat IR3535, the strongest bands of the spectra are located at 1736 cm^{-1} and 1651 cm^{-1} assigned to the carbonyl stretch vibrations of the ester and amide groups, respectively. The band associated to the IR3535 amide group is well-separated from the PLLA bands, allowing identification of IR3535 in the spectra obtained from PLLA/IR3535 extrudates. As expected, in the PLLA/IR3535 mixtures, the intensities of these bands increase with the IR3535 content. More important, when comparing the spectra of extruded mixtures with the spectrum obtained from neat IR3535, there is no shift of the characteristic bands observed, indicating that the repellent was able to withstand the thermomechanical history during processing. Independent studies of the thermal stability of IR3535, available in the literature [35,44], in contrast, suggested slight oxidative degradation by observation of a new band near 1690 cm^{-1} when exposed to air for four months at 50 °C. Here, in our study, new carbonyl bands are not observed.

The right plot of Figure 5 shows details of the FTIR spectra in the wavenumber range between 890 and 970 cm^{-1}, which allows one to obtain information about the possible presence of ordered PLLA structures. As such, PLLA/IR3535 extrudates with 82 and 77 m% PLLA show an additional band at 922 cm^{-1} (see dashed line) that is assigned to PLLA crystals (see right plot) [86–89]. This band is not detected for other extrudates of lower repellent content, and indicates the absence of crystals after storing these samples at room temperature for 6 months. These results are consistent with DSC data shown above.
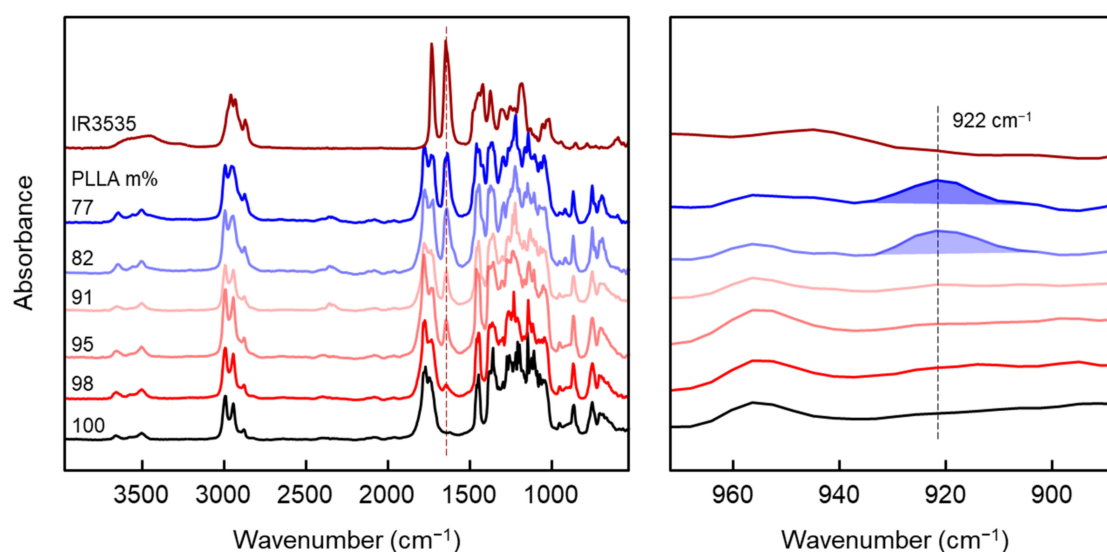
Figure 5. FTIR spectra of PLLA/IR3535 extrudates stored at room temperature for 6 months (**left**). The **right** plot shows details in the wavenumber range of 890 to 970 cm^{-1}.

3.5. WAXS and SAXS Analysis

X-ray scattering was used to assess the structure of extrudates, including the crystallinity and crystal structure of PLLA. The left plot of Figure 6 shows WAXS curves of extrudates of PLLA containing different amounts of IR3535, stored at room temperature for about 9 months (bold curves), and of samples stored at room temperature for 17 days and additionally annealed for 3–4 weeks at 60 °C after extrusion (thin curves; labelled 'x-ann', with x representing the PLLA content). The initial purpose of annealing the extrudates at 60 °C was to remove the repellent, followed by observation of the morphology in order to trace the location of the repellent. However, by chance, it was found that the samples changed their appearance from clear to turbid, except in the case of neat PLLA and the extrudate with 77 m% PLLA. With the suspicion that turbidity was caused by crystallization, these samples were also investigated by X-ray scattering. Note that annealing at 60 °C was performed until the mass of the samples was constant.

The WAXS patterns of non-annealed, neat PLLA and extrudates containing less than 18 m% IR3535 display a broad amorphous halo, which confirms the lack of crystals, as was also concluded from the DSC analysis (see Figure 4, right). However, for samples annealed at 60 °C, distinct scattering peaks are observed, except for neat PLLA, which only shows a single small peak (see arrow).

Long-term annealing of the extrudates at 60 °C shows a major effect on the structure of the samples containing 5 and 9 m% IR3535 (red and light red curves, respectively). In these two cases, non-annealed samples displayed only an amorphous halo, while after annealing intense scattering peaks are detected, proving the formation of crystals during the annealing step.

Inspection of the sets of peaks detected, we assume that α-crystals are the predominant crystal form. This assumption is mainly based on scattering peaks measured at scattering angles slightly higher than 12 and 22 deg 2θ [69,90,91]. This observation was not expected since in the case of neat PLLA low-temperature crystallization typically yields disordered α'-crystals. Obviously, the presence of the dissolved liquid repellent supports the formation of the more ordered α-crystal form; similar results have been observed for solution-crystallized PLLA, regardless the crystallization temperature [28,40,92]. These results are consistent with DSC heating curves (not shown) obtained from annealed samples, which did not display the typical exothermic α'- to α-crystal transformation peak [93], except in the case of the sample containing 2 m% IR3535.
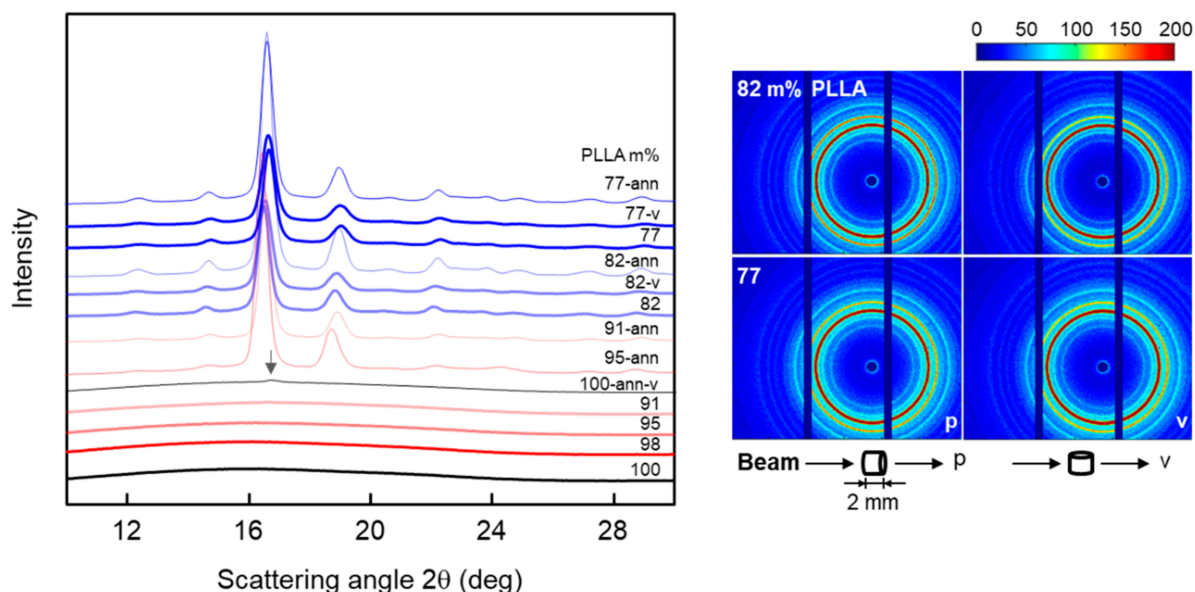
Figure 6. 1D (**left**) and 2D WAXS patterns (**right**) of PLLA/IR3535 extrudates stored at room temperature for about 9 months (bold curves), and 1D WAXS patterns of extrudates stored at room temperature for 17 days and additionally annealed at 60 °C for 3–4 weeks (thin curves), with the latter labeled 'x-ann' and with x indicating the polymer content in mixture. The cylindrical samples with a diameter of about 2 mm and a length of 2 mm were measured in two directions, with the beam parallel (p) and vertical (v) to the extrusion direction, marked 'p' and 'v' in the 2D scattering pattern (**right**).

Regarding the PLLA/IR3535 extrudates with 82 and 77 m% PLLA, the cylindrical samples with a diameter of about 2 mm and a length of 2 mm were measured in two directions, with the beam parallel (p) and vertically (v) oriented with respect to the extrusion direction, marked 'p' and 'v' in the 2D WAXS scattering patterns (right plot of Figure 6), respectively. The results indicate that crystals in the PLLA/IR3535 extrudates do not show preferred orientation.

The left plot of Figure 7 shows Lorentz-corrected SAXS curves of PLLA/IR3535 extrudates stored at room temperature for about 9 months (bold curves) and after additional annealing at 60 °C for 3–4 weeks (thin curves), respectively. The curves were evaluated by calculating the interface distribution function [94,95], revealing information about the long period (*LP*), and the thickness of lamellae (d_c) and of the amorphous layer (d_a), presented as a function of the sample composition with the right plot in Figure 7. Except for neat PLLA, all curves in the left plot show a distinct long-period maximum, which corresponds to a distance of about 16 nm, and indicating formation of stacks of lamellae. It appears that the presence of IR3535 enhances the formation of lamellar stacks since the intensity of the long-period maximum increases with its content; in the case of the cold-crystallized, annealed samples containing 9 and 18 m% IR3535, even higher-order long-period maxima are observed. Inspection of the position of the long-period maximum reveals an only minor effect of the sample composition: *LP* decreases from 17 nm in PLLA containing 5 m% IR3535 to around 15 nm in the case of the sample containing 23 m% IR3535. Similarly, the thickness of lamellae decreases from around 14 nm to 11 nm, respectively, while the amorphous layer thickness is only 3 nm, being almost independent of the IR3535 content. Calculation of the linear crystallinity ($d_c/(d_a + d_c) \times 100\%$) [96,97], then yields values of around 80% for all samples containing between 5 and 18 m% IR3535. This value confirms a recent study about the SAXS crystallinity of PLLA [84].
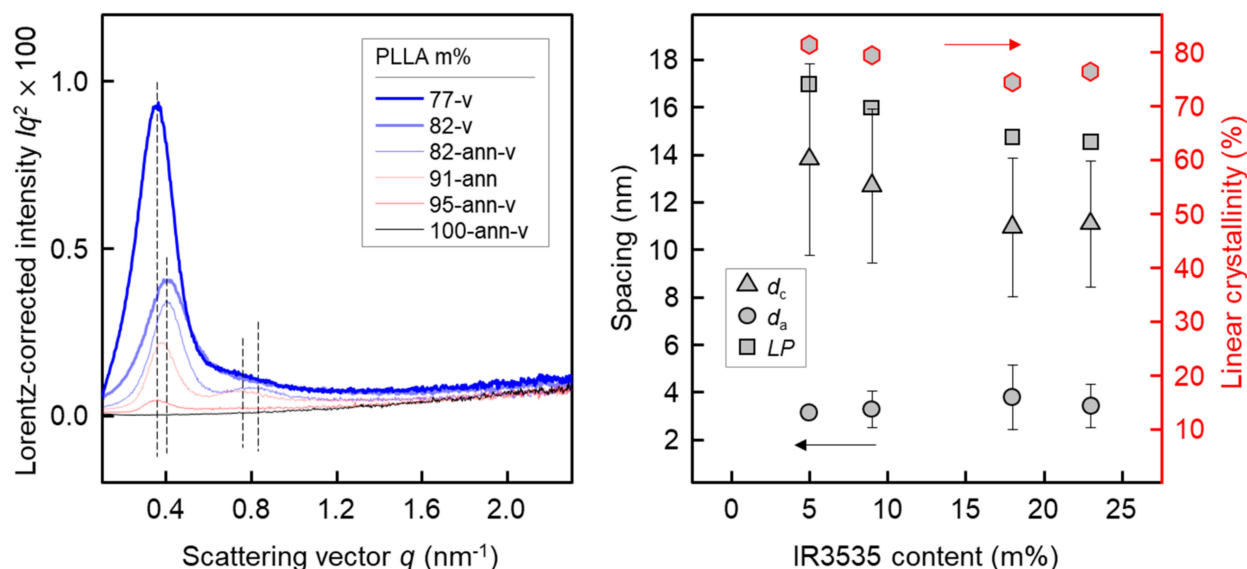
Figure 7. Lorentz-corrected SAXS curves of PLLA/IR3535 extrudates of different composition as indicated in the legend, stored at room temperature for about 9 months and annealed at 60 °C for 3–4 weeks, respectively (**left**). Long period (LP), and thickness of lamellae (d_c) and amorphous regions in lamellar stacks (d_a) as a function of the concentration of IR3535 in annealed PLLA/IR3535 extrudates (**right**). The red symbols represent the linear crystallinity (right axis). The bars represent the distribution of d_c and d_a.

3.6. POM Analysis of Annealed PLLA/IR3535 Extrudates

Figure 8 shows POM images of PLLA/IR3535 extrudates with a maximum content of IR3535 of 9 m%, annealed at 60 °C for 3–4 weeks. Preparation of thin sections of samples containing higher amounts of IR3535 was complicated due to their low glass transition temperature (see Figure 4, left), being below RT; the images are therefore not shown. Upper and lower images in Figure 8 were observed at different magnification, as indicated with the scale bars; the upper images, in fact, provide an overview of the cross-section of the pellets. WAXS data of neat PLLA suggested a fully amorphous state, and as such the images are featureless and black when observed with the sample located between crossed polarizers. In the case of samples containing IR3535, crystallization occurred, and the POM micrographs show numerous white spots due to birefringence related to the presence of crystals. Such morphology is probably related to the nucleation pathway [55,56,98,99]. Fast cooling, followed by long-term annealing near T_g, causes the generation of a large number of homogeneous nuclei, which then, upon reheating, grow to crystals, with similar morphologies also reported for PLLA in the literature [73,89]. Due to the high nuclei number, growth of large superstructures, such as spherulites, is then not possible, causing the observed spotty structure. A distinct and systematic effect of the repellent concentration, however, is not observed. Note that we do not assume that the white spots are single crystals, rather that we consider them as aggregates of lamellae/lamellar stacks.

3.7. Mechanical Properties of PLLA/IR3535 Extrudates

In order to finalize the material for an engineering product or industrial application, mechanical properties are a very important consideration. Figure 9 shows the elastic modulus of injection-molded bars, reprocessed from extrudates, at room temperature evaluated by tensile stress–strain testing and DMA in tensile mode, respectively. The data of both tests are consistent and reveal a constant elastic modulus for PLLA/IR3535 extrudates containing between 2 and 9 m% IR3535, a strong decrease in the IR3535 concentration range of 9 to 18 m%, and then constancy when increasing the IR3535 content to 23 m%.

The obtained modulus of neat PLLA and for mixtures with low amounts of IR3535 agrees with values available in the literature, being slightly higher than 3 GPa [100,101], indicative of presence of a glassy amorphous phase. The dropdown of the modulus of elasticity at repellent concentrations higher than 5 m% is caused by the change in T_g to near or even below the measurement temperature of around 22 °C (see also Figure 4, left) and the transition of the PLLA glass into the rubbery state, regardless the presence of crystals.
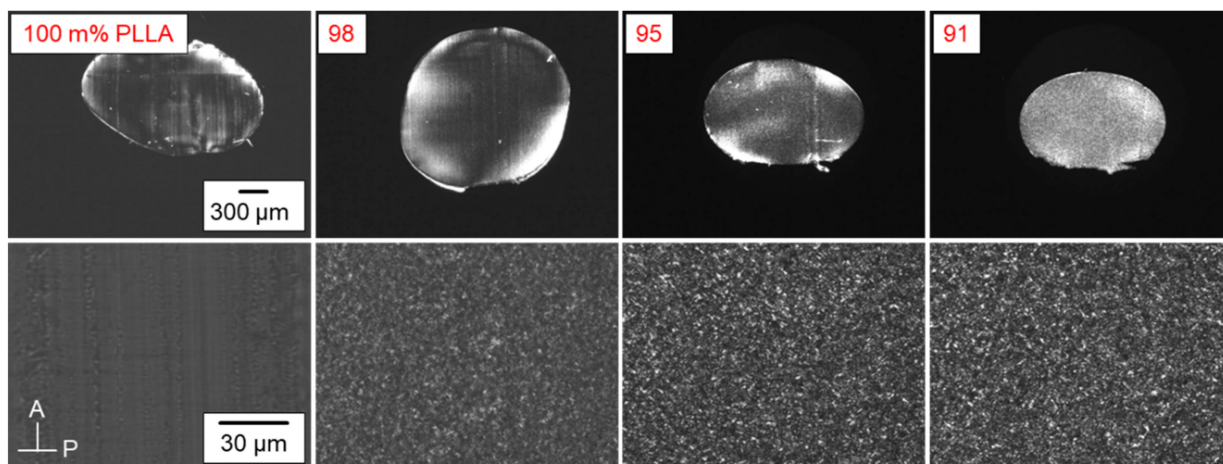

Figure 8. POM images of PLLA/IR3535 extrudates stored at room temperature for 17 days and then annealed at 60 °C for 3–4 weeks.
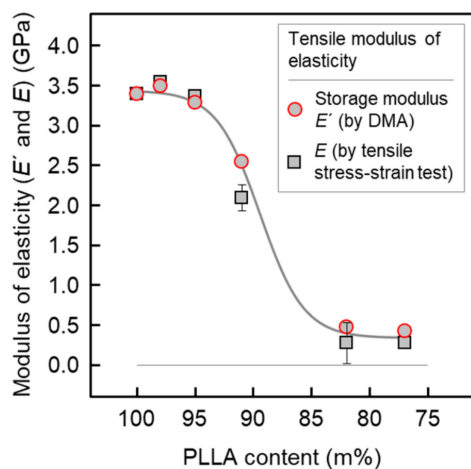

Figure 9. Modulus of elasticity of PLLA/IR3535 of injection-molded bars, reprocessed from extrudates, and measured by tensile stress–strain testing (black squares) and DMA (red circles) at room temperature. The line is drawn to guide the eye.

Figure 10 depicts the loss factor tan-δ (left plot) and shear modulus (right plot) as a function of temperature, respectively, estimated by DMA using a 2 K/min temperature ramp from −40 °C to 140 °C. In the left plot of Figure 10, the peak temperature in the tan-δ curves is regarded as T_g, confirming the trend obtained by DSC analyses described above. For neat PLLA, T_g is around 65 °C, and then it decreases with increasing IR3535 content, first slightly for repellent concentrations up to 9 m%, and then stronger for higher IR3535 concentrations; for the samples containing 18 and 23 m% IR3535, tan-δ maxima are hardly observed.
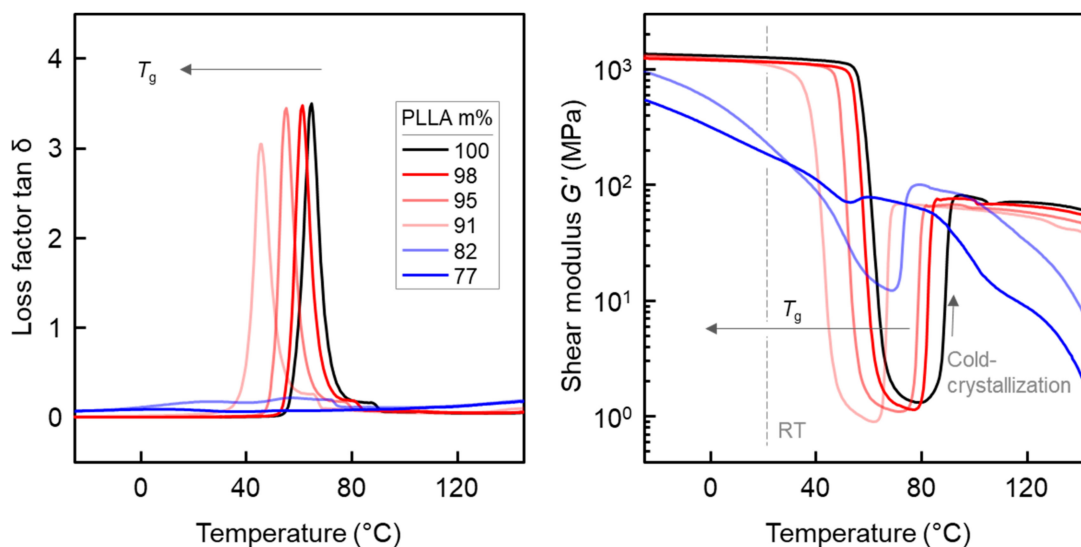
Figure 10. DMA curves, loss factor tan-δ (**left**) and shear modulus G' (**right**) as a function of temperature, respectively, of PLLA/IR3535 extrudates upon heating at 2 K/min.

As presented in the right plot of the Figure 10, at low temperatures, PLLA/IR3535 injection-molded bars, reprocessed from extrudates, with a PLLA content between 91 and 100 m% display a shear modulus G' of about 1.3 GPa (around 1/3 of the tensile modulus presented in the Figure 9) at low temperatures, with slight variations among the different samples. By increasing the temperature, a sudden drop of G', associated with the glass transition of the amorphous phase of PLLA containing IR3535, is detected, with the temperature of the dropdown decreasing with increasing IR3535 content.

Upon further increase in the temperature, at about 80 °C for neat PLLA and lower temperatures for samples with less than 23 m% IR3535, PLLA chains gain sufficient mobility to allow cold crystallization, resulting in an increase in G', being in general accord with the DSC observations (see the right plot of Figure 3). The minor difference between the temperatures of (kinetically controlled) cold crystallization obtained by DSC and DMA is caused by the different heating rates in these experiments [102,103]. After completion of cold crystallization, the modulus scales with the degree of crystallinity achieved in the various samples, being highest in the case of neat PLLA, since the crystalline phase is much stiffer than the rubbery amorphous phase [104–106]. In terms of the extrudates with 82 and 77 m% PLLA, the shear modulus at all temperatures is much lower than in the other samples, and cold crystallization is less distinct or even completely absent since crystallization almost completed before the DMA experiment (see the right plot of Figure 3).

Summarizing the DMA and tensile tests, liquid IR3535 acts as a plasticizer for PLLA, causing a decrease in T_g and affecting mechanical properties, in particular at temperatures slightly above room temperature. At higher repellent concentration of around 20 m%, a rather strong effect was also observed at ambient temperature (see vertical gray line in the right plot of Figure 10), making the material soft and ductile/non-brittle.

3.8. Repellent Release

For application of PLLA/IR3535 extrudates as repellent release devices, as well as plasticized/ductile material, knowledge regarding the release rate/evaporation characteristics at ambient and body temperature is of major importance. The kinetics of the repellent release from the polymer matrix was investigated by isothermal TGA experiments at temperatures ranging from 50 °C to 100 °C, allowing extrapolation of the release behavior of repellent at room temperature/body temperature. This temperature range is selected

because the repellent release rate is accelerated by increasing the temperature while the sample structure is not damaged/changed.

Figure 11 presents the repellent release of PLLA/IR3535 mixtures initially containing 18 m% IR3535, stored at room temperature for about 10 months, at different release temperatures between 50 and 100 °C. This sample was selected since, on one hand, absence of bleeding before analysis was assured, while on the other hand, the repellent content appears sufficient from the point of view of using it as a repellent delivery device. In terms of the temperature dependence of the repellent release, the IR3535 release rate increases with increasing evaporation temperature. At an evaporation temperature of 100 °C (bottom curve), there is still some IR3535 left even after 24 h. However, at relatively low temperatures of, e.g., 50 °C, only about 14% out of the total initial repellent content evaporated within the analyzed time frame of 24 h, which suggests that the repellent release at temperatures below 50 °C may last many days, and thus, is difficult to measure by TGA. For this reason, we attempted to obtain the experimentally accessible temperature dependence of characteristic release times τ between 50 and 100 °C, and then extrapolated to the temperature of interest. Release time constants τ were determined by fitting the experimental mass loss curves with a single-exponential decay function, allowing their extrapolation and observation of a characteristic release constant τ, in this case the time of reducing the IR3535 mass to $1/e \times 100\%$ of its initial value, that is, the time when sample released 63.2% $((1 - 1/e) \times 100\%)$ of the initial IR3535 content. However, it seems that this approach is not applicable for release experiments performed between 80 and 100 °C, as the obtained TGA curves exhibit a double exponential decrease in the sample mass as a function of time, with a fast initial process followed by a much slower release. This may be caused by a change in the physical structure of the polymer during heating, such as cold crystallization or crystal reorganization, or by a change in intermolecular interactions between the polymer and repellent. As such, a single exponential decay function was used to fit the data obtained at temperatures between 50 and 70 °C [107], while for the experiment performed at 100 °C, the time at which 63.2% of the initial repellent evaporated was directly read from the measured TGA curve. For measurements performed at 80 and 90 °C, even after 24 h, the release was less than 63.2% of the initial repellent content; therefore, the release time constants were not determined.
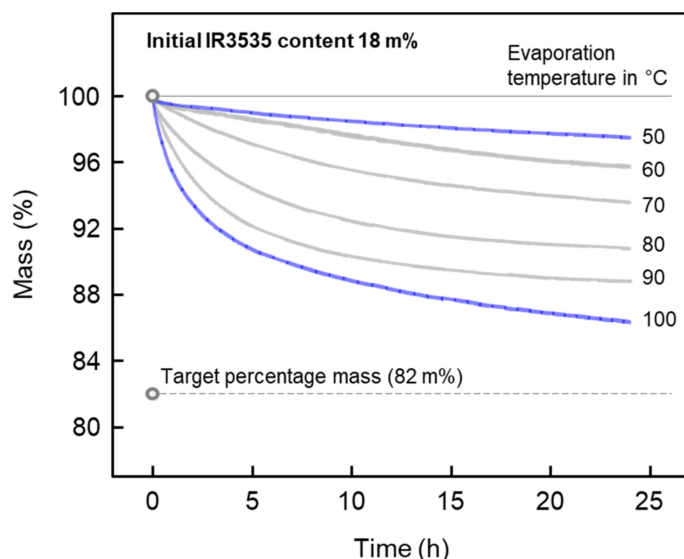

Figure 11. Percentage mass of a PLLA/IR3535 extrudate initially containing 18 m% IR3535 as a function of time during annealing at temperatures between 50 and 100 °C.

The left plot of Figure 12 shows characteristic repellent release time constants τ of the PLLA/IR3535 extrudate initially containing 18 m% IR3535 as a function of the release temperature. The data suggest a non-linear increase in the characteristic evaporation time with decreasing temperature, being few hours at 100 °C and more than 100 days at 50 °C. Apparently, there is observed an exponential temperature dependence of time constants, pointing to an Arrhenius-type change in diffusion rate constants with temperature. Quantitative information regarding the release kinetics is obtained by plotting the logarithm of the inverse characteristic time, log (1/τ), as a function of the inverse release temperature, 1/T, as shown in the right plot of Figure 12. There is a linear dependence of data observed, suggesting characteristic repellent release times of 1.4 and 5.0 years at body temperature (37 °C) and room temperature (21 °C).
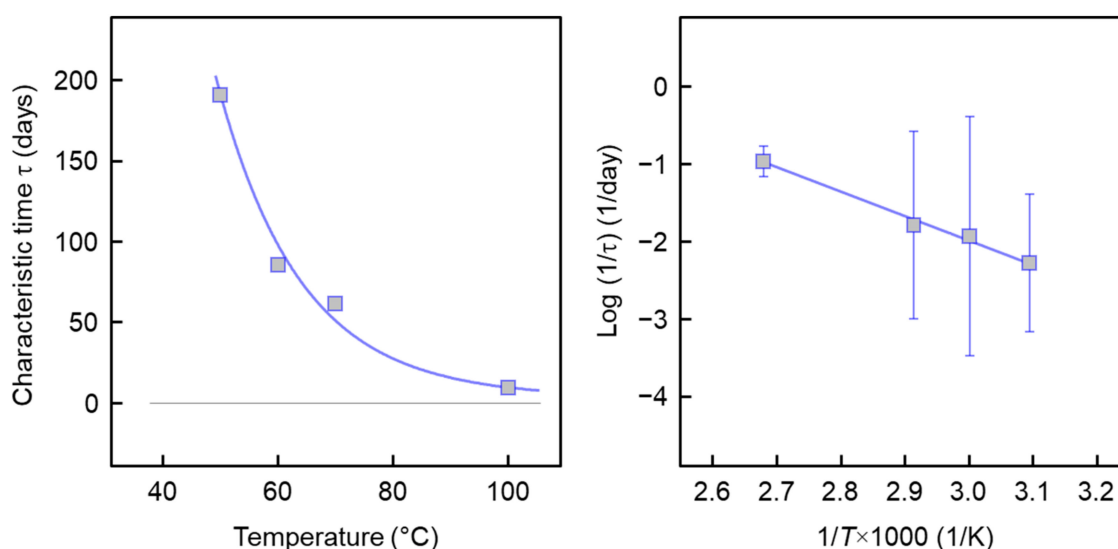

Figure 12. Characteristic repellent release time of strands with a diameter of about 2 mm of PLLA/IR3535 extrudates initially containing 18 m% IR3535 as a function of temperature (**left**), and logarithm of the inverse of the characteristic time, log (1/τ), as a function of inverse release temperature (1/T) (**right**). Each data point represents the average of two measurements; the error bars are smaller than the size of the symbols, and are therefore not shown.

4. Conclusions

The present work is a continuation of our research efforts to contribute to the development of wearable insect repellent delivery devices, by incorporating liquid insect repellents into biosourced and biodegradable polymers, for slow subsequent release into the environment. With the focus on the polymer/repellent system composed of poly (L-lactic acid) (PLLA) and ethyl butylacetylaminopropionate (IR3535), PLLA/IR3535 mixtures at various compositions were prepared via melt extrusion technology, with the advantage of cost-efficient large-scale processing.

In the analyzed composition range of 2 to 23 m% IR3535, PLLA and IR3535 are miscible. Liquid IR3535 acts as a plasticizer for PLLA, causing a decrease in T_g and affecting the morphology, crystallization, and mechanical properties of the host polymer. PLLA/IR3535 extrudates containing between 2 and 9 m% IR3535 are amorphous, even after storing at room temperature for around 1 year after extrusion, while PLLA/IR3535 extrudates with 18 and 23 m% IR3535 showed an increase in the crystallinity over time, due to the low glass transition temperature. Despite the increase in the crystallinity, however, the presence of IR3535 softens PLLA and decreases its elastic modulus.

Furthermore, with the slow release of the repellent to the environment over a period of months or years, it is expected that the initial decrease in the glass transition temperature

reverts. Both repellent-induced crystallization and evaporation of the repellent are expected to cause embrittlement, thus being disadvantageous regarding mechanical properties. On the other hand, the slow release of the repellent offers the opportunity to use extrudates as delivery devices, if engineered such that the mechanical performance is not important.

References

1. Teo, A.J.T.; Mishra, A.; Park, I.; Kim, Y.J.; Park, W.T.; Yoon, Y.J. Polymeric biomaterials for medical implants and devices. *ACS Biomater. Sci. Eng.* **2016**, *2*, 454–472. [CrossRef] [PubMed]
2. Becker, M.L.; Burdick, J.A. Introduction: Polymeric biomaterials. *Chem. Rev.* **2021**, *121*, 10789–10791. [CrossRef]
3. Uhrich, K.E.; Cannizzaro, S.M.; Langer, R.S.; Shakesheff, K.M. Polymeric systems for controlled drug release. *Chem. Rev.* **1999**, *99*, 3181–3198. [CrossRef] [PubMed]
4. Calori, I.R.; Braga, G.; de Jesus, P.d.C.C.; Bi, H.; Tedesco, A.C. Polymer scaffolds as drug delivery systems. *Eur. Polym. J.* **2020**, *129*, 109621. [CrossRef]
5. Shamsuddin, I.M.; Jafar, J.A.; Shawai, A.S.A.; Yusuf, S.; Lateefah, M.; Aminu, I. Bioplastics as better alternative to petroplastics and their role in national sustainability: A review. *Adv. Biosci. Bioeng.* **2017**, *5*, 63–70. [CrossRef]
6. Srivastava, A.; Srivasatva, A.K.; Singh, A.; Singh, P.; Verma, S.; Vats, M.; Sagadevan, S. Biopolymers as renewable polymeric materials for sustainable development—An overview. *Polimery* **2022**, *67*, 185–196. [CrossRef]
7. Armentano, I.; Bitinis, N.; Fortunati, E.; Mattioli, S.; Rescignano, N.; Verdejo, R.; Lopez-Manchado, M.A.; Kenny, J.M. Multifunctional nanostructured PLA materials for packaging and tissue engineering. *Prog. Polym. Sci.* **2013**, *38*, 1720–1747. [CrossRef]
8. Faizan, M.; Nadeem, H.; Arif, A.; Zaheer, W. Bioplastics from biopolymers: An eco-friendly and sustainable solution of plastic pollution. *Polym. Sci. Ser. C* **2021**, *63*, 47–63. [CrossRef]
9. Saeidlou, S.; Huneault, M.A.; Li, H.B.; Park, C.B. Poly(lactic acid) crystallization. *Prog. Polym. Sci.* **2012**, *37*, 1657–1677. [CrossRef]
10. Di Lorenzo, M.L.; Androsch, R. *Synthesis, Structure and Properties of Poly (Lactic Acid)*; Springer: Cham, Switzerland, 2018; Volume 279.
11. Di Lorenzo, M.L.; Androsch, R. *Industrial Applications of Poly(Lactic Acid)*; Springer: Cham, Switzerland, 2018; Volume 282.
12. Lim, L.T.; Auras, R.; Rubino, M. Processing technologies for poly(lactic acid). *Prog. Polym. Sci.* **2008**, *33*, 820–852. [CrossRef]
13. Capuana, E.; Lopresti, F.; Ceraulo, M.; La Carrubba, V. Poly-L-lactic acid (PLLA)-based biomaterials for regenerative medicine: A review on processing and applications. *Polymers* **2022**, *14*, 1153. [CrossRef] [PubMed]
14. Rasal, R.M.; Janorkar, A.V.; Hirt, D.E. Poly(lactic acid) modifications. *Prog. Polym. Sci.* **2010**, *35*, 338–356. [CrossRef]
15. Liu, H.; Zhang, J. Research progress in toughening modification of poly(lactic acid). *J. Polym. Sci. Part B Polym. Phys.* **2011**, *49*, 1051–1083. [CrossRef]
16. Jamshidian, M.; Tehrany, E.A.; Imran, M.; Jacquot, M.; Desobry, S. Poly-lactic acid: Production, applications, nanocomposites, and release studies. *Compr. Rev. Food Sci. Food Saf.* **2010**, *9*, 552–571. [CrossRef]
17. Martin, O.; Averous, L. Poly(lactic acid): Plasticization and properties of biodegradable multiphase systems. *Polymer* **2001**, *42*, 6209–6219. [CrossRef]
18. Hu, Y.; Hu, Y.S.; Topolkaraev, V.; Hiltner, A.; Baer, E. Aging of poly(lactide)/poly(ethylene glycol) blends. Part 2. Poly(lactide) with high stereoregularity. *Polymer* **2003**, *44*, 5711–5720. [CrossRef]

19. Kulinski, Z.; Piorkowska, E.; Gadzinowska, K.; Stasiak, M. Plasticization of poly(L-lactide) with poly(propylene glycol). *Biomacro-molecules* **2006**, *7*, 2128–2135. [CrossRef]

20. Li, H.; Huneault, M.A. Effect of nucleation and plasticization on the crystallization of poly(lactic acid). *Polymer* **2007**, *48*, 6855–6866. [CrossRef]

21. Ge, H.; Yang, F.; Hao, Y.; Wu, G.; Zhang, H.; Dong, L. Thermal, mechanical, and rheological properties of plasticized poly(L-lactic acid). *J. Appl. Polym. Sci.* **2013**, *127*, 2832–2839. [CrossRef]

22. Avolio, R.; Castaldo, R.; Gentile, G.; Ambrogi, V.; Fiori, S.; Avella, M.; Cocca, M.; Errico, M.E. Plasticization of poly(lactic acid) through blending with oligomers of lactic acid: Effect of the physical aging on properties. *Eur. Polym. J.* **2015**, *66*, 533–542. [CrossRef]

23. Dobrzynska-Mizera, M.; Knitter, M.; Mallardo, S.; Del Barone, M.C.; Santagata, G.; Di Lorenzo, M.L. Thermal and thermo-mechanical properties of poly(L-lactic Acid) biocomposites containing beta-cyclodextrin/D-limonene inclusion complex. *Materials* **2021**, *14*, 2569. [CrossRef] [PubMed]

24. Di Lorenzo, M.L.; Longo, A. *N*,*N*-Diethyl-3-methylbenzamide (DEET): A mosquito repellent as functional plasticizer for poly(L-lactic acid). *Thermochim. Acta* **2019**, *677*, 180–185. [CrossRef]

25. Aliotta, L.; Vannozzi, A.; Panariello, L.; Gigante, V.; Coltelli, M.B.; Lazzeri, A. Sustainable micro and nano additives for controlling the migration of a biobased plasticizer from pla-based flexible films. *Polymers* **2020**, *12*, 1336. [CrossRef] [PubMed]

26. Bohbot, J.D.; Strickman, D.; Zwiebel, L.J. The future of insect repellent discovery and development. *Outlooks Pest Manag.* **2014**, *25*, 265–270. [CrossRef]

27. Tavares, M.; da Silva, M.R.M.; de Oliveira de Siqueira, L.B.; Rodrigues, R.A.S.; Bodjolle-d'Almeida, L.; dos Santos, E.P.; Ricci-Júnior, E. Trends in insect repellent formulations: A review. *Int. J. Pharm.* **2018**, *539*, 190–209. [CrossRef]

28. Sungkapreecha, C.; Iqbal, N.; Gohn, A.M.; Focke, W.W.; Androsch, R. Phase behavior of the polymer/drug system PLA/DEET. *Polymer* **2017**, *126*, 116–125. [CrossRef]

29. Sungkapreecha, C.; Beily, M.J.; Kressler, J.; Focke, W.W.; Androsch, R. Phase behavior of the polymer/drug system PLA/DEET: Effect of PLA molar mass on subambient liquid-liquid phase separation. *Thermochim. Acta* **2018**, *660*, 77–81. [CrossRef]

30. Sungkapreecha, C.; Iqbal, N.; Focke, W.W.; Androsch, R. Crystallization of poly (L-lactic acid) in solution with the mosquito-repellent N, N-diethyl-3-methylbenzamide. *Polym. Cryst.* **2019**, *2*, e10029. [CrossRef]

31. Sungkapreecha, C.; Focke, W.W.; Androsch, R. Competition between liquid-liquid de-mixing, crystallization, and glass transition in solutions of PLA of different stereochemistry and DEET. *Chin. J. Polym. Sci.* **2020**, *38*, 174–178. [CrossRef]

32. Bonadies, I.; Longo, A.; Androsch, R.; Jehnichen, D.; Göbel, M.; Di Lorenzo, M.L. Biodegradable electrospun PLLA fibers containing the mosquito-repellent DEET. *Eur. Polym. J.* **2019**, *113*, 377–384. [CrossRef]

33. Ferreira, I.; Brünig, H.; Focke, W.; Boldt, R.; Androsch, R.; Leuteritz, A. Melt-spun poly (D,L-lactic acid) monofilaments containing N, N-diethyl-3-methylbenzamide as mosquito repellent. *Materials* **2021**, *14*, 638. [CrossRef] [PubMed]

34. Izadi, H.; Focke, W.W.; Asaadi, E.; Maharaj, R.; Pretorius, J.; Loots, M.T. A promising azeotrope-like mosquito repellent blend. *Sci. Rep.* **2017**, *7*, 10273. [CrossRef]

35. Mapossa, A.B.; Sitoe, A.; Focke, W.W.; Izadi, H.; Du Toit, E.L.; Androsch, R.; Sungkapreecha, C.; Van Der Merwe, E.M. Mosquito repellent thermal stability, permeability and air volatility. *Pest Manag. Sci.* **2020**, *76*, 1112–1120. [CrossRef] [PubMed]

36. Butylacetylaminopropionate, E. WHO Specifications and Evaluations for Public Health Pesticides. Available online: https://archive.epa.gov/osa/hsrb/web/pdf/whoir3535evaluationapril2006.pdf (accessed on 16 September 2022).

37. World Health Organization. *World Malaria Report 2021*; World Health Organization: Geneva, Switzerland, 2022.

38. WHO Guidelines for Malaria. Available online: WHO-UCN-GMP-2022.01-Rev.2-eng.pdf (accessed on 16 September 2022).

39. Du, F.; Schick, C.; Androsch, R. Full-composition-range glass transition behavior of the polymer/solvent system poly (lactic acid)/ethyl butylacetylaminopropionate (PLA/IR3535®). *Polymer* **2020**, *209*, 123058. [CrossRef]

40. Du, F.; Yener, H.E.; Hillrichs, G.; Boldt, R.; Androsch, R. Crystallization-induced polymer scaffold formation in the polymer/drug delivery system poly(L-lactic acid)/ethyl butylacetylaminopropionate (PLLA/IR3535). *Biomacromolecules* **2021**, *22*, 3950–3959. [CrossRef] [PubMed]

41. Mapossa, A.B.; López-Beceiro, J.; Díaz-Díaz, A.M.; Artiaga, R.; Moyo, D.S.; Mphateng, T.N.; Focke, W.W. Properties of mosquito repellent-plasticized poly(lactic acid) strands. *Molecules* **2021**, *26*, 5890. [CrossRef]

42. Lloyd, D.R. Microporous membrane formation via thermally induced phase separation. I. Solid-liquid phase separation. *J. Membr. Sci.* **1990**, *50*, 239–261. [CrossRef]

43. Kim, S.S.; Lloyd, D.R. Thermodynamics of polymer/diluent systems for thermally induced phase separation: 3. Liquid-liquid phase separation systems. *Polymer* **1992**, *33*, 1047–1057. [CrossRef]

44. Du, F.; Rupp, H.; Jariyavidyanont, K.; Janke, A.; Petzold, A.; Binder, W.; Androsch, R. 3D-Printing of the polymer/insect-repellent system poly(L-lactic acid)/ethyl butylacetylaminopropionate (PLLA/IR3535). *Int. J. Pharm.* **2022**, *624*, 122023. [CrossRef]

45. Product information, TotalEnergies Corbion Ltd. 2021. Available online: https://www.totalenergies-corbion.com/media/w5cgez0x/pds-luminy-l175-rmb20.pdf (accessed on 11 July 2022).

46. Carbolution Chemicals GmbH, Ethyl butylacetylaminopropionate Product Information. Available online: https://www.carbolution.de/product_info.php?products_id=3221 (accessed on 16 September 2022).

47. DIN EN ISO 527-2:2012-06; Plastics—Determination of Tensile Properties—Part 2: Test Conditions for Moulding and Extrusion plastics (ISO 527-2:2012); German Version EN ISO 527-2:2012. 2012. Available online: https://www.beuth.de/en/standard/din-en-iso-527-2/148232494 (accessed on 7 August 2022).

48. Price, D.M.; Hourston, D.J.; Dumont, F. Thermogravimetry of polymers. In *Encyclopedia of Analytical Chemistry*; Meyers, R.A., Ed.; Wiley: Chichester, UK, 2000; pp. 8094–8105.

49. Saadatkhah, N.; Carillo Garcia, A.; Ackermann, S.; Leclerc, P.; Latifi, M.; Samih, S.; Patience, G.S.; Chaouki, J. Experimental methods in chemical engineering: Thermogravimetric analysis—TGA. *Can. J. Chem. Eng.* **2020**, *98*, 34–43. [CrossRef]

50. Gerasimov, D.N.; Yurin, E.I. *Kinetics of Evaporation*; Springer: Cham, Switzerland, 2018; Volume 68.

51. Sakurada, I.; Nakajima, A.; Fujiwara, H. Vapor pressures of polymer solutions. II. Vapor pressure of the poly (vinyl alcohol)-water system. *J. Polym. Sci.* **1959**, *35*, 497–505. [CrossRef]

52. Wei, X.F.; Linde, E.; Hedenqvist, M.S. Plasticiser loss from plastic or rubber products through diffusion and evaporation. *NPJ Mater. Degrad.* **2019**, *3*, 1–8. [CrossRef]

53. McNeill, I.C.; Leiper, H.A. Degradation studies of some polyesters and polycarbonates—1. Polylactide: General features of the degradation under programmed heating conditions. *Polym. Degr. Stab.* **1985**, *11*, 267–285. [CrossRef]

54. Kopinke, F.D.; Remmler, M.; Mackenzie, K.; Möder, M.; Wachsen, O. Thermal decomposition of biodegradable polyesters—II. Poly (lactic acid). *Polym. Degr. Stab.* **1996**, *53*, 329–342. [CrossRef]

55. Androsch, R.; Di Lorenzo, M.L.; Schick, C. Optical microscopy to study crystal nucleation in polymers using a fast scanning chip calorimeter for precise control of the nucleation pathway. *Macromol. Chem. Phys.* **2018**, *219*, 1700479. [CrossRef]

56. Schick, C.; Androsch, R. Nucleation-controlled semicrystalline morphology of bulk polymers. *Polym. Cryst.* **2018**, *1*, e10036. [CrossRef]

57. Miyata, T.; Masuko, T. Crystallization behaviour of poly (L-lactide). *Polymer* **1998**, *39*, 5515–5521. [CrossRef]

58. Yasuniwa, M.; Tsubakihara, S.; Iura, K.; Ono, Y.; Dan, Y.; Takahashi, K. Crystallization behavior of poly (L-lactic acid). *Polymer* **2006**, *47*, 7554–7563. [CrossRef]

59. Giles, H.F., Jr.; Mount, E.M., III; Wagner, J.R., Jr. *Extrusion, The Definitive Processing Guide and Handbook*; William Andrew Inc.: Norwich, UK, 2005.

60. Sitoe, A.; Mapossa, A.B.; Focke, W.W.; Muiambo, H.; Androsch, R.; Wesley-Smith, J. Development, characterization and modeling of mosquito repellent release from microporous devices. *SPE Polym.* **2020**, *1*, 90–100. [CrossRef]

61. Mapossa, A.B.; Sibanda, M.M.; Sitoe, A.; Focke, W.W.; Braack, L.; Ndonyane, C.; Mouatcho, J.; Smart, J.; Muaimbo, H.; Androsch, R.; et al. Microporous polyolefin strands as controlled-release devices for mosquito repellents. *Chem. Eng. J.* **2019**, *360*, 435–444. [CrossRef]

62. Yener, H.E.; Erdmann, R.; Jariyavidyanont, K.; Mapossa, A.B.; Focke, W.W.; Hillrichs, G.; Androsch, R. Slow-DEET-release mosquito-repellent system based on poly(butylene succinate). *ACS Omega* **2022**, *7*, 8377–8384. [CrossRef]

63. Pyda, M.; Bopp, R.C.; Wunderlich, B. Heat capacity of poly (lactic acid). *J. Chem. Thermodyn.* **2004**, *36*, 731–742. [CrossRef]

64. Mano, J.F.; Ribelles, J.G.; Alves, N.M.; Sanchez, M.S. Glass transition dynamics and structural relaxation of PLLA studied by DSC: Influence of crystallinity. *Polymer* **2005**, *46*, 8258–8265. [CrossRef]

65. Pan, P.; Zhu, B.; Inoue, Y. Enthalpy relaxation and embrittlement of poly (L-lactide) during physical aging. *Macromolecules* **2007**, *40*, 9664–9671. [CrossRef]

66. Naeem Iqbal, H.M.; Sungkapreecha, C.; Androsch, R. Enthalpy relaxation of the glass of poly (L-lactic acid) of different D-isomer content and its effect on mechanical properties. *Polym. Bull.* **2017**, *74*, 2565–2573. [CrossRef]

67. Pan, P.; Zhu, B.; Kai, W.; Dong, T.; Inoue, Y. Effect of crystallization temperature on crystal modifications and crystallization kinetics of poly (L-lactide). *J. Appl. Polym. Sci.* **2008**, *107*, 54–62. [CrossRef]

68. Pan, P.; Inoue, Y. Polymorphism and isomorphism in biodegradable polyesters. *Prog. Polym. Sci.* **2009**, *34*, 605–640. [CrossRef]

69. Kawai, T.; Rahman, N.; Matsuba, G.; Nishida, K.; Kanaya, T.; Nakano, M.; Okamoto, H.; Kawada, J.; Usuki, A.; Honma, N.; et al. Crystallization and melting behavior of poly(L-lactic acid). *Macromolecules* **2007**, *40*, 9463–9469. [CrossRef]

70. Wasanasuk, K.; Tashiro, K.; Hanesaka, M.; Ohhara, T.; Kurihara, K.; Kuroki, R.; Tamada, T.; Ozeki, T.; Kanamoto, T. Crystal structure analysis of poly (L-lactic acid) α form on the basis of the 2-dimensional wide-angle synchrotron X-ray and neutron diffraction measurements. *Macromolecules* **2011**, *44*, 6441–6452. [CrossRef]

71. Kolstad, J.J. Crystallization kinetics of poly (L-lactide-co-meso-lactide). *J. Appl. Polym. Sci.* **1996**, *62*, 1079–1091. [CrossRef]

72. Di Lorenzo, M.L.; Rubino, P.; Luijkx, R.; Hélou, M. Influence of chain structure on crystal polymorphism of poly (lactic acid). Part 1: Effect of optical purity of the monomer. *Colloid Polym. Sci.* **2014**, *292*, 399–409. [CrossRef]

73. Salmerón Sánchez, M.; Mathot, V.B.F.; Vanden Poel, G.; Gómez Ribelles, J.L. Effect of the cooling rate on the nucleation kinetics of poly (L-lactic acid) and its influence on morphology. *Macromolecules* **2007**, *40*, 7989–7997. [CrossRef]

74. Androsch, R.; Iqbal, H.M.N.; Schick, C. Non-isothermal crystal nucleation of poly (L-lactic acid). *Polymer* **2015**, *81*, 151–158. [CrossRef]

75. Androsch, R.; Schick, C.; Di Lorenzo, M.L. Kinetics of nucleation and growth of crystals of poly (L-lactic acid). *Adv. Polym. Sci.* **2017**, *279*, 235–272.

76. Flory, P.J. Thermodynamics of crystallization in high polymers. IV. A Theory of crystalline states and fusion in polymers, copolymers, and their mixtures with diluents. *J. Chem. Phys.* **1949**, *17*, 223–240. [CrossRef]

77. Rim, P.B.; Runt, J.P. Melting point depression in crystalline/compatible polymer blends. *Macromolecules* **1984**, *17*, 1520–1526. [CrossRef]

78. Burghardt, W.R. Phase diagrams for binary polymer systems exhibiting both crystallization and limited liquid-liquid miscibility. *Macromolecules* **1989**, *22*, 2482–2486. [CrossRef]

79. Xiao, H.; Lu, W.; Yeh, J.T. Effect of plasticizer on the crystallization behavior of poly (lactic acid). *J. Appl. Polym. Sci.* **2009**, *113*, 112–121. [CrossRef]

80. Paul, D.R.; Barlow, J.W. Crystallization from miscible polymer blends. In *Polymer Alloys II*; Springer: Boston, MA, USA, 1980; pp. 239–253.

81. Ali, F.; Chang, Y.W.; Kang, S.C.; Yoon, J.Y. Thermal, mechanical and rheological properties of poly (lactic acid)/epoxidized soybean oil blends. *Polym. Bull.* **2009**, *62*, 91–98. [CrossRef]

82. Schick, C.; Donth, E. Characteristic length of glass transition: Experimental evidence. *Phys. Scripta* **1991**, *43*, 423–429. [CrossRef]

83. Arndt, M.; Stannarius, R.; Groothues, H.; Hempel, E.; Kremer, F. Length scale of cooperativity in the dynamic glass transition. *Phys. Rev. Lett.* **1997**, *79*, 2077–2080. [CrossRef]

84. Jariyavidyanont, K.; Du, M.; Yu, Q.; Thurn-Albrecht, T.; Schick, C.; Androsch, R. Bulk Enthalpy of melting of poly (L-lactic acid) (PLLA) determined by fast scanning chip calorimetry. *Macromol. Rap. Commun.* **2022**, *43*, 2200148. [CrossRef]

85. Jariyavidyanont, K.; Schick, C.; Androsch, R. The bulk enthalpy of melting of α′-crystals of poly (L-lactic acid) determined by fast scanning chip calorimetry. *Thermochim. Acta* **2022**, *717*, 179349. [CrossRef]

86. Zhang, J.; Duan, Y.; Sato, H.; Tsuji, H.; Noda, I.; Yan, S.; Ozaki, Y. Crystal modifications and thermal behavior of poly (L-lactic acid) revealed by infrared spectroscopy. *Macromolecules* **2005**, *38*, 8012–8021. [CrossRef]

87. Meaurio, E.; López-Rodríguez, N.; Sarasua, J.R. Infrared spectrum of poly (L-lactide): Application to crystallinity studies. *Macromolecules* **2006**, *39*, 9291–9301. [CrossRef]

88. Chen, X.; Han, L.; Zhang, T.; Zhang, J. Influence of crystal polymorphism on crystallinity calculation of poly (L-lactic acid) by infrared spectroscopy. *Vibr. Spectr.* **2014**, *70*, 1–5. [CrossRef]

89. Du, M.; Jariyavidyanont, K.; Boldt, R.; Tariq, M.; Fischer, M.; Spoerer, Y.; Kuehnert, I.; Androsch, R. Crystal-nuclei formation during injection-molding of poly (L-lactic acid). *Polymer* **2022**, *250*, 124897. [CrossRef]

90. Pan, P.; Kai, W.; Zhu, B.; Dong, T.; Inoue, Y. Polymorphous crystallization and multiple melting behavior of poly (L-lactide): Molecular weight dependence. *Macromolecules* **2007**, *40*, 6898–6905. [CrossRef]

91. Cocca, M.; Di Lorenzo, M.L.; Malinconico, M.; Frezza, V. Influence of crystal polymorphism on mechanical and barrier properties of poly (L-lactic acid). *Eur. Polym. J.* **2011**, *47*, 1073–1080. [CrossRef]

92. Miyata, T.; Masuko, T. Morphology of poly(L-lactide) solution-grown crystals. *Polymer* **1997**, *38*, 4003–4009. [CrossRef]

93. Androsch, R.; Schick, C.; Di Lorenzo, M.L. Melting of conformationally disordered crystals (α′-phase) of poly (L-lactic acid). *Macromol. Chem. Phys.* **2014**, *215*, 1134–1139. [CrossRef]

94. Schulz, M.; Seidlitz, A.; Kurz, R.; Bärenwald, R.; Petzold, A.; Saalwächter, K.; Thurn-Albrecht, T. The underestimated effect of intracrystalline chain dynamics on the morphology and stability of semicrystalline polymers. *Macromolecules* **2018**, *51*, 8377–8385. [CrossRef]

95. Seidlitz, A.; Thurn-Albrecht, T. Chapter 9. Small-angle X-ray scattering for morphological analysis of semicrystalline polymers. *Polym. Morphol. Princ. Charact. Process.* **2016**, *15*, 151–164.

96. Runt, J.; Kanchanasopa, M. Crystallinity Determination. In *Encyclopedia of Polymer Science and Technology*; Wiley: New York, NY, USA, 2002.

97. Ryan, A.J.; Bras, W.; Mant, G.R.; Derbyshire, G.E. A direct method to determine the degree of crystallinity and lamellar thickness of polymers: Application to polyethylene. *Polymer* **1994**, *35*, 4537–4544. [CrossRef]

98. Toda, A.; Androsch, R.; Schick, C. Insights into polymer crystallization and melting from fast scanning chip calorimetry. *Polymer* **2016**, *91*, 239–263. [CrossRef]

99. Schick, C.; Androsch, R.; Schmelzer, J.W.P. Homogeneous crystal nucleation in polymers. *J. Phys. Cond. Matter* **2017**, *29*, 453002. [CrossRef]

100. Cristea, M.; Ionita, D.; Iftime, M.M. Dynamic mechanical analysis investigations of PLA-based renewable materials: How are they useful? *Materials* **2020**, *13*, 5302. [CrossRef]

101. Perego, G.; Cella, G.D.; Bastioli, C. Effect of molecular weight and crystallinity on poly (lactic acid) mechanical properties. *J. Appl. Polym. Sci.* **1996**, *59*, 37–43. [CrossRef]

102. Mathot, V.; Pyda, M.; Pijpers, T.; Poel, G.V.; Van de Kerkhof, E.; Van Herwaarden, S.; Van Herwaarden, F.; Leenaers, A. The Flash DSC 1, a power compensation twin-type, chip-based fast scanning calorimeter (FSC): First findings on polymers. *Thermochim. Acta* **2011**, *522*, 36–45. [CrossRef]

103. Kolesov, I.; Mileva, D.; Androsch, R.; Schick, C. Structure formation of polyamide 6 from the glassy state by fast scanning chip calorimetry. *Polymer* **2011**, *52*, 5156–5165. [CrossRef]

104. Crist, B.; Fisher, C.J.; Howard, P.R. Mechanical properties of model polyethylenes: Tensile elastic modulus and yield stress. *Macromolecules* **1989**, *22*, 1709–1718. [CrossRef]

105. Zia, Q.; Radusch, H.J.; Androsch, R. Deformation behavior of isotactic polypropylene crystallized via a mesophase. *Polym. Bull.* **2009**, *63*, 755–771. [CrossRef]

106. Youssef, G. *Applied Mechanics of Polymers: Properties, Processing, and Behavior*; Elsevier: Amsterdam, The Netherlands, 2021.
107. Ryan, J.J.; Casalini, R.; Orlicki, J.A.; Lundin, J.G. Controlled release of the insect repellent picaridin from electrospun nylon-6,6 nanofibers. *Polym. Adv. Technol.* **2020**, *31*, 3039–3047. [CrossRef]

4.4 3D-Printing of the polymer/insect-repellent system poly(L-lactic acid)/ethyl butylacetylaminopropionate (PLLA/IR3535)

Fanfan Du[a], Harald Rupp[b], Katalee Jariyavidyanont[a], Andreas Janke[c], Albrecht Petzol[d], Wolfgang Binder[b,*], René Androsch[a,*]

[a] Interdisciplinary Center for Transfer-oriented Research in Natural Sciences, Martin Luther University Halle-Wittenberg, 06099 Halle/Saale, Germany

[b] Institute of Chemistry, Martin Luther University Halle-Wittenberg, 06099 Halle/Saale, Germany

[c] Leibniz-Institut für Polymerforschung Dresden e. V., Hohe Str. 6, 01069 Dresden, Germany

[d] Institute of Physics, Martin Luther University Halle-Wittenberg, 06099 Halle/Saale, Germany

Graphical abstract:

Highlights:

❖ The polymer/repellent system PLLA/IR3535 can be 3D-printed to obtain a drug-delivery device, raising the expectation to be used for wearable personalized protection.

❖ The maximum repellent loading achieved was 25 m%.

❖ During the 3D printing process, only minor repellent was lost, and the repellent did not degrade.

❖ Evaporation of IR3535 at body temperature lasts at least 5–10 days.

3D-printing of the polymer/insect-repellent system poly(L-lactic acid)/ethyl butylacetylaminopropionate (PLLA/IR3535)

Fanfan Du [a], Harald Rupp [b], Katalee Jariyavidyanont [a], Andreas Janke [c], Albrecht Petzold [d], Wolfgang Binder [b,*], René Androsch [a,*]

[a] *Interdisciplinary Center for Transfer-oriented Research in Natural Sciences, Martin Luther University Halle-Wittenberg, 06099 Halle/Saale, Germany*
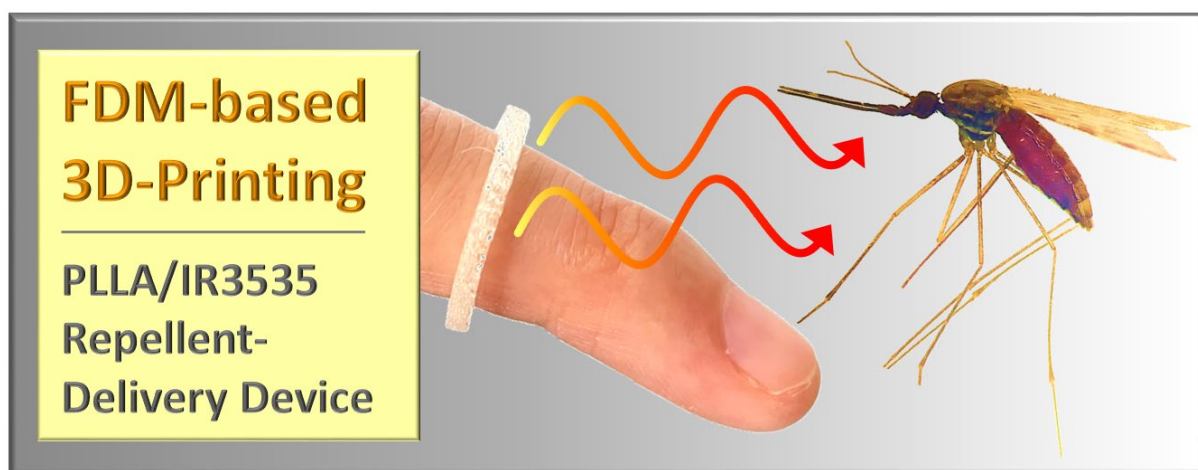[b] *Institute of Chemistry, Martin Luther University Halle-Wittenberg, 06099 Halle/Saale, Germany*
[c] *Leibniz-Institut für Polymerforschung Dresden e. V., Hohe Str. 6, 01069 Dresden, Germany*
[d] *Institute of Physics, Martin Luther University Halle-Wittenberg, 06099 Halle/Saale, Germany*

ARTICLE INFO

ABSTRACT

The polymer/solvent system poly (L-lactic acid)/ethyl butylacetylaminopropionate (PLLA/IR3535) is regarded as an insect-repellent-delivery system, serving, e.g., for fighting mosquito-borne tropical diseases. In such systems the solid polymer hosts the liquid repellent, with the latter slowly released to the environment, expelling mosquitoes. As a new approach, exceeding prior work about application of different technologies to obtain such devices, in this work, samples of the polymer/repellent system PLLA/IR3535 were prepared by 3D-printing. The experiments showed that it is possible to print 3D-parts containing up to 25 m% repellent, with an only minor loss of repellent during the printing process. For samples containing low amount of repellent, crystallization of PLLA was suppressed due to the rather fast cooling step and the low bed temperature of around 25 °C, being lower than the glass transition temperature of the homogeneous polymer/repellent strands. At higher repellent concentration, due to the lowering of the glass transition temperature to near or even below ambient temperature, the crystallinity slowly increased during storage after printing. For all samples, regardless of the initial repellent concentration, the repellent-release rate increases with temperature, and at ambient temperature the release-time constant is in the order of 10 days. The study successfully proved the applicability of the technology of extrusion-based 3D-printing for the preparation of polymer parts with a specific shape/design containing mosquito-repellent at a concentration which raises the expectation to be used as a repellent delivery-device.

1. Introduction

Mosquito-borne tropical diseases, such as malaria, cause hundreds of thousands of deaths each year and are still a public health issue (World malaria report, 2021). Insect repellents, to some extent, minimize the risk of infection of various mosquito-borne diseases, by forming a vapor barrier at the human skin, preventing mosquito-bites (Mapossa et al., 2021). Wearable mosquito-repellent personal protection devices, providing long-term protection over weeks or months, appear possible by incorporation of repellent into a polymeric carrier, hosting and slowly releasing the repellent to the surrounding (Mapossa et al., 2021; Revay et al., 2013; Rodriguez et al., 2017; Mapossa et al., 2019).

Conventional techniques for the preparation of such devices include thermally-induced phase separation (TIPS), solvent casting, salt leaching, melt molding, freeze drying, or gas foaming (Mapossa et al., 2021; Calori et al., 2020). TIPS may be considered the most versatile and simplest preparation technique and involves heating a polymer–solvent mixture to elevated temperature where it forms a solution, which then demixes on cooling by liquid–liquid (L-L) or crystallization-induced solid–liquid (S-L) phase separation (Kim and Lloyd, 1992; Kim and Lloyd, 1992; Kim and Lloyd, 1992). L-L phase separation typically occurs upon cooling the solution to a temperature below its stability limit (Arnauts et al., 1994). Such behavior has been proven valid for the polymer/repellent system consisting of linear low-density polyethylene (LLDPE) and the natural repellent citronellal (Akhtar and Focke, 2015). It was shown that on quenching extruded strands into ice-water a co-continuous structure of solid LLDPE (achieved by crystallization of the polymer after L-L phase separation) and liquid repellent formed, holding up to 40 mass percent (m%) of the latter. Similarly, extrusion of LLDPE or poly (ethylene-co-vinyl acetate) (EVA) with up to 30 m% Icaridin or

N, *N*-diethyl-3-methylbenzamide (DEET) into ice-water induced a spinodal phase separation of the components and led to the formation of microporous scaffolds (Mapossa et al., 2019).

S-L phase separation, in general, proceeds *via* growth of either polymer or solvent crystals in solution (Kim and Lloyd, 1992), and in case of polymer crystallization, a solid scaffold of a tailorable structure hosting the liquid repellent can form. Since from the point-of-view of environment-friendliness, bio-based and biodegradable polymers are considered as effective alternatives to traditional, petroleum-based polymers, recently poly (L-lactic acid) (PLLA) (Sungkapreecha et al., 2017; Sungkapreecha et al., 2019; Sungkapreecha et al., 2018; Sungkapreecha et al., 2020) and poly (butylene succinate) (PBS) (Yener et al., 2021; Yener et al., 2022) were employed for generation polymer/repellent systems forming scaffolds by S-L demixing. In view of PLLA, which is in foreground in the present study, the phase behavior in combination with DEET as repellent was comprehensively evaluated (Sungkapreecha et al., 2017; Sungkapreecha et al., 2019). PLLA dissolves in DEET, allowing scaffold formation by S-L TIPS if the cooling conditions/composition of mixtures support crystallization. Otherwise, as found by analysis of the phase behavior of non-crystallizable poly (D/L-lactic acid) (PDLLA) and DEET, L-L phase separation occurs slightly below ambient temperature (Sungkapreecha et al., 2018; Sungkapreecha et al., 2020).

The possibility of using PLLA as a carrier for the specific repellent ethyl butylacetylaminopropionate (IR3535) as a promising repellent with less side effects on environment and human beings compared to DEET, e.g., allowing possible application for pregnant women and children ((Puccetti et al., 2006; merck, xxxx; (Tavares et al., 2018); (Mapossa et al., 2020); (epa, xxxx)), was investigated (Du et al., 2021). It was found that PDLLA and IR3535 are thermodynamically miscible in the entire composition range, as proven by in-depth analysis of the glass transition temperature, using fast scanning chip calorimetry combined with *in-situ* evaporation of the liquid for controlled change of the system composition (Du et al., 2020). When using PLLA as a system component, cooling the solutions leads to formation of scaffolds which are tuneable by both, the crystallization temperature and the polymer content from pore size point-of-view. Microporous scaffolds of different fine-structure were obtained, hosting the mosquito-repellent in intra- and interspherulitic pores, with the intraspherulitic pore size of PLLA increasing with crystallization temperature and decreasing with the polymer content (Du et al., 2021).

For practical reasons, besides knowledge of the thermodynamics of possible polymer/repellent combinations, reliable and efficient engineering routes for obtaining repellent-delivery devices are required. Technologies tested to date include melt-extrusion of strands (Mapossa et al., 2019; Mapossa et al., 2020; Di Lorenzo and Longo, 2019; Sitoe et al., 2020; Mapossa et al., 2021); electrospinning of mats of fibers with a diameter of around 1 μm (Bonadies et al., 2019; Ryan et al., 2020), or melt-spinning of monofilaments or bi-component fibers with a diameter of several 10 μm (Ferreira et al., 2021). In all these cases, the repellent content can be adjusted up to a maximum loading of around 30–40 m%, which for extruded strands has been shown to be sufficient in view of an efficient repelling of the mosquitoes (Mapossa et al., 2019). With the present study, we attempt exploring the possibility of generating polymer-parts accommodating liquid mosquito repellent by fused deposition modeling/three-dimensional printing (3D-printing). The main difference to the above described technologies of continuous production of semi-finished products (strands, films, or fibers) is that 3D-printing provides the opportunity to produce parts with intricate geometries, offering the advantages of additional functionalities, or of obtaining end-user products (An et al., 2015; Daminabo et al., 2020; Kishore and Sinha, 2021; Rupp and Binder, 2021). To the best of our knowledge, there exist no studies in the field of 3D-printing of polymer/repellent systems in general, including the PLLA/IR3535 system of interest here, being therefore subject of this work.

2. Experimental

2.1. Materials and preparation

Total Corbion (Amsterdam, Netherlands) provided an extrusion-grade PLLA, named L-175, containing less than 1 % D-isomer co-units. The melt-flow index of the material is reported as 8 g/10 min (210 °C/ 2.16 kg) (total, xxxx). The as-received PLLA pellets were dried in an oven at 100 °C for 1 h in vacuum, before further processing. IR3535 with a purity of 98 % was purchased from Carbolution Chemicals GmbH (St. Ingbert, Germany) and was used without further purification (Chemicals, xxxx). It is a clear liquid at room temperature, and exhibits a glass transition temperature of around −90 °C (Du et al., 2020). The estimated metastable boiling point at atmospheric pressure is slightly below 300 °C and about 110 °C at 0.02 kPa. The vapor pressure is reported to be around 0.15 Pa at 20 °C (Mapossa et al., 2020; epa, xxxx). PLLA and IR3535 mixtures with a total mass of 2 g, at percentage mass ratios of 100/0, 95/5, 90/10, 85/15, 80/20, and 75/25 were dissolved at room temperature in 40 mL dichloromethane (DCM), obtained from OQEMA (Korschenbroich, Germany). The solutions were then concentrated under reduced pressure at 40 °C to minimize the DCM content. The obtained solid samples were cut into small pieces with a size of 3–5 mm, fitting the cylindrical storage tank with a diameter of 15 mm of the 3D-printer, and then dried for 4 h at reduced pressure of 0.2–0.3 kPa at room temperature. The prepared samples were then stored in closed vials in the fridge at a temperature of 5 °C. If not stated otherwise, in the following, we use the sample code PLLAxx, with 'xx' indicating the mass-percentage of PLLA in PLLA/IR3535 mixtures.

2.2. Instrumentation

Thermogravimetric analysis (TGA). The degradation behavior of neat PLLA and the content of IR3535 in mixtures were investigated using a TGA 2 LF/1100/694 (Mettler Toledo, Greifensee, Switzerland). Samples of unprocessed and processed materials with a mass of 3.0 ± 0.3 mg were placed into alumina crucibles with a volume of 70 μL and heated in nitrogen (N_2) atmosphere from 30 to 600 °C at a rate of 5 K/min. The N_2 flow rate was set to 50 mL/min. Measured data were automatically subtracted by a blank curve, using the instrument software. For isothermal repellent-release experiments, samples with a mass of 3.0 ± 0.1 mg were heated to predefined temperatures at a rate of 20 K/min in N_2 atmosphere, and then held at these temperatures for 12 h, to allow evaporation of the liquid repellent. Measured data were automatically compensated for buoyancy, using the instrument software.

Gel permeation chromatography (GPC). The average molar mass and polydispersity were determined by a Viscotek GPCmax VE 2002 system (MalvernPanalytical GmbH, Kassel, Germany), consisting of $H_{HR}H$ Guard-17369 and GMH_{HR}-N-18055 columns and a refractive index detector VE 3580 RI detector, operated at 40 °C. Neat PLLA and mixtures of PLLA with IR3535 with a total mass of 4 mg were first dissolved in 0.1 mL chloroform ($CHCl_3$), obtained from OQEMA (Korschenbroich, Germany), and further diluted with 0.9 mL tetrahydrofuran (THF) (VWR/BDH Prolabo, Darmstadt, Germany). As such, the sample concentration was 4 mg / [1 mL ($CHCl_3$ + THF)]. The flow rate of the THF eluent was 1.0 mL/min, and polystyrene standards with a molar-mass range from 0.3 to 170 kg/mol were used for calibration.

Differential scanning calorimetry (DSC). DSC was employed to analyze the thermal behavior of neat PLLA and PLLA containing IR3535, before and after 3D-printing. Measurements were performed using a calibrated heat-flux DSC 1 (Mettler-Toledo, Greifensee, Switzerland) equipped with the FRS5 sensor. The device was connected to a Huber TC100 intracooler (Offenburg, Germany). The furnace was purged with nitrogen gas at a flow rate of 60 mL/min. Samples prepared as described above were placed into 20-μL aluminum pans, with the sample mass being between 4 and 6 mg. The pans were covered with a lid and then heated to 200 °C at a rate of 20 K/min.

2

Nuclear magnetic resonance (NMR) spectroscopy. Proton NMR (^{1}H NMR) spectra were measured on a Varian Gemini 400 spectrometer (Agilent Technologies Co., Santa Clara, USA) at 27 °C with deuterated chloroform (CDCl$_3$) used as solvent. For interpretation of the NMR spectra, the MestReNova software (version 9.0.1-13254) was utilized and chemical shifts were referred to the CDCl$_3$ solvent signal. Splitting patterns are designated as follows: s, singlet; d, doublet; t, triplet; and m, multiplet. Chemical shifts were given in ppm and coupling constants in Hz. Repellent contents were evaluated by adding 10 μL toluene as a standard, offering a calibration integral value.

Fourier-transform infrared spectroscopy (FTIR). Attenuated total reflection (ATR)-FTIR-spectra were recorded on a Bruker Tensor VER-TEX 70 spectrometer equipped with a Golden Gate Diamond ATR system. Background-corrected spectra were measured at a resolution of 2 cm^{-1} in the wavenumber range from 4000 to 600 cm^{-1}, averaging 32 scans. The Opus-6.5 software was utilized for analyzing the data.

Wide-angle X-ray scattering (WAXS). X-ray scattering experiments were performed to analyze the structure of PLLA crystals formed after 3D-printing. We used a Retro-F laboratory setup (SAXSLAB, Massachusetts) equipped with a microfocus X-ray source (AXO Dresden GmbH, Germany) and an ASTIX multilayer X-ray optics (AXO Dresden GmbH, Germany) as monochromator for Cu Kα radiation with a wavelength of 0.154 nm. The instrument was used in transmission mode, and intensity data were recorded in vacuum using a PILATUS3 R 300 K detector (Dectris Ltd., Baden, Switzerland). The measurements were performed at a sample-detector distance of 88 mm and the measurement time at each detector position was 180 s.

Atomic force microscopy (AFM). Analysis of the nanometer length-scale structures of 3D-printed samples was performed with a Dimension FASTSCAN (Bruker-Nano, USA) operated in peak force tapping mode. Silicon nitride sensors SCANASYST-FLUID+ (Bruker, USA) with a nominal spring constant of 0.7 N/m and a tip radius of 2 nm were used, and the set point was 0.8 V. Prior to AFM analysis, embedded 3D-printed strands were cut by a Leica EM UC7 ultramicrotome (Wetzlar, Germany) with a diamond knife at room temperature. The cut sections were removed and the remaining smooth surface was used to observe AFM images.

3D-Printing. 3D-printing was performed using a 3D-printer regenHU 3DDiscovery (RegenHU, Villaz-St-Pierre, Switzerland), with further details of the device and of the printing process provided below.

3. Results and discussion

3.1. 3D-printing process and part geometries

Fused deposition modeling (FDM) is one of several additive manufacturing technologies to produce three-dimensional (3D) parts from computer models, and has been demonstrated to be a cost-efficient and easy accessible printing technique for the fabrication of parts from thermoplastic polymers hosting functional actives for medical applications (An et al., 2015; Daminabo et al., 2020; Kishore and Sinha, 2021; Rupp and Binder, 2021; Tümer and Erbil, 2021). In this work, bio-based PLLA in combination with the mosquito-repellent IR3535 was used to fabricate a (wearable) mosquito-repellent personal protection device by this technique, with the geometry of the printed parts programmed using the CAD software *BioCAD*^{TM} (regen, xxxx), as shown in Fig. 1. Fig. 1a depicts a 3D-grid with a 6×6 mm^2 base area and a height corresponding a stack of four layers. Two mutually perpendicular, and in height-direction alternating printing directions were used to produce the various layers. The strand thickness was set to 0.3 mm, that is, to 90 % of the inner diameter of the printing nozzle. Eleven parallel polymer strands were printed in every layer and the gap between the strands is about 0.3 mm, leading to a periodicity of 0.6 mm. For demonstration of the large variety of printable shapes, as needed for specific applications, in Fig. 1b and c, the lettering "MLU" and wearable rings in different sizes were designed, respectively. In both cases, four layers were printed too, however, with an unchanged printing direction.

For printing, PLLA/IR3535 samples of different composition were prepared by solution-mixing, as described in the Experimental section, and filled into the storage tank of the 3D-printer. The mixtures were then heated to 200 °C, and stored at this temperature for 30 min before extrusion/printing (Rupp et al., 2019; Rupp and Binder, 2020; Rupp and Binder, 2021); in case of neat PLLA, the storage temperature was 210 °C according to literature (Shin et al., 2019; Cunha-Filho et al., 2017; Dubinenko et al., 2020). The samples were transferred from the storage tank into the extruder-unit of the printer using compressed air at a pressure of 0.20 MPa and then extruded through a metal nozzle with a diameter of 330 μm, printing/depositing the obtained strands on adhesive tape, conditioned at room temperature, used for fixing the part. The screw speed of the extruder and movement speed of the printing head were 15 rpm/min and 10 mm/s, respectively (Rupp et al., 2019; Rupp and Binder, 2020; Rupp and Binder, 2021). With these printing parameters, referring to the 3D-grid of Fig. 1a, printing of a single layer was completed within 10 s while printing the whole part required approximately 40 s. Examples of 3D-prints are provided with the images of Fig. 2, showing in the top and center rows 3D-grids of different composition, containing up to 25 m% IR3535. The bottom row shows images of the lettering "MLU" (left), two rings of different diameter (center), and a possible use of the latter as a finger bangle (right). In these cases, the printed parts contain 15 m% IR3535. Beside parts with a specific geometry (see Fig. 2), also individual strands of identical diameter and using the same print speed have been printed for subsequent analysis of the structure and the evaporation behavior. In this case, however, the nozzle-to-substrate distance was increased.

The designed grid structures with eleven parallel strands per layer and four layers in height direction were successfully printed for samples of different PLLA/IR3535 composition, containing up to 25 m% IR3535, with the individual strands of uniform diameter clearly visible in the different layers. All grids/strands appeared optically transparent, except in case of the sample containing 25 m% IR3535 (PLLA75), pointing to
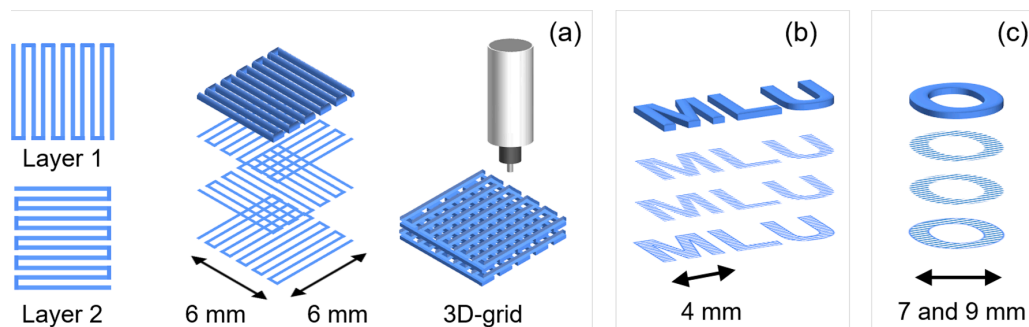

Fig. 1. Geometry of 3D-printed parts. (a) 3D-grid with a 6×6 mm^2 base area and height of 4 layers, (b) "MLU" lettering, and (c) rings of different diameter.
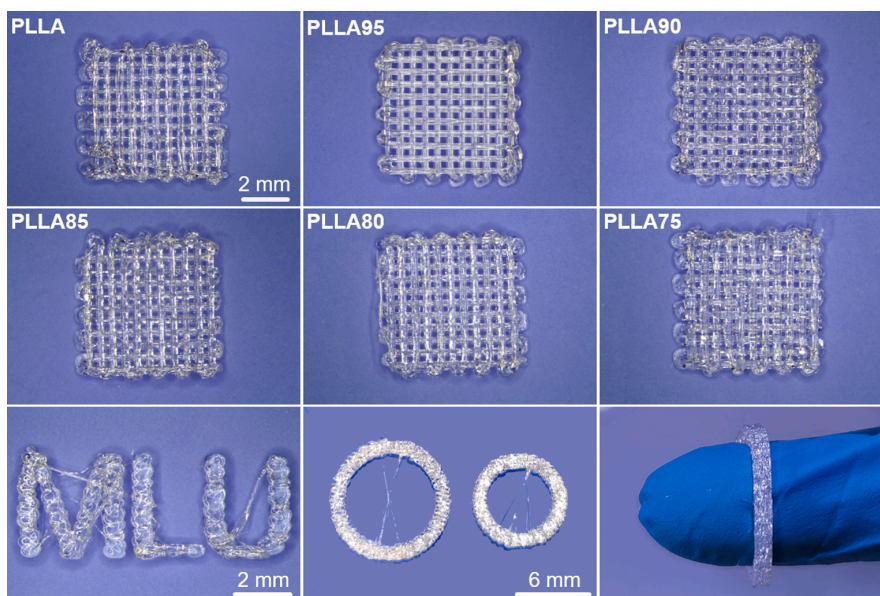
3

Fig. 2. Examples of prints of 3D-grids of samples of PLLA/IR3535 of different composition, as indicated (top and center row). The bottom row shows images of prints containing 15 m% IR3535, of the lettering "MLU" (left), of two rings of different diameter (center), and of their possible use as a finger bangle (right).

different structures at the micrometer length-scale. In view of mechanical properties, qualitatively, the behavior of the printed parts changed gradually from brittle to ductile with increasing repellent content, as judged by the response upon removal of the printed parts from the substrate/adhesive tape. In order to confirm the qualitative, subjective impression, the stiffness of individual strands was measured by DMA, decreasing with increasing repellent content in the strands, from around 3.5 GPa in neat PLLA-strands to well below 0.5 GPa in strands containing 20 and 25 m% IR3535. The decrease of the modulus may be attributed to the plasticizing effect of the liquid repellent when added to PLLA (Gui et al., 2014; Chaos et al., 2019; Alhanish and Abu Ghalia, 2021), further discussed below. Quantitative data about the stiffness of strands, including the dependence on the repellent concentration are provided in the Supporting Information S1.

3.2. Repellent content and thermal stability

3.2.1. Repellent content by TGA

The composition of prepared PLLA/IR3535 mixtures and their thermal stability before and after 3D-printing were evaluated by TGA using a heating rate of 5 K/min, as shown with the dash and solid lines in the left plot of Fig. 3, respectively. The right plot shows the first derivative of the TGA curves of PLLA/IR3535 mixtures subjected to 3D-printing, as well as of the TGA curves of the neat components. Information about the heating rate is explicitly provided since the temperature of mass loss in case of all samples depends on the heating rate; similar holds for the initial sample mass, being around 3 mg. The first mass-loss event in all samples containing the repellent is due to the evaporation of the repellent IR3535, as concluded from the analysis of neat IR3535. The mass loss of neat IR3535 starts at around 100 °C and evaporation is completed at 200 °C; the highest evaporation rate is observed at 185 °C (see Fig. 3, right). Neat PLLA starts to degrade at distinctly higher
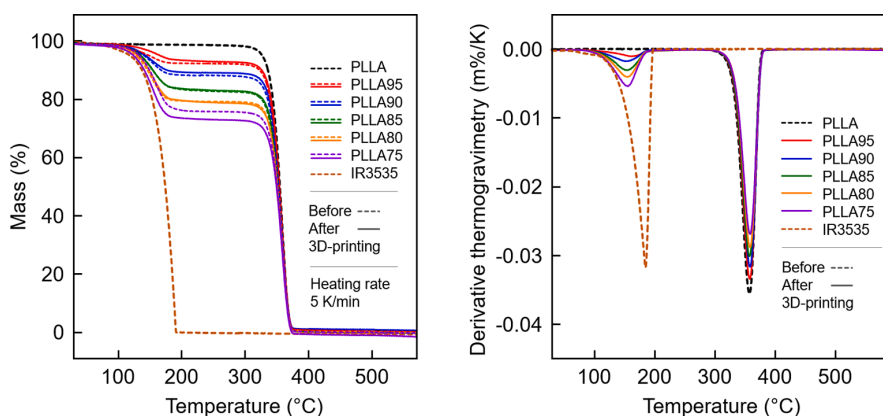
Fig. 3. TGA curves, normalized mass as a function of temperature of neat PLLA and IR3535, and of PLLA/IR3535 mixtures, as indicated in the legend, before 3D-printing (dash lines) and after 3D-printing (solid lines), recorded using a heating rate of 5 K/min in N_2-atmosphere (left). First derivative of the TGA curves obtained after 3D-printing (right). In case of 3D-printed samples, measurements were done on individually printed strands.

Table 1

Thermogravimetric analysis of the IR3535 content in PLLA/IR3535 mixtures before and after 3D-printing, based on the measurements shown in Fig. 3.

Sample	Expected IR3535 content (m%)	Measured IR3535 content (m%)		Peak temperature in the first derivative of TGA curves (°C)	
		Before 3D-printing	After 3D-printing	Before 3D-printing	After 3D-printing
PLLA	0	0.0	0.0	357.3	357.8
PLLA95	5	6.1 ± 0.7	5.5 ± 0.6	357.4; 153.5	357.6; 161.0
PLLA90	10	10.8 ± 0.4	9.5 ± 0.6	357.4; 152.4	357.7; 150.7
PLLA85	15	15.6 ± 0.9	14.8 ± 1.0	357.4; 152.4	357.3; 155.0
PLLA80	20	18.8 ± 0.9	19.0 ± 1.0	357.8; 153.6	357.8; 154.5
PLLA75	25	24.0 ± 0.7	25.0 ± 0.5	357.8; 160.4	357.8; 155.2
IR3535	100	100.0	–	185.2	–

The standard deviation is observed by measuring at least two times.

temperature of 300 °C, and therefore in PLLA/IR3535 mixtures two discrete mass-loss steps are observed, associated to evaporation of IR3535 and degradation of PLLA. The first, at lower temperature occurring mass-loss step allows determination of the repellent content, which is summarized in Table 1. The data reveal that the measured content on IR3535 in the mixtures is close to the expected values, regardless whether obtained on samples subjected to 3D-printing or not. In other words, printing, at the specific conditions described above, is not connected with a major loss of repellent and the 3D-printed objects contain the expected amount of repellent, despite, worth mentioning, samples were stored in the tank of the 3D-printer for up to 4 h at 200 °C, when printing a large number of samples successively. Note furthermore that all PLLA/IR3535 mixtures, before 3D-printing, showed only a single mass-loss step at a temperature lower than 300 °C, indicating the absence of residual DCM in the mixtures. The occasional observation of slightly higher repellent content after 3D-printing, compared to the value measured before 3D-printing, is probably related to experimental uncertainty. Data of 3D-printed samples in Fig. 3 were obtained on individually printed strands, however, additional measurements on grid-samples showed very similar results.

3.2.2. Repellent content by NMR spectroscopy

The content of IR3535 in PLLA/IR3535 mixtures and the chemical structure of the components after subjecting them to 3D-printing were analyzed by NMR spectroscopy. As an example, Fig. 4 shows ^{1}H NMR spectra of a PLLA/IR3535 mixture with an expected IR3535-content of 20 m%, containing 10 μL toluene for calibration, with samples taken before and after 3D-printing. In the spectra, the single peak at 2.36 ppm is assigned to the methyl protons of toluene, which is not overlapping with signals of the PLLA/IR3535 mixture. The shifts of IR3535 corresponding to the methylene protons next to the ester and acyl groups appear between 4.5 and 2.5 ppm. For PLLA, the characteristic signals located at 1.58 and 5.16 ppm are assigned to the methyl and methine groups, respectively.

The ratio of the integrated signals of IR3535 and toluene ($I_{IR3535}/I_{toluene}$) allows to obtain their molar ratio ($n_{IR3535}/n_{toluene}$) according to equation (1). As the mass of toluene ($m_{toluene}$) is fixed (8.7 mg) and the total mass of the PLLA/IR3535 sample (m_{total}) is also known, the mass fraction of IR3535 (m_{IR3535}) and the repellent content can be calculated by equations (2) and (3). The results are listed in Table 2 in analogy to Table 1, showing expected and measured IR3535-contents before and after 3D-printing. In short, the NMR-data confirm the TGA-results shown above, revealing close agreement of expected and measured values of the IR3535 content within the limit of the experimental uncertainty of around ± 3 % (absolute error). In addition, there is a no chemical shift for the mixture after 3D-printing detected at 5.30 ppm, which indicates that there was no residual DCM in the mixtures present after 3D-printing.

$$\frac{2 \times n_{IR3535}}{3 \times n_{toluene}} = \frac{I_{IR3535}}{I_{toluene}} \quad (1)$$

$$m_{IR3535} = M_{IR3535} \times n_{IR3535} = M_{IR3535} \times \frac{3 \times n_{toluene} \times I_{IR3535}}{2 \times I_{toluene}} \quad (2)$$

$$m\% \text{ of IR3535} = \frac{m_{IR3535}}{m_{total}} * 100 \quad (3)$$

In addition, the NMR-spectroscopy results reveal important information about the thermal stability of IR3535 in PLLA/IR3535 mixtures. During 3D-printing and extrusion, the repellent was exposed to 200 °C for up to 4 h inside the printing tank. However, there is no thermal decomposition of IR3535 detected, as concluded by comparing the NMR-spectra of samples measured before and after 3D-printing. In both spectra, the peak shifts and integral values for IR3535 are unchanged. The protons of the ester CH_2-group ($-O-C\textbf{\textit{H}}_2-CH_3$) for both samples are
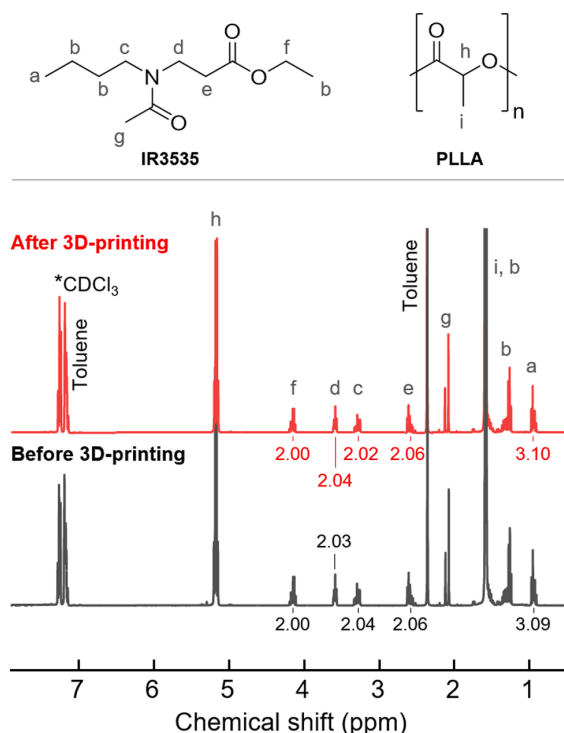
Fig. 4. ^{1}H NMR spectra obtained on a PLLA/IR3535 mixture containing 20 m% IR3535 with a fixed amount of toluene (as calibration standard) in CDCl$_3$, before (bottom, black) and after 3D-printing (top, red). The integral values of IR3535 are the same in both spectra. In case of 3D-printed samples, measurements were done on individually printed strands. (For interpretation of the references to color in this figure legend, the reader is referred to the web version of this article.)

5

Table 2
^{1}H NMR analysis of the IR3535 content in mixtures of PLLA/IR3535 before and after 3D-printing.

Sample	Expected IR3535 content (m%)	Measured IR3535 content (m%)	
		Before 3D-printing	After 3D-printing
PLLA	0	0.0	0.0
PLLA95	5	5.6 ± 0.1	5.2 ± 0.6
PLLA90	10	10.2 ± 1.3	9.3 ± 0.1
PLLA85	15	14.9 ± 0.9	14.8 ± 0.3
PLLA80	20	19.2 ± 0.9	19.3 ± 0.4
PLLA75	25	24.0 ± 2.9	23.1 ± 0.9

The standard deviation is observed by measuring at least two times.

located at 4.14 ppm (q, $J = 7.1$ Hz, 2H). Other functional groups show the same results, like the methylene groups next to the nitrogen atom (–N–C*H$_2$*–) at 3.58 ppm (t, $J = 7.1$ Hz, 2H) and 3.29 ppm (t, $J = 7.6$ Hz, 2H), as well as the ester CH$_2$-group (–CH$_2$–C*H$_2$*–CO–O–) at 2.61 ppm (t, $J = 7.1$ Hz, 2H) and the methyl group at 0.96 ppm (t, $J = 7.3$ Hz, 3H). As such, from chemical point of view, IR3535 is stable under the selected printing conditions applied here. The thermal stability of pure IR3535 also was verified by exposure to air for either 30 min at 200 °C or 4 months at 50 °C in an independent study (Mapossa et al., 2020).

3.2.3. Thermal stability by FTIR spectroscopy

The thermal stability of IR3535 after 3D-printing —an important aspect for further application of the repellents— was confirmed by FTIR measurements, presented in Fig. 5. For neat IR3535, the strongest bands in the spectra are the two carbonyl-stretch vibrations corresponding to the ester (1730 cm^{-1}) and amide (1639 cm^{-1}) functional groups. Also, the C-H bending vibration at 1421 cm^{-1} appears well-separated from the PLLA bands (see three vertical dash lines and the inset at the top of Fig. 5), allowing their identification in the spectra obtained on PLLA/IR3535 printouts. As expected, in the PLLA/IR3535 mixtures, the intensities of these bands increase with the IR3535 content. More important, when comparing the spectra of printed mixtures with the spectrum obtained on neat IR3535, a shift of the characteristic bands is not observed, leading to the conclusion that the repellent was able to withstand the thermo-mechanical history during processing; note again that the PLLA/IR3535 mixtures were exposed to air at high temperature of 200 °C during the printing process. The study of the thermal stability of IR3535 by Mapossa (Mapossa et al., 2020), in contrast, suggested
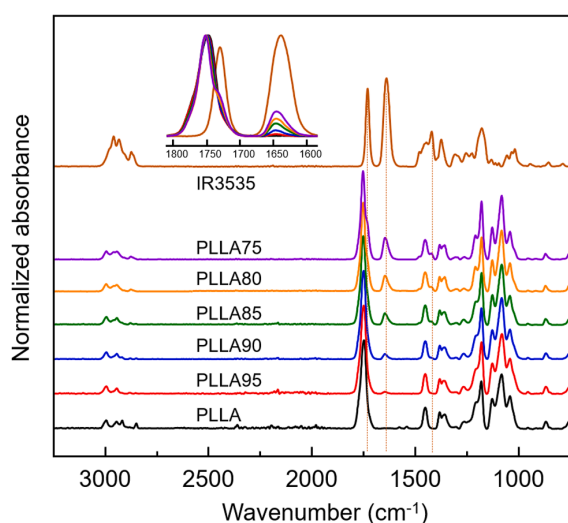
Fig. 5. FTIR spectra of PLLA/IR3535 mixtures of different composition after 3D-printing of individual strands.

slight oxidative degradation by observation of a new band near 1690 cm^{-1} when exposed to air for four months at 50 °C. Here, in our study, new carbonyl bands are not observed at around 1690 cm^{-1}, which is in agreement with the NMR data shown above. As such, the thermal stability of PLLA/IR3535 mixtures at 200 °C, up to 4 h, promotes the application of 3D-printing using the FDM technique.

3.3. Degradation of PLLA during 3D-printing

Thermo-mechanical degradation of thermoplastics during 3D-printing is a common observation, due to exposure to high temperature in combination with high shear rate when passing through the nozzle of the printing head (Zhang, 2018; Pillin et al., 2008). Therefore, GPC was used to analyze possible degradation of neat PLLA and PLLA in mixtures with IR3535, with mass-average molar masses (M_w) and polydispersity-index values (PDI) as summarized in Table 3. As such, the (relative) mass-average molar mass and polydispersity of as-received, neat PLLA, as determined using the specific experimental setup described in the Experimental part, are 199.6 kg/mol and 1.5, respectively. However, after 3D-printing, the values changed to 77.9 kg/mol and 2.1, that is, the (relative) average molar mass significantly decreased. Since a change of the molar mass and PDI of PLLA was not observed when exposing pure PLLA at 200 °C for 2 h to a dry N$_2$ atmosphere, it is assumed that the mechanical history/shear forces in combination with the non-dry-air environment in the 3D-printer is a major reason for this degradation. It is worth noting that similar results were observed in a recent study of printing poly (ε-caprolactone) using the same printer, with the initial number-average molar mass of 45 kg/mol decreasing to 33 kg/mol (Rupp et al., 2019; Rupp and Binder, 2020). The data of Table 3, in addition, provide also information that the molar-mass change is not affected by the amount of repellent in the mixtures.

3.4. Structure of 3D-printed parts

The structure of 3D-printed objects/strands was assessed by calorimetry, microscopy, and X-ray scattering, yielding information about crystallization of PLLA, including the crystallinity and crystal structure, and the location of the liquid repellent. DSC heating scans, recorded at a rate of 20 K/min, of neat PLLA and PLLA/IR3535 mixtures of different composition are shown in the left plot in Fig. 6, with the bottom and top sets of curves representing data obtained on samples before and after 3D-printing, respectively. With regard to non-printed samples, besides the glass transition, only a single melting event is observed. Both, the glass transition and the melting temperature decrease with increasing IR3535-content in the mixture, indicating miscibility —at least partially— of the liquid repellent and the amorphous PLLA phase, and presence of PLLA crystals after the solvent (DCM and IR3535)-assisted preparation process. The lowered melting temperature of PLLA crystals in the mixtures probably is caused by the equilibrium-melting-point depression according to Flory (Flory, 1949).

Table 3
Mass-average molar mass (M_w) and polydispersity index (PDI) of neat PLLA and PLLA in mixtures with IR3535 before and after 3D-printing, obtained by GPC. In case of 3D-printed samples, measurements were done on individually printed strands.

Sample	Before 3D-printing		After 3D-printing	
	M_w (kg/mol)	PDI	M_w (kg/mol)	PDI
PLLA*	199.6	1.5	77.9	2.1
PLLA**	202.9	1.6		
PLLA95			98.8	1.7
PLLA90			91.8	1.9
PLLA85			106.4	1.8
PLLA80			88.4	1.8
PLLA75			118.7	1.7

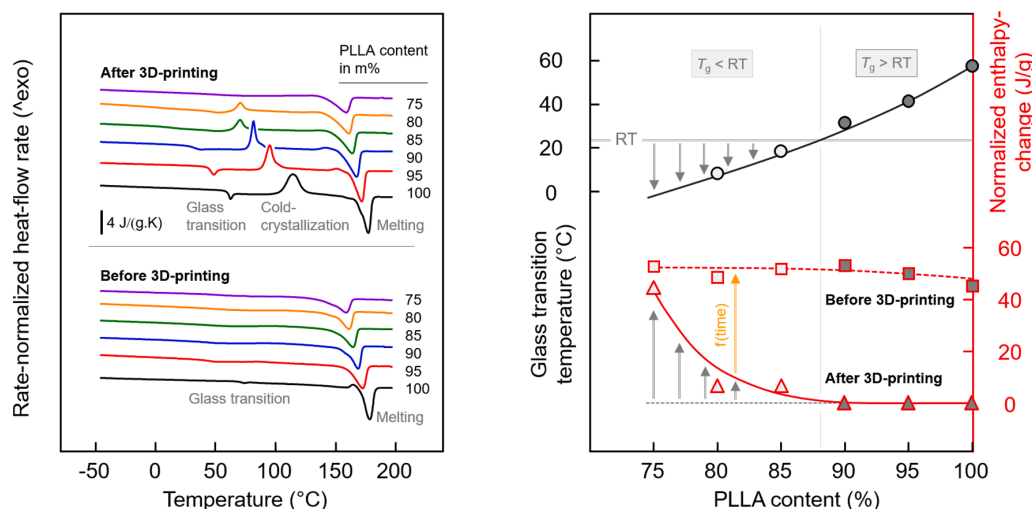* PLLA as-received; ** PLLA exposed to 200 °C for 2 h in N$_2$ atmosphere.

Fig. 6. DSC curves, rate-normalized heat-flow rate as a function of temperature, of PLLA and PLLA/IR3535 mixtures before (bottom) and after 3D-printing (top), recorded on heating at 20 K/min (left). Polymer-content-normalized-enthalpy change during heating of PLLA and PLLA/IR3535 mixtures, obtained before (red/gray squares) and after 3D-printing (red/gray triangles) and glass transition temperature of PLLA and PLLA/IR3535 mixtures after 3D-printing (black/gray circles) (right). Samples subjected to 3D-printing were annealed/stored at RT before the measurement for about 1–2 months if containing up to 10 m% IR3535, otherwise the storing time was at least one week. In case of 3D-printed samples, measurements were done on printed objects. (For interpretation of the references to color in this figure legend, the reader is referred to the web version of this article.)

For 3D-printed samples, neat PLLA shows the glass transition at around 60 °C, which is then, on further heating, followed by a small exothermic cold-crystallization peak at around 114 °C, and an endothermic melting peak at about 176 °C, as expected for a PLLA grade with negligible amount of D-isomers in the chains (Di Lorenzo and Androsch, 2016). Similar as for the non-printed samples, the addition of IR3535 into PLLA results in a decrease of the glass transition temperature T_g, reaching 14 °C in the sample containing 20 m% IR3535, and a lowering of the melting temperature. However, most important is the observation of a distinct cold-crystallization peak in almost all samples, pointing to incomplete crystallization during and after printing. Cold-crystallization fades with increasing IR3535-content and is completely absent in the mixture which contains 25 m% IR3535. Obviously, increasing amount of IR3535 in the samples promotes crystallization of PLLA during and after the print process.

Quantitative data about total enthalpy-changes (normalized to the PLLA content) during heating neat PLLA and PLLA/IR3535 mixtures before (red/gray squares) and after 3D-printing (red/gray triangles), and of glass transition temperatures of printed samples (black/gray circles) are shown as a function of the PLLA content in the right plot of Fig. 6. The total enthalpy-change, which equals the difference between the enthalpy of melting and enthalpy of cold-crystallization, is proportional to the crystal fraction in the sample at begin of the heating process in the DSC experiment and is independent on the PLLA content in the mixtures after the solution-crystallization preparation step (red/gray squares). The total enthalpy change is slightly higher than 50 J/g, which corresponds to an enthalpy-based crystallinity of around 50 % [≈ 52/ 101 × 100 %], with 101 J/g being the bulk enthalpy of melting of α-crystals of PLLA, when melting at around 180 °C (Jariyavidyanont et al., 2022). Samples subjected to the 3D-printing process, in contrast, show a distinct effect of the sample composition on the crystallinity of PLLA which can be interpreted by taking into account the glass transition temperature. For neat PLLA and mixtures with low amount of IR3535 up to 10 m% the crystallinity is rather low, since the melt is relatively fast cooled during the printing process. Subsequent annealing/storing these samples for about 1–2 months at ambient conditions does not change the crystallinity since T_g is higher than room temperature (RT). For samples with higher content on IR3535 of 15 to 25 m%,

in contrast, T_g is around 20 °C, or even lower, thus allowing continuation of the initially incomplete crystallization process during storing for at least one week; note that annealing times were not strictly controlled, since the long-term crystallization of strands was discovered by chance only. Obviously, as indicated with the gray vertical arrows, the crystallization rate (at RT) scales with the temperature-difference between RT [= crystallization temperature] and T_g, as is expected from the Turnbull-Fisher equation (Wunderlich, 1976). The orange, upward directed arrow is indicating that the crystallinity-data obtained after 3D-printing (gray/red triangles) represent a snapshot in the time domain only, since it is expected that long-term annealing will cause a further increase towards the maximum value, as shown with the squares.

Furthermore, it is worth noting that crystallization of the polymer will cause an increase of the repellent concentration in the amorphous phase surrounding the crystals, due to exclusion of the repellent from the PLLA-crystallization process. Such segregation leads to an increase of the repellent content in the amorphous phase to a value depending on the (time-controlled) PLLA-crystallinity, and with that to a change of T_g. The data in the right plot of Fig. 6 do not consider this phenomenon, that is, glass transition temperatures are shown as a function of the total PLLA concentration in the strands but not the actual PLLA concentration in the amorphous solution surrounding crystals, for the sake of simplicity in this initial study of the structure of strands.

The morphology of neat PLLA and PLLA/IR3535 mixtures after 3D-printing was attempted to be observed using polarized-light optical microscopy (POM). However, all images were featureless at the micrometer-length scale. In conclusion, the liquid repellent does not (macroscopically) segregate during printing to yield μm-sized separate domains, nor are crystals, if evident in samples of higher repellent concentration (see Fig. 6, right), arranging in a higher-order spherulitic superstructure. Note that observation of featureless POM images is common if the nuclei density is high and if crystals are small (Androsch et al., 2018; Schick and Androsch, 2018). POM-images obtained on the 3D-printed strands are shown in the Supporting Information S2.

The absence/presence of crystals, as suggested by the DSC measurements explained above, is further confirmed by WAXS patterns, as shown in Fig. 7 for selected 3D-printed grid-samples (see Fig. 2, top and center rows) containing 10, 20, and 25 m% IR3535. The bottom three
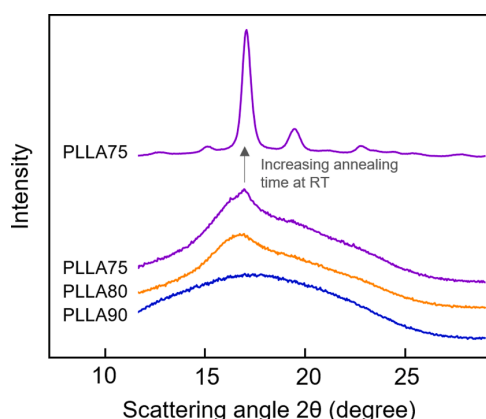
Fig. 7. WAXS-curves obtained on selected PLLA/IR3535 grid-samples (see Fig. 2, top and center rows). Samples have been stored for identical short time of two days at or below room temperature (RT) (bottom three curves) while the effect of long-term annealing for eight months at RT on the crystallinity of the sample containing 25 m% repellent is demonstrated with the upper curve. Color-coding is in accord with the above Figures. Note that the intensity-scale of the upper curve is different compared to that of the lower three curves. Measurements were done on printed objects/grids.

curves were obtained on samples stored at room temperature for rather short though identical time of two days, or at lower temperature. Obviously, the sample which contains 10 m% IR3535 (blue curve) is fully amorphous as there is only an amorphous halo but no peaks are visible. For the sample containing 20 m% IR3535 a broad peak emerges between 16 and 18 deg (2θ) which indicates the presence of small crystals. This additional peak sharpens with further increase in IR3535 content. Regardless the exact nature of the ordered phase in these samples, the data suggest rather negligible crystallinity, being in qualitative agreement with the DSC data of Fig. 6. Long-term annealing of samples containing IR3535, in contrast, for a period of eight months, causes a significant increase of the crystallinity, as is demonstrated with the top curve in Fig. 7 on example of the sample containing 25 m% IR3535, showing intense and narrow scattering peaks associated to the α-crystal form of PLLA (Wasanasuk et al., 2011).

Since POM failed to detect crystals in long-term annealed 3D-printed samples containing sufficient amount of IR3535, AFM was employed to gain further knowledge about the morphology. Fig. 8 shows AFM-height images of PLLA (left) and of a long-term annealed PLLA/IR3535-sample containing 25 m% IR3535 (right). Regarding neat PLLA, the structure of a quenched thin section of non-processed material (pellet) was evaluated. With the knowledge that this sample is amorphous, a homogeneous, featureless structure is expected which is confirmed by the left image. In contrast, the structure of the 3D-printed strand of the sample containing 25 m% IR3535 (right images) is qualitatively different. There

are detected randomly distributed heterogeneities with a typical dimension of 20–50 nm, apparently embedded in a spongy appearing matrix with a typical length scale of heterogeneities of 5–20 nm. Whether the particle-like objects and sponge-/scaffold-like structure of the matrix are caused by segregation of the liquid repellent or related to crystallization-induced phase-separation of PLLA is not known yet. Worth noting, due to the complex structure of annealed, IR3535-containing 3D-printed strands, AFM-analyses were performed several times on independently prepared specimens. As demonstrated with the two images shown in the right part of Fig. 8, high reproducibility of imaging the structure of the matrix is given, while the shape and size of the larger appearing heterogeneities appear slightly different in the various experiments; further images of the sample PLLA75 are provided in the Supporting Information S3. In any case, AFM-imaging of the structure of annealed 3D-printed PLLA-strands containing 25 m% IR3535 provides information about presence of distinct heterogeneities at the nm-length scale due to crystallization of the polymer component (see Figs. 6 and 7), and possible segregation of the liquid repellent. Note that the latter would not necessarily be in contradiction with the glass-transition-temperature analysis, as segregation may be incomplete.

3.5. Repellent-release kinetics

The kinetics of the repellent release from the polymer matrix was studied by performing isothermal TGA experiments in the temperature range from 50 °C to 100 °C, allowing conclusions about the release behavior at room temperature/body temperature by extrapolation. To permit a comparison of the release kinetics of samples of different initial repellent content, the 3D-printed strands were prepared such to obtain specimens of similar shape (strands with a diameter of around 300 μm and of 4–5 mm length) and mass. The left plot of Fig. 9 shows the repellent release of PLLA/IR3535 mixtures initially containing 25 m% IR3535 at different temperatures between 50 °C and 100 °C (for different concentrations see Supporting Information S4). For demonstration of the effect of the IR3535 content, the right plot of Fig. 9 shows the repellent release of PLLA/IR3535 mixtures containing 5 m% and 25 m% at 100 °C. Regarding the temperature-dependence (left plot), the release rate increases with increasing evaporation temperature. At 100 °C evaporation temperature (bottom curve), around 80 % of the initial content of 25 m% evaporated within 3 h, while after 12 h (720 min) almost all of the repellent left the sample, as the sample mass almost reached the expected target of 75 % (see gray dashed line). In contrast, at relatively low temperatures of e.g. 60 °C, only about 20 % out of the total initial repellent content evaporated within 12 h. The observation that isothermal annealing at 100 °C for 12 h leads to almost complete evaporation of the repellent holds for all samples of different initial repellent concentration, as is demonstrated with the right plot. Also here, the target values, indicated with the dashed lines, are almost reached within the 12-hour experiment-time frame.

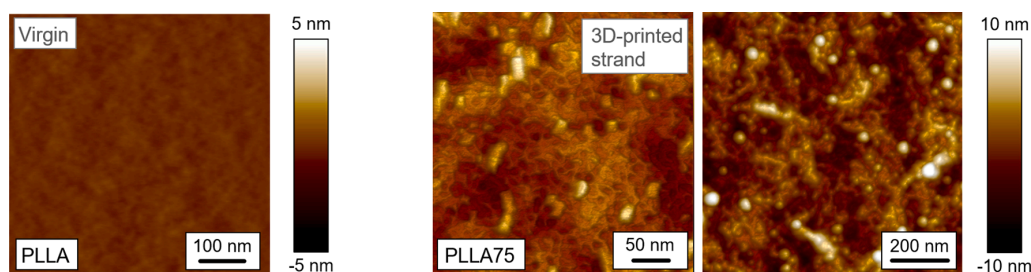For application of PLLA/IR3535-3D-printed parts as repellent-

Fig. 8. AFM-height images of the cross-section of neat, non-3D-printed amorphous PLLA (left) and of 3D-printed strands of PLLA containing 25 m% IR3535 (right images). Fully amorphous PLLA was prepared by quenching a thin section taken from an as-received pellet. The PLLA-strand containing 25 m% IR3535 was stored at ambient temperature for several weeks before imaging.
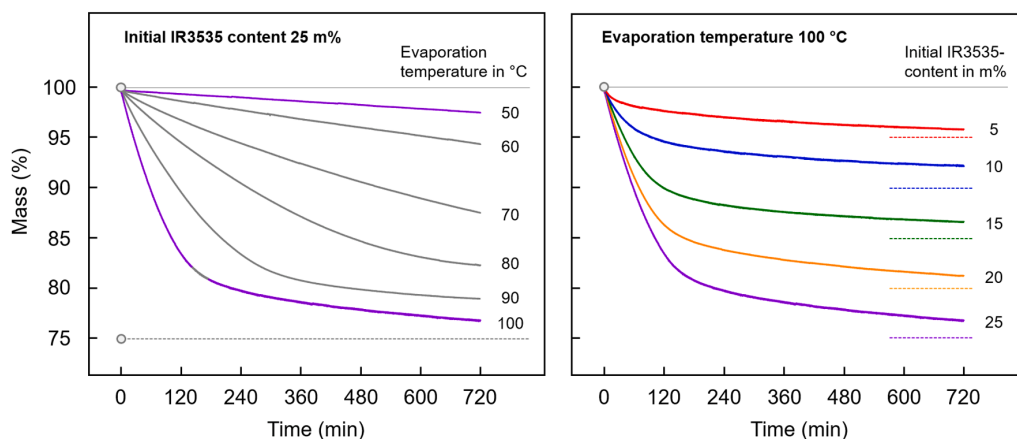
Fig. 9. Percentage mass of 3D-printed strands of a PLLA/IR3535 mixture containing 25 m% IR3535 as a function of time of annealing at temperatures between 50 and 100 °C (left), and percentage mass of 3D-printed strands of PLLA/IR3535 mixtures containing between 5 and 25 m% IR3535 as a function of time of annealing at 100 °C (right). The dash lines represent the expected final value of the samples mass after complete IR3535 evaporation.

release devices, knowledge about the evaporation characteristics at ambient and body temperature is of superior importance. The data of Fig. 9 (left plot) suggest that the repellent release at temperatures below 50 °C may last many days, impossible to measure by TGA. For this reason, it was attempted to obtain the experimentally accessible temperature-dependence of characteristic release-times between 50 and 100 °C, followed by extrapolation to the temperature of interest. Release-time constants may conveniently be determined by fitting the experimental mass-loss curves with single exponential-decay functions, yielding an exponential-decay constant [= time to reduce the IR3535-mass to $1/e \times 100$ % of its initial value]. This approach, however, seems not applicable for release-experiments performed at 90 and 100 °C. In these cases, visual inspection of the TGA-curves of Fig. 9 (left plot) suggest a double exponential decrease of the sample mass as a function of time, with a fast initial process followed by much slower release. As such, only data obtained at temperatures between 50 and 80 °C were fitted with a single-exponential decay function, as shown with equation (4), while for experiments performed at 90 and 100 °C, the time at which 63.2 % of the initial repellent content evaporated was directly obtained from the measured TGA-curves.

$$w_t = (100 - w_0) + w_0 \bullet e^{-\frac{t}{\tau}} \qquad (4)$$

In equation (4), w_t is the time-dependent total percentage sample

mass, normalized to the initial total sample mass, t is the time, w_0 is the initial m% of IR3535, and τ is a characteristic time revealing information when the sample released 63.2 % [= $(1-1/e) \times 100$ %] of the initial IR3535 content.

The left plot of Fig. 10 shows characteristic exponential-decay re-pellent-release-time constants of 3D-printed strands of PLLA/IR3535 mixtures containing between 10 and 25 m% IR3535 as a function of the evaporation temperature. Data obtained on the sample initially containing 5 m% IR3535, though analyzed, are not included since not showing the exponential temperature-dependence as in case of the strands containing between 10 and 25 m% IR3535, probably related to systematic data-evaluation errors related to TGA-experimentation when analyzing low mass-losses over long periods of time. The exponential temperature-dependence of time constants, observed for all other data sets, points to an Arrhenius-type temperature-dependence of diffusion-rate constants. For the sample initially containing 10 m% IR3535 (see blue circles), the repellent-release seems consistently slower than in the strands initially containing 15, 20, and 25 m% (gray symbols). A rough estimate of the repellent-evaporation characteristics of 3D-printed PLLA/IR3535 strands with a diameter of 300 μm at temperatures lower than 37 °C (see gray-shaded area in the left plot of Fig. 10, and star symbols) suggests that repellent is released over a period of at least 5–10 days, depending on the exact temperature.

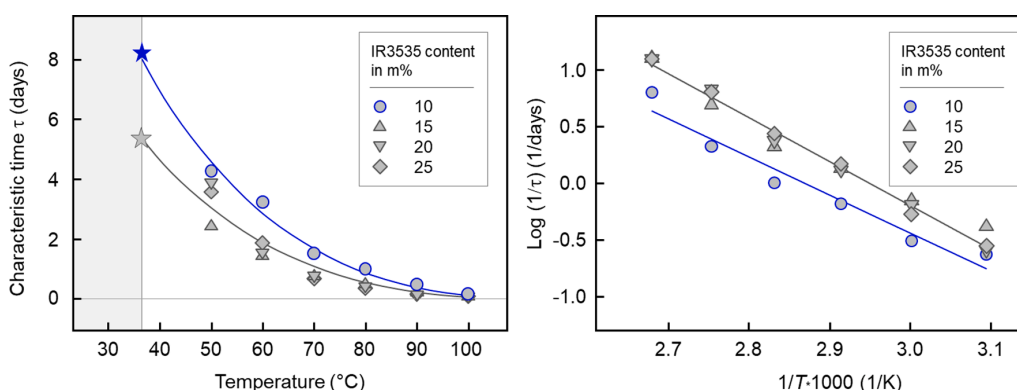Quantitative information about the release kinetics is obtained by

Fig. 10. Characteristic repellent-release time of 3D-printed strands with a diameter of 300 μm of PLLA/IR3535 mixtures containing between 10 and 25 m% IR3535 as a function of temperature (left), and logarithm of the inverse of the characteristic time, log(1/τ), as a function of inverse release temperature (1/T) (right). Each data point represents the average of at least two measurements, with the error bars being smaller than the size of the symbols, therefore not shown.

plotting the logarithm of the inverse characteristic time, $\log(1/\tau)$, as a function of the inverse release-temperature, $1/T$, shown with the right graph of Fig. 10. There is observed a linear dependence of data, suggesting an Arrhenius-type release kinetics. Linear fitting yields values of 16 days for the sample initially containing 10 m% IR3535 and 8–13 days for the samples with a repellent concentration higher than 15 m% at body temperature (37 °C). Detailed information about the fitting results are provided in the Supporting Information S5. The different repellent-release times may be related to structural differences of the PLLA matrix, controlling the diffusion of IR3535. Such structural differences can be related to heating-triggered crystallization, crystallization-caused change of the repellent-content in the amorphous PLLA/IR3535 phase, or evaporation-caused change of the glass transition temperature of the amorphous PLLA/IR3535 phase (Mapossa et al., 2021; Ryan et al., 2020).

The data of Figs. 9 and 10 are consistent with the conclusion drawn from Fig. 3, namely, that there is negligible evaporation of repellent during the 3D-printing process, regardless whether printing objects or individual strands at short or long nozzle-to-substrate distance, respectively. Considering a cooling time of only few seconds to reach the target temperature of around 25 °C of the build plate, as estimated for a typical setup in the literature (Yuan et al., 2020), the characteristic evaporation time at 100 °C is significantly longer (almost two hours for the sample containing 25 m% repellent).

4. Conclusions

Mosquito-bite protection, to inhibit transmission of diseases and to avoid pain, can be achieved by wearing personal insect-repellent-delivery devices. These can be based on polymers hosting dissolved or phase-separated liquid insect repellent, which slowly evaporates to the environment and forms a vapor barrier, repelling mosquitos. Preparation-techniques/technologies to obtain such devices, reported in the literature and holding up to 30–40 m% repellent, include melt-extrusion of strands, electrospinning of fibers, or melt-spinning of monofilaments or bi-component fibers. These technologies yield semi-finished products which, however, then need further re-processed to a wearable product. As an advantageous alternative, we propose the use of 3D-printing of parts with specific, easy to tailor geometries for obtaining end-user products. For testing the approach, we selected the polymer/repellent system poly (L-lactic acid)/ethyl butylacetylaminopropionate (PLLA/IR3535), with fundamental knowledge about the mixing-thermodynamics and phase behavior available from prior work. The performed experiments prove that the polymer/repellent system PLLA/IR3535 can be processed by 3D-printing and that solidification during 3D-printing is based on vitrification of PLLA/IR3535 solutions and PLLA-crystallization, depending on composition and time. We observed that the glass transition temperature of the solutions decreases with increasing repellent loading, requiring crystallization to obtain a solid part. Most importantly, we noted that the repellent does not degrade during 3D-printing, and thus does not lose its functionality. The maximum repellent-loading achieved 25 m% with the repellent-evaporation at body temperature lasting at least 5–10 days. Referring to a companion study performed on extruded polymer/repellent systems (Mapossa et al., 2019), we successfully proved here the general applicability of the technology of extrusion-based 3D-printing for preparation of polymer parts containing mosquito-repellent with sufficiently high concentration and release rate, raising the expectation to be used as a delivery-device. From the point-of-view of material selection, with the knowledge of the phase behavior of the polymer/repellent systems PLLA/DEET and PBS/DEET, further alternatives for generating 3D-printed insect-repellent-delivery devices are available, implicating different solidification characteristics, fine structure, maximum repellent loading, or evaporation kinetics, thus perhaps widening application ranges.

Appendix A. Supplementary material

Supplementary data to this article can be found online at https://doi.org/10.1016/j.ijpharm.2022.122023.

References

Akhtar, M.U., Focke, W.W., 2015. Trapping citronellal in a microporous polyethylene matrix. Thermochim. Acta 613, 61–65.

Alhanish, A., Abu Ghalia, M., 2021. Developments of biobased plasticizers for compostable polymers in the green packaging applications: A review. Biotechnol. Prog. 37 (6), e3210.

An, J., Teoh, J.E.M., Suntornnond, R., Chua, C.K., 2015. Design and 3D printing of scaffolds and tissues. Engineering 1 (2), 261–268.

Androsch, R., Di Lorenzo, M.L., Schick, C., 2018. Optical microscopy to study crystal nucleation in polymers using a fast scanning chip calorimeter for precise control of the nucleation pathway. Macromol. Chem. Phys. 219 (3), 1700479.

Arnauts, J., De Cooman, R., Vandeweerdt, P., Koningsveld, R., Berghmans, H., 1994. Calorimetric analysis of liquid—liquid phase separation. Thermochim. Acta 238, 1–16.

Bonadies, I., Longo, A., Androsch, R., Jehnichen, D., Göbel, M., Di Lorenzo, M.L., 2019. Biodegradable electrospun PLLA fibers containing the mosquito-repellent DEET. Eur. Polym. J. 113, 377–384.

Calori, I.R., Braga, G., de Jesus, P.D.C.C., Bi, H., Tedesco, A.C., 2020. Polymer scaffolds as drug delivery systems. Eur. Polym. J. 129, 109621.

Chaos, A., Sangroniz, A., Gonzalez, A., Iriarte, M., Sarasua, J.R., del Río, J., Etxeberria, A., 2019. Tributyl citrate as an effective plasticizer for biodegradable polymers: effect of plasticizer on free volume and transport and mechanical properties. Polym. Int. 68 (1), 125–133.

Carbolution Chemicals GmbH, Ethyl butylacetylaminopropionate Product information: https://www.carbolution.de/product_info.php?products_id=3221 (accessed 05/03/2022).

Cunha-Filho, M., Araújo, M.R., Gelfuso, G.M., Gratieri, T., 2017. FDM 3D printing of modified drug-delivery systems using hot melt extrusion: A new approach for individualized therapy. Ther. Deliv. 8 (11), 957–966.

Daminabo, S.C., Goel, S., Grammatikos, S.A., Nezhad, H.Y., Thakur, V.K., 2020. Fused deposition modeling-based additive manufacturing (3D printing): techniques for polymer material systems. Mater. Today Chem. 16, 100248. https://doi.org/10.1016/j.mtchem.2020.100248.

Di Lorenzo, M.L., Androsch, R., 2016. Stability and Reorganization of α'-Crystals in Random L/D-Lactide Copolymers. Macromol. Chem. Phys. 217 (13), 1534–1538.

Di Lorenzo, M.L., Longo, A., 2019. N, N-Diethyl-3-methylbenzamide (DEET): A mosquito repellent as functional plasticizer for poly (L-lactic acid). Thermochim. Acta 677, 180–185.

Du, F., Schick, C., Androsch, R., 2020. Full-composition-range glass transition behavior of the polymer/solvent system poly (lactic acid)/ethyl butylacetylaminopropionate (PLA/IR3535®). Polymer 209, 123058.

Du, F., Yener, H.E., Hillrichs, G., Boldt, R., Androsch, R., 2021. Crystallization-Induced Polymer Scaffold Formation in the Polymer/Drug Delivery System Poly (L-lactic acid)/Ethyl Butylacetylaminopropionate (PLLA/IR3535). Biomacromolecules 22 (9), 3950–3959.

Dubinenko, G.E., Zinoviev, A.L., Bolbasov, E.N., Novikov, V.T., Tverdokhlebov, S.I., 2020. Preparation of Poly (L-lactic acid)/Hydroxyapatite composite scaffolds by fused deposit modeling 3D printing. Mater. Today: Proc. 22, 228–234.

https://archive.epa.gov (assessed 27/10/2021); Butylacetylaminopropionate, E. WHO Specifications and Evaluations for public health pesticides.

Ferreira, I., Brünig, H., Focke, W.W., Boldt, R., Androsch, R., Leuteritz, A., 2021. Melt-Spun Poly (D, L-lactic acid) Monofilaments Containing N, N-Diethyl-3-Methylbenzamide as Mosquito Repellent. Materials 14 (3), 638.

Flory, P.J., 1949. Thermodynamics of crystallization in high polymers. IV. A theory of crystalline states and fusion in polymers, copolymers, and their mixtures with diluents. J. Chem. Phys. 17 (3), 223–240.

Gui, H., Li, Y.u., Chen, S., Xu, P., Zheng, B., Ding, Y., 2014. Effects of biodegradable imidazolium-based ionic liquid with ester group on the structure and properties of PLLA. Macromol. Res. 22 (6), 583–591.

Jariyavidyanont, K., Du, M., Yu, Q., Thurn-Albrecht, T., Schick, C., Androsch, R., 2022. Bulk enthalpy of melting of poly (L-lactic acid) (PLLA) determined by fast scanning chip calorimetry. Macromol. Rapid Commun., e2200148

Kim, S.S., Lloyd, D.R., 1992. Thermodynamics of polymer/diluent systems for thermally induced phase separation: 1. Determination of equation of state parameters, Polymer 33 (5), 1026–1035.

Kim, S.S., Lloyd, D.R., 1992. Thermodynamics of polymer/diluent systems for thermally induced phase separation: 2. Solid-liquid phase separation systems, Polymer 33 (5), 1036–1046.

Kim, S.S., Lloyd, D.R., 1992. Thermodynamics of polymer/diluent systems for thermally induced phase separation: 3. Liquid-liquid phase separation systems, Polymer 33 (5), 1047–1057.

Kishore, K., Sinha, M.K., 2021. A state-of-the-art review on fused deposition modelling process. Advances in Manufacturing and Industrial Engineering 855–864.

Mapossa, A.B., Sibanda, M.M., Sitoe, A., Focke, W.W., Braack, L., Ndonyane, C., Mouatcho, J., Smart, J., Muaimbo, H., Androsch, R., Loots, M.T., 2019. Microporous polyolefin strands as controlled-release devices for mosquito repellents. Chem. Eng. J. 360, 435–444.

Mapossa, A.B., Sitoe, A., Focke, W.W., Izadi, H., du Toit, E.L., Androsch, R., Sungkapreecha, C., van der Merwe, E.M., 2020. Mosquito repellent thermal stability, permeability and air volatility. Pest Manag. Sci. 76 (3), 1112–1120.

Mapossa, A.B., Focke, W.W., Tewo, R.K., Androsch, R., Kruger, T., 2021. Mosquito-repellent controlled-release formulations for fighting infectious diseases. Malar. J. 20 (1), 1–33.

Mapossa, A.B., López-Beceiro, J., Díaz-Díaz, A.M., Artiaga, R., Moyo, D.S., Mphateng, T. N., Focke, W.W., 2021. Properties of Mosquito Repellent-Plasticized Poly (lactic acid) Strands. Molecules 26 (19), 5890.

https://www.merckgroup.com/en/expertise/cosmetics/care-solutions/insect-repellent/faq.html (assessed 05/01/2022).

Pillin, I., Montrelay, N., Bourmaud, A., Grohens, Y., 2008. Effect of thermo-mechanical cycles on the physico-chemical properties of poly (lactic acid). Polym. Degrad. Stab. 93 (2), 321–328.

Puccetti, G., 2006. In: Insect Repellents: Principles, Methods, and Uses. CRC Press, pp. 353–360. https://doi.org/10.1201/9781420006650.ch21.

regenHU BioCAD, https://www.regenhu.com/3dbioprinting-solutions/shaper-3dprinting-software/ (assessed 05/03/2022).

Revay, E.E., Junnila, A., Xue, R.-D., Kline, D.L., Bernier, U.R., Kravchenko, V.D., Qualls, W.A., Ghattas, N., Müller, G.C., 2013. Evaluation of commercial products for personal protection against mosquitoes. Acta Trop. 125 (2), 226–230.

Rodriguez, S.D., Chung, H.N., Gonzales, K.K., Vulcan, J., Li, Y., Ahumada, J.A., Romero, H.M., De La Torre, M., Shu, F., Hansen, I.A., 2017. Efficacy of some wearable devices compared with spray-on insect repellents for the yellow fever mosquito, Aedes aegypti (L.) (Diptera: Culicidae). J. Insect Sci. 17 (1), 24.

Rupp, H., Binder, W.H., 2020. 3D Printing of Core-Shell Capsule Composites for Post – Reactive and Damage Sensing Applications. Adv. Mater. Technol. 5 (11), 2000509. https://doi.org/10.1002/admt.v5.1110.1002/admt.202000509.

Rupp, H., Binder, W.H., 2021. 3D Printing of Solvent-Free Supramolecular Polymers. Front. Chem. 9, 771974.

Rupp, H., Binder, W.H., 2021. Multicomponent Stress-Sensing Composites Fabricated by 3D-Printing Methodologies. Macromol. Rapid Commun. 42 (1), 2000450. https://doi.org/10.1002/marc.v42.110.1002/marc.202000450.

Rupp, H., Döhler, D., Hilgeroth, P., Mahmood, N., Beiner, M., Binder, W.H., 2019. 3D printing of supramolecular polymers: Impact of nanoparticles and phase separation on printability. Macromol. Rapid Commun. 40 (24), 1900467. https://doi.org/10.1002/marc.v40.2410.1002/marc.201900467.

Ryan, J.J., Casalini, R., Orlicki, J.A., Lundin, J.G., 2020. Controlled release of the insect repellent picaridin from electrospun nylon–6, 6 nanofibers. Polym. Adv. Technol. 31 (12), 3039–3047.

Schick, C., Androsch, R., 2018. Nucleation-controlled semicrystalline morphology of bulk polymers. Polym. Crystallization 1 (4), e10036.

Shin, S., Kim, T.H., Jeong, S.W., Chung, S.E., Lee, D.Y., Kim, D.-H., Shin, B.S., Uzun, E., 2019. Development of a gastroretentive delivery system for acyclovir by 3D printing technology and its in vivo pharmacokinetic evaluation in Beagle dogs. PLoS ONE 14 (5), e0216875. https://doi.org/10.1371/journal.pone.0216875.

Sitoe, A., Mapossa, A.B., Focke, W.W., Muiambo, H., Androsch, R., Wesley-Smith, J., 2020. Development, characterization and modeling of mosquito repellent release from microporous devices. SPE Polymers 1 (2), 90–100.

Sungkapreecha, C., Iqbal, N., Gohn, A.M., Focke, W.W., Androsch, R., 2017. Phase behavior of the polymer/drug system PLA/DEET. Polymer 126, 116–125.

Sungkapreecha, C., Beily, M.J., Kressler, J., Focke, W.W., Androsch, R., 2018. Phase behavior of the polymer/drug system PLA/DEET: Effect of PLA molar mass on subambient liquid-liquid phase separation. Thermochim. Acta 660, 77–81.

Sungkapreecha, C., Iqbal, N., Focke, W.W., Androsch, R., 2019. Crystallization of poly (L-lactic acid) in solution with the mosquito–repellent N, N-diethyl-3-methylbenzamide. Polym. Crystallization 2 (1), e10029.

Sungkapreecha, C., Focke, W.W., Androsch, R., 2020. Competition between liquid-liquid de-mixing, crystallization, and glass transition in solutions of PLA of different stereochemistry and DEET. Chin. J. Polym. Sci. 38 (2), 174–178.

Tavares, M., da Silva, M.R.M., de Oliviera, L.B., de Siqueira, R.A.S., Rodrigues, L., Bodjolle-d'Almeida, E.P.D., Santos, E.-J., 2018. Trends in insect repellent formulations: a review. Int. J. Pharm. 539 (1–2), 190–209.

https://www.total-corbion.com/media/eushodia/pds-luminy-l175-190507.pdf (assessed 05/01/2022).

Tümer, E.H., Erbil, H.Y., 2021. Extrusion-Based 3D Printing Applications of PLA Composites: A Review. Coatings 11 (4), 390.

Wasanasuk, K., Tashiro, K., Hanesaka, M., Ohhara, T., Kurihara, K., Kuroki, R., Tamada, T., Ozeki, T., Kanamoto, T., 2011. Crystal structure analysis of poly (L-lactic acid) α form on the basis of the 2-dimensional wide-angle synchrotron X-ray and neutron diffraction measurements. Macromolecules 44 (16), 6441–6452.

World Health Organization. World malaria report 2021. https://www.who.int/publications/i/item/9789240040496. ISBN: 978 92 4 004049 6 (assessed 05/04/2022).

B. Wunderlich, Macromolecular Physics, Vol. 2, Crystal nuclaeation, growth, annealing, Academic Press, New York, 1976.

Yener, H.E., Hillrichs, G., Androsch, R., 2021. Phase behavior of solvent-rich compositions of the polymer/drug system poly (butylene succinate) and N, N-diethyl-3-methylbenzamide (DEET). Colloid Polym. Sci. 299 (5), 873–881.

Yener, H.E., Erdmann, R., Jariyavidyanont, K., Mapossa, A.B., Focke, W.W., Hillrichs, G., Androsch, R., 2022. Slow-DEET-Release Mosquito-Repellent System Based on Poly (butylene succinate). ACS Omega 7 (10), 8377–8384.

Yuan, Y., Abeykoon, C., Mirihanage, W., Fernando, A., Kao, Y.C., Harings, J.A.W., 2020. Prediction of temperature and crystal growth evolution during 3D printing of polymeric materials via extrusion. Materials & Design 196, 109121.

Zhang, S.U., 2018. Degradation classification of 3D printing thermoplastics using Fourier transform infrared spectroscopy and artificial neural networks. Appl. Sci. 8 (8), 1224.

Supporting Information for Chapter 4.4 (3D Printing of PLLA/IR3535)

Figure S1. Storage modulus of PLLA/IR3535 strands after 3D-printing as a function of the PLLA content at room temperature.

The data were obtained on single cylindrical 3D-printed strand with an approximate diameter of around 300 µm and length of 6 mm at room temperature, using a DMTA-3E instrument from Rheometric Scientific. Measurements were performed at a frequency of 1 Hz in tensile mode, with the deformation amplitude set to 0.05 %. The data reveals a decrease of the modulus of elasticity with increasing content on IR3535, due to plasticization and the related decrease of the glass transition temperature. Samples containing less than 15 m% IR3535 are amorphous, and partial crystallization of samples containing 15 and 20 m% IR3535 cannot compensate the plasticization effect. Importantly, reproducibility of measurements performed on samples containing 15 and 20 m% IR3535 is low, and therefore data collected on such samples are, at best, considered qualitative; data points of these two samples are therefore shown in gray color, to emphasize difficulties in analyses.

Figure S2. Polarized-light optical microscopy (POM) images of the cross-section of PLLA/IR3535 3D-printed strands containing 10, 20, 25 m% IR3535 at different magnifications.

The images were obtained after long-term storage of 3D-printed strands at room temperature for about two months. Samples containing 20 and 25 m% IR3535 are partially crystallized while the sample containing 10 m% IR3535 is amorphous. Images of the left column show the epoxy-embedded strands (see yellow arrows), while the images of the right column show details of the strand cross-section.

The images are featureless at the micrometer-length scale, indicating that the liquid repellent does not (macroscopically) segregate during and after 3D-printing at the analyzed length-scale. In addition, crystals evident in samples of higher repellent concentration are not visible, suggesting absence of formation of a higher-order spherulitic superstructure. The image obtained on the sample containing 25 m% IR3535 (bottom right) shows brightening between the crossed polarizers (see their orientation in the right bottom image) which may be related to the PLLA-crystallization process during long-term annealing at room temperature.
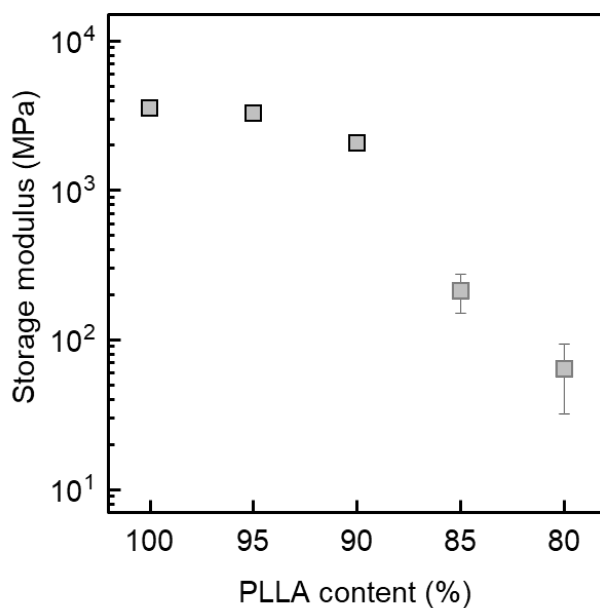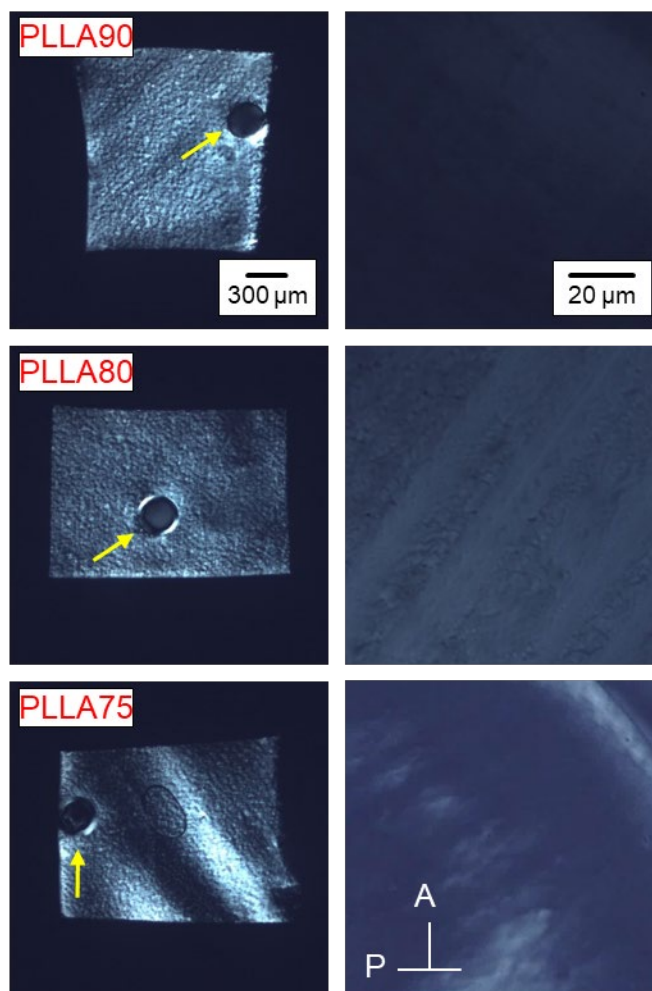
Figure S3. Atomic force microscopy (AFM) images of the cross-section of PLLA/IR3535 3D-printed strands containing 25 m% IR3535 at different magnifications.

The images were obtained on strands stored at room temperature for 6–8 months, thus being partially crystallized. The images of the top and bottom row were obtained on different samples of the printed strands, within independent experiment-sessions, for the sake of gaining information about the reproducibility of imaging.

A common/reproducible feature is the detection of two types of heterogeneities. There are observed (a) bright-appearing isolated particle-like objects and (b) a spongy/network-like matrix. Reproducibility of the shape of the isolated-particles (a) is not given.
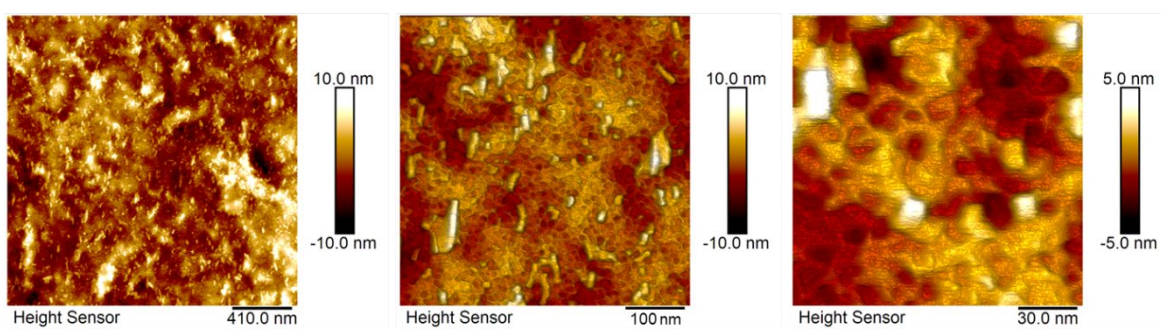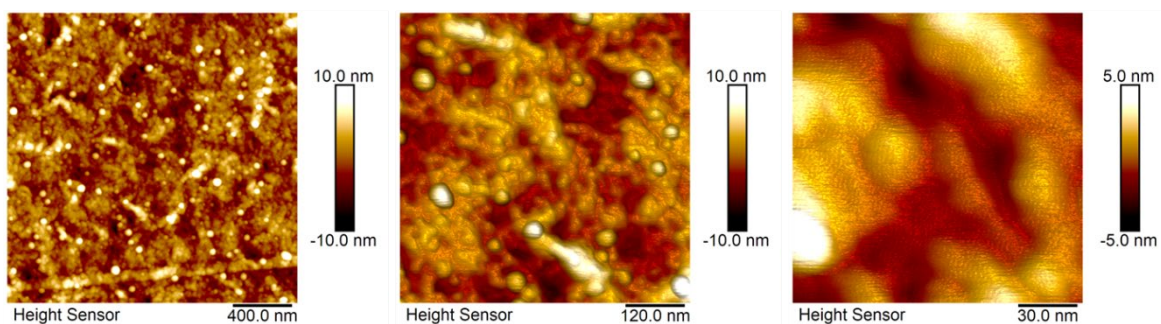
Figure S4. Percentage mass of 3D-printed strands of PLLA/IR3535 mixtures initially containing (a) 20 m%, (b) 10 m%, (c) 10 m%, and (d) 5 m% IR3535 as a function of time of annealing at temperatures between 50 and 100 °C. The expected final percentage sample mass is indicated with the dash line.
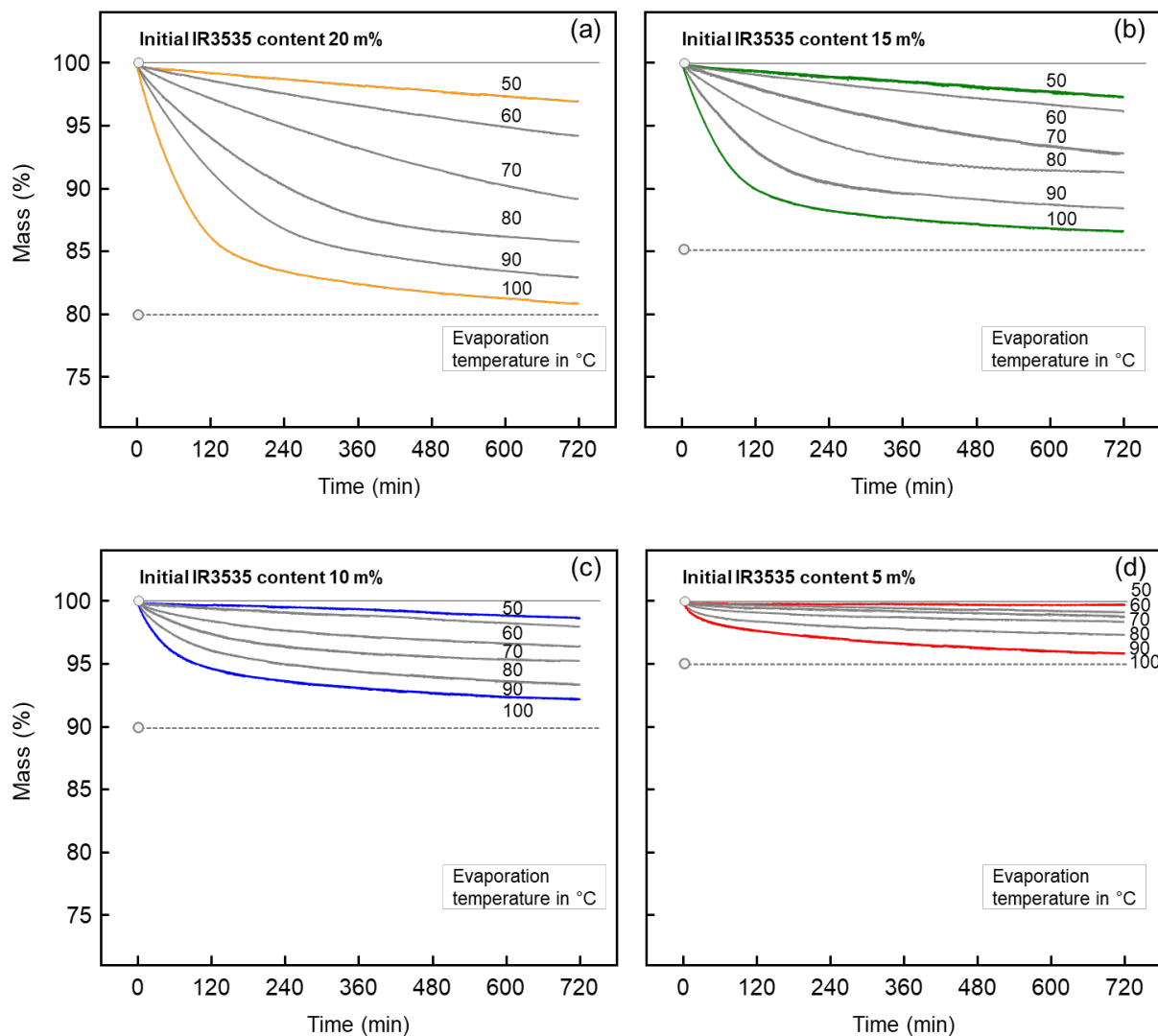
Table S1. Linear fit parameters of the dependence of the logarithm of the inverse of the characteristic release-time (log (1/τ)) as a function of the inverse of the release temperature (1/*T*)

Sample	Slope	Intercept	R^2	Characteristic time extrapolated to 37 °C (days)
PLLA90	-3365.80179	9.65712	0.95166	15.7
PLLA85	-3488.36640	10.32785	0.97310	8.3
PLLA80	-4041.49026	11.90800	0.99398	13.3
PLLA75	-4044.40364	11.92348	0.99628	13.1

4.5 Sustainable electrospun poly(ʟ-lactic acid) fibers for controlled release of the mosquito-repellent ethyl butylacetylaminopropionate (IR3535)

Fanfan Du[1*], Irene Bonadies[2], Alessandra Longo[2‖ *], Harald Rupp[3], Maria Laura Di Lorenzo[2] and René Androsch[1]

[1] Interdisciplinary Center for Transfer-oriented Research in Natural Sciences (IWE TFN), Martin Luther University Halle-Wittenberg, D-06099 Halle/Saale, Germany

[2] National Research Council (CNR), Institute of Polymers, Composites and Biomaterials (IPCB), Via Campi Flegrei 34, 80078 Pozzuoli, Italy

[3] Institut für Kunststofftechnologie und -recycling e.V., Gewerbepark 3, 06369 Weißandt-Gölzau, Germany

[‖] Present address: National Research Council (CNR), Institute of Polymers, Composites and Biomaterials (IPCB), Via Paolo Gaifami 18, 95126 Catania, Italy

Graphical abstract:

Highlights:

❖ PLLA/IR3535 mixtures with up to 40 m% IR3535 were prepared via electrospinning.
❖ Defect-free and uniform monoaxial fibers with a diameter of the order of magnitude of 1 μm were obtained.
❖ The presence of IR3535 promotes the crystallization of PLLA and the formation of orthorhombic α-crystals during electrospinning.
❖ Evaporation of IR3535 from PLLA fibers at body temperature lasts few days.

Sustainable Electrospun Poly(L-lactic acid) Fibers for Controlled Release of the Mosquito-Repellent Ethyl Butylacetylaminopropionate (IR3535)

Fanfan Du,* Irene Bonadies, Alessandra Longo,* Harald Rupp, Maria Laura Di Lorenzo, and René Androsch

Cite This: https://doi.org/10.1021/acsapm.3c00462   Read Online

ACCESS | Metrics & More | Article Recommendations | Supporting Information

ABSTRACT: Fibers composed of poly(L-lactic acid) (PLLA) and the mosquito-repellent ethyl butylacetylaminopropionate (IR3535) were prepared by solution electrospinning. Defect-free and uniform monoaxial fibers with a diameter of the order of magnitude of 1 μm were obtained. Thermogravimetric analyses showed that it is possible to incorporate more than 40 m% of IR3535 into the PLLA fibers. Thermal and structural characterization indicated that IR3535 facilitates the crystallization of PLLA and formation of orthorhombic α-crystals during electrospinning. IR3535 has a plasticizing effect on PLLA, as detected by the decrease in the glass transition temperature. The release of IR3535 from PLLA/IR3535 fibers to the environment was quantified by thermogravimetric analysis at different temperatures ranging from 60 to 100 °C, suggesting rather slow evaporation of the repellent, with a time constant of few days at body temperature. The observed results indicate a possible use of 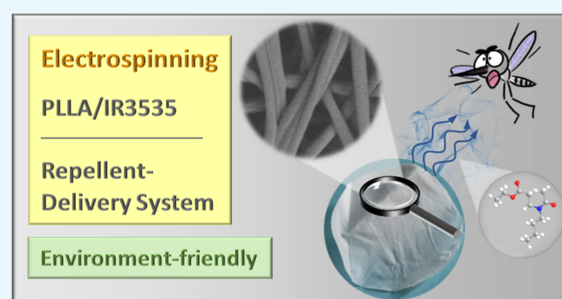electrospun PLLA/IR3535 fiber mats as part of a long-lasting repellent-delivery system and application in the field of combating diseases caused by mosquito bites.

KEYWORDS: solution electrospinning, poly(L-lactic acid) (PLLA), ethyl butylacetylaminopropionate (IR3535), uniform fibers, repellent release

INTRODUCTION

Mosquito-transmitted diseases, such as malaria, are a major threat to global human health, affecting hundreds of millions of people each year,[1] mostly children. In 2021, about 80% of all malaria-related casualties in Africa were children whose age had not reached five years yet.[2] There is an urgent need to find a solution to reduce such tremendous risk, possibly by developing vector-control devices that can be used also for babies and young children. Incorporation of insect-repellents into polymer nanofibers by electrospinning seems a rather feasible approach for generation of such a long-lasting repellent-release device.

Electrospinning, as a versatile fabrication technique, allows for the production of continuous fibers from solutions or melts, predominantly polymers. The continuous fibers have diameters varying from several micrometers down to a few nanometers, depending on the involved material properties and processing parameters.[3−6] Nanofibers of polyamide, e.g., used for production of fabrics, containing insect-repellents were successfully produced by electrospinning,[7−9] demonstrating the feasibility of this approach. For example, the repellents 2-(2-hydroxyethyl)-1-piperidinecarboxylic acid 1-methylpropyl

ester (picaridin) and *N*,*N*-diethyl-3-methylbenzamide (DEET) were incorporated into polyamide 66 (PA 66), with these fibers containing up to 50 m% of the repellent. For the case of picaridin-loaded fibers, release at 100 °C was still detected after 300 min, with an extrapolated half-time of about 130 h at 20 °C, while for DEET-containing fibers, repellency for about 200 h was estimated, exceeding, time-wise, common topical application.[7,8] In another work, the insecticide (3-phenoxyphenyl)methyl 3-(2,2-dichloroethenyl)-2,2-dimethyl-cyclopropane-1-carboxylate (permethrin) was added into a polyamide 6 (PA 6) solution for electrospinning, with the obtained fibers subsequently dip-coated on plasma-treated fiber surfaces.[9] The obtained permethrin-treated fabrics showed repellency and led to a higher percentage of mosquito escape compared to untreated preparations. DEET was also

incorporated into pyromellitic dianhydride (PMDA)/β-cyclo-dextrin-based nano-sponge microfibers, providing repellent release for over two weeks.[10]

Our own efforts in the research field of developing insect-repellent-release devices target the employment of biobased and therefore environment-friendly polymers, which, in addition, are biodegradable and biocompatible. As such, poly(L-lactic acid) (PLLA), fulfilling these demands,[11] was used for obtaining nanofibers by electrospinning, containing DEET at concentrations exceeding 50 m%, allowing a delayed evaporation of DEET compared to evaporation of the pure repellent.[12] In the context of sustainability, in the present study, DEET is replaced by biodegradable ethyl butylacetyla-minopropionate (IR3535), an insect repellent with a chemical structure resembling that of natural β-alanine, showing less side effects on both the environment and human beings, with applicability even for pregnant women and children.[13,14]

Initial studies demonstrated that PLLA can serve as a carrier/reservoir for IR3535 for its controlled and retarded release to the environment, aiming at the preparation of polymeric scaffolds by polymer crystallization-based thermally induced solid−liquid phase separation (S-L TIPS).[15] Micro-porous scaffolds of different fine structures were obtained from PLLA/IR3535 solutions, by adjusting the crystallization temperature and the polymer content. It was shown that the repellent was entrapped within intra- and interspherulitic pores of PLLA, and the size of intraspherulitic pores increased with the crystallization temperature and the IR3535 content. Prerequisite for S-L TIPS is solubility of the system components,[16,17] which advantageously has been investigated by using non-crystallizable poly(D/L-lactic acid) (PDLLA) as a polymer component, in analogy to earlier studies using DEET as a repellent.[18,19] Note that when using a non-crystallizable polymer component, mixing and demixing on temperature variation may not be masked by melting or crystallization, respectively. As such, in-depth analysis of the glass transition temperature by employing fast scanning chip calorimetry combined with in situ evaporation of the liquid to achieve controlled change of the system composition has revealed that PDLLA and IR3535 are thermodynamically miscible in the entire composition range.[20] Regarding the polymer-rich part of the PLLA/IR3535 system, IR3535 acts as a functional plasticizer of PLLA,[21,22] offering additional advantages from the point of view of reducing the inherent brittleness of PLLA.[23,24] Recently, PLLA-parts/products accommodating up to 25 m% of IR3535 were manufactured by classical melt extrusion[21,22] and 3D printing,[25] emphasizing their potential for controlled long-term release of IR3535. Since in the case of electrospun fibers, the carrier geometry/shape is qualitatively different compared to scaffold-like bulk structures and products with a rather low surface-to-volume ratio, it is expected that the IR3535-release characteristics are different, and that personal-protection devices based on fibers can be generated.

In this work, the possibility of incorporation of IR3535 into PLLA by electrospinning is evaluated, focusing on the effects of electrospinning parameters and fiber composition on the fiber morphology, physical structure, and repellent-release kinetics.

■ EXPERIMENTAL SECTION

Materials and Preparation. An extrusion-grade PLLA contain-ing more than 99% L-isomer, named L175, was provided by Total Corbion (Amsterdam, The Netherlands). The melt-flow rate of this

PLLA grade is 8 g/10 min (210 °C, 2.16 kg),[26] and the mass-average molar mass is 120 kg/mol.[27] IR3535, purchased from Carbolution Chemicals GmbH (St. Ingbert, Germany),[28] had a purity of 98% and was utilized as received without further purification. It is a transparent liquid at room temperature and has a glass transition temperature of approximately −90 °C.[20,28] The boiling point at atmospheric pressure is slightly below 300 °C and about 110 °C at 0.02 kPa, and its vapor pressure at 20 °C is reported being around 0.15 Pa.[13,29] Chloroform (CHCl$_3$) and dimethylformamide (DMF) with a purity ≥99.8%, both used as solvents for the electrospinning process, were obtained from Sigma-Aldrich (Burlington, USA) and used as received without further purification. PLLA solutions were prepared by dissolving PLLA in CHCl$_3$ or a CHCl$_3$/DMF 90/10% v/v solution at room temperature. Then, IR3535 was added to the PLLA/CHCl$_3$ or PLLA/(CHCl$_3$/DMF) solutions in the needed amounts. Detailed information about sample formulations is provided in Table 1. The

Table 1. Formulation of PLLA/IR3535/(CHCl$_3$/DMF) Solutions

code[a]	PLLA (mg)	CHCl$_3$ (mL)	DMF (mL)	IR3535 (mL)	Ex.[b]	Me.[c,d]
P10IR0	500	4.5	0.5	0	0	0
P10IR1	500	4.5	0.5	0.1	16.7	16.1 ± 1.6
P10IR2	500	4.5	0.5	0.2	28.6	28.6 ± 0.4
P10IR3	500	4.5	0.5	0.3	37.5	36.7 ± 1.2
P10IR4	500	4.5	0.5	0.4	44.4	43.3 ± 3.1
P12.5[e]	625	5			0	
P12.5IR0	625	4.5	0.5	0	0	
P15IR0	750	4.5	0.5	0	0	

[a]P*X*IR*Y*, P represents polymer PLLA and the subsequent number *X* indicates the PLLA content in the initial solutions with CHCl$_3$/DMF 90/10% v/v [= (mass of polymer in g)/(volume of solvent in mL) × 100]; IR is the acronym of IR3535 and the subsequent number *Y* indicates the volume (in 0.1-mL units) of IR3535 added to the PLLA/(CHCl$_3$/DMF) solutions. [b]Ex. represents the expected IR3535 content in PLLA fibers (m%). [c]Me. represents the measured IR3535 content in PLLA fibers (m%). [d]Standard deviation is observed by non-isothermal TGA experiments, measured at 5 and 10 K/min, for a total of three times. [e]PLLA dissolved into CHCl$_3$ without DMF.

sample codes (left column) contain four parts. The first letter (P) and the subsequent number denote the polymer content in the initial solutions with either CHCl$_3$ or CHCl$_3$/DMF [= (mass of polymer in g)/(volume of solvent in mL) × 100]. The second acronym (IR) and the subsequent number represent the volume (in 0.1-mL units) of IR3535 added to the PLLA/CHCl$_3$ or PLLA/(CHCl$_3$/DMF) solutions. As such, there were prepared initial solutions containing 6.5, 8.0, and 9.5 m% PLLA in 90/10% v/v CHCl$_3$/DMF solvent, and 7.7 m% PLLA in CHCl$_3$, while different amounts of IR3535 were added to solutions containing 6.5 m% PLLA.

Instrumentation. *Electrospinning Apparatus.* An Electrospin-ning Setup NF103 (MECC Co., Ltd., Fukuoka, Japan) was employed to produce electrospun monofilament fibers, using a single nozzle and a plate collector. After optimization of the process parameters, detailed below, the flow rate was set at a fixed value of 0.2 mL/h. The applied voltage and the distance between the nozzle and the collector, covered with aluminum foil, were set to 20 kV and 25 cm, respectively, to ensure the production of defect-free/flawless fibers for further characterization. Electrospinning was performed at room temperature and a relative humidity of 15−35%. Using a stationary collector, in-plane randomly oriented fiber mats were observed. For thermal and structural analysis and measurement of the kinetics of the repellent release, fibers were collected for about 2 h.

Thermogravimetric Analysis (TGA). Thermal degradation of pure PLLA fibers, the content of repellent in electrospun PLLA/IR3535 fibers, and the repellent-release kinetics were investigated using a TGA 2 LF/1100/694 (Mettler-Toledo, Greifensee, Switzerland). In
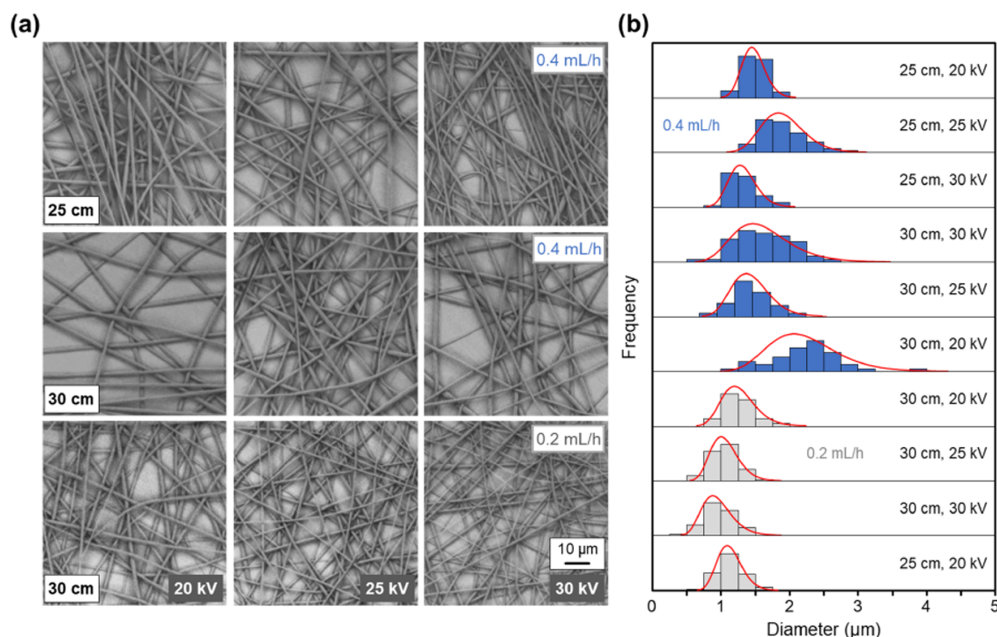
B

Figure 1. SEM micrographs (a) and diameter-distribution (b) of fibers produced from $CHCl_3$/DMF 90/10% v/v solutions containing 10% m/v PLLA (P10IR0) at voltages of 20, 25, and 30 kV using flow rates of 0.2 and 0.4 mL/h and nozzle-to-collector distances of 25 and 30 cm, as indicated. The scale bar in the bottom right micrograph applies to all images. The diameter of fibers for each condition was estimated by analysis of 50 fibers. Note that fibers observed using a nozzle-to-collector distance of 25 cm, voltage of 20 kV, and flow rate of 0.2 mL/h are not shown; however, their diameter-distribution is reported in the bottom of (b). All histograms in (b) are fitted by a lognormal distribution.

terms of non-isothermal IR3535-evaporation experiments, sample pieces with a mass of 1.5 ± 0.1 mg were prepared by cutting the fiber mats and placing them into alumina crucibles with a volume of 70 μL before heating them from 30 to 600 °C at 5 K/min in a N_2 atmosphere with a flow rate of 50 mL/min. The instrument software automatically subtracts the blank curve to obtain the measured data. The samples were also measured at 10 K/min. Fibers of each concentration were measured a total of three times. For isothermal IR3535-release experiments, samples with a mass of 1.5 ± 0.1 mg were heated to desired temperatures ranging from 60 to 100 °C at a rate of 20 K/min in a N_2 atmosphere with a flow rate of 50 mL/min and then kept at these temperatures for 12 h to allow evaporation of the repellent. After the isothermal release of the repellent, the sample was further heated to 600 °C at 5 K/min in a N_2 atmosphere to analyze the remaining repellent content in the fibers. The instrument software automatically subtracts the blank curve to obtain the measured data.

Scanning Electron Microscopy (SEM). An FEI Phenom Desktop Scanning Electron Microscope (Thermo Fisher Scientific, Eindhoven, The Netherlands) was used to observe the morphology of the fibers. Prior to analysis, the samples went through coating with a Au–Pd alloy using a Baltec Med 020 Sputter Coater System (Balzers AG, Balzers, Liechtenstein) and were subsequently mounted on aluminum stubs. ImageJ software (National Institutes of Health, Bethesda, USA) was utilized to analyze the average fiber-diameter distribution.

Nuclear Magnetic Resonance Spectroscopy (NMR). Proton NMR (^{1}H NMR) spectra were obtained using a Varian Gemini 400 spectrometer (Agilent Technologies Co., Santa Clara, USA) at 27 °C with deuterated chloroform ($CDCl_3$) as a solvent and 10 μL of toluene as a calibration standard. MestReNova software (version 9.0.1-13254) was used to interpret the NMR spectra, and chemical shifts in ppm were referenced to the $CDCl_3$ solvent signal.

Differential Scanning Calorimetry (DSC). Calorimetric analyses of fibers were carried out using a calibrated heat-flux DSC 1 (Mettler-Toledo, Greifensee, Switzerland) equipped with the FRS5 sensor. The calibration of temperature and heat-flow rate signals of the calorimeter

was performed by analyzing the extrapolated onset temperature and area of the melting peak of indium, respectively. The instrument was attached to a Huber TC100 intracooler (Peter Huber Kältemaschinenbau AG, Offenburg, Germany), and the furnace was purged with nitrogen gas at a flow rate of 60 mL/min. Samples with a mass between 2 and 3 mg were placed in 20 μL aluminum pans with pin and covered with lid. Each sample was subjected to heating from −50 to 200 °C at a rate of 20 K/min, keeping at this temperature for 3 min and re-cooling to −50 °C at a rate of 10 K/min, enabling analyses of the glass transition, crystallization, and melting behavior of the fibers. All experiments were conducted at least twice to ensure repeatability, with a fresh specimen used for each analysis.

Wide-Angle X-ray Scattering (WAXS). X-ray scattering experiments were performed to analyze the structure of PLLA fibers after electrospinning in transmission mode employing a Retro-F laboratory setup (SAXSLAB, Holyoke, USA) equipped with a microfocus X-ray source (AXO Dresden GmbH, Dresden, Germany) and an ASTIX multilayer X-ray optics (AXO Dresden GmbH, Dresden, Germany) as a monochromator for Cu Kα radiation with a wavelength of 0.154 nm. Aluminum discs with a central hole (diameter of 2 mm) were used as sample holders. Measurements were recorded at vacuum conditions using a PILATUS3 R 300K detector (Dectris AG, Baden-Daettwil, Switzerland). The sample-to-detector distance and measurement time were 86 mm and 300 s, respectively.

Fourier Transform Infrared Spectroscopy (FTIR). Attenuated total reflection (ATR)-FTIR spectra were acquired on a PerkinElmer FTIR Spectrometer Model Spectrum 100 (PerkinElmer, Inc., Waltham, USA) equipped with a PerkinElmer Universal ATR sampling accessory with a diamond crystal. Background-corrected spectra with a resolution of 4 cm^{-1} were obtained in the wavenumber range from 4000 to 650 cm^{-1}, averaging 16 scans.

■ RESULTS AND INITIAL DISCUSSION

Optimization and Selection of Electrospinning Parameters. To analyze the effect of the solution character-

istics (solvents and polymer concentration) and processing parameters (voltage, nozzle-to-collector distance, and feed rate) on the morphology of fibers, both sets of variables were changed systematically and then the morphology and diameters of obtained fibers were analyzed.

First, the influence of the solvent on the fiber morphology was analyzed. We tested $CHCl_3$ and DMF, which are both good solvents for PLLA.[30] As demonstrated with the SEM micrographs shown in the Supporting Information (SI) Figure S1, starting from a polymer solution of 12.5% m/v in $CHCl_3$ (Figure S1a), the fiber morphology was modified by adding DMF at low amounts while keeping the processing parameters of 25 kV, 30 cm, and 0.5 mL/h constant (Figure S1b). In fact, as evidenced by SEM micrographs (Figure S1), beaded fibers with different diameters were obtained by using only $CHCl_3$, whereas, with the mix of solvents, fibers became homogeneous and uniform in size. This result is related to the addition of DMF, being a dipolar aprotic solvent with a high dielectric constant/polarity and low vapor pressure, that facilitates the electrospinning process and enhances the stretching of the solution jet.[31−35] Therefore, contributing to the generation of good, that is, bead-free fibers, the 90/10% v/v mix of $CHCl_3$ and DMF is used as a solvent.

After solvent selection, the polymer concentration in the solutions is evaluated for optimization. The polymer concentration and molar mass are parameters that distinctly impact nanofiber production since they determine the extent of chain entanglement in the solution. If the molar mass of the polymer is constant, then the number of entanglements increases with the polymer concentration, being above the critical entanglement concentration.[36] Figure S2 shows the morphology of PLLA fibers prepared from solutions with a PLLA content of 15% m/v (P15IR0, Figure S2a), 12.5% m/v (P12.5IR0, Figure S2b), and 10% m/v (P10IR0, Figure S2c) in 90/10% v/v $CHCl_3$/DMF using identical flow rates and nozzle-to-collector distances but different voltages of 20 kV (top row), 25 kV (center row), and 30 kV (bottom row). For P15IR0 and P12.5IR0 solutions, a voltage of 20 kV leads to generation of discontinuous fibers containing spindle-like beads. Thinner and more uniform fibers, with a circular cross section, are observed by decreasing the PLLA concentration to 10% m/v. Furthermore, it is noticeable that at a constant concentration, it is possible to obtain uniform and thinner fibers by increasing the voltage (see Figure S2). Thus, the solution containing 10% m/v PLLA has been selected to further study the effect of processing parameters on fiber morphology.

After evaluation of the effects of the solvent composition and the polymer concentration, the influence of the processing parameters on the fiber morphology is studied. Figure 1 shows the micrographs of fibers generated from P10IR0 solutions prepared at different processing conditions (Figure 1a) and related fiber-diameter distributions (Figure 1b). All PLLA fibers appear uniform, and the diameter distribution is monomodal. Regarding the electrospinning conditions, a clear trend is only observed by varying the flow rate. At the same nozzle-to-collector distance and voltage, the fiber diameter is smaller when using a lower flow rate (see center- and bottom-row images in Figure 1a as well as Figure 1b). Otherwise, systematic variation of the voltage, and using different nozzle-to-collector distances, has an only minor effect on the fiber diameter.

Electrospinning of PLLA Fibers Containing IR3535. After optimizing the solution characteristics and processing parameters, the morphology of fibers containing different amounts of repellent is analyzed. Figure 2 shows, in the left
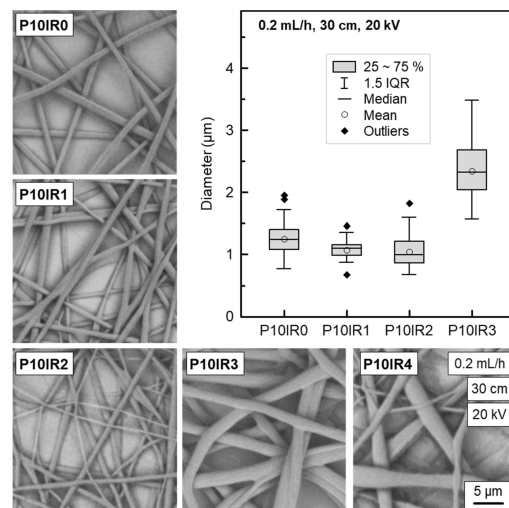

Figure 2. SEM micrographs and fiber-diameter distribution, presented as a boxplot, of PLLA/IR3535 fibers prepared from ($CHCl_3$/DMF)/ IR3535 solutions, containing different amounts of IR3535, as indicated (see also Table 1). Fibers were prepared using a flow rate of 0.2 mL/h, a voltage of 20 kV, and a nozzle-to-collector distance of 30 cm. The scale bar in the bottom right micrograph applies to all images. In the boxplot, the lower and upper end of the box correspond to the first and third quartiles (the 25th and 75th percentiles), and the solid line within the box indicates the median. The upper whisker extends from the upper end of the box to the maximum value no more than 1.5 times of the Interquartile Range (IQR, distance between the first and third quartiles) from the end of the box. The lower whisker correspondingly extends from the lower end of the box to the minimum value at most 1.5 times of the IQR of the end of the box. Data beyond the end of the whiskers are considered outliers. The diameter of fibers for each condition was estimated by analysis of 50 fibers.

part, the SEM micrographs of PLLA/IR3535 fibers containing different amounts of IR3535, increasing from top to bottom and, in the right part, the related diameter distributions. For the selected, constant electrospinning conditions (flow rate 0.2 mL/h, voltage 20 kV, nozzle-to-collector distance 30 cm), increasing the amount of IR3535 causes the cross-section change from circular to flat-ribbon-like, because, as explained before, the presence of additives lowers the vapor pressure of the solvent mixture ($CHCl_3$/DMF + IR3535) and delays evaporation of $CHCl_3$/DMF from the polymer jet, thus reducing the stretching of the solution jet.[31,35,37] The fibers all have a smooth surface and exhibit a uniform structure without beads, except those prepared from P10IR4 solutions, containing the largest amount of IR3535, where the presence of beads is observed, as shown in Figure S3. In the sample P10IR3, fibers look partially attached to each other, while fibers with lower IR3535 content appear isolated. All fibers (besides the fibers prepared from P10IR4 solutions) show a monomodal fiber-diameter distribution; however, the width of the distribution increases with the IR3535 content. Overall, the addition of IR3535 has only a slight impact on both the

average fiber diameter and the polydispersity at identical processing conditions, except in the case of fibers with the highest repellent content.

The effect of processing parameters (voltage and distance) on fiber formation from solutions containing IR3535 was also studied, in particular for the sample P10IR3, demonstrated with the micrographs and fiber-diameter boxplot in Figure 3.
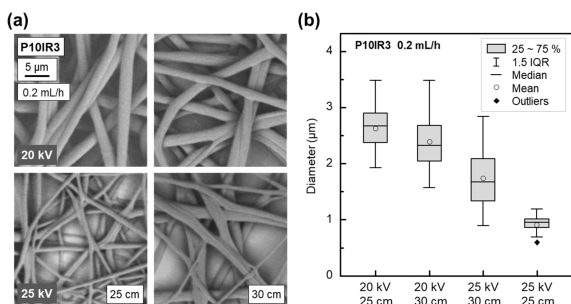

Figure 3. SEM micrographs of fibers electrospun from P10IR3 solutions at the indicated voltage and nozzle-to-collector distance using a flow rate of 0.2 mL/h (a). Fiber diameters are shown as boxplot (b). The diameter of fibers for each condition was estimated by analysis of 50 fibers.

The feed rate was fixed at 0.2 mL/h, and the distance and voltage were changed as indicated. As such, when applying a voltage of 25 kV, the fiber diameter increases by increasing the nozzle-to-collector distance, whereas at a voltage of 20 kV, the distance has no significant effect on the fiber diameter. Most uniform and thinner fibers are obtained at 25 kV and 25 cm nozzle-to-collector distance. Therefore, optimum processing parameters for obtaining PLLA fibers containing the insect-repellent IR3535 in the solutions include a combination of a voltage of 25 kV, a nozzle-to-collector distance of 25 cm, and a flow rate of 0.2 mL/h.

Repellent Content in Electrospun PLLA Fibers. The content of IR3535 in electrospun fibers was evaluated by TGA

upon heating and purging the sample environment with nitrogen at a flow rate of 50 mL/min. The left plot of Figure 4 shows the TGA curves (Figure 4a), while in the right plot, their first derivatives are shown (Figure 4b). The degradation of neat IR3535, measured at identical conditions in an independent study,[25] commences at around 100 °C and is completed at about 200 °C, with the highest evaporation rate occurring at 185 °C. For PLLA fibers containing IR3535, two mass loss events are observed. The low-temperature mass-loss event at the lower temperature is attributed to the evaporation of the repellent IR3535, while the high-temperature mass-loss event is caused by decomposition of PLLA. The presence of a single evaporation-related mass-loss step below 200 °C proves the absence of residual $CHCl_3$ and DMF in the prepared fibers, as also confirmed by NMR measurements in Figure S4 (the characteristic peaks of DMF at 2.88, 2.96, and 8.02 ppm in $CDCl_3$ are not observed). The degradation of PLLA in the repellent-containing fibers begins at the same temperature as in pure PLLA fibers, indicating that there is no effect of IR3535 on the thermal stability of PLLA. A nearly constant mass plateau at around 250 °C is observed for all PLLA fibers containing IR3535 when evaporation of the repellent is completed (see also the vertical arrow in Figure 4b, verifying the zero slope of the TGA curves at around 250 °C), enabling an estimation of the actual IR3535 content in the fibers. The observed data suggest that the measured IR3535 content in the fibers is close to the concentration in the solutions, with quantitative data provided in Figure 4a. This result indicates that there is no distinct evaporation of the liquid IR3535 during electrospinning, conducted at ambient conditions. The content of IR3535, determined by non-isothermal TGA, is confirmed by isothermal TGA measurements of the repellent-release kinetics, discussed below.

Structure of PLLA in Electrospun PLLA/IR3535 Fibers. Information regarding the physical structure of PLLA in electrospun fibers was obtained by DSC and WAXS. Figure 5a shows the DSC curves, recorded on heating at 20 K/min, of PLLA/IR3535 fibers with different compositions, increasing from bottom to top. Regarding neat PLLA fibers (bottom
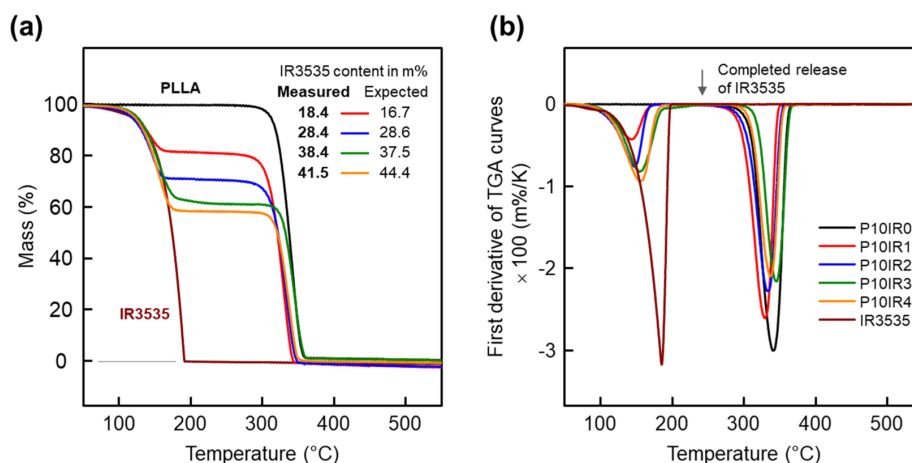
Figure 4. TGA curves of neat PLLA, neat IR3535, and PLLA/IR3535 electrospun fibers, normalized mass as a function of temperature, obtained using a heating rate of 5 K/min and N_2 as a purge gas (a) and first derivative of the TGA curves (b). Measurements were performed on the fiber mat samples prepared at a voltage of 20 kV, a flow rate of 0.2 mL/h, and a nozzle-to-collector distance of 25 cm. IR3535 data were adapted with permission from ref 25. Copyright 2022 Elsevier.
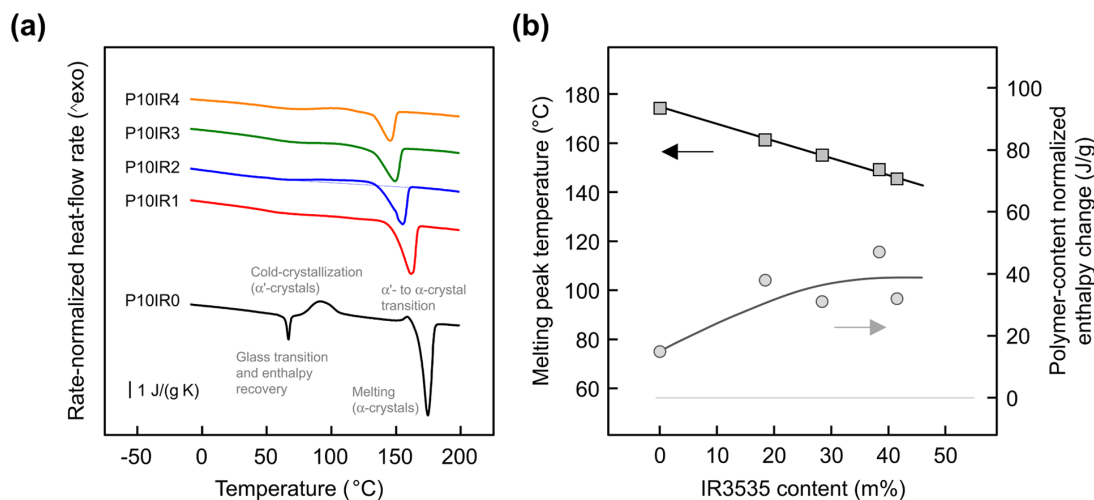
Figure 5. DSC curves, rate-normalized heat-flow rate as a function of temperature, of PLLA/IR3535 fibers recorded during heating at 20 K/min (a) and melting peak temperature (squares) and polymer content-normalized enthalpy change (circles) as a function of the repellent content (b).

curve, black), a glass transition at about 60 °C, overlapping with an enthalpy-recovery peak resulting from storage at room temperature and physical aging of the glassy phase,[38−40] a cold-crystallization peak at about 91 °C, a further small exothermic peak slightly above 150 °C, and then a melting peak at about 174 °C are detected with increasing temperature. Cold-crystallization yields metastable α'-crystals,[41,42] which first transform to α-crystals[43−46] before their melting near 180 °C. The presence of the repellent IR3535 in the fibers influences the occurrence and location of all these thermal events. The glass transition becomes weaker and its temperature decreases with increasing repellent content as is expected from an earlier in-depth study,[20] that is, the repellent acts as a plasticizer (also see the cooling curves after first heating in Figure S5) in the amorphous PLLA phase.[21] Furthermore, distinct cold-crystallization in PLLA fibers containing IR3535 is absent, suggesting that crystallization during electrospinning is enhanced in these samples. Similar enhancement of crystallization of PLLA was also noted upon electrospinning of PLLA/DEET fibers.[12] In addition, the melting temperature of crystals in PLLA/IR3535 fibers systematically decreases with increasing amount of IR3535, which likely is attributed to the solvent-caused equilibrium melting point depression according to Flory.[47−49] Quantitative data about melting-peak temperatures as a function of the repellent content are shown with the squares and left axis in Figure 5b, while the circles and right axis provide information about the polymer content-normalized total enthalpy change (considering both the enthalpy of melting and enthalpy of cold-crystallization) during heating, being proportional to the enthalpy-based PLLA crystallinity.[50−52] As such, the crystallinity in neat PLLA fibers is negligible, while for fibers containing IR3535, sizable amount of crystals is evident. A rough estimation of the crystal fraction in fibers containing 42 m% IR3535 (sample P10IR4) yields a value of 38% [= 34 J/g (measured enthalpy of crystallization)/90 J/g (bulk enthalpy of melting of α-crystals with a melting temperature of 150 °C)[50,52] × 100%]. Obviously, the addition of IR3535 increases the mobility of the polymer chains, causing a decrease in the glass transition temperature and allowing for faster crystallization of PLLA.

This is consistent with a previous, quantitative study of the kinetics of solution-crystallization of PLLA.[15,53]

Figure 6 presents the WAXS curves obtained on the electrospun PLLA fiber mats containing varying amounts of
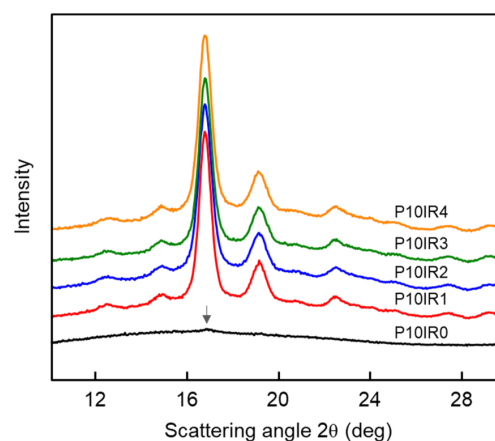
Figure 6. WAXS curves of PLLA/IR3535 fibers containing varying amounts of IR3535 as indicated.

IR3535. The WAXS pattern of neat PLLA fibers exhibits a very weak peak at a scattering angle 2θ of 16.8° (see arrow), which indicates the presence of only minor amount of crystals, in agreement with the DSC data discussed above. All PLLA/IR3535 fibers display two prominent scattering peaks at scattering angles 2θ of 16.8 and 19.1° and relatively strong peaks at 14.9 and 22.5°, being attributed to the (110)/(200), (203), (010), and (015)/(211) lattice planes of the orthorhombic unit cell of the α-crystal form.[41,42,54] Further, rather weak peaks are detected at scattering angles of 12.6, 20.8, 24.0, and 25.2°, by scattering at the (004/103), (204), (016), and (206) planes, respectively.[41,42,54] As such, as suggested by the peak positions, the presence of liquid repellent favors the formation of ordered α-crystals of PLLA instead of α'-crystals. A similar result, that is, α-crystal

formation on solution-crystallization, regardless of the crystallization temperature, has been observed in independent studies.[15,18,55]

The interaction between PLLA and IR3535 was verified by ATR-FTIR, as shown in Figure S6. In the spectra of pure IR3535, the most prominent absorbance bands are the two carbonyl-stretch vibrations associated with the ester group at 1730 cm^{-1} and amide group at 1639 cm^{-1} (see Figure S6a); the C−H bending vibration at 1421 cm^{-1} is also clearly distinguishable from the PLLA bands; they are indicated by the three vertical dashed lines at the top of Figure S6b. It is worth noting that upon incorporating IR3535 into the PLLA fibers, a slight increase in the wavenumber of the carbonyl stretching at around 1640 cm^{-1} was observed. This shift in carbonyl stretching and its peak shape changing from symmetric to asymmetric indicate the possibility of interaction between IR3535 and PLLA within the polymer nanofibers.

Repellent Release. In the context of applying PLLA/IR3535 fibers as repellent-release devices, understanding the release rate/evaporation characteristics at ambient and body temperature is important. Isothermal TGA experiments at temperatures ranging from 60 to 100 °C were conducted to investigate the kinetics of the repellent release from the polymer. The reason for choosing this temperature range is the sufficiently fast repellent release for its convenient monitoring at the time scale of minutes and hours. A direct measurement of the repellent release at ambient temperature, using TGA, is complicated since it lasts for days or weeks. However, based on the assumption that the release mechanism and the physical structure of the fibers are not changing between ambient temperature and 100 °C, it is anticipated that the data collected at higher temperatures allow an extrapolation to lower temperatures. The preservation of the sample structure and the absence of IR3535 evaporation from the fibers while heating the samples from near room temperature to the release temperature are proven by thermal analysis as the DSC data obtained on the PLLA/IR3535 fibers on heating at 20 K/min (see Figure 5a) indicate the absence of melting and distinct cold-crystallization in this temperature range. The structure of PLLA in the fibers may change during isothermal evaporation, including the vitrification of the amorphous phase (due to the increase in the glass transition temperature during evaporation at temperatures lower than 60 °C)[20] and crystal reorganization, often causing annealing peaks in DSC experiments.[56,57] However, whether the mobility of the amorphous phase and crystal morphology exhibit measurable effects on the release characteristics of IR3535 is not yet clear.

Figure 7 depicts the repellent release from PLLA/IR3535 fibers initially containing different IR3535 amounts at a temperature of 100 °C and also the release for fibers generated from P10IR2 solution at 60 and 80 °C to demonstrate exemplarily the effects of the initial concentration of the repellent and the evaporation temperature, respectively. The full set of collected TGA curves is available in Figure S7. The data yield information about the kinetics of the repellent release and the repellent content in the fibers. The latter is provided in the legend, with the listed mass-percentages being averages obtained from data collected at three different temperatures (60, 80, and 100 °C). After the isothermal release of the repellent for 720 min (12 h), samples were heated to detect any repellent that was not yet released in the isothermal evaporation stage. The total repellent content is then calculated as sum of repellent released at the isothermal
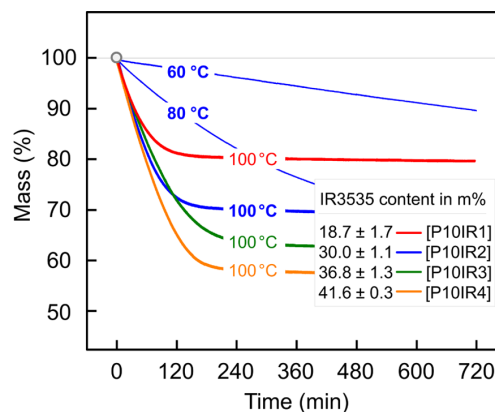

Figure 7. Isothermal TGA curves of fibers prepared from the solutions P10IR1 (red), P10IR2 (blue), P10IR3 (green), and P10IR4 (orange) recorded at 100 °C. For fibers prepared from the solution P10IR2, evaporation at 80 and 60 °C is also shown (blue). The legend provides information about the IR3535 content, with the calculation details given in the text.

stage plus repellent released during subsequent heating. The observed data show close agreement with data obtained from non-isothermal TGA measurements (see Figure 4a). Regarding the effect of repellent content on the repellent release rate, the higher the repellent content, the faster the repellent release rate. IR3535 has a plasticizing effect on PLLA, which increases the mobility of the polymer chains and reduces the T_g of the fibers. This causes an increased release rate of the repellent from the polymeric matrix due to the faster diffusion of repellent through the polymer matrix. Additionally, the plasticizing effect of IR3535 can also create more space for itself to diffuse through, further enhancing the release rate. With regard to the temperature dependence of the repellent release, the IR3535-release rate increases with the evaporation temperature such that evaporation at 100 °C completes within about 4 h, while at 60 °C, only about 20−30% of the total repellent amount is released within 12 h.

Quantitative data about the release kinetics are obtained by fitting the experimental mass-loss curves using a single-exponential decay function (eq 1):[7]

$$w(t) = (100 - w_0) + w_0 \times e^{-t/\tau} \qquad (1)$$

Here, $w(t)$ is the time-dependent total percentage sample mass, t is the time, w_0 is the initial repellent in m%, and τ is a characteristic time, representing the time when the sample released 63.2% $[= (1-1/e) \times 100\%]$ of the initial IR3535 content. Figure 8a shows the observed characteristic exponential-decay repellent-release-time constants as a function of temperature, revealing an exponential increase with decreasing temperature. As deduced already from the TGA raw data of Figure 7, repellent release at 100 °C completes within few hours, while at 60 °C, evaporation of about 2/3 $[= 1 - 1/e]$ of the initial repellent content lasts for dozens of hours. The vertical arrow indicates that the characteristic release time increases with the initial repellent content (w_0) in the fibers. The logarithm of the inverse characteristic time, $\log(1/\tau)$, as a function of the inverse release temperature, $1/T$, as shown in Figure 8b, provides the proof for the exponential increase in the characteristic evaporation time with decreasing temperature. The observed linear dependence of the data suggests an
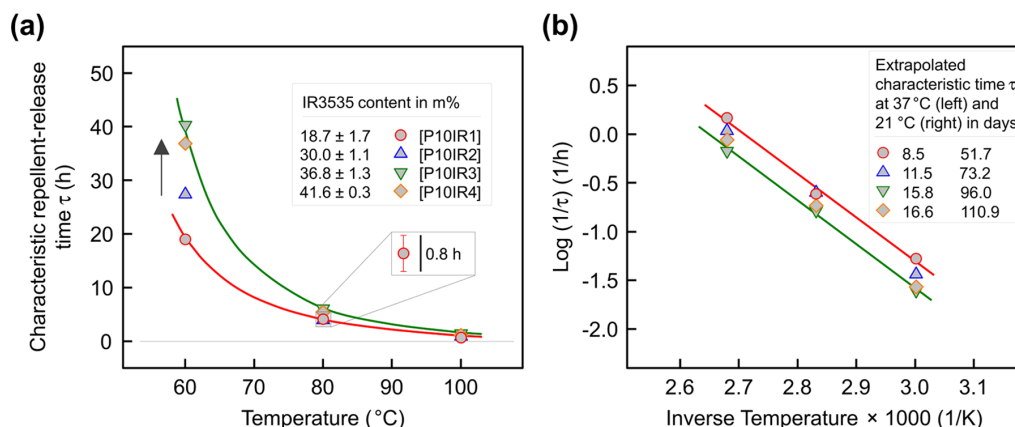
G

Figure 8. Characteristic repellent-release time of electrospun fibers produced from the solutions indicated in the legend as a function of temperature (a) and logarithm of the inverse of the characteristic time, $\log(1/\tau)$, as a function of the inverse release temperature $(1/T)$ (b). The error bars are smaller than the symbol size and are therefore omitted; only one error bar is shown in a zoomed window in (a), and measurements were performed four times.

Arrhenius-type release kinetics, and linear extrapolation yields τ-values at body temperature (37 °C) and room temperature (21 °C) of about 9 days and 52 days, respectively, for fibers initially containing about 19 m% IR3535 (P10IR1) and about 17 days and 111 days for fibers with an initial repellent concentration higher than 40 m% (P10IR4), as listed in the legend of Figure 8b. The corresponding linear fit parameters are shown in the SI, Table S1.

The Weibull distribution (eq 2) and its linearized form (eq 3) serve as valuable tools for obtaining information about release mechanisms in new/complex systems:[58−61]

$$y = e^{-(kt)^n} \tag{2}$$

$$\ln(-\ln(y)) = n\ln(k) + n\ln(t) \tag{3}$$

where y is the retention of repellent during release, k is the rate constant, t is the time, and n (the slope of eq 3) is a parameter denoting the release mechanism of the active through the polymer matrix.[62] The calculated values of n for all concentrations of PLLA fibers are presented in Figure S8 and Table 2. If $n \leq 0.75$, the release mechanism is Fickian

Table 2. Values of n Calculated from the Fit According to the Linearized Form of the Weibull Distribution

code[a]	n (60 °C)	n (80 °C)	n (100 °C)
P10IR1	0.49; 0.97	0.99	1.11
P10IR2	0.46; 0.98	1.01	1.12
P10IR3	0.44; 0.95	1.05	1.08
P10IR4	0.45; 0.95	1.14	1.17

diffusion in either fractal or Euclidian spaces; if $0.75 < n < 1$, the results are indicative of a combined mechanism (Fickian diffusion and Case II transport (non-Fickian diffusion)); if $n \approx 1$, the release can be explained by a classical first-order mechanism, and if $n > 1$, the release mechanism is complex and rapid.[62]

For all PLLA/IR3535 samples, the diffusional exponent ranges from 0.44 to 0.98 at 60 °C, which indicates a coupling of Fickian diffusion and Case II transport mechanism, that is, Fickian diffusion occurs first and then changes to a Case II

transport mechanism. Case II transport profiles signify the coupling of diffusion and relaxation mechanisms. Relaxation is associated with a transition from a rubbery to a glassy state.[63] The dominant relaxation mechanisms indicate the stresses developed in the polymer during swelling.[64] In addition, the diffusional exponent slightly decreases with IR3535 content at 60 °C. For certain concentrations, the diffusional exponent increases with temperature, indicating that the release starts to follow a first-order mechanism. At elevated temperatures, the PLLA/IR3535 interaction may be overcome, leading to diffusion controlled by concentration.

■ CONCLUSIONS

In contrast to the gold standard and large-scale used repellent DEET, IR3535 is regarded as a promising alternative repellent with less side effects on the environment and human beings, including pregnant women and children who are the most vulnerable population regarding mosquito-borne diseases, such as malaria. Incorporating the repellent IR3535 into bio-sourced and biodegradable PLLA opens the way to the realization of an environment-friendly repellent-delivery device. After successful testing of melt extrusion[21,22] and 3D printing[25] of semi-finished and final products of the PLLA/IR3535 system, in this work, electrospinning of fiber mats as an alternative technology for obtaining such an environment-friendly repellent-delivery system is investigated. By systematic variation of the electrospinning parameters, including voltage, nozzle-to-collector distance, flow rate, and solution composition, uniform fibers with a diameter close to 1 μm and containing a large amount of the repellent, exceeding 40 m%, were obtained. Such a high amount of repellent was impossible to incorporate into the polymeric carrier by melt extrusion and 3D printing,[21,22,25] where only up to about 25 m% IR3535 was added. Thermal and structural analyses revealed that IR3535 results in a decrease in the glass transition temperature of the polymer component, confirming thermodynamic solubility, as suggested in earlier works,[20,21] and causing plasticization of the amorphous PLLA phase. In addition, the presence of IR3535 enhances crystallization of PLLA, with the crystals presumably contributing to the mechanical properties of the fibers, as proven for bulk PLLA.[65] Important from the point of view of

functionality, evaporation/release of IR3535 is delayed in the electrospun fibers, allowing a continuous controlled release of the insect repellent for periods of the order of magnitude of many days/few weeks. As such, electrospun PLLA fibers containing IR3535 have potential to be used for controlled release of IR3535, suggesting, for example, possible use for the production of fabrics and textiles with long-lasting and active insect protection.

■ ASSOCIATED CONTENT

Ⓢ Supporting Information

The Supporting Information is available free of charge at https://pubs.acs.org/doi/10.1021/acsapm.3c00462.

> SEM micrographs of PLLA fibers and PLLA/IR3535 fibers prepared from different solutions and processing conditions, NMR, DSC, FTIR, release profile of repellent from PLLA/IR3535 fibers by TGA, and corresponding fit parameters (PDF)

■ AUTHOR INFORMATION

Corresponding Authors

Fanfan Du − *Interdisciplinary Center for Transfer-Oriented Research in Natural Sciences (IWE TFN), Martin Luther University Halle-Wittenberg, D-06099 Halle/Saale, Germany;* ⓞ orcid.org/0000-0002-5129-5860; Email: fanfan.du@iw.uni-halle.de

Alessandra Longo − *National Research Council (CNR), Institute of Polymers, Composites and Biomaterials (IPCB), 80078 Pozzuoli, Italy;* Present Address: National Research Council (CNR), Institute of Polymers, Composites and Biomaterials (IPCB), Via Paolo Gaifami 18, 95126, Catania, Italy (A.L.); ⓞ orcid.org/0000-0002-0714-8193; Email: alessandra.longo@ipcb.cnr.it

Authors

Irene Bonadies − *National Research Council (CNR), Institute of Polymers, Composites and Biomaterials (IPCB), 80078 Pozzuoli, Italy*

Harald Rupp − *Institut für Kunststofftechnologie und -recycling e.V, 06369 Weißandt-Gölzau, Germany*

Maria Laura Di Lorenzo − *National Research Council (CNR), Institute of Polymers, Composites and Biomaterials (IPCB), 80078 Pozzuoli, Italy;* ⓞ orcid.org/0000-0001-6430-0860

René Androsch − *Interdisciplinary Center for Transfer-Oriented Research in Natural Sciences (IWE TFN), Martin Luther University Halle-Wittenberg, D-06099 Halle/Saale, Germany;* ⓞ orcid.org/0000-0002-7924-0159

Complete contact information is available at: https://pubs.acs.org/10.1021/acsapm.3c00462

Notes

The authors declare no competing financial interest.

■ ACKNOWLEDGMENTS

■ REFERENCES

(1) World Health Organization *World malaria report 2022*, www.who.int/publications/i/item/9789240064898 (accessed 24/01/2023).

(2) World Health Organization *Fact Sheets, Malaria*, www.who.int/news-room/fact-sheets/detail/malaria#:~:text=Malaria%20is%20an%20acute%20febrile (accessed 24/01/2023).

(3) Greiner, A.; Wendorff, J. H. Electrospinning: a fascinating method for the preparation of ultrathin fibers. *Angew. Chem., Int. Ed.* **2007**, *46*, 5670−5703.

(4) Bhardwaj, N.; Kundu, S. C. Electrospinning: a fascinating fiber fabrication technique. *Biotechnol. Adv.* **2010**, *28*, 325−347.

(5) Weng, L.; Xie, J. Smart electrospun nanofibers for controlled drug release. Recent advances and new perspectives. *Curr. Pharm. Des.* **2015**, *21*, 1944−1959.

(6) Xue, J.; Wu, T.; Dai, Y.; Xia, Y. Electrospinning and electrospun nanofibers: Methods, materials, and applications. *Chem. Rev.* **2019**, *119*, 5298−5415.

(7) Ryan, J. J.; Casalini, R.; Orlicki, J. A.; Lundin, J. G. Controlled release of the insect repellent picaridin from electrospun nylon-6,6 nanofibers. *Polym. Adv. Technol.* **2020**, *31*, 3039−3047.

(8) Thum, M. D.; Weise, N. K.; Casalini, R.; Fulton, A. C.; Purdy, A. P.; Lundin, J. G. Incorporation of N,N-diethyl-meta-toluamide within electrospun nylon-6/6 nanofibers. *J. Appl. Polym. Sci.* **2022**, *139*, No. e53237.

(9) Xiang, C.; Etrick, N. R.; Frey, M. W.; Norris, E. J.; Coats, J. R. Structure and properties of polyamide fabrics with insect-repellent functionality by electrospinning and oxygen plasma-treated surface coating. *Polymers* **2020**, *12*, 2196.

(10) Cecone, C.; Caldera, F.; Trotta, F.; Bracco, P.; Zanetti, M. Controlled release of DEET loaded on fibrous mats from electrospun PMDA/cyclodextrin polymer. *Molecules* **2018**, *23*, 1694.

(11) Di Lorenzo, M. L.; Androsch, R. Synthesis, Structure and Properties of Poly(lactic acid). *Adv. Polym. Sci.* **2018**, *279*.

(12) Bonadies, I.; Longo, A.; Androsch, R.; Jehnichen, D.; Göbel, M.; Di Lorenzo, M. L. Biodegradable electrospun PLLA fibers containing the mosquito-repellent DEET. *Eur. Polym. J.* **2019**, *113*, 377−384.

(13) Ethyl butylacetylaminopropionate *WHO Specifications and Evaluations for public health pesticides.* https://archive.epa.gov/osa/hsrb/web/pdf/whoir3535evaluationapril2006.pdf (accessed 01/01/2023).

(14) Tavares, M.; da Silva, M. R. M.; de Oliveira de Siqueira, L. B.; Rodrigues, R. A. S.; Bodjolle-d'Almeida, L.; dos Santos, E. P.; Ricci-Júnior, E. Trends in insect repellent formulations: A review. *Int. J. Pharm.* **2018**, *539*, 190−209.

(15) Du, F.; Yener, H. E.; Hillrichs, G.; Boldt, R.; Androsch, R. Crystallization-induced polymer scaffold formation in the polymer/drug delivery system poly(L-lactic acid)/ethyl butylacetylaminopropionate (PLLA/IR3535) *Biomacromolecules* **2021**, *22*, 3950−3959.

(16) Kim, S. S.; Lloyd, D. R. Thermodynamics of polymer/diluent systems for thermally induced phase separation: 2. Solid-liquid phase separation systems. *Polymer* **1992**, *33*, 1036−1046.

(17) Kim, S. S.; Lloyd, D. R. Thermodynamics of polymer/diluent systems for thermally induced phase separation: 3. Liquid-liquid phase separation systems. *Polymer* **1992**, *33*, 1047−1057.

(18) Sungkapreecha, C.; Iqbal, N.; Gohn, A. M.; Focke, W. W.; Androsch, R. Phase behavior of the polymer/drug system PLA/DEET. *Polymer* **2017**, *126*, 116−125.

(19) Sungkapreecha, C.; Beily, M. J.; Kressler, J.; Focke, W. W.; Androsch, R. Phase behavior of the polymer/drug system PLA/DEET: Effect of PLA molar mass on subambient liquid-liquid phase separation. *Thermochim. Acta* **2018**, *660*, 77−81.

(20) Du, F.; Schick, C.; Androsch, R. Full-composition-range glass transition behavior of the polymer/solvent system poly (lactic acid) / ethyl butylacetylaminopropionate (PLA/IR3535®). *Polymer* **2020**, *209*, No. 123058.

(21) Du, F.; Erdmann, R.; Petzold, A.; Wutzler, A.; Leuteritz, A.; Nase, M.; Androsch, R. Structure, properties, and release kinetics of the polymer/insect repellent system poly (ʟ-lactic acid)/ethyl butylacetylaminopropionate (PLLA/IR3535). *Pharmaceutics* **2022**, *14*, 2381.

(22) Mapossa, A. B.; López-Beceiro, J.; Díaz-Díaz, A. M.; Artiaga, R.; Moyo, D. S.; Mphateng, T. N.; Focke, W. W. Properties of mosquito repellent-plasticized poly(lactic acid) strands. *Molecules* **2021**, *26*, 5890.

(23) Razavi, M.; Wang, S. Q. Why is crystalline poly (lactic acid) brittle at room temperature? *Macromolecules* **2019**, *52*, 5429−5441.

(24) Li, H.; Huneault, M. A. Effect of nucleation and plasticization on the crystallization of poly (lactic acid). *Polymer* **2007**, *48*, 6855−6866.

(25) Du, F.; Rupp, H.; Jariyavidyanont, K.; Janke, A.; Petzold, A.; Binder, W.; Androsch, R. 3D-printing of the polymer/insect-repellent system poly(ʟ-lactic acid)/ethyl butylacetylaminopropionate (PLLA/IR3535). *Int. J. Pharm.* **2022**, *624*, No. 122023.

(26) *Product information, Total Energies Corbion Ltd. 2021*, www.totalenergies-corbion.com/media/w5cgez0x/pds-luminy-l175-rmb20.pdf (accessed 31/12/2022).

(27) Corbion, personal information (10/08/2018).

(28) *Product information, Carbolution Chemicals GmbH, Ethyl butylacetylaminopropionate*: www.carbolution.de/product_info.php?products_id=3221 (accessed 01/01/2023).

(29) Mapossa, A. B.; Sitoe, A.; Focke, W. W.; Izadi, H.; Du Toit, E. L.; Androsch, R.; Sungkapreecha, C.; Van Der Merwe, E. M. Mosquito repellent thermal stability, permeability and air volatility. *Pest Manage. Sci.* **2020**, *76*, 1112−1120.

(30) Zubir, A. A. M.; Khairunnisa, M. P.; Surib, N. A.; NorRuwaida, J.; Rashid, M. Electrospinning of PLA with DMF: Effect of polymer concentration on the bead diameter of the electrospun fibre. *IOP Conf. Ser.: Mater. Sci. Eng.* **2020**, *778*, No. 012087.

(31) Casasola, R.; Thomas, N. L.; Trybala, A.; Georgiadou, S. Electrospun poly lactic acid (PLA) fibres: Effect of different solvent systems on fibre morphology and diameter. *Polymer* **2014**, *55*, 4728−4737.

(32) Wannatong, L.; Sirivat, A.; Supaphol, P. Effects of solvents on electrospun polymeric fibers: preliminary study on polystyrene. *Polym. Int.* **2004**, *53*, 1851−1859.

(33) Lee, K. H.; Kim, H. Y.; La, Y. M.; Lee, D. R.; Sung, N. H. Influence of a mixing solvent with tetrahydrofuran and N,N-dimethylformamide on electrospun poly(vinyl chloride) nonwoven mats. *J. Polym. Sci., Polym. Phys.* **2002**, *40*, 2259−2268.

(34) Lee, K. H.; Kim, H. Y.; Khil, M. S.; Ra, Y. M.; Lee, D. R. Characterization of nano-structured poly(epsilon-caprolactone) non-woven mats via electrospinning. *Polymer* **2003**, *44*, 1287−1294.

(35) Casasola, R.; Thomas, N. L.; Georgiadou, S. Electrospinning of poly(lactic acid): Theoretical approach for the solvent selection to produce defect-free nanofibers. *J. Polym. Sci., Polym. Phys.* **2016**, *54*, 1483−1498.

(36) Porter, R. S.; Johnson, J. F. The entanglement concept in polymer systems. *Chem. Rev.* **1966**, *66*, 1−27.

(37) Asran, A. S.; Salama, M.; Popescu, C.; Michler, G. H. Solvent influences the morphology and mechanical properties of electrospun poly(ʟ-lactic acid) scaffold for tissue engineering applications. *Macromol. Symp.* **2010**, *294*, 153−161.

(38) Mano, J. F.; Gómez Ribelles, J. L.; Alves, N. M.; Salmerón Sanchez, M. Glass transition dynamics and structural relaxation of PLLA studied by DSC: Influence of crystallinity. *Polymer* **2005**, *46*, 8258−8265.

(39) Pan, P.; Zhu, B.; Inoue, Y. Enthalpy relaxation and embrittlement of poly(ʟ-lactide) during physical aging. *Macromolecules* **2007**, *40*, 9664−9671.

(40) Naeem Iqbal, H. M.; Sungkapreecha, C.; Androsch, R. Enthalpy relaxation of the glass of poly (ʟ-lactic acid) of different ᴅ-isomer content and its effect on mechanical properties. *Polym. Bull.* **2016**, *74*, 2565−2573.

(41) Pan, P.; Zhu, B.; Kai, W.; Dong, T.; Inoue, Y. Effect of crystallization temperature on crystal modifications and crystallization kinetics of poly(ʟ-lactide). *J. Appl. Polym. Sci.* **2008**, *107*, 54−62.

(42) Pan, P.; Inoue, Y. Polymorphism and isomorphism in biodegradable polyesters. *Prog. Polym. Sci.* **2009**, *34*, 605−640.

(43) Zhang, J.; Tashiro, K.; Tsuji, H.; Domb, A. J. Disorder-to-order phase transition and multiple melting behavior of poly(ʟ-lactide) investigated by simultaneous measurements of WAXD and DSC. *Macromolecules* **2008**, *41*, 1352−1357.

(44) Androsch, R.; Schick, C.; Di Lorenzo, M. L. Melting of conformationally disordered crystals (α'-phase) of poly(ʟ-lactic acid). *Macromol. Chem. Phys.* **2014**, *215*, 1134−1139.

(45) Kawai, T.; Rahman, N.; Matsuba, G.; Nishida, K.; Kanaya, T.; Nakano, M.; Okamoto, H.; Kawada, J.; Usuki, A.; Honma, N.; Nakajima, K.; Matsuda, M. Crystallization and melting behavior of poly (ʟ-lactic acid). *Macromolecules* **2007**, *40*, 9463−9469.

(46) Androsch, R.; Zhuravlev, E.; Schick, C. Solid-state reorganization, melting and melt-recrystallization of conformationally disordered crystals (α'-phase) of poly (ʟ-lactic acid). *Polymer* **2014**, *55*, 4932−4941.

(47) Flory, P. J. Thermodynamics of crystallization in high polymers. IV. A theory of crystalline states and fusion in polymers, copolymers, and their mixtures with diluents. *J. Chem. Phys.* **1949**, *17*, 223−240.

(48) Martuscelli, E. Influence of composition, crystallization conditions and melt phase structure on solid morphology, kinetics of crystallization and thermal behavior of binary polymer/polymer blends. *Polym. Eng. Sci.* **1984**, *24*, 563−586.

(49) Burghardt, W. R. Phase diagrams for binary polymer systems exhibiting both crystallization and limited liquid-liquid miscibility. *Macromolecules* **1989**, *22*, 2482−2486.

(50) Jariyavidyanont, K.; Du, M.; Yu, Q.; Thurn-Albrecht, T.; Schick, C.; Androsch, R. Bulk enthalpy of melting of poly (ʟ-lactic acid) (PLLA) determined by fast scanning chip calorimetry. *Macromol. Rapid Commun.* **2022**, *43*, 2200148.

(51) Mathot, V. B. F.; Pijpers, M. F. J. Heat capacity, enthalpy and crystallinity of polymers from DSC measurements and determination of the DSC peak base line. *Thermochim. Acta* **1989**, *151*, 241−259.

(52) Jariyavidyanont, K.; Schick, C.; Androsch, R. The bulk enthalpy of melting of α'-crystals of poly (ʟ-lactic acid) determined by fast scanning chip calorimetry. *Thermochim. Acta* **2022**, *717*, No. 179349.

(53) Sungkapreecha, C.; Iqbal, N.; Focke, W. W.; Androsch, R. Crystallization of poly (ʟ-lactic acid) in solution with the mosquito-repellent N,N-diethyl-3-methylbenzamide. *Polym. Cryst.* **2019**, *2*, No. e10029.

(54) Righetti, M. C.; Gazzano, M.; Di Lorenzo, M. L.; Androsch, R. Enthalpy of melting of α'- and α-crystals of poly(ʟ-lactic acid). *Eur. Polym. J.* **2015**, *70*, 215−220.

(55) Miyata, T.; Masuko, T. Morphology of poly (ʟ-lactide) solution-grown crystals. *Polymer* **1997**, *38*, 4003−4009.

(56) Androsch, R.; Toda, A.; Furushima, Y.; Schick, C. Insertion-crystallization-induced low-temperature annealing peaks in melt-crystallized poly (ʟ-lactic acid). *Macromol. Chem. Phys.* **2021**, *222*, 2100177.

(57) Schick, C.; Androsch, R. The origin of annealing peaks in semicrystalline polymers: enthalpy recovery or melting? *Macromolecules* **2020**, *53*, 8751−8756.

(58) Soottitantawat, A.; Yoshii, H.; Furuta, T.; Ohgawara, M.; Forssell, P.; Partanen, R.; Poutanen, K.; Linko, P. Effect of water activity on the release characteristics and oxidative stability of ᴅ-limonene encapsulated by spray drying. *J. Agric. Food Chem.* **2004**, *52*, 1269−1276.

(59) Soottitantawat, A.; Bigeard, F.; Yoshii, H.; Furuta, T.; Ohkawara, M.; Linko, P. Influence of emulsion and powder size on the stability of encapsulated ᴅ-limonene by spray drying. *Innovative Food Sci. Emerging Technol.* **2005**, *6*, 107−114.

(60) Khounvilay, K.; Estevinho, B. N.; Sittikijyothin, W. Citronella oil microencapsulated in carboxymethylated tamarind gum and its controlled release. *Eng. J.* **2019**, *23*, 217−227.

(61) Mapossa, A. B.; Focke, W. W.; Tewo, R. K.; Androsch, R.; Kruger, T. Mosquito-repellent controlled-release formulations for fighting infectious diseases. *Malar. J.* **2021**, *20*, 165.

(62) Papadopoulou, V.; Kosmidis, K.; Vlachou, M.; Macheras, P. On the use of the Weibull function for the discernment of drug release mechanisms. *Int. J. Pharm.* **2006**, *309*, 44−50.

(63) Sitoe, A.; Mapossa, A. B.; Focke, W. W.; Muiambo, H.; Androsch, R.; Wesley-Smith, J. Development, characterization and modeling of mosquito repellent release from microporous devices. *SPE Polym.* **2020**, *1*, 90−100.

(64) Marabi, A.; Livings, S.; Jacobson, M.; Saguy, I. S. Normalized Weibull distribution for modeling rehydration of food particulates. *Eur. Food Res. Technol.* **2003**, *217*, 311−318.

(65) Jariyavidyanont, K.; Yu, Q.; Petzold, A.; Thurn-Albrecht, T.; Glüge, R.; Altenbach, H.; Androsch, R. Young's modulus of the different crystalline phases of poly (L-lactic acid). *J. Mech. Behav. Biomed. Mater.* **2023**, *137*, No. 105546.

Supporting Information for Chapter 4.5 (Electrospinning of PLLA/IR3535)

Figure S1. SEM micrographs of PLLA fibers, electrospun from a solution of 12.5% m/v PLLA in $CHCl_3$ (P12.5, a) and $CHCl_3$-DMF (90/10% v/v) (P12.5IR0, b), using a voltage of 25 kV, a nozzle-to-collector distance of 30 cm, and a flow rate of 0.5 mL/h.
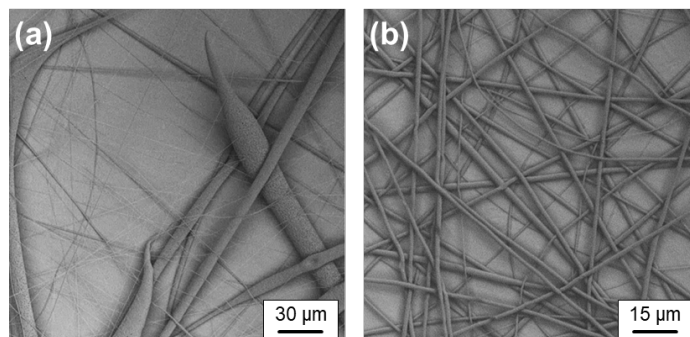
Figure S2. SEM micrographs of PLLA fibers prepared from solutions with a PLLA content of 15 (P15IR0, left column), 12.5 (P12.5IR0, center column), and 10% m/v (P10IR0, right column) in CHCl3-DMF (90/10% v/v). The flow rate was 0.2 mL/h and a nozzle-to-collector distance of 30 cm was used. Images of the top, center, and bottom rows were obtained by applying voltages of 20, 25, and 30 kV, respectively. The scale bar corresponds a distance of 10 μm.
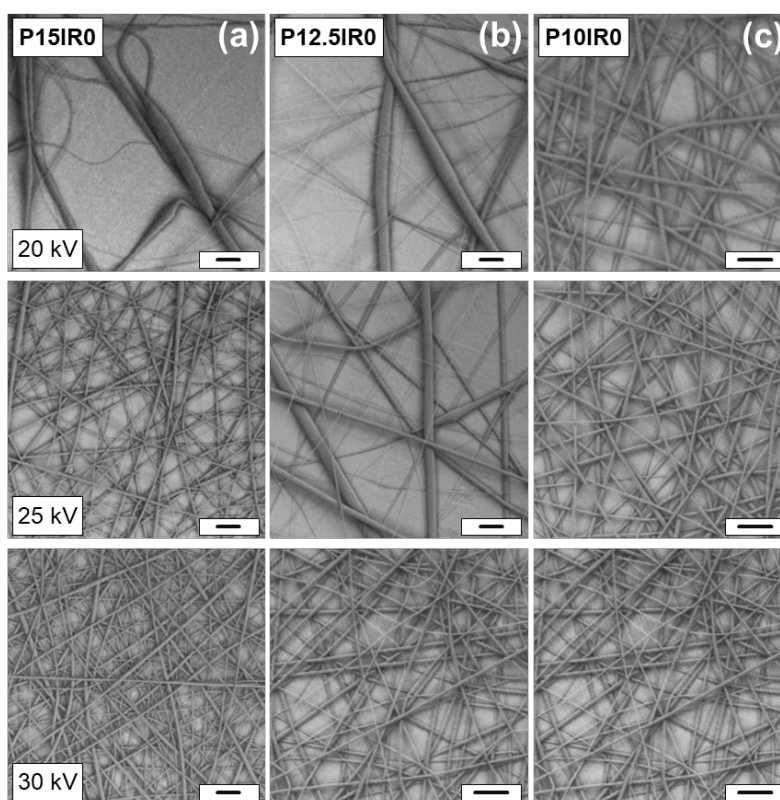
Figure S3. SEM micrographs of PLLA/IR3535 fibers prepared from P10IR4 solutions, using a flow rate of 0.2 mL/h, a voltage of 20 kV, and a nozzle-to-collector distance of 30 cm, at different magnifications.
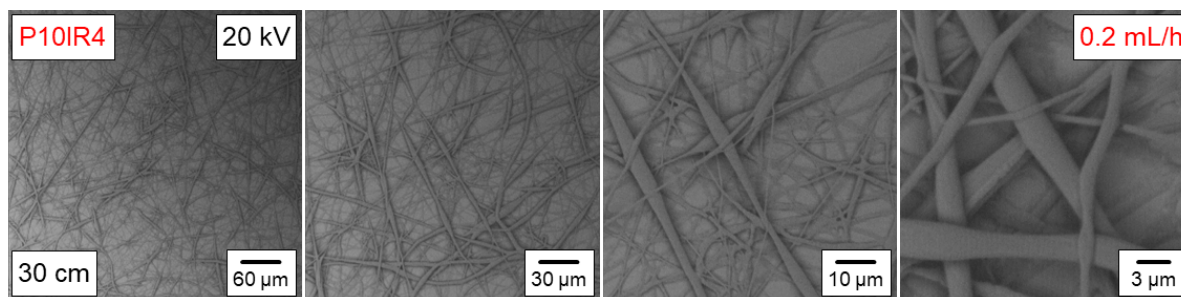
Figure S4. ^{1}H NMR spectra obtained on PLLA/IR3535 electrospun fibers containing different IR3535 content, as indicated in the legend, with a fixed amount of toluene (as calibration standard) in CDCl$_3$. Measurements were done on individual fiber mats.
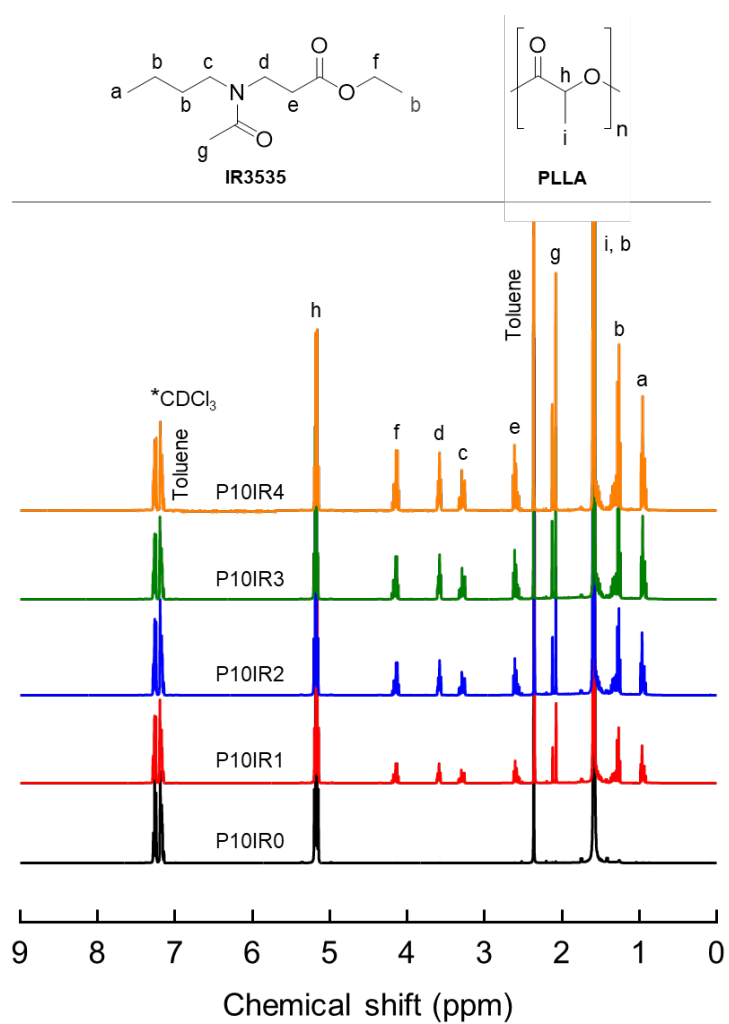
Figure S5. DSC curves, rate-normalized heat-flow rate as a function of temperature, of PLLA/IR3535 fibers recorded during cooling at 10 K/min after removing heat history.
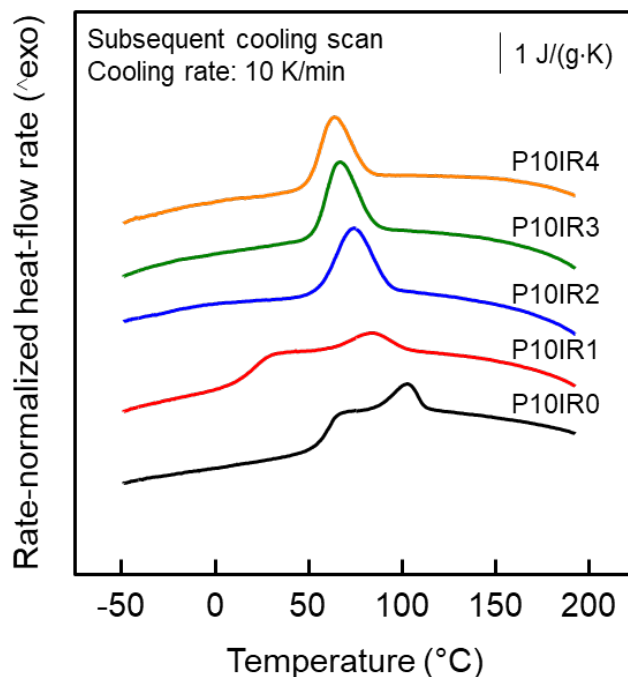
Figure S6. FTIR spectra of PLLA and PLLA/IR3535 electrospun fibers, as well as pure IR3535 (a), and their enlarged graph in the wavenumber range of 1330–1870 cm^{-1} (b). IR3535 data was adapted from International Journal of Pharmaceutics, 624, Fanfan Du, Harald Rupp, Katalee Jariyavidyanont, Andreas Janke, Albrecht Petzold, Wolfgang Binder, René Androsch, 3D-printing of the polymer/insect-repellent system poly (L-lactic acid)/ethyl butylacetylaminopropionate (PLLA/IR3535), 122023, Copyright (2022), with permission from Elsevier (Ref. [178]).
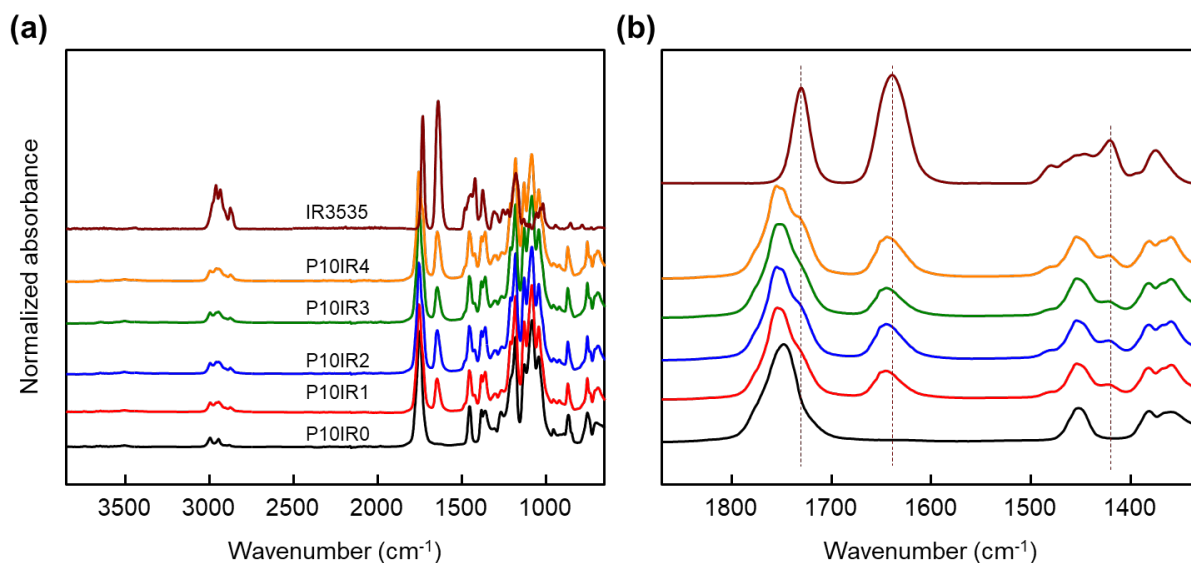
Figure S7. Percentage mass of electrospun fibers of PLLA/IR3535 prepared from the solutions P10IR1 (red), P10IR2 (blue), P10IR3 (green), and P10IR4 (orange), as a function of release time, being recorded at 60 °C, 80 °C, 100 °C, respectively. The average IR3535 content is shown at the bottom of each plot.
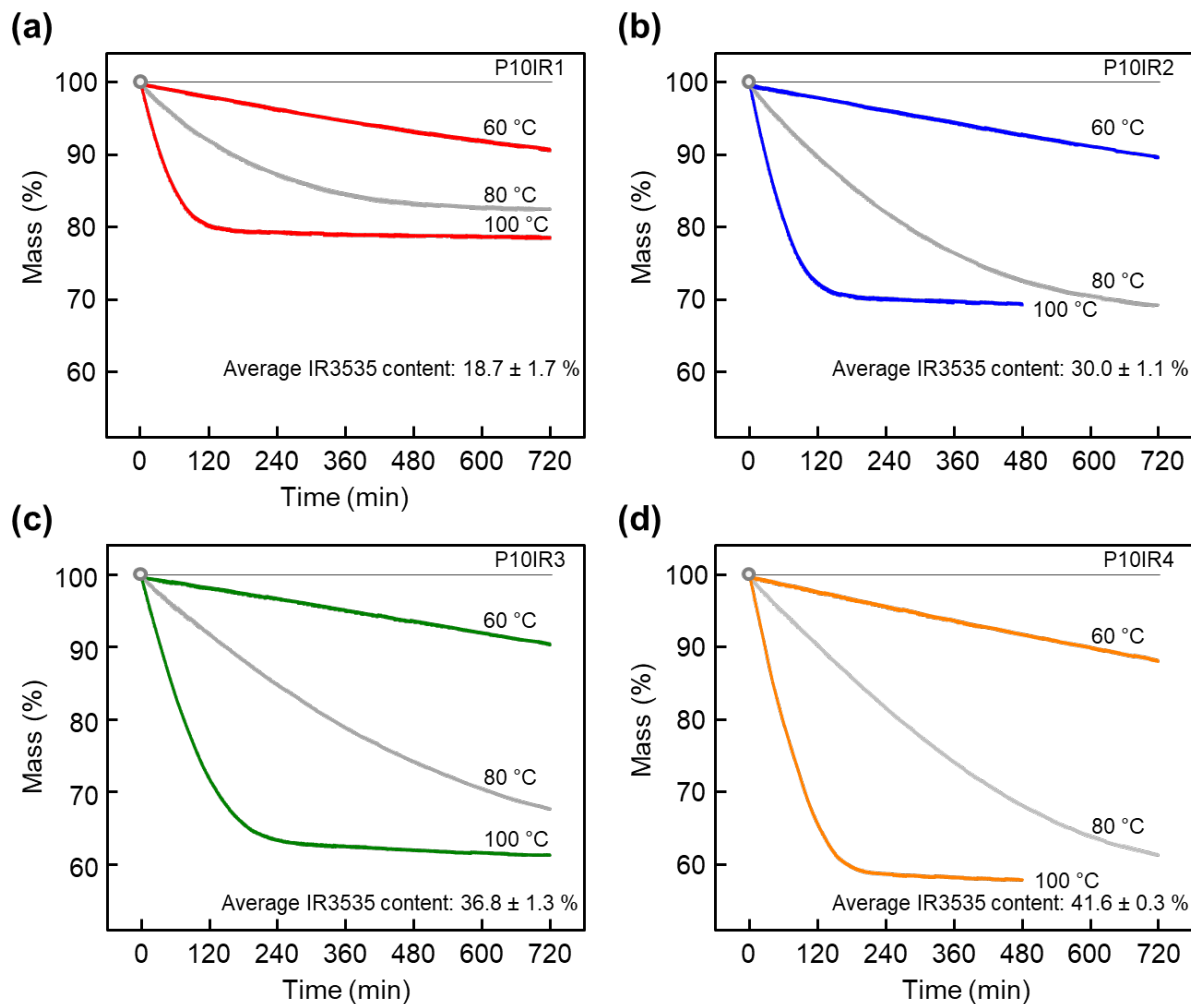
Figure S8. The release profile for electrospun fibers from P10IR1 (a), P10IR2 (b), P10IR3 (c) and P10IR4 (d) to determine the shape parameter, n, as the slope of the linear fit according to Equation (3) in the publication of this Chapter. The release profiles were obtained from isothermal experiments at 60, 80, and 100 °C (broad line). The data from the linear fit (thin line) to the data is given below.
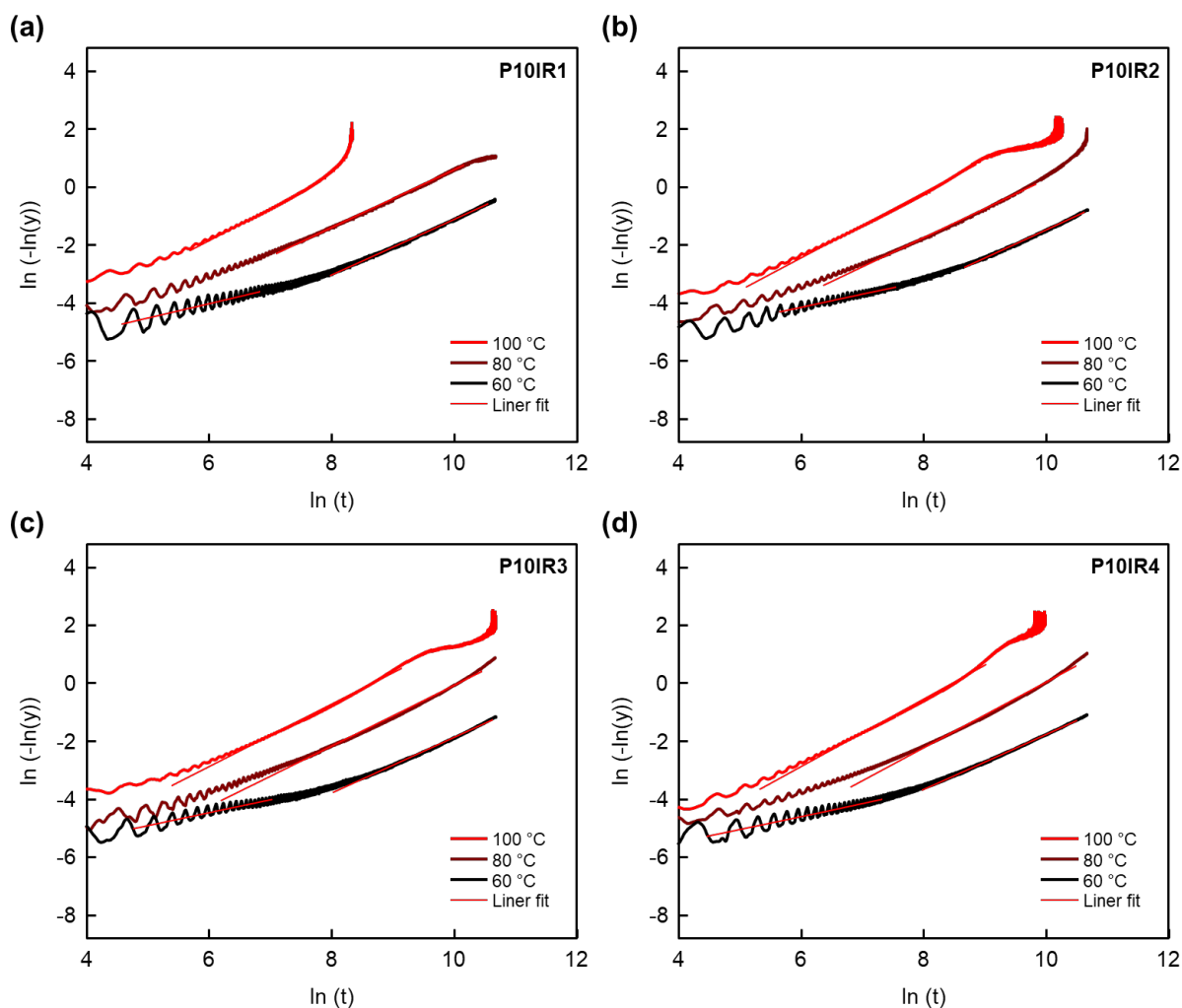
Continued to next page

Figure S8 (*continued*)

Sample	Temperature (°C)	Slope	Intercept	R^2
P10IR1	60	0.96609	-10.78043	0.99774
		0.49221	-6.98107	0.72736
	80	0.99238	-9.34620	0.99896
	100	1.10858	-8.49752	0.99692
P10IR2	60	0.98005	-11.2822	0.99794
		0.45730	-6.90202	0.88024
	80	1.00955	-9.82808	0.99630
	100	1.12444	-9.19877	0.99631
P10IR3	60	0.95478	-11.42581	0.99524
		0.43734	-7.09923	0.80088
	80	1.04789	-10.5624	0.99325
	100	1.08120	-9.37328	0.99403
P10IR4	60	0.94661	-11.24656	0.99779
		0.44529	-7.28476	0.84112
	80	1.13631	-11.32637	0.99154
	100	1.16738	-9.89364	0.99407

Table S1. Linear fit parameters of the dependence of the logarithm of the inverse of the characteristic release-time ($\log(1/\tau)$) as a function of the inverse of the release temperature ($1/T$) for Figure 8b in the publication of this Chapter.

Sample	Slope	Intercept	R^2	Extrapolated characteristic time (days)	
				at 37 °C	**at 21 °C**
P10IR1	-4.48491	12.15295	0.99374	8.5	51.7
P10IR2	-4.58739	12.35082	0.99772	11.5	73.2
P10IR3	-4.46579	11.81963	0.99736	15.8	96.0
P10IR4	-4.69878	12.54903	0.99920	16.6	110.9

5. CONCLUSIONS AND OUTLOOK

The polymer/repellent system PLA/IR3535 exhibits great application prospects as a personal mosquito-repellent delivery device to prevent mosquito bites and inhibit the transmission of diseases. In such a device, the polymer hosts the liquid mosquito repellent IR3535, which slowly evaporates to the environment and forms a vapor barrier to repel mosquitoes.

The first attempt is to elucidate the miscibility of the system components. Non-crystallizable PDLLA was chosen due to crystallizable PLLA may mask the information of thermodynamic miscibility. Cloud-point measurements and calorimetric analyses, including conventional and fast scanning chip calorimetry for controlled and stepwise evaporation of solvent IR3535 at elevated temperature and evaluation of the glass transition temperature during in-between cooling and reheating, showed that PDLLA and IR3535 are miscible in the entire concentration range. This new strategy of analyzing glass transition temperatures as function of the system composition avoids labor-intensive and time-consuming preparation of individual polymer-rich solutions for subsequent analysis.

Secondly, crystallizable PLLA scaffolds hosting IR3535 were prepared by PLLA-crystallization-related S-LTIPS when cooling the PLLA/IR3535 homogeneous solutions formed at elevated temperatures. The phase separation temperature, obtained by cloud point measurements and non-isothermal crystallization of PLLA/IR3535 solution, decreases with increasing the cooling rate and IR3535 concentration. As for the isothermal crystallization behavior of PLLA/IR3535 solutions, the addition of IR3535 obviously accelerate the crystallization rate of PLLA, and at the same crystallization temperature, PLLA content from 10 to 50 m%, the crystallization rate increases with PLLA content. The nucleation rate or nucleation density increases with supercooling, as well as with PLLA content. With regard to crystal growth, the maximum crystal growth rate decreases with IR3535 content, which is attributed to the longer diffusion pathways of polymer molecules when the polymer content decreases. IR3535 was characterized as located in the inter- and intraspherulitic pores of PLLA. The intraspherulitic pore size increases with crystallization temperature at the same PLLA content and decreases with increasing the PLLA content at the same crystallization temperature. The effects of the cooling rate, crystallization temperature and polymer content on structure formation provides the necessary knowledge to tailor the bimodal distribution of the repellent inside and outside the spherulites.

Then, PLLA/IR3535 mixtures with polymer-rich composition were prepared via melt extrusion technology, with the advantage of cost-efficient large-scale processing. Within the analyzed composition range of 2 to 23 m% IR3535, PLLA and IR3535 are miscible at the length range related to the glass transition temperature. IR3535 acts as a plasticizer for PLLA, resulting in a decrease in glass transition temperature as well as in the elastic modulus. PLLA/IR3535 extrudates with between 2 and 9 m% IR3535 are amorphous, even after storing at room temperature for around 1 year after extrusion, while PLLA/IR3535 extrudates containing 18 and 23 m% IR3535 showed an increase in the crystallinity over time because of the low glass transition temperature. Moreover, quantification of the release of IR3535 into the environment indicates an extremely low release rate with a time constant of the order of magnitude of 1–2 years at body temperature.
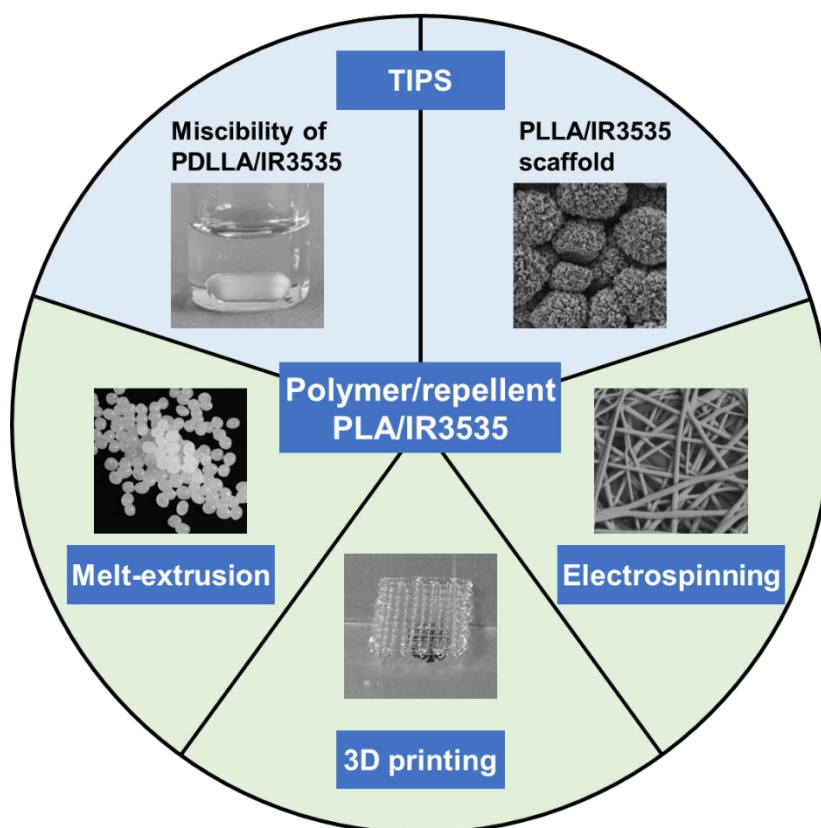
Figure 19. A summary of this dissertation.

As an advantageous alternative, 3D printing of parts with specific, easily customizable geometries for end-user products is proposed. The experiments demonstrate that the polymer/repellent system PLLA/ IR3535 processed by 3D printing is feasible and the maximum repellent-loading of 3D parts achieved 25 m%, with only minor loss of repellent and the repellent does not degrade thus it does not lose its functionality during the 3D-printing process. The solidification of parts is based on the vitrification of PLLA/IR3535 mixtures and PLLA-crystallization during 3D printing, which depends on composition and time. The glass transition temperature of the mixtures also decreases with repellent loading, requiring crystallization to obtain a solid part. For all 3D-printed samples, regardless of the initial repellent concentration, the repellent-release rate increases with temperature, and the release-time constant at body temperature is approximately in the order of 10 days. Compared to the extruded polymer/repellent system, the general applicability of the extrusion-based 3D-printing technique for the manufacture of polymer parts with a specific shape/design containing mosquito-repellent at a concentration raises the expectation to be used as a repellent delivery device.

Incorporating repellent IR3535 into PLLA fibers by electrospinning for preventing mosquito bites thereby reducing infection of diseases is viable. The fibers are micro-sized and uniform, even containing larger amounts (about 40 m%) of IR3535 compared to melt extrusion and 3D printing that up to 25 m%. Thermal and structural analyses revealed that the presence of IR3535 facilitates the crystallization of PLLA into α-modification during the process of electrospinning. Evaporation of IR3535 from PLLA fibers at body temperature lasts few days. In other words, electrospun PLLA fibers containing IR3535 have potential as new material to

be used for controlled release of IR3535, which highlight the possibility for the preparation of fabrics and textiles with long lasting and active insect protection.

In conclusion, this dissertation bridges the fundamental study of thermodynamic miscibility and crystallization behaviors of polymer/repellent system to application-oriented research of industrial processing, such as melt extrusion, electrospinning, and 3D printing, which is a useful portfolio for battle with mosquito-borne diseases. With these manufacturing techniques, various PLLA/IR3535 products/parts were obtained and the quantification of IR3535 released into the environment from different PLLA matrices indicates that incorporating the mosquito repellent into a polymer can slow down the release rate, thus extending the protection time. The release rate of the repellent depends on factors such as the release temperature, the geometric shape/surface area and structures of the processed products/parts and the repellent concentration. The higher the release temperature, the repellent concentration and the surface-to-volume ratio of the processed products/parts, the faster the release rate. The magnitude of the release-time constant ranges from a few days to several years. The performed study provides a sound basis for further research in the field of development of mosquito-repellent personal protection devices using a biodegradable polymer as a carrier for environment-friendly after-use disposal and an effective and biodegradable repellent, with less side effects on human beings and the environment.

Outlook

Further application of wearable PLA/IR3535 devices as drug-delivery system, "arm/foot in cage" tests in laboratory are required and further field trails should be carried out to test the polymer-repellent devices under real-life conditions, as well as assessment of risk to the impact of this technique on transmission of diseases. This will verify the true and effective insect repellency of the prepared parts by different processing techniques. If the repellency works, this will reduce the frequency of mosquito bites and followed disease transmission and contribute towards disease eradication and human and social well-beings. In addition, for outdoor activities, whether one is going for sports, exploring lakes or jungles, hiking and camping outdoors, canoeing on a river, or just relaxing on a beach watching the sunset, IR3535 based wearable devices will be effective for long time protection.

Furthermore, from the point-of-view of material selection, with the knowledge of the phase behavior of the polymer/repellent system PLA/IR3535, further alternatives for generating 3D-pinted insect-repellent-delivery devices or other drug-delivery devices are available, implicating different solidification characteristics, fine structure, maximum repellent/drug loading, or evaporation kinetics, thus perhaps widening application ranges.

REFERENCES

(1) Kaura, T.; Walter, N. S.; Kaur, U.; Sehgal, R. Different strategies for mosquito control: Challenges and alternatives. In *Mosquito Research-Recent Advances in Pathogen Interactions, Immunity, and Vector Control Strategies*; IntechOpen, **2022**.

(2) Kasai, S.; Itokawa, K.; Uemura, N.; Takaoka, A.; Furutani, S.; Maekawa, Y.; Kobayashi, D.; Imanishi-Kobayashi, N.; Amoa-Bosompem, M.; Murota, K.; Higa, Y. Discovery of super-insecticide-resistant dengue mosquitoes in Asia: Threats of concomitant knockdown resistance mutations. *Sci. Adv.* **2022**, *8* (51), eabq7345.

(3) World Health Organization. *Global vector vontrol response 2017–2030*. Geneva: World Health Organization, **2017**. https://www.who.int/publications/i/item/9789241512978 (accessed 2022-12-28).

(4) *Vector-borne diseases*. https://www.who.int/news-room/fact-sheets/detail/vector-borne-diseases#:~:text=Vector%2Dborne%20diseases%20account%20for,infection%20transmitted%20by%20Anopheline%20mosquitoes (accessed 2022-10-30).

(5) World Health Organization. *World malaria report 2022*. Geneva: World Health Organization, **2022**. https://www.who.int/publications/i/item/9789240064898 (accessed 2022-12-30).

(6) *Malaria*. https://www.who.int/news-room/fact-sheets/detail/malaria#:~:text=Malaria%20is%20an%20acute%20febrile,of%20infected%20female%20Anopheles%20mosquitoes (accessed 2023-01-03).

(7) *Malaria*. https://ourworldindata.org/malaria (accessed 2023-01-03).

(8) *Mosquito-borne diseases*. https://www.cdc.gov/niosh/topics/outdoor/mosquito-borne/default.html (accessed 2022-09-28).

(9) *Malaria parasite life cycle*. https://www.malariavaccine.org/malaria-and-vaccines/vaccine-development/life-cycle-malaria-parasite (accessed 2022-09-28).

(10) *What is a mosquito*? https://www.cdc.gov/mosquitoes/about/what-is-a-mosquito.html (accessed 2022-10-10).

(11) Zhao, Z.; Zung, J. L.; Hinze, A.; Kriete, A. L.; Iqbal, A.; Younger, M. A.; Matthews, B. J.; Merhof, D.; Thiberge, S.; Ignell, R.; Strauch, M. Mosquito brains encode unique features of human odour to drive host seeking. *Nature* **2022**, *605* (7911), 706–712.

(12) Jackman, J. A.; Olson, J. K. Mosquitoes and the diseases they transmit. *Texas Farmer Collection* **2002**.

(13) Ciera, L. W. Functionalizing textile materials with mosquito repellents in melt extrusion and electrospinning. Ph.D. dissertation, Ghent University, Ghent, Belgium, **2014**.

(14) Ng'ang'a, P. N.; Aduogo, P.; Mutero, C. M. Long lasting insecticidal mosquito nets (LLINs) ownership, use and coverage following mass distribution campaign in Lake Victoria basin, Western Kenya. *BMC Public Health* **2021**, *21* (1), 1046.

(15) Sharma, S. K.; Tyagi, P. K.; Upadhyay, A. K.; Haque, M. A.; Mohanty, S. S.; Raghavendra, K.; Dash, A. P. Efficacy of permethrin treated long-lasting insecticidal nets on malaria transmission and observations on the perceived side effects, collateral benefits and human safety in a hyperendemic tribal area of Orissa, India. *Acta Trop.* **2009**, *112* (2), 181–187.

(16) World Health Organization. *Indoor residual spraying: An operational manual for indoor residual spraying (IRS) for malaria transmission control and elimination*. Geneva: World Health Organization, **2015**. https://www.who.int/publications/i/item/9789241508940 (accessed 2023-01-03).

(17) Jaga, K.; Dharmani, C. Sources of exposure to and public health implications of organophosphate pesticides. *Rev. Panam. Salud Publica* **2003**, *14* (3), 171–185.

(18) U.S. president's Malaria initiative. *End Malaria faster—U.S. president's Malaria initiative strategy 2021–2026*. USA: U.S. president's Malaria initiative led by United States Agency for International Development (USAID) and Centers for Disease Control and Prevention (CDC), **2021**. https://d1u4sg1s9ptc4z.cloudfront.net/uploads/2021/10/10.04Final_USAID_PMI_Report_50851.pdf (accessed 2023-02-20).

(19) *Evaluation of Indoor Residual Household Spraying (IRHS): Challenges faced by Ndola urban district*. https://www.texilajournal.com/public-health/article/1279-evaluation-of-indoor (accessed 2023-02-20).

(20) Braack, L.; Hunt, R.; Koekemoer, L. L.; Gericke, A.; Munhenga, G.; Haddow, A. D.; Becker, P.; Okia, M.; Kimera, I.; Coetzee, M. Biting behaviour of African malaria vectors: 1. Where do the main vector species bite on the human body? *Parasites Vectors* **2015**, *8*, 76.

(21) Kenea, O.; Balkew, M.; Tekie, H.; Gebre-Michael, T.; Deressa, W.; Loha, E.; Lindtjorn, B.; Overgaard, H. J. Human-biting activities of Anopheles species in south-central Ethiopia. *Parasites Vectors* **2016**, *9*, 527.

(22) Pavela, R.; Benelli, G. Ethnobotanical knowledge on botanical repellents employed in the African region against mosquito vectors—A review. *Exp. Parasitol.* **2016**, *167*, 103–108.

(23) *Find the repellent that is right for you*. https://www.epa.gov/insect-repellents/find-repellent-right-you (accessed 2022-10-10).

(24) Islam, J.; Zaman, K.; Duarah, S.; Raju, P. S.; Chattopadhyay, P. Mosquito repellents: An insight into the chronological perspectives and novel discoveries. *Acta Trop.* **2017**, *167*, 216–230.

(25) Lupi, E.; Hatz, C.; Schlagenhauf, P. The efficacy of repellents against Aedes, Anopheles, Culex and Ixodes spp.—A literature review. *Travel Med. Infect. Dis.* **2013**, *11* (6), 374–411.

(26) Tavares, M.; da Silva, M. R. M.; de Oliveira de Siqueira, L. B.; Rodrigues, R. A. S.; Bodjolle-d'Almeida, L.; Dos Santos, E. P.; Ricci-Júnior, E. Trends in insect repellent formulations: A review. *Int. J. Pharm.* **2018**, *539* (1–2), 190–209.

(27) Nerio, L. S.; Olivero-Verbel, J.; Stashenko, E. Repellent activity of essential oils: A review. *Bioresour. Technol.* **2010**, *101* (1), 372–378.

(28) da Silva, M. R. M.; Ricci-Júnior, E. An approach to natural insect repellent formulations: From basic research to technological development. *Acta Trop.* **2020**, *212*, 105419.

(29) Esmaili, F.; Sanei-Dehkordi, A.; Amoozegar, F.; Osanloo, M. A review on the use of essential oil-based nanoformulations in control of mosquitoes. *Biointerface Res. Appl. Chem.* **2021**, *11* (5), 12516–12529.

(30) U.S. Environmental Protection Agency (EPA). *Reregistration Eligibility Decision (RED): Limonene*. Washington: U.S. EPA, **1994**. https://archive.epa.gov/pesticides/reregistration/web/pdf/3083.pdf (accessed 2023-01-03).

(31) Maia, M. F.; Moore, S. J. Plant-based insect repellents: A review of their efficacy, development and testing. *Malar. J.* **2011**, *10* (1), 1–15.

(32) Curtis, C. F.; Lines, J. D.; Baolin, L.; Renz, A. Natural and synthetic repellents. In *Appropriate technology in vector control*; CRC Press, **1990**; pp 75–92.

(33) Barasa, S. S.; Ndiege, I. O.; Lwande, W.; Hassanali, A. Repellent activities of stereoisomers of p-menthane-3,8-diols against Anopheles gambiae (Diptera: Culicidae). *J. Med. Entomol.* **2002**, *39* (5), 736–741.

(34) Barbosa, L.; Filomeno, C.; Teixeira, R. Chemical variability and biological activities of Eucalyptus spp. essential oils. *Molecules* **2016**, *21* (12), 1671.

(35) Benelli, G.; Pavela, R.; Rakotosaona, R.; Nzekoue, F. K.; Canale, A.; Nicoletti, M.; Maggi, F. Insecticidal and mosquito repellent efficacy of the essential oils from stem bark and wood of Hazomalania voyronii. *J. Ethnopharmacol.* **2020**, *248*, 112333.

(36) Southwell, I. A.; Stiff, I. A. Differentiation between Melaleuca alternifolia and M. linariifolia by monoterpenoid comparison. *Phytochemistry* **1990**, *29* (11), 3529–3533.

(37) Roberts, J. R.; Reigart, J. R. Does anything beat DEET? *Pediatr. Ann.* **2004**, *33* (7), 444–453.

(38) Wylie, B. J.; Hauptman, M.; Woolf, A. D.; Goldman, R. H. Insect repellants during pregnancy in the era of the Zika virus. *Obstet. Gynecol.* **2016**, *128* (5), 1111–1115.

(39) *DEET*. http://npic.orst.edu/factsheets/DEETgen.html (accessed 2023-01-06).

(40) Klier, M.; Kuhlow, F. Neue Insektenabwehrmittel—am Stickstoffdisubstituierte beta-Alaninderivate. *J. Soc. Cosmet. Chem.* **1976**, *27*, 141–153.

(41) *Insect repellents: Principles, methods, and uses*; Debboun, M., Frances, S. P., Strickman, D., Eds.; CRC press, **2006**.

(42) Carroll, S. P. Prolonged efficacy of IR3535 repellents against mosquitoes and blacklegged ticks in North America. *J. Med. Entomol.* **2008**, *45* (4), 706–714.

(43) Nasci, R. S.; Zielinski-Gutierrez, E.; Wirtz, R. A.; Brogdon, W. G. Protection against mosquitoes, ticks, & other Insects & arthropods. In *CDC Health Information for International Travel 2014: The Yellow Book*; Vol. 56; Oxford University Press, **2013**; pp 94–99.

(44) *IR3535®*. https://www.merckgroup.com/en/brands/pm/ir3535.html (accessed 2023-01-06).

(45) U.S. Environmental Protection Agency (EPA). *WHO specifications and evaluations for public health pesticides: Ethyl butylacetylaminopropionate (IR3535®)*. Washington: U.S. EPA, **2006**. https://archive.epa.gov/osa/hsrb/web/pdf/whoir3535evaluationapril2006.pdf (accessed 2023-01-01).

(46) Regulation (EU) n°528/2012. *Ethyl butylacetylaminopropionate (Product-type 19) assessment report*. Belgium: Competent Authority Report, **2014**. https://echa.europa.eu/documents/10162/aaf5b78 c-82ca-40a3-25a4-1cc4339c9407 (assessed 2022-06-27).

(47) *Picaridin*. http://npic.orst.edu/factsheets/archive/Picaridintech.html (accessed 2023-01-06).

(48) Alpern, J. D.; Dunlop, S. J.; Dolan, B. J.; Stauffer, W. M.; Boulware, D. R. Personal protection measures against mosquitoes, ticks, and other arthropods. *Med. Clin. North Am.* **2016**, *100* (2), 303–316.

(49) *Permethrin*. http://npic.orst.edu/factsheets/PermGen.html (accessed 2023-01-06).

(50) Khater, H. F.; Selim, A. M.; Abouelella, G. A.; Abouelella, N. A.; Murugan, K.; Vaz, N. P.; Govindarajan, M. Commercial mosquito repellents and their safety concerns. In *Malaria*; IntechOpen, **2019**; Vol. 1, pp 1–27.

(51) Banks, S. D.; Murray, N.; Wilder-Smith, A.; Logan, J. G. Insecticide-treated clothes for the control of vector-borne diseases: A review on effectiveness and safety. *Med. Vet. Entomol.* **2014**, *28* (Suppl. 1), 14–25.

(52) Kimani, E. W.; Vulule, J. M.; Kuria, I. W.; Mugisha, F. Use of insecticide-treated clothes for personal protection against malaria: A community trial. *Malar. J.* **2006**, *5*, 63.

(53) U.S. Environmental Protection Agency (EPA). *Permethrin Facts*. Washington: U.S. EPA, **2009**. https://archive.epa.gov/pesticides/reregistration/web/pdf/permethrin-facts-2009.pdf (accessed 2023-01-06).

(54) Nguyen, Q.-B. D.; Vu, M.-A. N.; Hebert, A. A. Insect repellents: An updated review for the clinician. *J. Am. Acad. Dermatol.* **2023**, *88* (1), 123–130.

(55) Kalyanasundaram, M.; Mathew, N. *N,N*-diethyl phenylacetamide (DEPA): A safe and effective repellent for personal protection against hematophagous arthropods. *J. Med. Entomol.* **2006**, *43* (3), 518–525.

(56) Diaz, J. H. Chemical and plant-based insect repellents: Efficacy, safety, and toxicity. *Wilderness Environ. Med.* **2016**, *27* (1), 153–163.

(57) Katz, T. M.; Miller, J. H.; Hebert, A. A. Insect repellents: Historical perspectives and new developments. *J. Am. Acad. Dermatol.* **2008**, *58* (5), 865–871.

(58) *Insect repellents*. http://npic.orst.edu/factsheets/repellents.html (accessed 2023-01-07).

(59) Sungkapreecha, C.; Iqbal, N.; Gohn, A. M.; Focke, W. W.; Androsch, R. Phase behavior of the polymer/drug system PLA/DEET. *Polymer* **2017**, *126*, 116–125.

(60) Directive 98/8/EC. *N,N-diethyl-meta-toluamide (DEET, Product-type 19) assessment report*. Sweden: Annex I, **2010**. https://echa.europa.eu/documents/10162/a9b111f6-37b7-c179-dce4-361b6217484d (accessed 2023-02-21).

(61) Du, F.; Schick, C.; Androsch, R. Full-composition-range glass transition behavior of the polymer/solvent system poly (lactic acid) /ethyl butylacetylaminopropionate (PLA/IR3535®). *Polymer* **2020**, *209*, 123058.

(62) Regulation (EU) No 528/2012. *Icaridin (Product-type 19) assessment report*. Denmark, **2019**. https://echa.europa.eu/documents/10162/58d77648-e39e-6498-e743-d64df39cdc24 (accessed 2023-02-20).

(63) Regulation (EU) No 528/2012. *Permethrin (Product-type 18) assessment report*. Ireland, **2014**. https://echa.europa.eu/documents/10162/ff18b40c-e4f6-469e-377d-6e5aca835bd2 (accessed 2023-02-20).

(64) Vijayaraghavan, R.; Rao, S. S.; Suryanarayana, M. V. S.; Swamy, R. V. Acute and subacute inhalation toxicity studies of a new broad spectrum insect repellent, *N,N*-diethylphenylacetamide. *Toxicology* **1991**, *67* (1), 85-96.

(65) *Diethylphenyl acetamide (DEPA)*. https://alkylamines.com/product/diethyl-phenyl-acetamide-depa/ (accessed 2023-02-21).

(66) Drapeau, J. Insect repellents based on para-menthane-3,8-diol. Ph.D. dissertation, University of Regensburg, Regensburg, Germany, **2019**.

(67) Reifenrath, W. G.; Robinson, P. B. In vitro skin evaporation and penetration characteristics of mosquito repellents. *J. Pharm. Sci.* **1982**, *71* (9), 1014–1018.

(68) Mapossa, A. B.; Focke, W. W.; Tewo, R. K.; Androsch, R.; Kruger, T. Mosquito-repellent controlled-release formulations for fighting infectious diseases. *Malar. J.* **2021**, *20*, 165.

(69) Kim, S.; Lee, Y. M. Rigid and microporous polymers for gas separation membranes. *Prog. Polym. Sci.* **2015**, *43*, 1–32.

(70) O'Brien, F. J. Biomaterials & scaffolds for tissue engineering. *Mater. Today* **2011**, *14* (3), 88–95.

(71) Conoscenti, G.; Carrubba, V. L.; Brucato, V. A Versatile technique to produce porous polymeric scaffolds: The thermally induced phase separation (TIPS) method. *Arch. Chem. Res.* **2017**, *1* (2), 1–3.

(72) Calori, I. R.; Braga, G.; de Jesus, P. d. C. C.; Bi, H.; Tedesco, A. C. Polymer scaffolds as drug delivery systems. *Eur. Polym. J.* **2020**, *129*, 109621.

(73) Dorati, R.; Detrizio, A.; Modena, T.; Conti, B.; Benazzo, F.; Gastaldi, G.; Genta, I. Biodegradable scaffolds for bone regeneration combined with drug-delivery systems in osteomyelitis therapy. *Pharmaceuticals* **2017**, *10* (4), 96.

(74) Mapossa, A. B. Slow release of mosquito repellents from microporous polyolefin strands. Ph.D. dissertation, University of Pretoria, Pretoria, South Africa, **2019**.

(75) Maibach, H. I.; Akers, W. A.; Johnson, H. L.; Khan, A. A.; Skinner, W. A. Topical insect repellents. *Clin. Pharmacol. Ther.* **1974**, *16* (5 Part 2), 970–973.

(76) Smith, C. N.; Gilbert, J. H.; Gouck, H. K.; Bowman, M. C.; Agree, F.; Schmidt, C. H. Factors affecting the protection period of mosquito repellents. *U.S. Dept. of Agriculture, Agricultural Research Service, Technical Bulletin* **1963**, *1285*, 1–36.

(77) Rueda, L. M.; Rutledge, L. C.; Gupta, R. K. Effect of skin abrasions on the efficacy of the repellent deet against Aedes aegypti. *J. Am. Mosq. Control Assoc.* **1998**, *14* (2), 178–182.

(78) *Bioplastic materials*. https://www.european-bioplastics.org/bioplastics/materials/ (accessed 2022-12-17).

(79) Lackner, M. Bioplastics. In *Kirk-Othmer Encyclopedia of Chemical Technology*, 6th ed.; Wiley, **2015**; pp 1–41.

(80) Goel, V.; Luthra, P.; Kapur, G. S.; Ramakumar, S. S. V. Biodegradable/Bio-plastics: Myths and realities. *J. Polym. Environ.* **2021**, *29* (10), 3079–3104.

(81) Muneer, F.; Nadeem, H.; Arif, A.; Zaheer, W. Bioplastics from biopolymers: An eco-friendly and sustainable solution of plastic pollution. *Polym. Sci., Ser. C* **2021**, *63* (1), 47–63.

(82) Shamsuddin, I. M.; Jafar, J. A.; Shawai, A. S. A.; Yusuf, S.; Lateefah, M.; Aminu, I. Bioplastics as better alternative to petroplastics and their role in national sustainability: A review. *Adv. Biosci. Bioeng.* **2017**, *5* (4), 63–70.

(83) Peng, Y.-Y.; Srinivas, S.; Narain, R. Modification of polymers. In *Polymer Science and Nanotechnology*; Elsevier, **2020**; pp 95–104.

(84) *Modification of polymer properties*; Jasso-Gastinel, C. F., Kenny, J. M., Eds.; William Andrew, **2016**.

(85) Muobom, S. S.; Umar, A. M. S.; Soongseok, Y.; Brolin, A. P. A review on plasticizers and eco-friendly bioplasticizers: Biomass sources and market. *Int. J. Eng. Res. Technol.* **2020**, *9* (5), 1138–1144.

(86) Wypych, G. *Handbook of plasticizers*; ChemTec Publishing, **2004**.

(87) Bocqué, M.; Voirin, C.; Lapinte, V.; Caillol, S.; Robin, J.-J. Petro-based and bio-based plasticizers: Chemical structures to plasticizing properties. *J. Polym. Sci., Part A: Polym. Chem.* **2016**, *54* (1), 11–33.

(88) Wypych, A. *Databook of plasticizers*; Elsevier, **2023**.

(89) Aslam, H. M. U.; Qadir, A.; Ahmad, A.; Aslam, M.; Mumtaz, M.; Ahmad, S. R. Impacts of plasticizers on riverine ecological tntegrity in context to sustainability challenges. In *Microplastic Pollution: Environmental Occurrence and Treatment Technologies*; Springer, **2022**; pp 323–346.

(90) *Synthesis, structure and properties of poly(lactic acid)*; Di Lorenzo, M. L., Androsch, R., Eds.; Springer, **2018**.

(91) *Industrial applications of poly(lactic acid)*; Di Lorenzo, M. L., Androsch, R., Eds.; Springer, **2018**.

(92) Lunt, J. Large-scale production, properties and commercial applications of polylactic acid polymers. *Polym. Degrad. Stab.* **1998**, *59* (1–3), 145–152.

(93) Gupta, A. P.; Kumar, V. New emerging trends in synthetic biodegradable polymers—Polylactide: A critique. *Eur. Polym. J.* **2007**, *43* (10), 4053–4074.

(94) Pan, P.; Inoue, Y. Polymorphism and isomorphism in biodegradable polyesters. *Prog. Polym. Sci.* **2009**, *34* (7), 605–640.

(95) Zheng, Y.; Pan, P. Crystallization of biodegradable and biobased polyesters: Polymorphism, cocrystallization, and structure-property relationship. *Prog. Polym. Sci.* **2020**, *109*, 101291.

(96) Di Lorenzo, M. L.; Cocca, M.; Malinconico, M. Crystal polymorphism of poly(L-lactic acid) and its influence on thermal properties. *Thermochim. Acta* **2011**, *522* (1–2), 110–117.

(97) Pan, P.; Kai, W.; Zhu, B.; Dong, T.; Inoue, Y. Polymorphous crystallization and multiple melting behavior of poly(L -lactide): Molecular weight dependence. *Macromolecules* **2007**, *40* (19), 6898–6905.

(98) Hoogsteen, W.; Postema, A. R.; Pennings, A. J.; Tenbrinke, G.; Zugenmaier, P. Crystal-structure, conformation, and morphology of solution-spun poly(L-lactide) Fibers. *Macromolecules* **1990**, *23* (2), 634–642.

(99) J. Puiggalia; Y. Ikadab; H. Tsujic; L. Cartiera; T. Okiharaa; Lotza, B. The frustrated structure of poly(L-lactide). *Polymer* **2000**, *41* (25), 8921–8930.

(100) Wang, H.; Zhang, J.; Tashiro, K. Phase transition mechanism of poly(L-lactic acid) among the α, δ, and β forms on the basis of the reinvestigated crystal structure of the β form. *Macromolecules* **2017**, *50* (8), 3285–3300.

(101) Cartier, L.; Okihara, T.; Ikada, Y.; Tsuji, H.; Puiggali, J.; Lotz, B. Epitaxial crystallization and crystalline polymorphism of polylactides. *Polymer* **2000**, *41* (25), 8909–8919.

(102) Zeinali, R.; del Valle, L. J.; Torras, J.; Puiggalí, J. Recent progress on biodegradable tissue engineering scaffolds prepared by thermally-induced phase separation (TIPS). *Int. J. Mol. Sci.* **2021**, *22* (7), 3504.

(103) Castro, A. J. Methods for making microporous products. US 4247498, **1981**.

(104) Akhtar, M. U.; Focke, W. W. Trapping citronellal in a microporous polyethylene matrix. *Thermochim. Acta* **2015**, *613*, 61–65.

(105) Kim, S. S.; Lloyd, D. R. Thermodynamics of polymer/diluent systems for thermally induced phase separation: 3. Liquid-liquid phase separation systems. *Polymer* **1992**, *33* (5), 1047–1057.

(106) Lloyd, D. R. Microporous membrane formation via thermally induced phase separation. I. Solid-liquid phase separation. *J. Membr. Sci.* **1990**, *50*, 239–261.

(107) Skripov, V. P.; Skripov, A. V. Spinodal decomposition (phase-transition via unstable states). *Sov. Phys. Usp.* **1979**, *22* (6), 389–410.

(108) Knychała, P.; Timachova, K.; Banaszak, M.; Balsara, N. P. 50th anniversary perspective: Phase behavior of polymer solutions and blends. *Macromolecules* **2017**, *50* (8), 3051–3065.

(109) Hou, S.; Yu, J.; Zhuang, X.; Li, D.; Liu, Y.; Gao, Z.; Sun, T.; Wang, F.; Yu, X. Phase separation of P3HT/PMMA blend film for forming semiconducting and dielectric layers in organic thin-film transistors for high-sensitivity NO_2 detection. *ACS Appl. Mater. Interfaces* **2019**, *11* (47), 44521–44527.

(110) Maguire, S. M.; Boyle, M. J.; Bilchak, C. R.; Demaree, J. D.; Keller, A. W.; Krook, N. M.; Ohno, K.; Kagan, C. R.; Murray, C. B.; Rannou, P.; Composto, R. J. Grafted nanoparticle surface wetting during phase separation in polymer nanocomposite films. *ACS Appl. Mater. Interfaces* **2021**, *13* (31), 37628–37637.

(111) Zhang, G.; Qin, Z.; Qian, Y.; Zhu, J. Microstructural evolution and kinetics of phase separation in binary polymer blends under electric fields. *Comput. Mater. Sci.* **2022**, *213*, 111659.

(112) Flory, P. J. *Principles of polymer chemistry*; Cornell University Press, **1953**.

(113) Sasaki;, S.; Asakura, T. Helix distortion and crystal structure of the α-form of poly(L-lactide). *Macromolecules* **2003**.

(114) Wasanasuk, K.; Tashiro, K.; Hanesaka, M.; Ohhara, T.; Kurihara, K.; Kuroki, R.; Tamada, T.; Ozeki, T.; Kanamoto, T. Crystal structure analysis of poly(L-lactic acid) α form on the basis of the 2-dimensional wide-angle synchrotron X-ray and neutron diffraction measurements. *Macromolecules* **2011**, *44* (16), 6441–6452.

(115) Wasanasuk, K.; Tashiro, K. Crystal structure and disorder in poly(L-lactic acid) δ form (α′ form) and the phase transition mechanism to the ordered α form. *Polymer* **2011**, *52* (26), 6097–6109.

(116) Marubayashi, H.; Akaishi, S.; Akasaka, S.; Asai, S.; Sumita, M. Crystalline structure and morphology of poly(L-lactide) formed under high-pressure CO_2. *Macromolecules* **2008**, *41* (23), 9192–9203.

(117) Marubayashi, H.; Asai, S.; Sumita, M. Complex crystal formation of poly(L-lactide) with solvent molecules. *Macromolecules* **2012**, *45* (3), 1384–1397.

(118) Rizzo, P.; Ianniello, G.; Venditto, V.; Tarallo, O.; Guerra, G. Poly(L-lactic acid): Uniplanar orientation in cocrystalline films and structure of the cocrystalline form with cyclopentanone. *Macromolecules* **2015**, *48* (20), 7513–7520.

(119) Garancher, J.-P.; Fernyhough, A.; Kirby, N. Effects of liquid CO_2 exposure on semicrystalline polylactic acid. *Macromol. Symp.* **2014**, *336* (1), 53–60.

(120) Koido, S.; Kawai, T.; Kuroda, S.; Nishida, K.; Kanaya, T.; Kato, M.; Kurose, T.; Nakajima, K. Mesomorphic phase formation of plasticized poly(L-lactic acid). *J. Appl. Polym. Sci.* **2014**, *131* (2), 39762.

(121) Lan, Q.; Li, Y. Mesophase-mediated crystallization of poly(L-lactide): Deterministic pathways to nanostructured morphology and superstructure control. *Macromolecules* **2016**, *49* (19), 7387–7399.

(122) Lan, Q.; Li, Y.; Chi, H. Highly enhanced mesophase formation in glassy poly(L-lactide) at low temperatures by low-pressure CO_2 that provides moderately increased molecular mobility. *Macromolecules* **2016**, *49* (6), 2262–2271.

(123) Sibanda, M.; Focke, W.; Braack, L.; Leuteritz, A.; Brunig, H.; Tran, N. H. A.; Wieczorek, F.; Trumper, W. Bicomponent fibres for controlled release of volatile mosquito repellents. *Mater. Sci. Eng. C* **2018**, *91*, 754–761.

(124) Mapossa, A. B.; Sibanda, M. M.; Sitoe, A.; Focke, W. W.; Braack, L.; Ndonyane, C.; Mouatcho, J.; Smart, J.; Muaimbo, H.; Androsch, R.; Loots, M. T. Microporous polyolefin strands as controlled-release devices for mosquito repellents. *Chem. Eng. J.* **2019**, *360*, 435–444.

(125) Lloyd, D. R.; Kim, S. S.; Kinzer, K. E. Microporous membrane formation via thermally-induced phase separation. II. Liquid-liquid phase separation. *J. Membr. Sci.* **1991**, *64* (1–2), 1–11.

(126) Pochivalov, K. V.; Basko, A. V.; Lebedeva, T. N.; Ilyasova, A. N.; Yurov, M. Y.; Golovanov, R. Y.; Artemov, V. V.; Volkov, V. V.; Ezhov, A. A.; Volkov, A. V.; Kudryavtsev, Y. V. Thermally induced phase separation in semicrystalline polymer solutions: How does the porous structure actually arise? *Mater. Today Commun.* **2021**, *28*, 102558.

(127) van de Witte, P.; Dijkstra, P. J.; van den Berg, J. W. A.; Feijen, J. Phase separation processes in polymer solutions in relation to membrane formation. *J. Membr. Sci.* **1996**, *117* (1–2), 1–31.

(128) Ogienko, A. G.; Drebushchak, V. A.; Bogdanova, E. G.; Yunoshev, A. S.; Ogienko, A. A.; Boldyreva, E. V.; Manakov, A. Y. Thermodynamic aspects of freeze-drying: A case study of an "organic solvent–water" system. *J. Therm. Anal. Calorim.* **2017**, *127* (2), 1593–1604.

(129) Bedell, M. L.; Guo, J. L.; Xie, V. Y.; Navara, A. M.; Mikos, A. G. Polymer scaffold fabrication. In *Principles of Tissue Engineering*; Academic Press, **2020**; pp 295–315.

(130) Gorth, D.; Webster, T. J. Matrices for tissue engineering and regenerative medicine. In *Biomaterials for Artificial Organs*; Woodhead Publishing, **2011**; pp 270–286.

(131) Allaf, R. M. Melt-molding technologies for 3D scaffold engineering. In *Functional 3D Tissue Engineering Scaffolds*; Woodhead Publishing, **2018**; pp 75–100.

(132) Zheng, Y.; Pokorski, J. K. Hot melt extrusion: An emerging manufacturing method for slow and sustained protein delivery. *Wiley Interdiscip. Rev.: Nanomed. Nanobiotechnol.* **2021**, *13* (5), e1712.

(133) Tambe, S.; Jain, D.; Agarwal, Y.; Amin, P. Hot-melt extrusion: Highlighting recent advances in pharmaceutical applications. *J. Drug Delivery Sci. Technol.* **2021**, *63*, 102452.

(134) Greiner, A.; Wendorff, J. H. Electrospinning: a fascinating method for the preparation of ultrathin fibers. *Angew. Chem., Int. Ed. Engl.* **2007**, *46* (30), 5670–5703.

(135) Taylor, G. Disintegration of water drops in an electric field. *Proc. R. Soc. Lond. A* **1964**, *280* (1382), 383–397.

(136) Doshi, J.; Reneker, D. H. Electrospinning process and applications of electrospun fibers. *J. Electrost.* **1995**, *35* (2–3), 151–160.

(137) Luraghi, A.; Peri, F.; Moroni, L. Electrospinning for drug delivery applications: A review. *J. Controlled Release* **2021**, *334*, 463–484.

(138) Nathanael, A. J.; Oh, T. H. Encapsulation of calcium phosphates on electrospun nanofibers for tissue engineering applications. *Crystals* **2021**, *11* (2), 199.

(139) Brown, T. D.; Dalton, P. D.; Hutmacher, D. W. Melt electrospinning today: An opportune time for an emerging polymer process. *Prog. Polym. Sci.* **2016**, *56*, 116–166.

(140) Lian, H.; Meng, Z. Melt electrospinning vs. solution electrospinning: A comparative study of drug-loaded poly(ε-caprolactone) fibres. *Mater. Sci. Eng. C* **2017**, *74*, 117–123.

(141) Liu, Z.; Ramakrishna, S.; Liu, X. Electrospinning and emerging healthcare and medicine possibilities. *APL Bioeng.* **2020**, *4* (3), 030901.

(142) Bachs-Herrera, A.; Yousefzade, O.; del Valle, L. J.; Puiggali, J. Melt electrospinning of polymers: Blends, nanocomposites, additives and applications. *Appl. Sci.* **2021**, *11* (4), 1808.

(143) *Handbook of nanofibers*; Barhoum, A., Bechelany, M., Makhlouf, A. S. H., Eds.; Springer, **2019**.

(144) Gajjar, C. R.; Stallrich, J. W.; Pasquinelli, M. A.; King, M. W. Process-property relationships for melt-spun poly(lactic acid) yarn. *ACS Omega* **2021**, *6* (24), 15920–15928.

(145) Elkasabgy, N. A.; Mahmoud, A. A.; Maged, A. 3D printing: An appealing route for customized drug delivery systems. *Int. J. Pharm.* **2020**, *588*, 119732.

(146) Tracy, T.; Wu, L.; Liu, X.; Cheng, S.; Li, X. 3D printing: Innovative solutions for patients and pharmaceutical industry. *Int. J. Pharm.* **2022**, *631*, 122480.

(147) Kim, J. H.; Kim, K.; Jin, H.-E. Three-dimensional printing for oral pharmaceutical dosage forms. *J. Pharm. Invest.* **2022**, *52* (3), 293–317.

(148) Daminabo, S. C.; Goel, S.; Grammatikos, S. A.; Nezhad, H. Y.; Thakur, V. K. Fused deposition modeling-based additive manufacturing (3D printing): Techniques for polymer material systems. *Mater. Today Chem.* **2020**, *16*, 100248.

(149) Bácskay, I.; Ujhelyi, Z.; Fehér, P.; Arany, P. The evolution of the 3D-printed drug delivery systems: A Review. *Pharmaceutics* **2022**, *14* (7), 1312.

(150) Kishore, K.; Sinha, M. K. A state-of-the-art review on fused deposition modelling process. In *Advances in Manufacturing and Industrial Engineering*; Singari, R. M., Mathiyazhagan, K., Kumar, H., Eds.; Lecture Notes in Mechanical Engineering; Springer, **2021**; pp 855–864.

(151) *3D Printing infill: The basics for perfect results*. https://all3dp.com/2/infill-3d-printing-what-it-means-and-how-to-use-it/ (accessed 2022-12-27).

(152) Huang, B.; Meng, S.; He, H.; Jia, Y.; Xu, Y.; Huang, H. Study of processing parameters in fused deposition modeling based on mechanical properties of acrylonitrile-butadiene-styrene filament. *Polym. Eng. Sci.* **2019**, *59* (1), 120–128.

(153) Masood, S. H. Advances in fused deposition modeling. In *Comprehensive Materials Processing*; Elsevier, **2014**; pp 69–91.

(154) Keridou, I.; Franco, L.; Martínez, J. C.; Turon, P.; Del Valle, L. J.; Puiggalí, J. Electrospun scaffolds for wound healing applications from poly(4-hydroxybutyrate): A biobased and biodegradable linear polymer with high elastomeric properties. *J. Appl. Polym. Sci.* **2021**, *139* (1), e51447.

(155) Tamir, T. S.; Xiong, G.; Fang, Q.; Dong, X.; Shen, Z.; Wang, F.-Y. A feedback-based print quality improving strategy for FDM 3D printing: An optimal design approach. *Int. J. Adv. Manuf. Technol.* **2022**, *120* (3–4), 2777–2791.

(156) Xu, B.; Zheng, Q.; Song, Y.; Shangguan, Y. Calculating barrier properties of polymer/clay nanocomposites: Effects of clay layers. *Polymer* **2006**, *47* (8), 2904–2910.

(157) Pavlidou, S.; Papaspyrides, C. D. A review on polymer-layered silicate nanocomposites. *Prog. Polym. Sci.* **2008**, *33* (12), 1119–1198.

(158) Sitoe, A.; Mapossa, A. B.; Focke, W. W.; Muiambo, H.; Androsch, R.; Wesley-Smith, J. Development, characterization and modeling of mosquito repellent release from microporous devices. *SPE Polym.* **2020**, *1* (2), 90–100.

(159) Xiang, C.; Etrick, N. R.; Frey, M. W.; Norris, E. J.; Coats, J. R. Structure and properties of polyamide fabrics with insect-repellent functionality by electrospinning and oxygen plasma-treated surface coating. *Polymers* **2020**, *12* (10), 2196.

(160) Ryan, J. J.; Casalini, R.; Orlicki, J. A.; Lundin, J. G. Controlled release of the insect repellent picaridin from electrospun nylon-6,6 nanofibers. *Polym. Adv. Technol.* **2020**, *31* (12), 3039–3047.

(161) Thum, M. D.; Weise, N. K.; Casalini, R.; Fulton, A. C.; Purdy, A. P.; Lundin, J. G. Incorporation of *N,N*-diethyl-meta-toluamide within electrospun nylon-6/6 nanofibers. *J. Appl. Polym. Sci.* **2022**, *139* (48), e53237.

(162) Saeidlou, S.; Huneault, M. A.; Li, H. B.; Park, C. B. Poly(lactic acid) crystallization. *Prog. Polym. Sci.* **2012**, *37* (12), 1657–1677.

(163) Lim, L. T.; Auras, R.; Rubino, M. Processing technologies for poly(lactic acid). *Prog. Polym. Sci.* **2008**, *33* (8), 820–852.

(164) Önder, Ö. C.; Yilgör, E.; Yilgör, I. Fabrication of rigid poly(lactic acid) foams via thermally induced phase separation. *Polymer* **2016**, *107*, 240–248.

(165) Sungkapreecha, C.; Iqbal, N.; Focke, W. W.; Androsch, R. Crystallization of poly(L-lactic acid) in solution with the mosquito-repellent *N,N*-diethyl-3-methylbenzamide. *Polym. Cryst.* **2019**, *2* (1), e10029.

(166) Sungkapreecha, C.; Beily, M. J.; Kressler, J.; Focke, W. W.; Androsch, R. Phase behavior of the polymer/drug system PLA/DEET: Effect of PLA molar mass on subambient liquid-liquid phase separation. *Thermochim. Acta* **2018**, *660*, 77–81.

(167) Sungkapreecha, C.; Focke, W. W.; Androsch, R. Competition between liquid-liquid de-mixing, crystallization, and glass transition in solutions of PLA of different stereochemistry and DEET. *Chin. J. Polym. Sci.* **2020**, *38* (2), 174–178.

(168) Di Lorenzo, M. L.; Longo, A. *N,N*-Diethyl-3-methylbenzamide (DEET): A mosquito repellent as functional plasticizer for poly(L-lactic acid). *Thermochim. Acta* **2019**, *677*, 180–185.

(169) Bonadies, I.; Longo, A.; Androsch, R.; Jehnichen, D.; Göbel, M.; Di Lorenzo, M. L. Biodegradable electrospun PLLA fibers containing the mosquito-repellent DEET. *Eur. Polym. J.* **2019**, *113*, 377–384.

(170) Ferreira, I.; Brünig, H.; Focke, W.; Boldt, R.; Androsch, R.; Leuteritz, A. Melt-spun poly(D,L-lactic acid) monofilaments containing *N,N*-diethyl-3-methylbenzamide as mosquito repellent. *Materials* **2021**, *14* (3), 638.

(171) Ferreira, I.; Leuteritz, A.; Brünig, H.; Focke, W.; Androsch, R. Effect of DEET on the crystallinity of bicomponent poly(lactic acid) monofilaments. In *AIP Conference Proceedings*; AIP Publishing, **2020**; Vol. 2289, 020058.

(172) Mapossa, A. B.; López-Beceiro, J.; Díaz-Díaz, A. M.; Artiaga, R.; Moyo, D. S.; Mphateng, T. N.; Focke, W. W. Properties of mosquito repellent-plasticized poly(lactic acid) strands. *Molecules* **2021**, *26* (19), 5890.

(173) Yener, H. E.; Hillrichs, G.; Androsch, R. Phase behavior of solvent-rich compositions of the polymer/drug system poly(butylene succinate) and *N,N*-diethyl-3-methylbenzamide (DEET). *Colloid Polym. Sci.* **2021**, *299*, 873–881.

(174) Yener, H. E.; Erdmann, R.; Jariyavidyanont, K.; Mapossa, A. B.; Focke, W. W.; Hillrichs, G.; Androsch, R. Slow-DEET-release mosquito-repellent system based on poly(butylene succinate). *ACS Omega* **2022**, *7* (10), 8377–8384.

(175) Mphateng, T. N.; Mapossa, A. B.; Wesley-Smith, J.; Ramjee, S.; Focke, W. W. Cellulose acetate/organoclay nanocomposites as controlled release matrices for pest control applications. *Cellulose* **2022**, *29* (7), 3915–3933.

(176) Cecone, C.; Caldera, F.; Trotta, F.; Bracco, P.; Zanetti, M. Controlled release of DEET loaded on fibrous mats from electrospun PMDA/cyclodextrin polymer. *Molecules* **2018**, *23* (7), 1694.

(177) Du, F.; Yener, H. E.; Hillrichs, G.; Boldt, R.; Androsch, R. Crystallization-induced polymer scaffold formation in the polymer/drug delivery system poly(L-lactic acid)/ethyl butylacetylaminopropionate (PLLA/IR3535). *Biomacromolecules* **2021**, *22* (9), 3950–3959.

(178) Du, F.; Rupp, H.; Jariyavidyanont, K.; Janke, A.; Petzold, A.; Binder, W.; Androsch, R. 3D-Printing of the polymer/insect-repellent system poly(L-lactic acid)/ethyl butylacetylaminopropionate (PLLA/IR3535). *Int. J. Pharm.* **2022**, 122023.

(179) Annandarajah, C.; Norris, E. J.; Funk, R.; Xiang, C.; Grewell, D.; Coats, J. R.; Mishek, D.; Maloy, B. Biobased plastics with insect-repellent functionality. *Polym. Eng. Sci.* **2019**, *59* (s2), E460–E467.

(180) Zhang, Z.; Yang, K.; Han, X.; Yu, X.; Cheng, Z. Novel mosquito repellent fiber mat containing nepeta essential oil prepared by coaxial electrospinning. *Polym. Adv. Technol.* **2022**, *33* (9), 2943–2951.

LIST OF PUBLICATIONS

Publications during the period of PhD study

(The symbol "*'' represents corresponding authors)

Longo, A.; Di Maio, E.; Du, F.; Androsch, R.; Di Lorenzo, M. L.* CO_2-Diffusion controlled mesophase formation in poly(L-lactic acid) and its effect on cold-crystallization. *Polymer* **2023**, 126380.

Zhou, X.; Li, C.; Bhandary, R.; Katcharava, Z.; Du, F.; Androsch, R.; Marinow, A.; Binder, W.* Catalyst-free, mechanically robust, and ion-conductive vitrimers for self-healing ionogel electrolytes. *ACS Appl. Eng. Mater.* **2023**, *1* (8), 1997–2003.

Du, F.*; Bonadies, I.; Longo, A.*; Rupp, H.; Di Lorenzo, M. L.; Androsch, R. Sustainable electrospun poly(L-lactic acid) fibers for controlled release of the mosquito-repellent ethyl butylacetylaminopropionate (IR3535). *ACS Appl. Polym. Mater.* **2023**, *5* (7), 4838–4848.

Mitteldeutsche Zeitung: Ring soll Mücken plagen. Halle, Germany, 22.11.**2022**.

Du, F.*; Erdmann, R.; Petzold, A.; Wutzler, A.; Leuteritz, A.; Nase, M.; Androsch, R.* Structure, properties and release kinetics of the polymer/insect-repellent system poly(L-lactic acid)/ethyl butylacetylaminopropionate (PLLA/IR3535). *Pharmaceutics* **2022**, *14* (11), 2381.

Zhang, R.*; Du, F.; Jariyavidyanont, K.; Zhuravlev, E.; Schick, C.; Androsch, R. Glass transition temperature of poly(D,L-lactic acid) of different molar mass. *Thermochim. Acta* **2022**, *718*, 179387.

Deutsche Apotheker Zeitung (DAZ): 3D-Druck: Insektenschutz am Ringfinger. Düsseldorf, Germany, 24.10.**2022**.

Press release: Scientists develop a new kind of printable, wearable insect repellent. (Number 125/2022, 11. October **2022**)

Du, F.; Rupp, H.; Jariyavidyanont, K.; Janke, A.; Petzold, A.; Binder, W.*; Androsch, R.* 3D-Printing of the polymer/insect-repellent system poly(L-lactic acid)/ethyl butylacetylaminopropionate (PLLA/IR3535). *Int. J. Pharm.* **2022**, *624*, 122023.

Du, F.; Yener, H. E.; Hillrichs, G.; Boldt, R.; Androsch, R.* Crystallization-induced polymer scaffold formation in the polymer/drug delivery system poly(L-lactic acid)/ethyl butylacetylaminopropionate (PLLA/IR3535). *Biomacromolecules* **2021**, *22* (9), 3950–3959.

Du, F.; Schick, C.; Androsch, R.* Full-composition-range glass transition behavior of the polymer/solvent system poly (lactic acid)/ethyl butylacetylaminopropionate (PLA/IR3535®). *Polymer* **2020**, *209*, 123058.

Other publications

Other publications that are unrelated to my PhD study can be found in my Google Scholar profile: https://scholar.google.de/citations?user=LSKAN0kAAAAJ&hl=en&oi=sra

CURRICULUM VITAE

Fanfan Du

Date of birth: ********

Nationality: Chinese

Address: ********

E-mail: ********

Website: https://scholar.google.de/citations?user=LSKAN0kAAAAJ&hl=en&oi=sra

Education

07.2019–06.2023 **PhD in Polymer Material Science**

Martin Luther University Halle-Wittenberg, Germany

▪ PhD researcher of AGRIPOLY at Martin Luther University Halle-Wittenberg with full scholarship from European Social Fund (ESF).

▪ Exchange at National Research Council of Italy – Institute of Polymers, Composites and Biomaterials (CNR-IPCB).

▪ Awarded ''Hugo-Junkers-Preis 2023'' finalist.

▪ Academic visitor of "Chunhui Project 2023" of the China Ministry of Education.

09.2016–03.2019 **Master in Chemical Engineering and Technology**

Zhejiang University, China

▪ Member of Institute of Polymer and Polymerization Engineering, State Key Laboratory of Ch.E.

▪ Project researcher of National Key R&D Project "Controlled Preparation of Medical Polymer Materials by Ring-Opening Polymerization of Lactone".

▪ Awarded National Graduate Scholarship, Academic Scholarship and Outstanding Graduate Student of Zhejiang University.

09.2012–06.2016 **Bachelor in Chemical Engineering and Technology**

Taiyuan University of Technology, China

▪ Awarded National Encouragement Scholarship, Professional Study Scholarship (three times), Science and Technology Scholarship.

▪ Honored first prize of the 5th Mathematics Competition Preliminaries for National College Students and title of Excellent Student, Outstanding Graduate, etc.

Professional Experience

07.2019–current **Crystallization-controlled PLLA Scaffold Structure for Tailoring Drug Delivery**

▪ Designed and evaluated PLLA scaffold formation from solutions with repellent and tailored the conditions of solution-crystallization and PLLA/repellent ratio to realize the controlled drug delivery.

▪ Achieved wearable biopolymer-repellent personal protection devices by 3D printing, electrospinning and melt-extrusion techniques.

▪ Published 8 papers in *Biomacromolecules*, *Int. J. Pharm.*, *Pharmaceutics*, *ACS Appl. Polym. Mater.*, *Polymer* and *Thermochim. Acta*, etc.

▪ The pioneering work about 3D printing of wearable PLLA-IR3535 fingerings was reported by *Mitteldeutsche Zeitung, Deutsche Apotheker Zeitung,* as well as *University Press Release,* and was awarded ''*Hugo-Junkers-Preis 2023*'' finalist.

09.2016–03.2019 **Controlled Preparation of Organo-catalysts for Medical Polymer Materials by ROP of Lactone**

▪ Screened the experimental system, designed and built the experimental facilities, analyzed and summarized the data independently.

▪ Synthesized and characterized green organo-catalysts to achieve controlled ring-opening polymerization of lactones and investigated the thermal behavior and crystalline structures of the synthesized polyesters.

▪ Published 3 research papers in *J. Polym. Sci., Part A: Polym. Chem.*, *Cryst. Growth Des.*, *Chem. J. Chin. Univ.* and 1 review in *Prog. Chem*.

12.2015–06.2016 **Crystallization and Phase Transformation of PB-1 and EPDM Blends**

▪ Studied the crystallization properties and phase transition behavior of polymer blends (PB-1/EPDM).

▪ Providing theoretical and experimental basis for the optimization of functional composites.

▪ Got the award of excellent graduation thesis.

Skills

Software:	National Computer Rank Examination (NCRE, Level 2)
	Good skills in MS Office, Chemical Office, LaTeX, Auto CAD
	Data analysis with Origin, STARe, Saxsgui, MestReNova, MATLAB
	Image evaluation with ImageJ, GIMP, NanoScope Analysis, Gwyddion
Languages:	English – Fluent German – A2.2
	Chinese – Native
Hobbies:	Hiking, Badminton, Running, Cooking

EIGENSTÄNDIGKEITSERKLÄRUNG

Hiermit erkläre ich an Eides statt, dass ich die vorliegende Arbeit selbstständig und ohne fremde Hilfe verfasst habe. Andere als die angegebenen Quellen und Hilfsmittel wurden nicht benutzt und die den benutzten Werken wörtlich oder inhaltlich entnommenen Stellen wurden als solche kenntlich gemacht.

Außerdem erkläre ich, dass ich die vorliegende Dissertation an keiner anderen wissenschaftlichen Einrichtung zur Erlangung eines akademischen Grades eingereicht zu haben.

Halle (Saale), den

_____   _____
            Datum   Fanfan Du